The Stereodynamics of the Inelastic Collisions of $NO(A^2\Sigma^+)$ with Atoms and Molecules

Thomas Frederick Murray Luxford

Submitted for the Degree of Doctor of Philosophy

Heriot-Watt University

Institute of Chemical Sciences

School of Engineering and Physical Sciences

May 2017

Abstract

A newly constructed crossed molecular beam velocity map imaging experiment is used to study vector correlations for the rotationally inelastic collisions of NO($A^2\Sigma^+$) with a range of atoms and diatomic molecules. Measurements are made of the differential cross section (DCS), and the $A_{q+}^{\{2\}}(\theta)$ moments. Where possible, the experimental vector correlations are compared to the results of quantum scattering (QS) calculations performed on literature *ab initio* potential energy surfaces (PESs).

Collisions of NO(A) with Ar and Ne lead to distinct features in the DCS, with a sharp, forward-scattered peak caused by scattering through the attractive region of the PES, and broader, higher-angle rotational rainbow peaks caused by scattering through the repulsive region of the PES. Sharp, angle-dependent fluctuations are observed in the $A_{q+}^{\{2\}}(\theta)$ moments. While there is generally good agreement between the experimental and QS results, deviations in the QS DCS highlight inaccuracies in the literature PESs.

Collisions of NO(A) with He are controlled entirely through interactions on the repulsive region of the PES. Excellent agreement between experiment and QS calculations was found for both the DCS and $A_{q+}^{\{2\}}(\theta)$ moments, showing that the literature PES is accurate. Collisions of NO(A) with D_2 produced results similar to He, showing that the uncalculated NO(A)-D_2 PES is similar to the NO(A)-He PES. Differences in the experimental results for the two systems were used to provide details on the differences between the two PESs.

DCSs and $A_{q+}^{\{2\}}$ moments are successfully recorded for the collisions of NO(A) with N_2, O_2 and CO as a function of rotational excitation of the unobserved partner. Trends in the DCSs for different degrees of rotational energy transfer to the unobserved collision partner are found to be consistent with collisions with the repulsive region of the PES leading to quenching collisions, rather than rotational energy transfer.

Acknowledgements

First and foremost, I would like to thank my supervisor Prof. Matthew Costen for all of his help and support over the course of my PhD. His detailed and patient descriptions have helped me understand a wide range of complicated subjects. I am especially grateful for his help in the last several months, reading drafts of this thesis and making corrections. Thanks also to my co-supervisor, Prof. Kenneth McKendrick, for all of his help and very insightful advice.

Dr Thomas Sharples cannot be thanked enough for all of his work on the experiment, designing and building the apparatus, writing the acquisition and fitting code, performing the quantum scattering calculations and much more besides. All while taking the time to answer whatever questions I had at any given moment.

Thanks to Joseph Leng for taking over the experiment from me. I hope it continues to produce interesting data and won't break too often.

Finally, thanks to everyone else from the laser lab, past and present, both for their help with the small things and for making the last three and a half years really enjoyable.

ACADEMIC REGISTRY
Research Thesis Submission

Name*:*	Thomas Luxford		
School:	Engineering and Physical Sciences		
Version: *(i.e. First, Resubmission, Final)*	First	Degree Sought:	Doctor of Philosophy

Declaration

In accordance with the appropriate regulations I hereby submit my thesis and I declare that:

1) the thesis embodies the results of my own work and has been composed by myself
2) where appropriate, I have made acknowledgement of the work of others and have made reference to work carried out in collaboration with other persons
3) the thesis is the correct version of the thesis for submission and is the same version as any electronic versions submitted*.
4) my thesis for the award referred to, deposited in the Heriot-Watt University Library, should be made available for loan or photocopying and be available via the Institutional Repository, subject to such conditions as the Librarian may require
5) I understand that as a student of the University I am required to abide by the Regulations of the University and to conform to its discipline.
6) I confirm that the thesis has been verified against plagiarism via an approved plagiarism detection application e.g. Turnitin.

* *Please note that it is the responsibility of the candidate to ensure that the correct version of the thesis is submitted.*

Signature of Candidate*:*		Date:	01/05/2017

Submission

Submitted By *(name in capitals):*	THOMAS LUXFORD
Signature of Individual Submitting:	
Date Submitted:	01/05/2017

For Completion in the Student Service Centre (SSC)

Received in the SSC by *(name in capitals):*			
Method of Submission *(Handed in to SSC; posted through internal/external mail):*			
*E-thesis Submitted (**mandatory for final theses)***			
Signature:		Date:	

Please note this form should be bound into the submitted thesis.
Academic Registry/Version (1) August 2016

Contents

Chapter 6 Conclusions and Outlook

Glossary

CCD	Charge coupled device
CMB	Crossed molecular beam
DCS	Differential cross section
FWHM	Full width at half maximum
KA	Kinematic apse
ICS	Integral cross section
LIF	Laser induced fluorescence
PEM	Photoelastic modulator
PES	Potential energy surface
QCT	Quasi-classical trajectory
QS	Quantum scattering
MCP	Microchannel plate
REMPI	Resonance enhanced multiphoton ionisation
SVD	Singular value decomposition
VMI	Velocity map imaging

Publications

Thomas R. Sharples, Thomas F. M. Luxford, Dave Townsend, Kenneth G. McKendrick, and Matthew L. Costen

J. Chem. Phys., 2015, **143**, 204301

Rotationally inelastic scattering of NO($A^2\Sigma^+$) + Ar: Differential cross sections and rotational angular momentum polarization

Thomas F. M. Luxford, Thomas R. Sharples, Dave Townsend, Kenneth G. McKendrick, and Matthew. L. Costen

J. Chem. Phys., 2016, **145**, 084312

Comparative stereodynamics in molecule-atom and molecule-molecule rotational energy transfer: NO($A^2\Sigma^+$) + He and D_2

Thomas F. M. Luxford, Thomas R. Sharples, Kenneth G. McKendrick, and Matthew L. Costen

J. Chem. Phys., 2016, **145**, 174304

Experimental testing of ab initio potential energy surfaces: Stereodynamics of NO($A^2\Sigma^+$) + Ne inelastic scattering at multiple collision energies

Thomas F. M. Luxford, Thomas R. Sharples, Kenneth G. McKendrick, and Matthew. L. Costen

J. Chem. Phys., 2016, **147**, 013912

Pair-correlated stereodynamics for diatom-diatom rotational energy transfer: NO($A^2\Sigma^+$) + N_2

Chapter 1

Introduction

1.1 General Introduction

Real world chemical systems, such as combustion, plasmas and the atmosphere are incredibly complex, with vast numbers of different atoms and molecules continuously interacting. Accurate modelling of these systems necessarily involves a detailed understanding of the constituent events which occur within them.[1]

On the most fundamental level, molecules interact through collisions. A collision occurs when two molecules pass each other at a short enough distance that they exert a force on each other. There are three possible outcomes of a collision. The simplest outcome is an *elastic collision*, in which the total kinetic energy of the molecules is conserved. In *inelastic collisions*, the total kinetic energy of the molecules is not conserved, as it is transferred to, or from, internal energy of one, or both, of the colliders. This internal energy can be rotational, vibrational, electronic, or some combination thereof.[2–6] Due to the much smaller spacing of molecular rotational levels, compared to vibrational levels, rotational energy transfer is by far the most commonly observed class of inelastic collision.[2] Electronic energy transfer is only accessible for certain collisions, in which the potential energy surfaces (see Section 1.2) of the two electronic states are coupled together through a conical intersection or an intersystem crossing.[6] Typically,

these electronically inelastic collisions "quench" a molecule in an electronically excited state back to the ground state, although transitions between two electronically excited states has also been observed. *Reactive collisions* lead to a rearrangement of the chemical bonds of the molecules, and lead to formation of one or more new chemical species.[7,8]

The field of molecular collision dynamics investigates the processes which govern the collisions of molecules, using both experimental and theoretical methods. Experimentally, one or more property of the molecules, such as velocity or quantum state, is selected prior to a collision, and either the same or a different parameter is measured after the collision. A related process which can be studied is photodissociation, often referred to as a half-collision, which is governed by the same forces as a collision. In these experiments, the dissociation of a stable molecule or a weakly bound complex is induced by the absorption of one or more photons, and properties of the products are recorded.[9,10] Correlations between the parameters before and after a collision or dissociation provide a fundamental insight into the forces which govern the event. Theoretical studies complement the experiments and are used to provide more detailed insight into the event.[11] The experiments presented in this thesis use a crossed molecular beam (CMB) experiment to study the rotationally inelastic collisions of NO($A^2\Sigma^+$) with a range of atomic and molecular collision partners.

1.2 The Potential Energy Surface

Whether a particular collision is elastic, inelastic or reactive will depend on the nature of the forces exhibited in the collision. These interactions determine the potential energy for a particular arrangement of the colliders, which can be obtained theoretically using the time-independent Schrodinger equation:[12]

$$\hat{H}\Psi = E\Psi \qquad (1.1)$$

Here, E is the energy of the system, Ψ is the wavefunction, and $\hat{H}$ is the Hamiltonian, which describes the interactions within the system. Within the Born-Oppenheimer approximation, motion of the nuclei and electrons can be treated separately, and $\hat{H}$ is given by:

$$\hat{H} = \hat{T}_N(R) + \hat{T}_e(r) + \hat{V}_{eN}(r,R) + \hat{V}_{NN}(R) + \hat{V}_{ee}(r) \qquad (1.2)$$

Here, $\hat{T}_N(R)$ and $\hat{T}_e(r)$ are the kinetic energies of the nuclei and electrons respectively, and $\hat{V}_{NN}(R)$, $\hat{V}_{ee}(r)$ and $\hat{V}_{eN}(r,R)$ are the potential energies at nuclear coordinates R, and electronic coordinates r.

By mapping the potential energy across a range of nuclear coordinates, a *potential energy surface* (PES) is generated. Within the Born-Oppenheimer approximation, the gradient of the PES describes the force applied to the molecules at that geometry,[13] meaning that the PES can be used to investigate the collisions which occur on it. The literature *ab initio* PESs used in this thesis are all for the non-reactive collisions of a diatom with an atom. These PESs can be most easily expressed in Jacobi coordinates: ***r***, the separation of the nuclei in the diatomic molecule; ***R***, the separation of the atom from the centre of mass of the diatomic molecule; and θ, the angle between the vectors ***r*** and ***R*** (see Figure 1.1). As the diatomic molecule is typically in the v = 0 vibrational level, fluctuations in length of ***r*** are negligibly small, and it can be fixed at the equilibrium bond length. This leaves the scalar variables R and θ, for which the potential energy needs to be mapped.

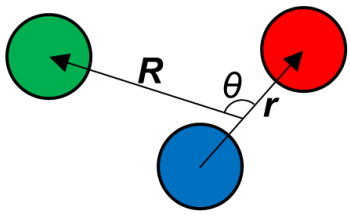

Figure 1.1: Jacobi coordinates, ***R***, ***r*** and θ for a three-atom system, described in the main text.

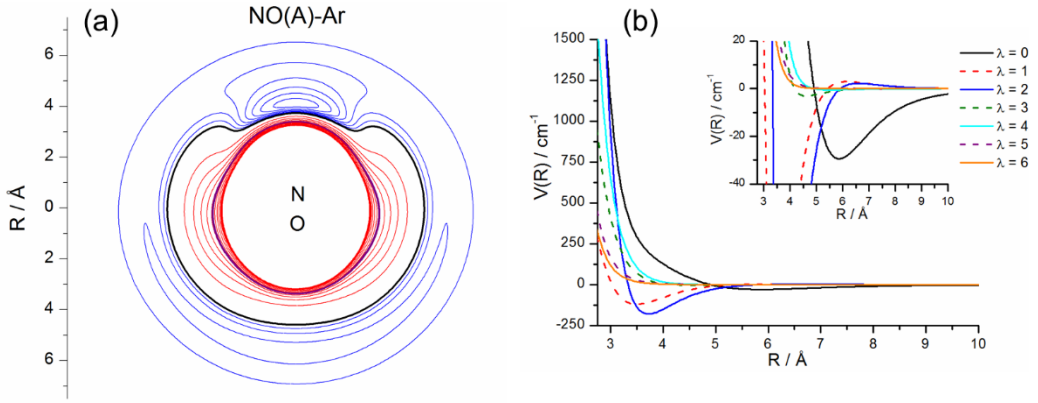

Figure 1.2: The *ab initio* NO(A)-Ar potential energy surface, calculated by Kłos *et al.*[14] (a) as a contour plot, where contours represent the potential energy of the coordinate, with red being positive (repulsive) energies in steps of 100 cm^{-1}, blue being negative (attractive) energies in steps of 10 cm^{-1}, and black being 0 cm^{-1} (b) as an expansion of Legendre moments.

In such a system, the potential energy is typically calculated on a grid of discrete values of R and θ. A function is fitted to this grid of coordinates to obtain a representation of the full surface. The most intuitive way to represent the PES is through a contour plot, which is shown in Figure 1.2(a) for the NO(A)-Ar PES, calculated by Kłos *et al.*[14] In this representation, the N and O atoms of NO(A) are fixed at the relevant R and θ coordinates, such that **r** is fixed along the 0° to 180° line with the centre of mass of the diatomic molecule at the origin and the contours indicate the potential energy for different coordinates of the Ar atom. The other representation that will be used in this thesis is a plot of the Legendre moments of the PES as a function of R, as shown in Figure 1.2(b). Here, the PES is represented as an expansion of radial terms showing the contribution of different orders, λ, of the Legendre moments, $P_\lambda(\cos\theta)$. These plots provide a convenient representation of the anisotropy of the PES, or how the potential energy varies with θ at a fixed R.

The broad structure of all diatom-atom PESs are similar. At short distances, the potential is dominated by repulsive forces, while at longer ranges, attractive forces are more prominent. The exact details of the PESs vary considerably from system to system, including the gradient of the repulsive region, the depth of the attractive region and the anisotropy across the entire range of R.

1.3 Theory of Collisions

1.3.1 Elastic Atom + Atom Collisions

To begin, the classical collisions of two hard-shell atoms, with well-defined radii r_1 and r_2, will be considered.[1] In the centre-of-mass frame, the two atoms move directly towards each other with trajectories parallel, and offset by the impact parameter, b. If the value of b is less than $r_1 + r_2$, there will be a collision, while if it is larger, there will not. The size of the $r_1 + r_2$ "target" for which a collision will occur gives the collision cross section, σ:

$$\sigma = \pi(r_1 + r_2)^2 \tag{1.3}$$

When a collision occurs, atoms with a value of b will lead to a single angle of deflection, χ, which for a hard-shell potential can be simply calculated, as:

$$\chi = 2\arccos\left(\frac{b}{r_1 + r_2}\right) \tag{1.4}$$

Next, a realistic potential will be considered. As described in the Section 1.2, the forces applied to the colliding species at a given set of coordinates can be approximated by the gradient of the potential. In a typical system, for very long range trajectories, with a high b, there will be a very small interaction of the atoms, and χ will be zero. As b decreases, the trajectories sample the attractive region of the potential more strongly and χ becomes more negative (scattering towards the other atom), until the attractive forces are counteracted by the shorter-range repulsive forces. Scattering which occurs at the most negative deflection is referred to as an *L-type rainbow*. As b decreases further and the

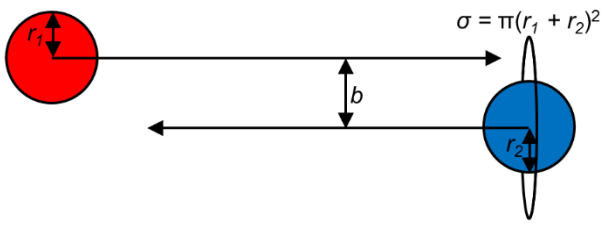

Figure 1.3: Collision of two hard shell two atoms showing the impact parameter, b, and the collision cross section, σ, described in the main text.

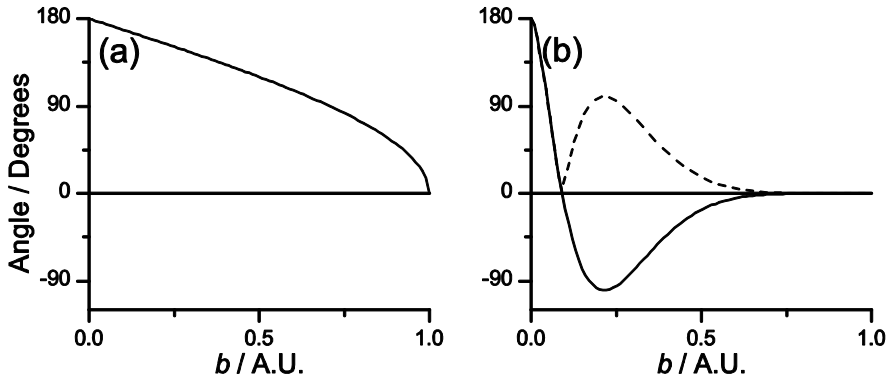

Figure 1.4: The deflection functions, showing the effect of b on χ (solid line) and θ (dashed line), for the classical elastic collisions of two atoms on (a) a hard-shell potential, (b) a realistic potential.

trajectories sample the repulsive region more strongly, χ increases, passing through zero and becoming positive (scattering away from the other atom). The point at which the attractive and repulsive forces are equivalent, and $\chi = 0$ is referred to as *glory* scattering. The relationships between χ and b are shown as deflection functions in Figure 1.4 for both hard-shell and realistic-potential collisions of two atoms.

Because the scattering systems are cylindrically symmetric, the sign of χ cannot be measured, and the systems are therefore usually given in terms of the scattering angle, θ, where $\theta = |\chi|$. Experiments can also not resolve b, which is averaged across all possible values. Typically, experimental measurements are made of the differential cross section (DCS), $d\sigma/d\omega$, which is defined as the flux of atoms scattered into a given solid angle, $d\Omega = \sin\theta\, d\theta\, d\phi$, divided by the incident flux of atoms. It is related to the deflection function by the equation:

$$\frac{d\sigma}{d\omega} = \sum \frac{b}{\sin\theta\, d\theta/db} \qquad (1.5)$$

Equation 1.5 leads to singularities when $d\theta/db = 0$, which occurs for the L-type rainbow and glory scattering, at which the densities of the classical scattering trajectories rise to infinity (in reality, these singularities are reduced to finite values by interference effects, see below). The structure of the DCS is very closely related to the structure of the form of the potential, especially the rainbow angle, which depends on the depth of the attractive well.[1,15]

Quantum mechanically, when two trajectories lead to collisions at the same θ, the DCS will exhibit interference effects, which cannot be modelled classically. If a classical scattering trajectory is treated as a wave, the two trajectories will undergo different phase shifts over the course of the collision, and so may constructively or destructively interfere. For scattering at angles greater than the *L*-type rainbow, there is only one trajectory which leads to a given angle, and so interference effects are not observed. For angles less than the *L*-type rainbow though, three trajectories lead to every angle, and so interference effects are observed, adding additional structure to the DCS.[15]

1.3.2 Inelastic Molecule + Atom Collisions

The above description of the elastic scattering of two atoms will now be extended to cover the features observed in the DCSs of rotationally inelastic scattering of a diatomic molecule with an atom. Different trajectories lead to different amounts of torque being applied to the diatomic molecule, and so different degrees of rotational excitation.

L-type rainbows occur in atom + atom elastic scattering from collisions which probe the attractive region of the PES.[1] They are also observed in inelastic scattering, where the *L*-type rainbow angle, θ_L, is approximated by:[16]

$$\theta_L = \frac{\varepsilon}{E_{col}} \tag{1.6}$$

Here, ε is the average attractive well depth of the PES and E_{col} is the collision energy. For inelastic collisions, *L*-type rainbows are most prominently observed for collisions which lead to a relatively low amount of rotational excitation, as the amount of torque which can be applied by collisions through the attractive region is typically much lower than the more anisotropic repulsive region.

Trajectories which probe the repulsive region of the PES give rise to *rotational rainbow* peaks, which are not observed in atom + atom scattering. The rotational rainbow angle corresponds to the minimum scattering angle at which sufficient translational motion can be converted into rotation of the molecule, and smaller angles than this are

classically forbidden.[17] For a molecule + atom collision, modelled by a hard-shell ellipsoidal potential with major and minor axis *A* and *B*, respectively, the rotational rainbow angle, θ_r, is given by:[18]

$$\sin\left(\frac{1}{2}\theta_r\right) = \frac{\Delta j}{2(A-B)} \tag{1.7}$$

The rotational rainbow angle for heteronuclear diatomic molecules will be different for collisions with the two ends of the molecule, leading to multiple rotational rainbow angles, and a more complex structure for the DCS.

As with atom + atom scattering, interference effects can cause additional features in the DCS. Diffraction oscillations are high-frequency fluctuations in the DCS which arise from interference between trajectories scattering at negative and positive deflection angles. The phase difference between the two sets of trajectories varies smoothly with scattering angle, leading to regular oscillations in the DCS.[19] Purely repulsive collisions can lead to measurable signal in the physically forbidden region of the DCS thanks to Fraunhofer diffraction interference effects.[20] Interference effects are also observed in rotational rainbow structure, from trajectories for collisions which occur at opposite ends of a heteronuclear diatomic molecule.[21,22]

1.4 Preparation of Molecules

Experiments which probe bimolecular collisions rely on a large number of techniques. These can be split into two categories: those used to prepare the molecules before the collision and those that detect them after the collision. The different properties of the molecules that can be prepared, and the techniques used to prepare them are discussed in this section.

1.4.1 Initial Quantum State

Molecules in different rotational and vibrational states will undergo considerably different forces over the course of a collision. It is therefore important to select as narrow a range of energy levels before the collision as is possible.

Molecular beams are a useful way to select the initial quantum state of a molecule. As a gas passes through a small orifice from a high-pressure region into a vacuum, it undergoes rapid adiabatic collisional cooling, leading to the population of a narrow distribution of the lowest-energy rotational levels. The efficiency of the collisional cooling varies greatly for different gases and different expansion conditions.[23] It is common to seed the molecule of interest at a low partial pressure in a rare gas, as this leads to more efficient cooling, where a narrow distribution of the lowest energy rotational levels is typically obtained.[23,24] Molecular beams are limited in that they cannot distinguish between quantum states with similar energies. This is a particular concern for molecules such as NO($X^2\Pi$), which exhibit Λ-doublets (see Section 1.9), which are nearly isoenergetic, but have very different collision dynamics, due to their different parities.

A modern improvement for the state selectivity of a molecular beam is to pass it through a hexapole state selector. As a molecular beam passes through the hexapole state selector it is exposed to an electrostatic field. This field leads to a stable path for only a single quantum state, and thus, a very high quantum state purity of the selected molecule in the molecular beam, with almost perfect purities obtained in modern experiments. Hexapole state selection has been used by Stolte and co-workers[17,25,26] and Brouard and co-workers,[27–30] among other groups[31–33] in CMB experiments. Hexapole focussing uses the Stark effect, and so it is only applicable to non-Σ state molecules with a non-zero dipole moment.[34] Stark decelerators also use the Stark effect to obtain a high quantum state selectivity using electric fields. The most important difference between a Stark decelerator and a hexapole state selector is that the former is also able to control the speed of the molecular beam, which is described in more detail in Section 1.4.2.[34,35]

For experiments investigating the collisions of electronically excited molecules, as presented in this thesis, an optical preparation step is typically used.[36–48] If an isolated spectroscopic transition is used for this step, only a single rovibrational level of the

excited state molecule will be generated. This technique can be limited by spectral congestion, which occurs when the wavelength of two, or more, spectroscopic transitions overlap, meaning that multiple rotational levels will be prepared simultaneously. In addition to electronically excited states, optical preparation can be used to prepare vibrationally excited levels of the ground electronic state, either by stimulated emission pumping[49] or stimulated Raman pumping.[50]

1.4.2 Initial Velocity

Molecular beams are also effective tools for the selection of velocities, as the random motion of gas behind the valve is converted into a narrow, highly directional distribution as it passes through the orifice of the valve. The initial angular distribution of a molecular beam varies considerably depending on the design of the valve.[51] The angular distribution can be greatly reduced by passing the molecular beam through one or more collimating skimmers, which only allow the passage of a narrow range of angles around the centreline of the beam. The distribution of speeds in the molecular beam is often found to be well defined by a Gaussian function. The mean speed of the molecular beam depends on the mass and heat capacity of the gas, as well as the source temperature.[23] This means that the mean speed can be controlled by seeding the target gas in different carrier gases, or by heating or cooling the valve.

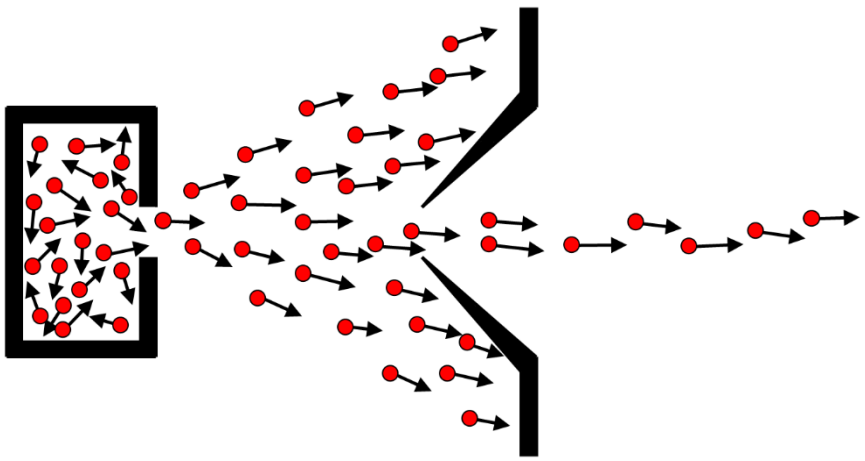

Figure 1.5: Schematic view of a molecular beam source region and skimmer. The red circles represent the position of molecules within the gas, and the arrows represent their velocity.

As stated in Section 1.4.1, the speed distribution of a molecular beam can be controlled much more finely by passing it through a Stark decelerator. For molecules which exhibit a first-order Stark effect, an electric field creates high and low-potential energy regions along the beam path. By rapidly altering the electric field, a subset of the molecules in the beam can be decelerated to any arbitrary velocity.[34,35] In addition to being able to arbitrarily set the speed of the molecular beam, the distribution of speeds obtained using a Stark decelerator is much narrower than is possible with a typical molecular beam. Stark decelerators have been used by van de Meerakker and co-workers to study the collisions of NO(X) with a range of different rare gases, making use of the narrow speed distribution that the technique provides.[20,31,52,53] While it is an extremely powerful tool, the Stark decelerator only works for molecules with a non-zero dipole moment, and an appropriate first-order Starke effect (and hence for those not in a Σ state), and so the technique is not universally applicable. For atoms and molecules that have a small or zero dipole moment, but possess an unpaired electron, a Zeeman slower can be used instead, which uses magnetic fields to control the speed of the beam.[35,54,55]

1.4.3 Initial Orientation of the Bond Axis

Using the same principles as a hexapole state selector or a Stark decelerator, an electric field can be used to orient the bond axis of a molecule prior to the collision. The dipole moment of a molecule will interact with a static electric field, such that one orientation of the bond axis has a lower potential energy than the other. Using this method, collisions with opposite ends of a molecule can be probed independently.[26,56,57]

1.4.4 Initial Rotational Angular Momentum Polarisation

The simplest method to generate an initial polarisation of the rotational angular momentum of a molecule is through optical preparation (see Section 1.4.1). The probability of a photon being absorbed depends on the overlap of the electric vector of the photon with the transition dipole moment, which is linked to the rotational angular

momentum vector (see Figure 1.6).[58] A linearly polarised laser beam will lead to an alignment in the rotational angular momentum of the molecules, while a circularly polarised laser beam will lead to an orientation of the rotational angular momentum as well as an alignment.[58] See Section 1.6 for more details about the polarisation of angular momentum.

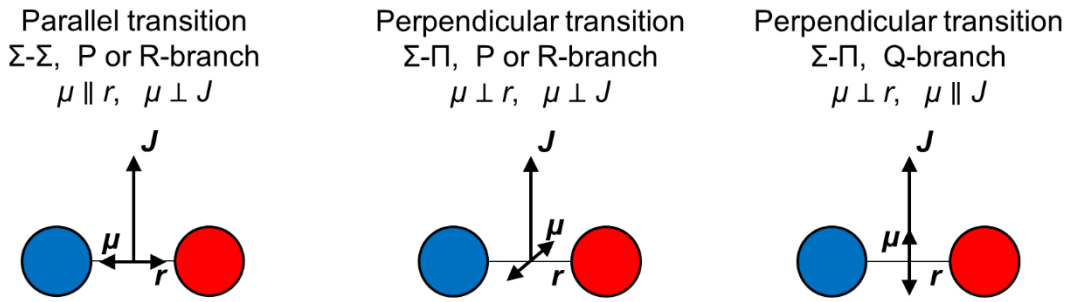

Figure 1.6: The relationship between the bond axis of a diatomic molecule, ***r***, the transition dipole moment, ***μ*** and the angular momentum vector, ***J***, for Σ-Σ and Σ-Π transitions. Adapted from Reference [58].

1.5 Observables

Once a system has been prepared using the techniques described in the previous section and collisions have occurred, one or more property of the collided molecules is measured. This section will describe the different properties that can be measured, and the techniques used to measure them.

1.5.1 Final Quantum State

The overwhelming majority of modern experiments studying collisions are sensitive to the final quantum state of the target molecule using spectroscopic methods. The simplest technique which can be used for this is absorption spectroscopy, which measures the amount of light absorbed by a sample as a function of wavelength.[59,60] In laser-induced fluorescence (LIF), a laser is used to optically prepare a molecule in an electronically excited state, and as the molecule fluoresces back to the ground state, the emitted photon

is detected.[59,61,62] Resonance enhanced multiphoton ionisation (REMPI) uses multiple photons from the same or different laser sources to selectively ionise a molecule from a single quantum state through an intermediate state. The resulting ion is then detected in some way.[59] The experiments in this thesis use a 1 + 1′ REMPI scheme to state-selectively ionise NO(A) through an intermediate $E^2\Sigma^+$ state.

The signal sizes obtained using these methods are directly related to the population of the molecules in the different quantum states. Therefore, experiments can determine the relative population distribution, either as a rate constant or an integral cross section (ICS) from the relative signal sizes.[31,63,64] In addition to experiments that purely measure the relative population of the different quantum states, many experiments record a different property, such as final velocity or rotational angular momentum polarisation, as a function of quantum state.

1.5.2 Final Velocity

The final velocity of a molecule is one of the most fundamental properties to measure, and its measurement can reveal a great amount of information. The final velocity of a molecule can be split into two components, its final speed and its angle relative to the initial velocity, both of which can be measured.

Early CMB experiments used a rotatable mass spectrometer to measure the angular distribution of scattered molecules.[65–67] The ionisation region of the mass spectrometer was physically moved to different experimental geometries, so that it detected product flux as a function of angle, which was converted into a velocity distribution. The speed component of the molecule could be determined from the time-of-flight, from a fixed zero-time. A laser-based ionisation technique can allow for quantum state resolution of the scattered products, however, the practical difficulties associated with aligning a laser with the rotatable source mean that ionisation is typically done with a general source, such as electron-impact ionisation. Even without laser-based ionisation, the identity of the detected molecule can be determined from its mass to charge ratio. This also enables the detection of multiple scattered products simultaneously, which is useful in certain

experiments. Experiments which use rotatable mass spectrometer detection typically have very long acquisition times, and, because different scattering angles are recorded separately, are therefore are prone to suffer from detection biases caused by subtle experimental instabilities. For these reasons, rotatable mass spectrometer detectors have been replaced by the two techniques described below, and are only used when the target molecule does not have a convenient spectroscopy, or where multiple products must be detected simultaneously.[68]

A much more efficient method to measure the final velocity in a CMB experiment is to use velocity map imaging (VMI). VMI is an extremely powerful technique, which allows for the precise measurement of a molecule's velocity.[69–71] First, a molecule is ionised, typically using a REMPI scheme, within an electric field, which accelerates the ion towards a position-sensitive detector. The electric field also focusses the ions, such that the position the ion strikes the detector depends entirely on the molecule's initial velocity in the plane of the detector at the moment of ionisation, and not on its position. The 2-D distribution of velocities recorded can be reconstructed in order to obtain the full 3-D distribution.[71] Alternately, the 3-D distribution of the velocity can be directly extracted from the time-of-flight of each ion strike, which can be determined using slice-imaging,[72,73] or using a time-resolved detector such as a PImMS camera[74,75] or a delay line anode.[76] VMI is widely used in dynamics experiments, both for the study of bimolecular collisions[32,77–80] and of single-molecule photo-fragmentation.[70,81–84] VMI is the technique used to measure the final velocity in the experiments in this thesis. The interpretation of a velocity map image acquired for the CMB experiment of this thesis will be explained in Section 1.7.

An alternate method for detection product velocity is Doppler spectroscopy. As the Doppler profile of a transition is related to the velocity of the target molecule along the laser propagation axis, a high-resolution laser can be used to determine the velocity distribution.[85,86] This technique is only sensitive to the velocity in a single direction, making the reconstruction of the full 3-D velocity distribution more complex, but it can be used for molecules which are not amenable to ionisation, such as CN.[87]

1.5.3 Final Rotational Angular Momentum Polarisation

Polarisation of the rotational angular momentum vector induced by a collision can be detected using a polarised laser beam in the detection scheme.[88] The detection sensitivity depends on the overlap of the electric vector of the laser with the transition dipole moment, and so is also linked to the polarisation of the rotational angular momentum vector (see Figure 1.6). Therefore, different signal sizes from different relative geometries of the probe laser and experimental axis can be used to recover the distribution of the rotational angular momentum. This polarisation is typically quantified as a suitable tensor expansion, for example, the Hertel-Stoll renormalized angular momentum moments ($A_{q\pm}^{\{k\}}$),[89] which are used throughout this thesis. The rank k = 1 moments describe the orientation of the rotational polarisation, and the rank k = 2 moments describe the alignment within a defined reference frame.[58,90] An explanation of the origins and meaning of these moments will be provided in Section 1.6.

In experiments where there is sensitivity to both the final velocity and final rotational angular momentum polarisation (such as CMB and photo-loc[44,91,92] experiments), the rotational angular momentum polarisation is typically reported as a function of scattering angle, for example, in the form of the angle dependent polarisation moments, $A_{q+}^{\{2\}}(\theta)$.[27,93]

1.6 Angular Momentum

1.6.1 Classical Description

The rotation of a molecule (or any other object) can be most conveniently defined by its angular momentum vector, ***J***. This can be polarised by a chemical event, with the result that it is more likely to point in certain directions. Polarisation of ***J*** can result in either an alignment, an orientation or both (although in practice, an orientation cannot be generated without an alignment). The polarisation is defined along a reference axis, ***Z***. In an orientation, ***J*** is preferentially pointed parallel or antiparallel to ***Z***, while in an alignment, ***J*** is preferentially pointed along or perpendicular to ***Z***, but has no directionality.

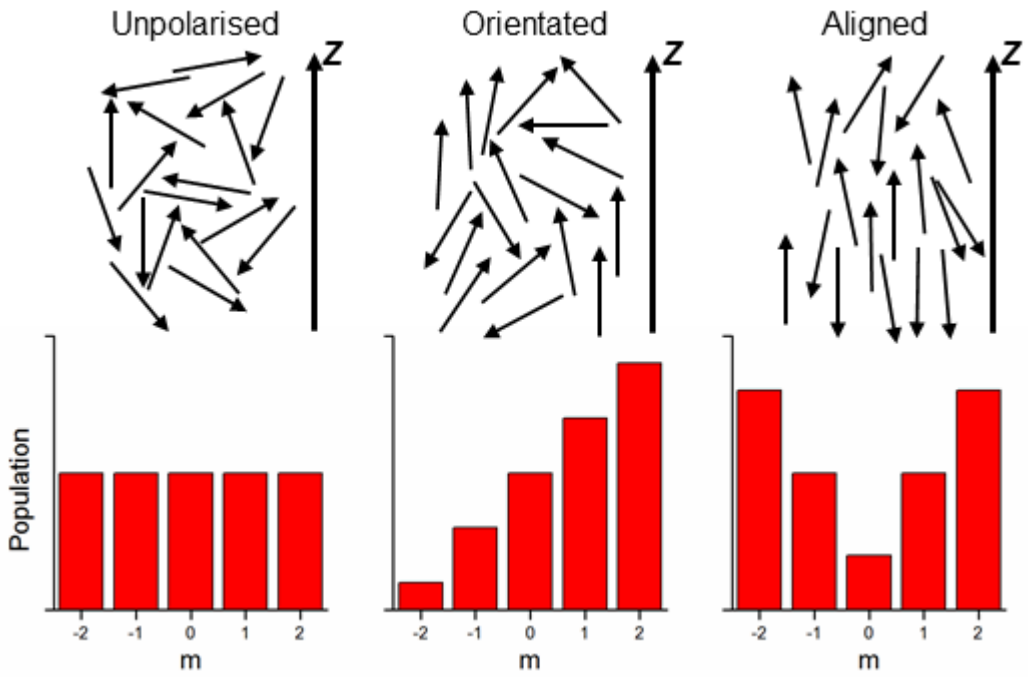

Figure 1.7: A simple representation of the polarisation of angular momentum vectors to reference axis ***Z***, with left: an unpolarised sample; middle: an oriented sample; right: an aligned sample. Top row: a classical representation, where the angular momentum vector is shown as an arrow. Bottom row, a quantum mechanical representation, where the polarisation of the angular momentum vector is provided by the distribution of magnetic sublevels, *m*.

Classically, ***J*** has a continuous distribution with respect to ***Z***, which can be described using the polar coordinates θ_j and ϕ_j. The distribution of θ_j and ϕ_j is most conveniently described as an expansion of modified spherical harmonics, $C^*_{k,q}(\theta_j,\phi_j)$:

$$P(\theta_j,\phi_j)=\frac{1}{4\pi}\sum_{k=0}^{\infty}\sum_{q=-k}^{k}(2k+1)a_q^{(k)}C^*_{k,q}(\theta_j,\phi_j) \qquad (1.8)$$

Here, $a_q^{(k)}$ are the expansion coefficients, which give the absolute contribution of $C^*_{k,q}(\theta_j,\phi_j)$ to the probability distribution.

As long as the system is cylindrically symmetric with respect to ***Z***, only the $q = 0$ moments will be non-zero. The $a_0^{(0)}$ moment is the monopole moment, which purely describes the population of the state. The $a_0^{(1)}$ and $a_0^{(2)}$ terms describe the cylindrically symmetric first and second order moments of the angular momentum distribution, corresponding to an orientation and an alignment respectively. Higher order terms

similarly describe higher order orientations and alignments of the distribution. If the cylindrical symmetry is broken, then the $q \neq 0$ moments will need to also be considered. These moments describe the distribution of the projection of ***J*** onto the ***XY*** plane of the reference frame.[58,94]

1.6.2 Quantum Description

Quantum mechanically, the direction of ***J*** is quantised, and is best represented by the populations of, and the coherences between, the magnetic sublevels, *M*, which describe the projection of ***J*** onto the ***Z*** axis.[13] This information is contained within the elements of the density matrix, $\rho_{m'm}$, where the diagonal elements give the *M* state distribution. The off-diagonal elements represent the coherences between the different *M* states, which contain information about the ***XY*** projection of ***J***.

Measurements of the rotational angular momentum polarisation are most commonly made based on the interaction of the molecule with light. The interaction of light with the molecule via the transition dipole moment and the electric vector of the light is best described by a spherical tensor approach, where the spherical tensors are operators with the same rotation properties as the spherical harmonics. It is therefore typical to describe the measurements of the angular momentum polarisation as the spherical tensor moments, which are the expectations of the spherical tensors, and act as the quantum analogue of the classical alignment moments defined above. The density matrix and the spherical tensor moments are freely interconvertible using the Equations 1.9 and 1.10.

$$\rho_q^{(k)} = \sum_{M',M} (-1)^{J-M'} (2k+1)^{1/2} \begin{pmatrix} J & k & J \\ -M & -q & M \end{pmatrix} \rho_{m'm} \tag{1.9}$$

$$\rho_{m'm} = \sum_{k,q} (-1)^{J-M'} (2k+1)^{1/2} \begin{pmatrix} J & k & J \\ -M & -q & M \end{pmatrix} \rho_q^{(k)} \tag{1.10}$$

Here, $\begin{pmatrix} J & k & J \\ -M & -q & M \end{pmatrix}$ is a Wigner 3j symbol, which arises in the angular momentum theory of coupling two angular momenta.[95] The spherical tensor moments are renormalized to give the polarisation moments, $A_q^{(k)}$, using Equation 1.11. The representation of the distribution of $\boldsymbol{J}$ as the polarisation moments provides a more convenient set of limits, which do not depend on the magnitude of $\boldsymbol{J}$.

$$A_q^{(k)} = \frac{(-1)^q c(k)}{[J(J+1)]^{k/2}} \frac{\left(J \| J^{(k)} \| J\right)}{\sqrt{2k+1}} \rho_{-q}^{(k)} \tag{1.11}$$

Here, $\left(J \| J^{(k)} \| J\right)$ is the reduced matrix element,[95] and $c(k)$ is a normalisation value where $c_1 = [j(j+1)]^{-1/2}$ and $c_2 = [j(j+1)(2j+3)(2j-1)]^{-1/2}$.[58] The $A_q^{(k)}$ polarisation moments as described above have complex values. Real-valued linear combinations of these moments, $A_{q\pm}^{\{k\}}$, are constructed using Equations 1.12-1.14.[89] Note that the curly brackets are used to specifically refer to the Hertel-Stoll renormalised polarisation moments used throughout this thesis.[89]

$$A_{0+}^{\{k\}} = A_0^{(k)} \tag{1.12}$$

$$A_{q+}^{\{k\}} = \frac{1}{\sqrt{2}} \left[(-1)^q A_q^{(k)} + A_{-q}^{(k)} \right], \qquad 1 \le q \le k \tag{1.13}$$

$$A_{q-}^{\{k\}} = \frac{1}{i\sqrt{2}} \left[(-1)^q A_q^{(k)} - A_{-q}^{(k)} \right], \qquad 1 \le q \le k \tag{1.14}$$

The quantum interpretations of the rank k = 1 and k = 2 polarisation moments are provided in Table 1.1. Only moments with rank k = even and component q+, and moments with rank k = odd and component q- are generated for non-chiral collisions, because of the reflection symmetry in the **k**-**k**′ plane.[94]

Table 1.1: Meanings of the Hertel-Stoll normalised $A_{q\pm}^{\{k\}}$ moments, adapted from Reference [94].

	Physical meaning		Directional meaning	
	Spherical harmonics	Quantum Operator	Positive values	Negative values
$A_{1-}^{\{1\}}$	$\langle \sin\theta\sin\phi \rangle$	$c_1\langle j_y \rangle$	Orientation parallel to **Y**	Orientation antiparallel to **Y**
$A_{0+}^{\{1\}}$	$\langle \cos\theta \rangle$	$c_1\langle j_z \rangle$	Orientation parallel to **Z**	Orientation antiparallel to **Z**
$A_{1+}^{\{1\}}$	$\langle \sin\theta\cos\phi \rangle$	$c_1\langle j_x \rangle$	Orientation parallel to **X**	Orientation antiparallel to **X**
$A_{2-}^{\{2\}}$	$\sqrt{3}\langle \sin^2\theta\sin 2\phi \rangle$	$2\sqrt{3}c_2\langle j_x j_y + j_y j_x \rangle$	Alignment along **X+Y**	Alignment along **X-Y**
$A_{1-}^{\{2\}}$	$2\sqrt{3}\langle \cos\theta\sin\theta\sin\phi \rangle$	$2\sqrt{3}c_2\langle j_y j_z + j_z j_y \rangle$	Alignment along **Y+Z**	Alignment along **Y-Z**
$A_{0+}^{\{2\}}$	$\langle 3\cos^2\theta - 1 \rangle$	$2c_2\langle 3j_z^2 - j^2 \rangle$	Alignment along **Z**	Alignment perpendicular to **Z**
$A_{1+}^{\{2\}}$	$2\sqrt{3}\langle \cos\theta\sin\theta\cos\phi \rangle$	$2\sqrt{3}c_2\langle j_z j_x + j_x j_z \rangle$	Alignment along **X+Z**	Alignment along **X-Z**
$A_{2+}^{\{2\}}$	$\sqrt{3}\langle \sin^2\theta\cos 2\phi \rangle$	$2\sqrt{3}c_2\langle j_x^2 - j_y^2 \rangle$	Alignment along **X**	Alignment along **Y**

1.7 The Crossed Molecular Beam Velocity Map Imaging Experiment

CMB experiments are widely used to study the interactions of atoms and molecules under single-collision conditions. Two molecular beams (described in Sections 1.4.1 and 1.4.2) intersect, and the density of molecules is such that only a small number of collisions occur, and there are a negligible number of secondary collisions. These experiments can be used to measure the DCS, which is obtained from the distribution of final velocities, typically measured using VMI. The angle-dependent rotational polarisation moments, described in Section 1.6, can also be measured using a polarised laser in the detection scheme.

1.7.1 The Differential Cross Section

A velocity map image obtained from the CMB experiment used in this thesis is presented in Figure 1.8. The structure of the image can be understood using the overlaid Newton diagram, which shows the correlation of the different relevant vectors in velocity space. The structure of the Newton diagram will be described here for a system in which NO(A) undergoes collisions with an atom or molecule, M. The molecular beams control the initial velocities of the two colliders in the laboratory (lab) frame, $\mathbf{v_{NO}}$ and $\mathbf{v_M}$. From these, the velocity of the centre-of-mass, $\mathbf{v_{CoM}}$, and the relative velocity vector, $\mathbf{k}$, are calculated using Equations 1.15 and 1.16, respectively.

$$\mathbf{v_{CoM}} = \frac{m_{NO}\mathbf{v_{NO}} + m_M \mathbf{v_M}}{m_{NO} + m_M} \tag{1.15}$$

$$\mathbf{k} = \mathbf{v_{NO}} - \mathbf{v}_M \tag{1.16}$$

Here, m_{NO} and m_M are the masses of the NO and the unobserved collider respectively. The collision energy, E_{Col} for the system is calculated using Equation 1.17.

$$E_{Col} = \frac{1}{2}\mu \mathbf{k}^2 \tag{1.17}$$

Where μ is the reduced mass of the collision:

$$\mu = \frac{m_{NO} m_M}{m_{NO} + m_M} \tag{1.18}$$

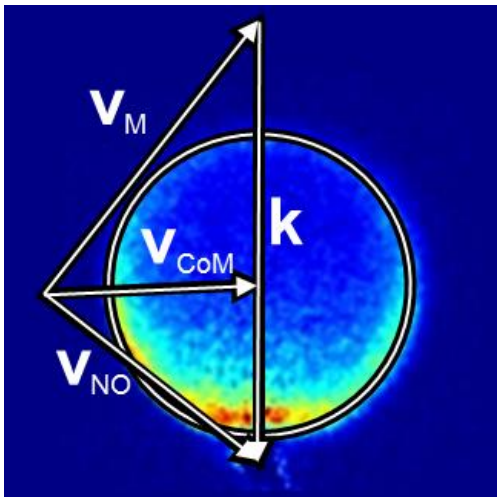

Figure 1.8: A velocity map image obtained for the collisions of NO(A, v = 0, N = 0, j = 0.5) with Ne at a mean collision energy of 523 cm^{-1} and final rotational level, N' = 8. The overlaid Newton diagram shows the correlation of different velocity vectors relevant to the experiment, which are described in the main text.

For the collisions of NO(A) with an atom, some of the collision energy will be transferred into rotational excitation of NO(A). Because the quantum state of the NO(A) is selected before the collision, and the REMPI detection scheme selects a single final rotational quantum state, the energy transferred into rotation (E_{rot}) is known. The remaining energy, E_{final} is distributed into translational energy of the two recoiling colliders (Equation 1.19). From this, the magnitude of the relative velocity vector after the collision, $\mathbf{k'}$, can be calculated from the inverse of Equation 1.17 (Equation 1.20), which can be used to determine the final speeds of the colliders in the centre-of-mass frame, $\mathbf{u'_{NO}}$ and $\mathbf{u'_{Col}}$ (Equations 1.21 and 1.22 respectively).

$$E_{final} = E_{Col} - E_{rot} \tag{1.19}$$

$$\mathbf{k}' = \left(2\frac{E_{final}}{\mu} \right)^{1/2} \tag{1.20}$$

$$\mathbf{u'_{NO}} = \frac{\mathbf{k'}}{1 + m_{NO}/m_M} \tag{1.21}$$

$$\mathbf{u'}_M = \frac{\mathbf{k'}}{1 + m_M/m_{NO}} \tag{1.22}$$

Because of conservation of linear momentum, for a given final rotational level of NO(A), $\mathbf{u'_{NO}}$ will be distributed on the surface of a *Newton sphere* in velocity space, centred on $\mathbf{v_{CoM}}$. This 3-D sphere is projected onto the 2-D detector, to produce the scattering image shown in Figure 1.8. The possible final values of $\mathbf{u'_{NO}}$ in the plane of the detector are represented by the circle on the Newton diagram. Blurring of the velocity map image occurs because the molecular beams lead to a distribution of $\mathbf{v_{NO}}$ and $\mathbf{v_M}$, rather than single values. This means that each individual collision will have a slightly different value of $\mathbf{k}$ and $\mathbf{v_{CoM}}$, leading to a distribution of the central position and radius of the Newton sphere. Newton diagrams are usually shown corresponding to the mean values of $\mathbf{v_{NO}}$ and $\mathbf{v_M}$ for a system.

The distribution of $\mathbf{u'_{NO}}$ onto the surface of this Newton sphere is described by the DCS, which, as described in Section 1.3, gives the probability of scattering into a solid angle, $\omega = \sin(\theta)\, d\theta\, d\phi$, and is typically reported in units $Å^2\ sr^{-1}$. As is the case for all two-vector correlations, the DCS is uniform with respect to ϕ, and so depends entirely on the angle θ. For the experiments in this thesis, the DCS is recorded as a function of the final rotational level of NO(A).

For collisions of NO(A) with a molecular partner, the collision energy is partitioned into rotation and translation of both the NO(A) and the unobserved collider, while the detection scheme is sensitive purely to the final rotational level of NO(A). This leads to a situation where $\mathbf{u'_{NO}}$ is distributed onto the surfaces of multiple nested Newton spheres, which are simultaneously projected onto the 2-D detector. This effect is shown in Newton diagrams in Figures 4.10 and 5.1.

1.7.2 Rotational Alignment Moments

In addition to the final velocity, this CMB VMI experiment is also sensitive to rotational alignment of the scattered NO(A) molecules. This alignment will vary depending on the scattering angle, θ, making it an example of a three-vector **k**-**k′**-**j′** correlation. Conventionally, the polarisation of **j′** is represented in the scattering frame, with the ***Z*** axis parallel to **k**, and with ***X*** lying in the **k**-**k′** plane. As was described in Section 1.5.3, it is possible to measure the polarisation of the rotational alignment using polarised lasers in the detection scheme.

In the experiments in this thesis, a linearly polarised laser is used in the 1 + 1′ REMPI scheme, providing sensitivity to the rank k = 2 angle-dependent alignment moments, $A_0^{\{2\}}(\theta)$, $A_{1+}^{\{2\}}(\theta)$ and $A_{2+}^{\{2\}}(\theta)$, which are scattering angle-dependent forms of the moments defined in Section 1.6. These moments affect the intensities of the images in different ways, which vary depending on the angle between the electric vector of the laser and **k** (see Equation 2.5). By measuring the differences in intensity caused by the different polarisations of the probe laser, the values of the alignment moments can be determined. An example of a pair of experimental images recorded using the two different probe laser polarisations in this experiment are shown in Figure 1.9. If there was no rotational alignment, the two images would be identical. The details of the effect of the different rotational alignment moments on the images in this experiment are discussed in Section 2.10.1.

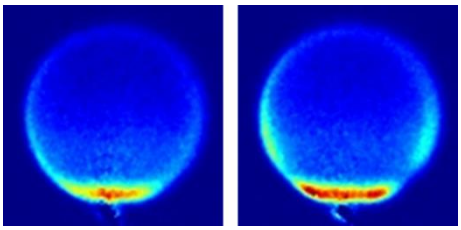

Figure 1.9: Experimental scattering images obtained for the collisions of NO(A, v = 0, N = 0, j = 0.5) with Ne at a mean collision energy of 523 cm^{-1} and final rotational level, N' = 7. The two images show the scattering images obtained with two different probe laser polarisations (see Chapter 2), and differences in intensity are the result of collision-induced rotational alignment.

1.8 Calculations

The experimental DCSs and rotational alignment moments are commonly compared to the results of calculations. These calculations use the PES to provide theoretical values of the DCS and rotational alignment moments using a range of methods.

1.8.1 Quantum Scattering Calculations

Quantum scattering (QS) calculations use the quantum theory of inelastic collisions to determine the outcome of collisions between molecules or atoms, in the form of the scattering matrix. The elements of the scattering matrix describe the probabilities for transitions from initial quantum states (including orbital angular momentum) to final quantum states.[96,97] The scattering amplitudes for the different $j\ m \rightarrow j'\ m'$ transitions are obtained from different weighted sums of the cross-products of elements in the scattering matrix, which are then used to give the DCS and $A_{q\pm}^{\{k\}}$ moments for the collision system. All QS calculations for the systems in this thesis were performed using the well-established HIBRIDON suite of programs.[98]

1.8.2 Quasi-Classical Trajectory Calculations

Quasi-classical trajectory (QCT) calculations are another method which can be used to provide a theoretical description of a scattering system. These calculations use classical, rather than quantum, mechanics to determine the motion of the colliders on the PES.[99,100] The QCT calculations often give an intuitive mechanical explanation for features of the scattering dynamics, which can be preferable to the more abstract quantum explanations provided by the QS calculations. QCT calculations can be used to determine whether a feature of the scattering is classical or quantum in nature, based on whether it appears in the results of QCT calculations.

1.8.3 Kinematic Apse Calculations

Kinematic apse (KA) calculations are an example of a hard-shell model, where the PES is represented by an infinitely high potential energy within a certain boundary, and zero potential energy elsewhere. In this model, the collision is treated as a sudden event on the surface of the hard-shell potential, from which the rotational energy transfer can be modelled. The magnitude of the transferred angular momentum is given by the vector product of the KA and the torque arm of the impact parameter, $\mathbf{b_n}$:

$$\Delta\mathbf{j} = \mathbf{a_k} \times \mathbf{b_n} \tag{1.23}$$

$\mathbf{a_k}$ is the vector of the KA, which lies on the axis normal to the hard-shell surface, where:

$$\mathbf{a_k} = \mathbf{k'} - \mathbf{k} \big/ \left| \mathbf{k'} - \mathbf{k} \right| \tag{1.24}$$

Here, $\mathbf{k}$ and $\mathbf{k}'$ are the initial and final relative velocity vectors respectively. The total angular momentum must be conserved for the collision, therefore:

$$\Delta\mathbf{j} - \Delta\left(\mathbf{r} \times \mathbf{k}\right) = 0 \tag{1.25}$$

Here, $\mathbf{r}$ is the distance between the centre of mass of the molecule and the location of the collision. In an instantaneous collision, $\mathbf{r}$ does not have time to change, meaning that it is a constant, and it can be shown:[101]

$$\Delta\mathbf{j} = \mathbf{r} \times \mathbf{a_k} \tag{1.26}$$

Therefore, for an instantaneous collision on a hard-shell potential, the projection of the angular momentum along the KA must be conserved over the course of the collision. Quantum mechanically, for an initially non-rotating molecule of integer j, the pre-collision angular momentum in the KA frame is described by the population in a single $m_j = 0$ state. After the collision, the molecule is in some final level, j', but the KA-frame population is still in $m_j = 0$. This leads to an angular momentum distribution in the KA frame for the product j':

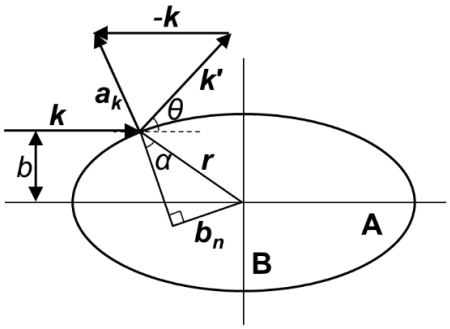

Figure 1.10: Definitions of the variables for an instantaneous diatom + atom collision on a hard-shell potential, described in the main text. Adapted from Reference [101].

$$A_0^{\{2\}}(KA) = -1 \tag{1.27}$$

$$A_{1+}^{\{2\}}(KA) = 0 \tag{1.28}$$

$$A_{2+}^{\{2\}}(KA) = 0 \tag{1.29}$$

These are converted into scattering angle-dependent alignment moments in the scattering frame using the equation:[95]

$$A_q^{\{K\}}(\theta) = \sum_p d_{pq}^{(K)}(\beta) A_p^{\{K\}}(KA) \tag{1.30}$$

Here, θ is the differential scattering angle and β is the Euler angle that rotates the KA-frame into the scattering-frame.[102] This leads to scattering-frame values of $A_{q+}^{\{2\}}(\theta)$:

$$A_0^{\{2\}}(\theta) = -P_2(\cos\beta) \tag{1.31}$$

$$A_{1+}^{\{2\}}(\theta) = \sqrt{3}\sin\beta\cos\beta \tag{1.32}$$

$$A_{2+}^{\{2\}}(\theta) = -\frac{\sqrt{3}}{2}\sin^2\beta \tag{1.33}$$

An important property of the KA model is that the rotation of the KA-frame moments into the scattering-frame is independent of the shape of the hard-shell potential. However, many PESs cannot be modelled accurately by a hard-shell potential, due to the presence of a strong attractive region, or shallow gradients of the repulsive part of the PES.

1.9 Spectroscopy of the NO Radical

In the experiments presented in this thesis, NO is initially present in the ground electronic state, $X^2\Pi$. This is optically excited to the $A^2\Sigma^+$ state, which is detected by 1 + 1′ REMPI, through the $E^2\Sigma^+$ state. NO($X^2\Pi$) has an electronic configuration with an unpaired electron in a π^* orbital. For the low-energy rotational levels which are present in the molecular beam, the coupling of angular momentum in NO(X) is best represented through a Hund's case (a) coupling.[59] In this scheme, the orbital angular momentum, $\boldsymbol{L}$, and the electron spin angular momentum, $\boldsymbol{S}$, couple strongly to the internuclear axis, $\boldsymbol{r}$. The projections of $\boldsymbol{L}$ and $\boldsymbol{S}$ onto $\boldsymbol{r}$ are labelled $\boldsymbol{\Lambda}$ and $\boldsymbol{\Sigma}$ respectively. $\boldsymbol{\Lambda}$ and $\boldsymbol{\Sigma}$ couple together to give the total orbital angular momentum, $\boldsymbol{\Omega}$ (Equation 1.34), which couples with the bond rotation angular momentum, $\boldsymbol{R}$, to give the total angular momentum, $\boldsymbol{J}$ (Equation 1.35).

$$\boldsymbol{\Omega} = |\boldsymbol{\Lambda} + \boldsymbol{\Sigma}| \tag{1.34}$$

$$\boldsymbol{J} = \boldsymbol{R} + \boldsymbol{\Omega} \tag{1.35}$$

The unpaired π^* electron means that for NO(X), $\boldsymbol{L}$ = 1 and $\boldsymbol{S}$ = 0.5, with projections onto $\boldsymbol{r}$, $\boldsymbol{\Lambda}$ = 1 and $\boldsymbol{\Sigma}$ = ±0.5. This leads to spin-orbit splitting of $\boldsymbol{J}$ into two ladders of quantum states, for $\boldsymbol{\Omega}$ = 0.5 and $\boldsymbol{\Omega}$ = 1.5, denoted as $^2\Pi_{1/2}$ and $^2\Pi_{3/2}$ respectively. The $^2\Pi_{3/2}$ states are 123 cm^{-1} higher in energy, and have a subtly different rotational constant than the $^2\Pi_{1/2}$ state.[103]

The two spin-orbit states of NO(X) are further split into Λ-doublet states, which occur as $\boldsymbol{L}$ couples with $\boldsymbol{R}$. A simplified visualisation of this effect is that one Λ-doublet has the orbital of the unpaired electron rotating in the plane of the bond axis rotation, while the other has it out of the plane. The difference in energy between the two Λ-doublets is very small, but the two states have opposite parity, meaning that the two states can be spectroscopically resolved. The parity of the Λ-doublet state which is higher in energy alternates for different rotational quantum states. Therefore, for molecules with half-integer values of $\boldsymbol{J}$, it is more intuitive to label them *e* when the total parity is $+(-1)^{j-1/2}$ and *f* when the total parity is $-(-1)^{j-1/2}$. For NO(X), this means that the higher-energy Λ-

doublet is always labelled *e*.[104] The complete energy level structure for NO(X) is shown in Figure 1.12.

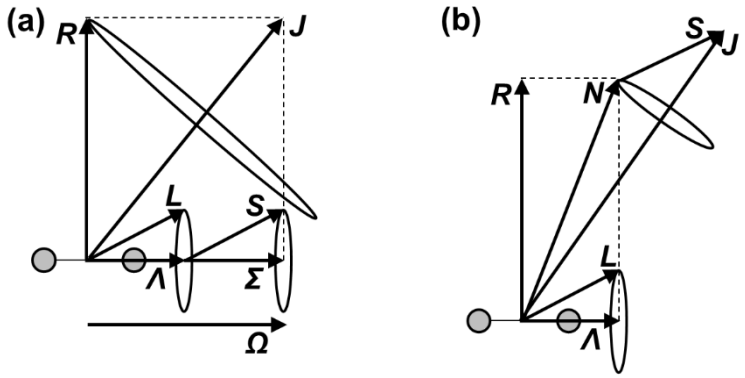

Figure 1.11: (a) Hund's coupling case (a), used to describe the angular momentum coupling in NO(X), (b) Hund's coupling case (b), used to describe the angular momentum coupling in NO(A).

In NO($A^2\Sigma^+$), the unpaired electron is promoted to the σ* LUMO orbital, and in NO($E^2\Sigma^+$), the electron is in a Rydberg orbital with σ symmetry. In both cases, $\boldsymbol{\Lambda} = 0$, and so $\boldsymbol{S}$ will not couple to the internuclear axis, and so they are accurately described by the Hund's case (b) coupling scheme.[59] In this case, $\boldsymbol{R}$ couples with $\boldsymbol{\Lambda}$ to give the total angular momentum without electron spin, $\boldsymbol{N}$ (Equation 1.36), to which $\boldsymbol{S}$ couples to give $\boldsymbol{J}$ (Equation 1.37). The complete energy level structure of NO(A) is shown in Figures 1.12 and 1.13 and NO(E) is shown in Figure 1.13.[104]

$$\boldsymbol{N} = \boldsymbol{R} + \boldsymbol{\Lambda} \tag{1.36}$$

$$\boldsymbol{J} = \boldsymbol{N} + \boldsymbol{S} \tag{1.37}$$

For the transition of a diatomic molecule between different electronic configurations, the rotational energy level cannot change arbitrarily. The selection rules depend on the orbital symmetry of the electronic states, and can be derived from the matrix elements of the electric dipole moment.[104] The selection rules which are relevant for the A ← X and E ← A transitions of NO are given in Equations 1.38-1.42.

$\Delta \boldsymbol{J} = 0, \pm 1$ *with the restriction:* $\Delta \boldsymbol{J} = 0 \nleftrightarrow \boldsymbol{J} = 0$ (1.38)

$\Delta \boldsymbol{N} = 0, \pm 1$ *with the restriction:* $\Delta \boldsymbol{N} \neq 0$ for Σ-Σ transitions (1.39)

$\Delta \boldsymbol{S} = 0$ (1.40)

$\Delta \boldsymbol{\Lambda} = 0, \pm 1$ (1.41)

Parity $+ \nleftrightarrow +$, $- \nleftrightarrow -$, $+ \leftrightarrow -$ (1.42)

The possible A ← X transitions for NO are shown in Figure 1.12. The transitions are labelled according to convention, with the general structure $\Delta \boldsymbol{J}_{FG}$, with ΔJ being labelled P, Q and R for $\Delta \boldsymbol{J}$ = -1, 0 and +1 respectively; F being labelled 1 and 2 for $\boldsymbol{J} = \boldsymbol{N}$ + 1/2 and $\boldsymbol{J} = \boldsymbol{N}$ - 1/2 in NO(A) respectively; and G being labelled 1 and 2 for $\boldsymbol{\Omega}$ = 1/2 and $\boldsymbol{\Omega}$ = 3/2 in NO(X) respectively. In cases where $F = G$, the label will be simplified to $\Delta \boldsymbol{J}_F$.[59] In practice, the spin-rotation splitting for NO(A) is smaller than the laser bandwidth, and so transitions which originate in the same lower level and prepare the opposite spin-rotation states from the same lower rotational level cannot be resolved.

The possible E ← A transitions of NO are shown in Figure 1.13. The transitions are labelled according to convention, with the general structure ${}^{\Delta N}\Delta \boldsymbol{J}_{FG}$, with $\Delta \boldsymbol{J}$ = -1, 0 and +1 labelled as P, Q and R for $\Delta \boldsymbol{J}$ = -1, 0 and +1 respectively; $\Delta \boldsymbol{N}$ labelled P and R for $\Delta \boldsymbol{N}$ = -1 and +1 respectively; F being labelled 1 and 2 for $\boldsymbol{J} = \boldsymbol{N}$ + 1/2 and $\boldsymbol{J} = \boldsymbol{N}$ - 1/2 in NO(E) respectively, and G being labelled 1 and 2 for $\boldsymbol{J} = \boldsymbol{N}$ + 1/2 and $\boldsymbol{J} = \boldsymbol{N}$ - 1/2 in NO(A) respectively. In the cases where $\Delta \boldsymbol{N} = \Delta \boldsymbol{J}$, the label will be simplified to $\Delta \boldsymbol{J}_{FG}$, and where $F = G$, the label will be simplified to ${}^{\Delta N}\Delta \boldsymbol{J}_F$.[59] In practice, the spin-rotation splitting of both the A and E states of NO are small compared to the bandwidth of the laser, meaning that the individual $\boldsymbol{N}' \leftarrow \boldsymbol{N}$ transitions cannot be resolved, and the observed transitions are labelled as P and R for $\Delta \boldsymbol{N}$= -1 and +1 respectively.

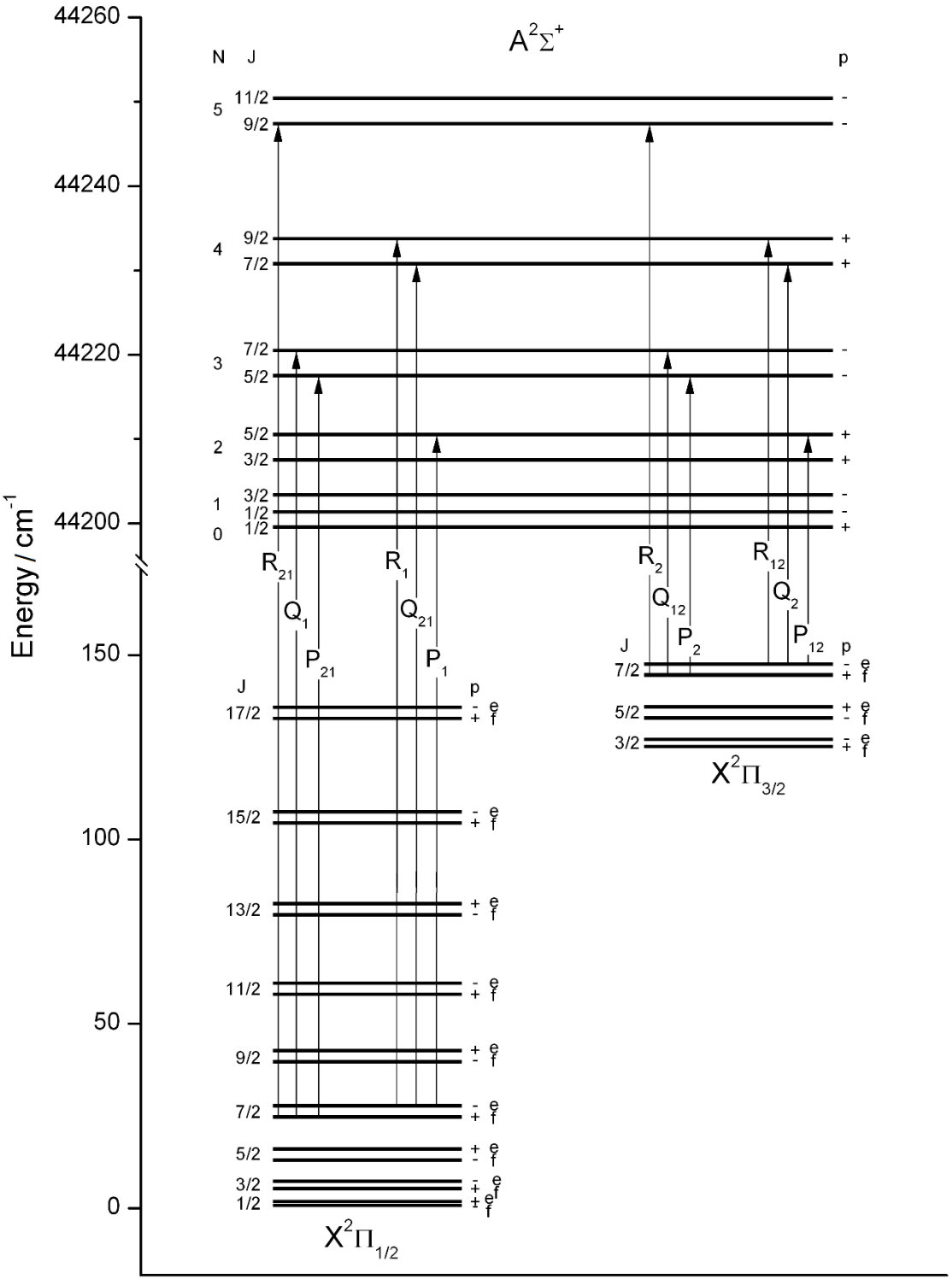

Figure 1.12: Rotational energy level structure for v = 0 of NO($X^2\Pi$) and NO($A^2\Sigma^+$), with possible spectroscopic transitions labelled. Λ-doublet splitting and spin-rotation splitting are exaggerated for visual clarity.

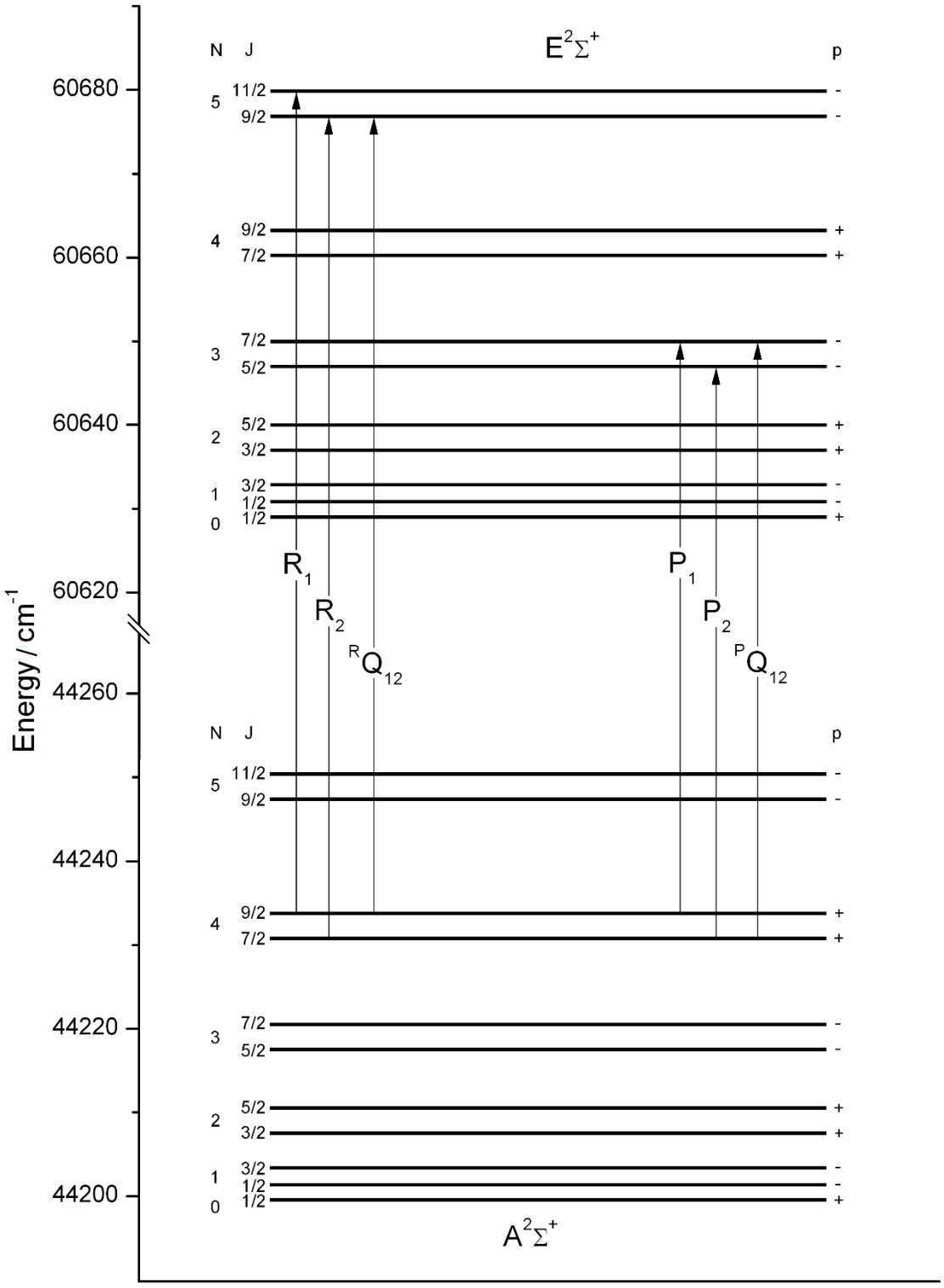

Figure 1.13: Rotational energy level structure for v = 0 of NO($A^2\Sigma^+$) and NO($E^2\Sigma^+$), with possible spectroscopic transitions labelled. Spin-rotation splitting is exaggerated for visual clarity.

1.10 Dynamical Studies using NO

NO is the most widely used molecule in CMB experiments, due to its room temperature stability, easy quantum state-resolved ionisation, and interesting chemical properties. This section will discuss the experiments which have investigated the collisions of NO in CMB experiments, focussing on recent (2010-2017) studies.

Early CMB experiments to measure the DCS for the collisions of NO(X) used a rotatable mass spectrometer detection scheme.[67,105,106] However, as described in Section 1.5.1, these experiments had very long acquisition times, and were prone to systematic errors. The first imaging experiments to study the collisions of NO used direct imaging of a time-of-flight experiment, with no additional focusing to investigate collisions of NO(X) with Ar.[107,108] After its development, VMI was quickly used in CMB experiments to study the inelastic collisions of NO(X) with Ar, by Suzuki and co-workers,[109,110] and Chandler and co-workers,[111,112]. Stolte and co-workers used a hexapole state selector to enable Λ-doublet selectivity of the NO(X) prior to the collision. This experiment was used to investigate the collisions of Λ-doublet resolved NO(X) with He[26] and D_2,[17] in which clear parity effects were observed in the DCS.

The most comprehensive study of the collisions of NO(X) using a CMB experiment has been made by Brouard and co-workers, who have investigated the rotationally inelastic collisions of NO(X) with different rare gas atoms, also using hexapole initial state selection. Similar to the NO(X) + He experiment by Stolte and co-workers,[26] parity effects were observed in the DCS for the collisions of NO(X) with Ne.[113] Parity-changing collisions were found to typically lead to a DCS with a single peak, while parity-conserving collisions typically led to DCSs with multiple peaks. QS calculations using a modified PES were used to show that the attractive forces on the DCS led to scattering at very small angles. The DCSs from experiments probing the collisions of NO(X) with Ar also contained parity-dependent oscillations.[21,22] Investigation of this effect using a quantum mechanical hard-shell model found that the oscillations were the result of interference effects, occurring between the trajectories of collisions at the two ends and the sides of the NO molecule. The rotational alignment moments were also determined for the NO(X) + Ar inelastic scattering system.[27] The prominent parity-dependent effects observed in the DCS were not found here, and the rotational alignment moments could

be closely approximated using the KA model (see Section 1.8.3).[93] Conversely, the orientation moments could not be modelled by a hard-shell classical model, as the symmetry prevents a preference in the direction of $\boldsymbol{j}$.[114] Measurements of the DCS were also made for NO(X) + Kr inelastic collisions, where the rotational alignment moments contained significant angle-dependent oscillations at low Δj, which were not reproduced by KA calculations.[28,115] This deviation, which was not observed for Ne or Ar, was attributed to scattering occurring through the attractive region of the PES. Across all of these systems, very good agreement was found between the experimental results and the results of QS calculations, indicating that the PESs for the NO(X) + Rg systems are accurate.

Following on from experiments of Stolte and co-workers,[26,56,116] Brouard and co-workers made measurements of the steric asymmetry for the collisions of NO(X) with He, Ar, Kr and O_2.[29,117] The steric asymmetry describes how the ICS is different for collisions with the N- and O-ends of the NO(X) molecule. At moderate Δj, all systems exhibited strong parity effects, with even Δj transitions being favoured for collisions at the O-end and odd Δj transitions being favoured for N-end transitions. At high Δj, all systems exhibited a preference for N-end collisions, which is consistent with a classical model, in which N-end collisions can exert more torque on the NO(X) molecule, leading to higher degrees of rotational excitation. Further experiments investigating the effect of orientation of the NO(X) bond axis recorded individual DCSs for collisions at the N- and O-ends of the molecule.[29,30,118] These DCSs contained more information than normal DCSs, as they resolved whether a feature in the DCS was caused by collisions with the different ends of the NO(X) molecule. The interference effects which were observed in the unoriented NO(X) + Ar DCSs[21,22] were not observed in these oriented DCSs.

Van de Meerakker and co-workers used a Stark decelerator to control the speed of NO in a molecular beam with a very high precision.[119] The Stark decelerator acts in the same way as a hexapole state selector, and generates a very pure sample of NO(X, v = 0, j = 0.5, f), which was used in CMB experiments to study the inelastic collisions with different rare gas atoms.[52,53] The very narrow speed distribution of NO(X) led to a very narrow distribution of collision energies, which combined with good collimation and low ionisation recoil, gave an extremely high angular resolution. Diffraction oscillations, which are not usually resolved in experimental measurements, were clearly visible for the

collisions of NO(X) with He, Ne and Ar.[53] The scattering angles at which the diffraction oscillations occur is strongly dependent on the collision energy, and under certain circumstances, an oscillation with an irregular intensity was observed.[20] QS calculations showed that this peak corresponded to a specific $m \rightarrow m'$ transition. The structure of the peak was reproduced using a model in which the scattering amplitude was given by the Fraunhofer equation, which describes the diffraction of waves from a solid object.[120] In a different measurement, van de Meerakker and co-workers used the extremely high collision energy resolution of the experiment to investigate scattering resonances for the NO(X) + He inelastic collisions.[121,122] At these scattering resonances, which occur over narrow ranges of collision energy, the DCS shifts from being predominantly forward scattered to being scattered over a much wider range of angles, displaying a clear forward-backward character. This effect, which was reproduced in QS calculations, corresponds to the formation of a short-lived quasi-bound state during the collision.

Initial crossed molecular beam measurements of the collisions of NO(A) with different rare gases were performed by our group in collaboration with Chandler and co-workers. In these measurements, the DCS was reported for the rotationally inelastic collisions of NO(A) with Ar and He.[45,46] For the inelastic collisions of the NO(A) + Ne system, measurements of the rotational alignment were made, in addition to the DCS.[47] Unlike the NO(X) + Ne and Ar systems, the rotational alignment moments for the NO(A) + Ne collisions contained large angle-dependent fluctuations, which were inconsistent with predictions made using the KA model. These proof-of-concept experiments were used to inform the construction of a new, purpose built CMB VMI apparatus to study the collisions of NO(A). It is the experiments using this apparatus that are the focus of the remainder of this thesis.

Chapter 2

Experimental Techniques

2.1 Introduction

The research presented in this thesis investigates vector correlations in the inelastic collisions of NO($A^2\Sigma^+$) with a range of atomic and molecular collision partners. These measurements were performed using a newly constructed CMB VMI experiment. The experimental apparatus was designed by Dr T. R. Sharples and Prof. M. L. Costen, as a compact crossed molecular beam machine, similar to that of Jansen *et al.*,[123] but with features to aid the optimal measurement of collisions of electronically excited molecules. At the beginning of my time working on the experiment, the design of the apparatus had been completed, but construction had not yet begun. I was directly involved in all stages of the construction, commissioning and optimisation of the apparatus, which will be described in the following sections of this chapter.

Briefly, the experimental setup consisted of two pulsed molecular beams, one contained NO seeded in a rare gas, the other was a neat beam of the collider, which crossed in the centre of a high vacuum chamber. In the crossing region, NO in the ground state was optically pumped to produce NO(A) in a single quantum state, which underwent collision-induced rotational energy transfer, and the products were state selectively probed using 1 + 1′ REMPI, in combination with VMI. The resulting velocity map images

were analysed using a forward-simulation process in order to extract the DCSs and the scattering angle dependent rotational alignment moments for the collisions.

2.2 Experimental Apparatus

The experimental apparatus consisted of three chambers, comprising two source cubes (Lewvac FL-CUBE63CF) connected by close couplers (Kimball Physics, MCF450-ClsCplr-E2) to a main scattering chamber (Kimball Physics, MCF600-SphSq-F2E4A4). Four fused silica viewports provided access to the main scattering chamber for the laser beams used in the experiment. Each of the source cubes was evacuated using a turbo molecular pump (Edwards, EXT75DX), with a third turbo molecular pump (Edwards, nEXT300D) used to evacuate the main chamber. These three turbo molecular pumps were backed by a dry scroll pump (Edwards, nXDS10). A flight tube was connected to the top of the main chamber, connecting it to the detector region. The detector chamber was comprised of a series of double-faced CF flanges, modified to house the detector and provide electrical feedthroughs. The detector chamber was evacuated using a fourth turbo molecular pump (Edwards, EXT75DX), which was backed by a second dry scroll pump (Edwards, nXDS6). A gate valve (VAT Series 10) at the top of the flight tube allowed the detector region to be sealed from the main scattering chamber, so that the detector could be kept under vacuum while the rest of the apparatus was vented for routine maintenance. The gate valve and the turbo molecular pump on the detector chamber were rigidly clamped to a support frame to minimise subtle mechanical instabilities of the apparatus (see Section 2.8 for the effect of this instability). The pressure was monitored using three wide range pressure gauges (Edwards, WRG-S-NW35), one on each of the source cubes and a third on the main chamber. The magnetic heads of the wide range gauges were removed during data acquisition, as the magnetic field produced by the gauges was found to result in a measureable depolarisation of the angular momentum alignment of the scattered NO(A) molecules. The pressure in the detector region was monitored using an active ion gauge (Edwards, AIGX-S-DN40CF). When the experiment was not actively running, the pressure across all the vacuum chambers and the detector region was typically in the range 2-4 $\times 10^{-9}$ mbar.

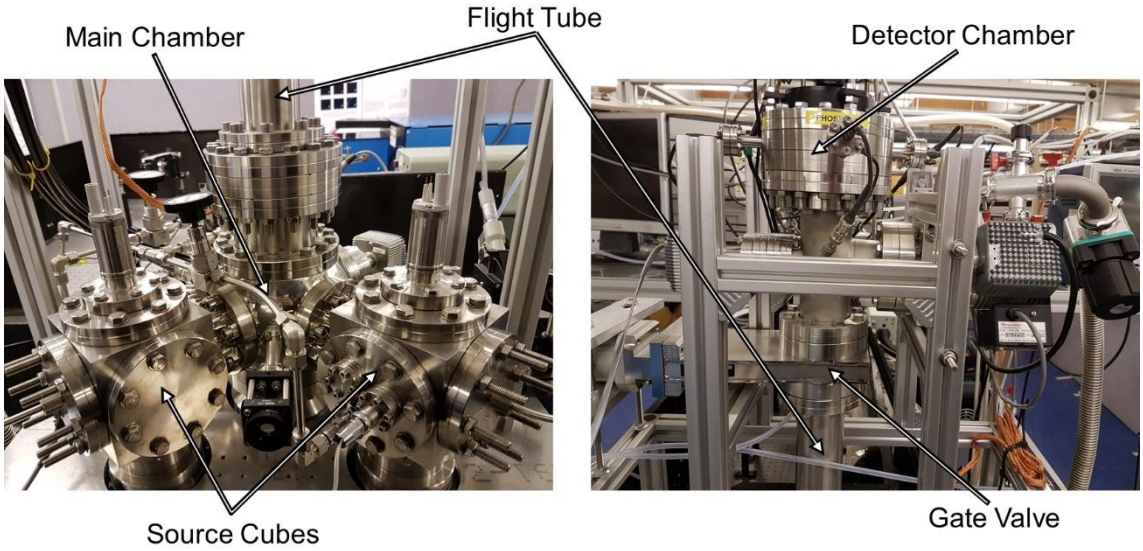

Figure 2.1: Photographs of the vacuum equipment with the main components labelled. Left: the source cubes and main chamber. Right: the detector region.

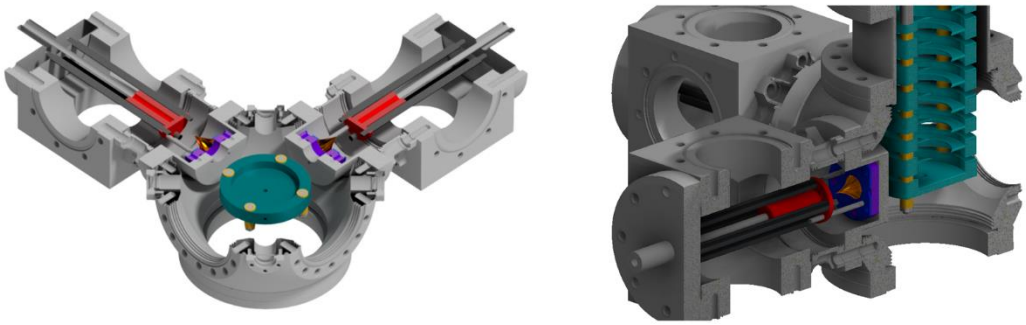

Figure 2.2: Cutaway schematics showing the source cubes and main chamber. A false colour scheme is used to highlight red: the valves, purple: the skimmer mounts, green: the ion optics.

A pair of pulsed valves (Parker Series 9 General Valve), each with a 500 μm orifice and a repetition rate of 10 Hz (to match the lasers), were positioned in the two source cubes to generate the molecular beams. In a typical experiment, the primary molecular beam consisted of NO seeded in a rare gas (He, Ne or Ar) at a partial pressure of 10% and a backing pressure of 3 bar (absolute pressure). The carrier gas enabled a more efficient collisional cooling of the NO than would be possible in a molecular beam of pure NO, leading to a narrower speed distribution of the molecular beam, and a higher fractional population in the $j = 0.5$ rotational level. Furthermore, the use of a carrier gas significantly reduces the formation of $(NO)_n$ clusters, the dissociation of which would lead to NO molecules moving in a different direction to the molecular beam. Finally, the

choice of carrier gas enabled some coarse control over the speed of the molecular beam, and as such, the collision energy of the experiments. The secondary molecular beam consisted of the collider gas, which was produced from a backing pressure of 5 bar. The two molecular beams each passed through 500 µm skimmers, positioned 20 mm from the valve orifices, which allowed the passage of the coldest molecules in the centre of the molecular beam into the main chamber, while blocking the warmer molecules on the peripheries of the beam. The skimmers also collimated the beams, resulting in a narrower angular spread of velocities. The two skimmed molecular beams continued to propagate through the main chamber, and intersected at 90° in the centre of the main chamber.

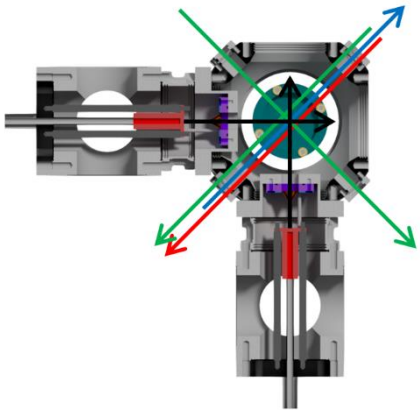

Figure 2.3: Schematic of the source cubes and main chambers cutaway through the scattering plane. Arrows represent: black: the paths of the two molecular beams, blue: the path of the preparation laser beam, red: the path of the probe laser beam, green: the paths of the ionisation laser beams. The paths of the three laser beams running top right to bottom left co- and counter-propagate, but are offset for visual clarity.

The initial population of NO(A) was prepared with a Nd-YAG (Continuum Surelite II-10) pumped dye laser (Sirah CTSG). Using Coumarin 450 dye, a tuneable laser beam of around 452 nm was produced, which was frequency doubled by a BBO crystal to around 226 nm, and was directed through the crossing region of the two molecular beams without being focussed. The wavelength of the 226 nm *preparation* laser was tuned to be resonant with a transition in the NO($A^2\Sigma^+ \leftarrow X^2\Pi$) (0,0) band, typically $Q_1(0.5)$, to prepare NO(A, v = 0, N = 0, j = 0.5). The fluence of the preparation laser was controlled using a Babinet-Soleil compensator in combination with a linear polariser (optics (a) and (b) in Figure 2.4). The prepared NO(A) molecules underwent collisions with the molecules in the secondary molecular beam, resulting in the rotational excitation of NO(A). After 360 ns, the rotationally excited NO(A) molecules were state-selectively

ionised using 1 + 1′ REMPI. The probability of an individual NO(A) molecule undergoing a collision was estimated to be 0.5%, from the molecular beam densities[23] and the total cross sections for the NO(A) + Ne collision.[124] As the probability of a collision occurring follows a Poisson distribution, there is therefore only a 0.002% probability than an individual NO(A) molecule will undergo two or more collisions, which can be safely ignored.

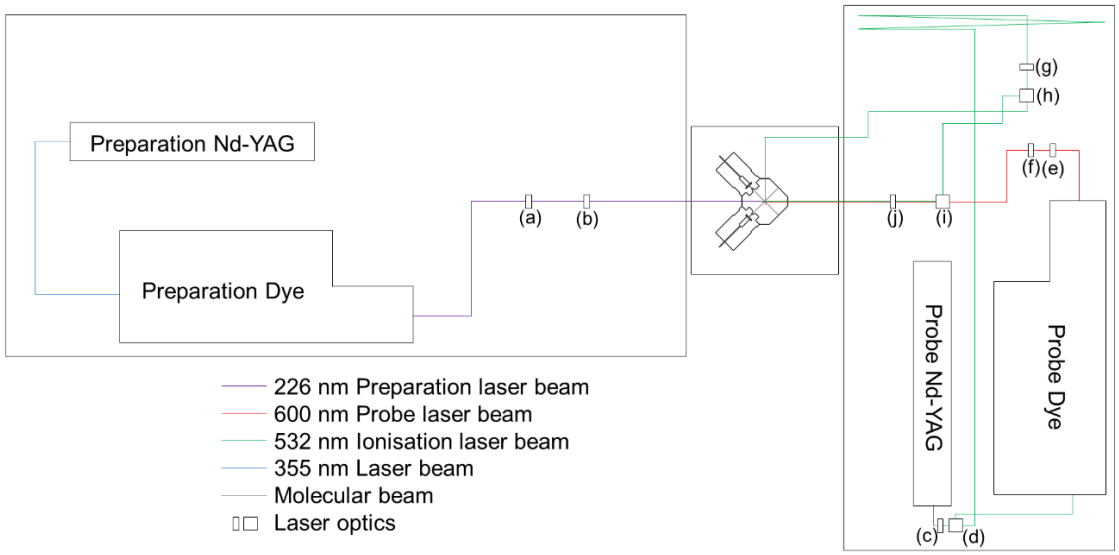

Figure 2.4: Schematic representation of the laser systems used in the experiment, with labelled laser optics: (a) Babinet-Soleil compensator, (b) polariser, (c) multi-order half-wave plate, (d) polarising beamsplitter, (e) half-wave plate, (f) polariser, (g) quarter-wave plate, (h) polarising beamsplitter, (i) polarising beamsplitter, (j) photoelastic modulator.

The 1 + 1′ REMPI detection scheme used two photons at different wavelengths, originating from the same laser system. The first photon was from a Nd-YAG (Continuum Surelite I-10) pumped dye laser (Sirah CSTR-DA24). The dye laser used Rhodamine B dye to generate a tuneable laser beam at around 600 nm, which was tuned to be resonant with a transition in the R branch of the NO($E^2\Sigma^+ \leftarrow A^2\Sigma^+$) (0,0) band. This unfocussed 600 nm *probe* laser beam passed through the crossing region of the two molecular beams, counter-propagating with the preparation laser beam. A half-wave plate and linear polariser (optics (e) and (f) in Figure 2.4) were used to control the fluence of the probe laser beam. To enable sensitivity to the alignment of the angular momentum vector of the scattered NO(A) molecules, the linearly polarised probe laser beam was passed through a photoelastic modulator (PEM, PEM-90, Hinds Inc., optic (j) on Figure 2.4), which was set to prepare the laser beam with either vertical (V) or horizontal (H) polarisation of the electric vector in the laboratory (lab) frame.

A fraction of the 532 nm output of the Surelight I-10 Nd-YAG laser was split from the main beam to provide the second photon used in the REMPI scheme. The exact fraction of light split was controlled using a zero-order half-wave plate and polarising beamsplitter cube (optics (c) and (d) on Figure 2.4), and was typically in the range of 1-20% of the total energy of the incoming laser beam. This 532 nm *ionisation* laser beam passed through the crossing region of the molecular beams, and ionised NO($E^2\Sigma^+$) from all rotational levels populated using the probe beam. An optical delay line ensured that the ionisation beam propagated through the interaction region after the probe beam. Before the ionisation beam entered the vacuum chamber, it was split into two beams of equal energy using a quarter-wave plate and polarising beamsplitter (optics (g) and (h) in Figure 2.4). The two resulting ionisation beams propagated through the interaction region at the same time. One of the ionisation beams was combined with the probe beam using a third polarising beamsplitter (optic (i) in Figure 2.4), and co-propagated with the probe beam through the photoelastic modulator, so that the two laser beams always had an orthogonal polarisation. The other ionisation beam propagated through the crossing region at 90° to the probe beam propagation direction, with horizontal polarisation, which was also always orthogonal to the polarisation of the probe beam. This arrangement ensured that the probe and ionisation beams had a consistent polarisation relative to each other, while minimising the overlap of the electric vectors of the ionisation laser beams. This arrangement of ionisation beams means that two of the three possible orthogonal polarisations are used, reducing any effects of polarisation sensitivity induced in the ionisation stage. Ideally, all three orthogonal polarisations would be used in the ionisation step, however, this was not practical to implement, due to space constraints with the current arrangement of the apparatus. Compared to a single-ionisation laser beam setup with twice the fluence, this setup minimises the unwanted non-resonant 532 + 532 nm ionisation (see Section 2.5 for more details), while keeping the scattering signal from resonant 600 + 532 nm ionisation constant.

The four laser beams used in the experiment each had a fixed diameter, which were controlled using an iris immediately before the viewports of the vacuum chamber. The probe and ionisation beams were set to diameters of 3 mm. The diameter of the preparation laser was adjusted for the different collision systems, such that NO molecules moving at the fastest possible speed in the laboratory frame would not have sufficient

time to leave the detection region, thus preventing a speed-dependent detection bias from occurring (see Section 2.10.4 for further details).

The resulting NO^+ ions were velocity mapped onto the detector using a set of ion optics, designed by Dr T. R. Sharples, consisting of a set of 8 electrodes mounted on four insulated posts. Compared to other sets of ion optics implemented in similar CMB experiments, the design of these ion optics was chosen to minimise the time-of-flight spread of ions with different velocities in the time-of-flight axis, and to maximise the time-of-flight spread of ions produced at different times. Together, these two features enable the optimal discrimination between NO^+ ions produced by 226 + 226 nm and 226 + 600 + 532 nm ionisation. Additionally, the ion optics were designed such that the velocity mapping volume was large enough to accommodate the creation of ions by the unfocussed laser beams. A more thorough description of the ion optic design can be found in the supplementary materials of Reference [102].

The detector consisted of a pair of microchannel plates (MCPs), with a phosphor screen (Photonis, 40 mm active diameter, P47 phosphor). As velocity mapped ions struck the MCP plates, there was a corresponding illumination of the phosphor screen, the location of which was detected using a charge coupled device (CCD) camera (Basler scA780-54fm, 782 × 582 pixel array). Additionally, a time resolved signal was measured using an avalanche photodiode (SensL, MicroFM-10035-X18), which was monitored using an oscilloscope (Lecroy Waverunner 44xi). In order to discriminate between scattered NO^+ ions produced by the ionisation beam, and unwanted background ions, the voltage applied to the rear MCP was switched between a low- and high-voltage state using a fast high-voltage switch (DEI PVX4140, ≤25 ns rise time). In the low-voltage state, the signal resulting from the ion strikes was of a low intensity, and so could not be detected by the camera (although a small signal could still be measured using the photodiode), while a clear signal corresponding to the ion strike could be measured by the camera in the high-voltage state. The detector was kept in the low-voltage state for the majority of the time, only switching to the high-voltage state for 120 ns coinciding with the arrival of NO^+ ions generated by the ionisation beam, effectively discriminating against the detection of ions produced through other processes, particularly those that result from the preparation laser (see Section 2.5).

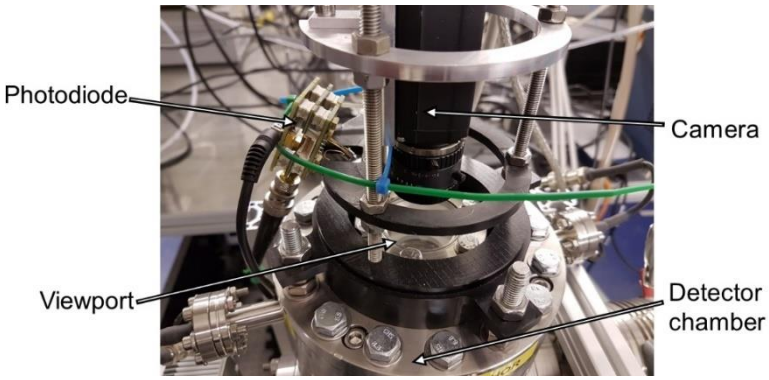

Figure 2.5: Photograph of the camera and photodiode with labels showing the main components. During experiments, this is covered by a black cloth to prevent the detection of light from the room.

Gating the detector did not result in discrimination against background NO^+ ions produced by the ionisation laser, particularly those that arise from non-resonant two-photon ionisation of NO(A) (see Section 2.5). These background ions were accounted for by recording *background* images, in addition to the *signal* images described above. In these background images, the primary molecular beam (containing NO seeded in a rare gas) was fired as normal, but the secondary molecular beam (containing the collider) was delayed by 1 ms, meaning that it no longer intersected with the primary molecular beam pulse, removing all scattering processes from the experiment, while leaving the background unchanged. By subtracting the background image from the signal image, a *background-subtracted* image was obtained, which contained only signal resulting from scattering processes. The specific details and implementation of the background subtraction process are described in Section 2.4.

2.3 Experimental Timings

The experimental timings were controlled by a delay generator (Quantum Composers 9520 series), which provided trigger pulses to the various components of the experiment, as shown in Figure 2.6. The primary clock for the experimental cycle was provided by the PEM, which oscillated at a fixed frequency of ~50 kHz. This was down-counted by a counter/timer (National Instruments, cDAQ-9171) to 10 Hz, to provide a trigger pulse to the delay generator, ensuring that the experiment was reliably synchronised to the compression cycle of the PEM.

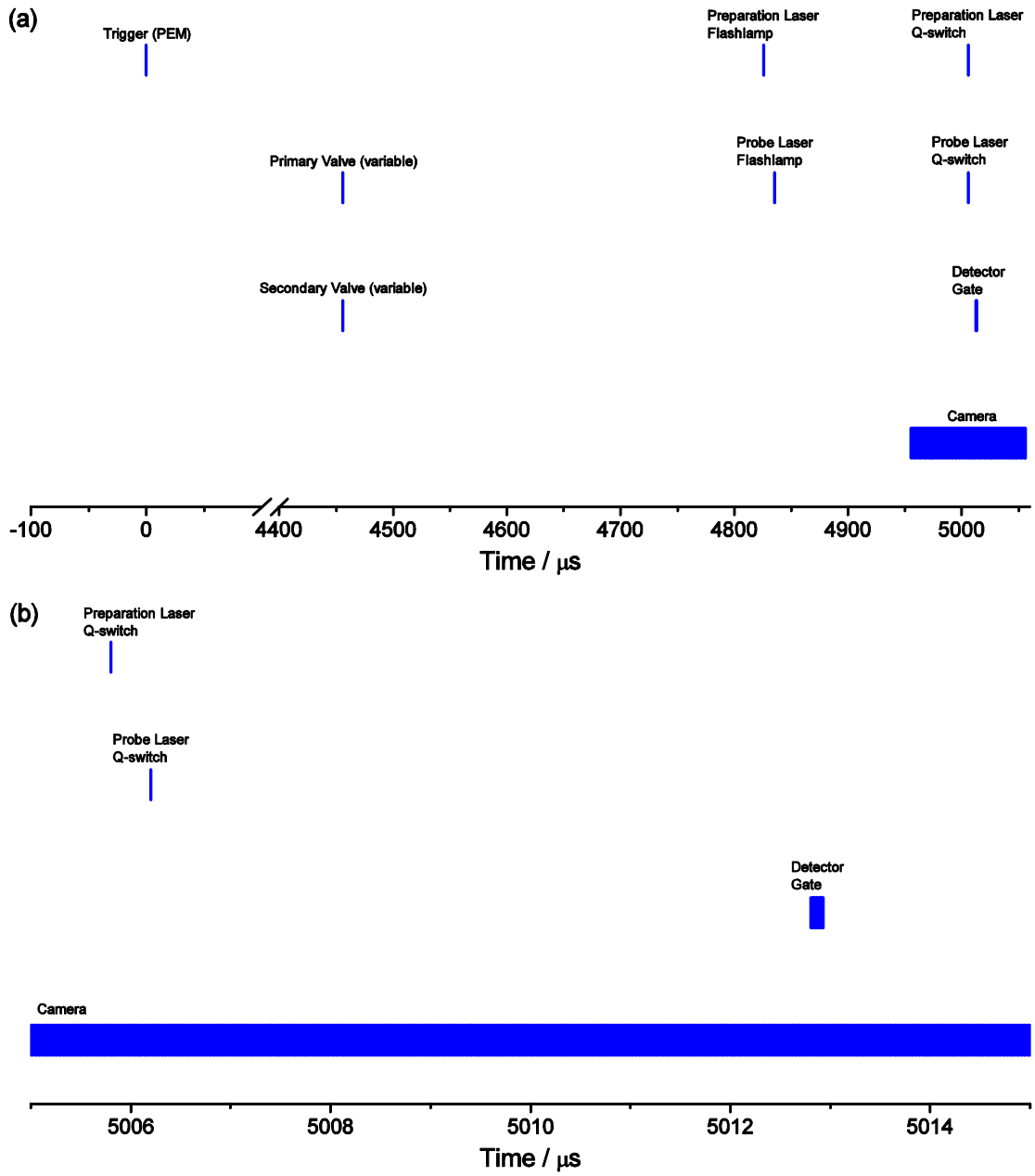

Figure 2.6: (a) Timings of different elements of the experiment, described in the main text, relative to the trigger pulse. (b) An expanded view of (a).

The flashlamps and Q-switches of both the preparation and probe Nd-YAG lasers were independently triggered, providing accurate relative timings of the preparation and probe laser pulses. The Q-switch delays of the preparation and probe Nd-YAG lasers were optimised to give the maximum output energy, at approximately 180 and 170 µs respectively. The timings of the two Nd-YAG lasers were set such that the probe pulse intersected the interaction region 360 ns after the preparation pulse. The optical delay line in the path of the ionisation beams ensured that they intersected the interaction region 4 ns after the probe laser pulse.

The timings of the primary and secondary valves were set to maximise the overlap of the two molecular beam pulses with the laser beams, which depended on the mean speeds of the molecular beams under different expansion conditions, and were typically in the range of -450 µs to -600 µs, relative to the Q-switch trigger of the preparation laser. In the acquisition of the background image, the secondary (collider) valve delay was shifted by +1 ms (not shown in Figure 2.6) to eliminate inelastic collisions from the experiment. A gating pulse was applied to the fast switch to activate the high-voltage state of the detector, to coincide with time at which the NO^+ ions generated by the ionisation laser struck the detector, beginning at 6.61 µs after the probe laser Q-switch time and lasting for 120 ns. The camera was triggered to be active for a 100 µs period, centred on the probe laser Q-switch trigger. The oscilloscope was triggered synchronously with the preparation laser Q-switch.

The precise timing of the probe pulse relative to the PEM was used to control the polarisation of the probe pulse, with ~5 µs variation required for the vertical to horizontal switching used in these experiments. This was controlled by varying the timing of the probe Nd-YAG laser flashlamp and Q-Switch triggers by the same amount to keep the energy of the pulse consistent. In addition to the probe laser timings, all other experimental timings were shifted by the same value, to keep the relative timings of the experiment consistent.

2.4 Data Acquisition

The data acquisition was controlled through a custom written program, coded in LabVIEW by Dr T. R. Sharples. The data acquisition occurred through a series of steps, which are illustrated in Figure 2.7, and are described below. *Individual camera shots*, containing the scattering signal, described in Section 2.2, were recorded by the camera as 8-bit bitmap files, which were converted into two-dimensional numeric arrays. The scattering signal only occupied a small fraction of the image acquired by the camera, and so the arrays were cropped to a smaller region of interest, in the range of 120×120 to 300×300 pixels in size. A number (typically 200) of these individual camera shot arrays were summed together to form a *frame*. For each step in the acquisition process, four

frames were recorded, with frames for the V and H polarisations of the probe laser, and for each, a signal background frame. For each of the V and H images, the background frame was subtracted from the signal frame to generate the background-subtracted frame.

To eliminate the detection bias resulting from Doppler selection of molecules moving at different lab-frame velocities, the wavelength of the probe laser was scanned over the Doppler profile of the NO(E ← A) transition. The step size of this scan was 0.0005 nm, which is less than the 0.0012 nm full width at half maximum (FWHM) spectral bandwidth of the probe dye laser.[125] The range over which the laser was scanned depended on the width of the Doppler profile, which is directly related to the diameter of the Newton sphere. For the experiments described in this thesis, the laser was scanned over a range of 14-18 points (0.0070-0.0090 nm) to completely cover the Doppler profile of the transition, with several points of baseline on either side. The points of baseline ensure that the entirety of the Doppler profile has been truly scanned, and also allowed for the wavelength of the probe laser to drift slightly (either as a result of changing temperature in the lab, or mechanical instabilities of the laser) without leading to a detection bias in the results. The acquisition of an *individual image* typically involved scanning the laser over the transition 5 times, taking approximately two hours for a typical acquisition, comprising 64,000 individual camera shots across all four different frames.

Multiple individual images were recorded across multiple days, with the exact number for a given product state varying widely depending on the experiment, ranging from 1 to 16. These individual images were translated appropriately to correct for the day-to-day drifts in zero-velocity pixel location, resulting from mechanical instabilities in the experimental apparatus (see Section 2.8). The individual images may also be combined to give an *averaged image*, although analysis was typically conducted on the individual images, to obtain multiple fits for each product state, thereby allowing error analysis to be conducted.

In addition to these images, the data acquisition code also acquired and stored additional information. A centroiding algorithm was used, which identified isolated areas of intensity on an individual camera shot as *objects*, and determined the centre-of-mass of the object as an x,y coordinate with subpixel resolution. These coordinates were recorded for all objects as a list for both the signal and background measurements, and

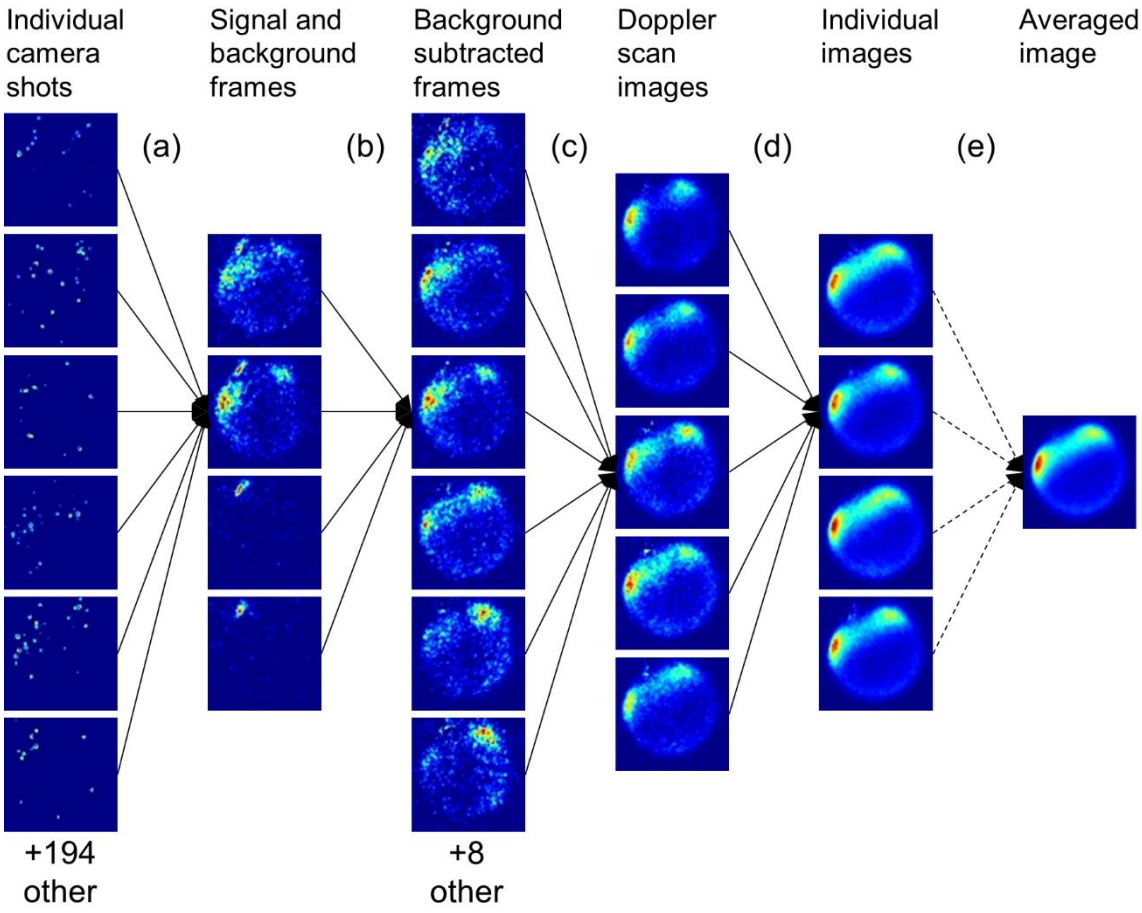

Figure 2.7: V + H image acquisition process for a single NO(A) product quantum state. Stage (a): Individual camera shots are averaged into frames. (b) Total and background, V and H frames are combined to generate a background subtracted V + H frame. (c) Background subtracted frames are recorded across the Doppler profile. (d) Multiple scans of the Doppler profile are made to generate an individual image. (e) (Optional) Individual images are averaged into an averaged image.

for the V and H probe laser polarisations. These centroided objects are useful, as they potentially provide sub-pixel precision for the location of an ion strike. However, due to the prevalence of overlapping ion strikes, which the centroiding algorithm was unable to resolve into separate objects, these centroided coordinates were not used in analysis of the results in this thesis. Spectra were also recorded, from both the photodiode signal and the number of centroided objects, for both of the total and background signals of both probe laser polarisations as the probe laser was scanned over the Doppler profile. Finally, for each acquisition, the region of interest of every individual camera shot was saved as an 8-bit bitmap file. These images took up a large amount of computer storage (roughly 3 GB for each individual image), but allowed for more detailed retroactive processing of the data, although this was not implemented for any of the data presented in this thesis.

2.5 Sources of Background Signal

There were a number of sources of background signal in the experiment. The first is the camera, where even in the absence of external illumination, each pixel reads a non-zero value. This arose from a combination of thermal and electrical noise in the CCD elements and electrical noise generated in the read-out process. While these dark counts could be removed by background subtraction, the signal to noise ratio of the experiment was improved considerably by pre-emptively eliminating it, by applying a threshold to the camera. This simply involved any pixels below an intensity of 20 being recorded as zero, thus removing this background signal while retaining the signal arising from ion strikes (see Section 2.6.8 for more details on the threshold).

The second source of background signal involved the ionisation of NO(A) through the absorption of a second 226 nm photon from the preparation laser beam. Ions formed in this way were predominantly discriminated against by gating of the detector (see Section 2.2), however despite this, a small fraction of these ions were still observed in the detection scheme. Tests indicate that these ions were dependent solely on the preparation laser, but the photodiode signal unambiguously showed that these ions struck the detector during the high-voltage state of the detector, indicating that the ions are not correctly time-of-flight mapped, rather than being an effect of bleed-through of signal from the low-voltage state. In addition to not being time-of-flight selected correctly, the ions were not effectively velocity mapped, with ion strikes occurring almost uniformly across the entire detector. The valve-laser delay profile for these ions closely matched that for the ungated two-photon ionisation of NO(X), confirming that these background ions were generated from the ionisation of NO in the molecular beam, rather than from residual NO which had remained in the vacuum chamber from the previous experimental cycle. This conclusion is supported by the REMPI spectrum of this background NO, which was rotationally cold and closely matched the spectrum of NO(X) in the molecular beam, whereas residual NO would have undergone multiple collisions with the chamber walls, leading to a thermalized, near room-temperature rotational distribution. The origin of this signal is not clear, but is seems that the NO(X) molecules are ionised by the preparation laser beam outside of the interaction region. This could occur if a tiny fraction of the NO molecules were reflected at a small angle as they passed through the skimmer, so that

some of the molecules intersected the preparation laser beam outside of the interaction region. If this is the cause of the signal, it could be eliminated by additional collimation of the molecular beam after the skimmer. As this signal was unaffected by the presence of the collider beam, this background signal was removed through the background subtraction process. However, this signal led to stochastic noise across the entire image, where individual pixels experience different numbers of ion-strikes in the signal and background frames, which reduced the signal-to-noise level of all experimental images.

The third source of background signal arises from the non-resonant ionisation of NO(A) by two 532 nm photons from the ionisation beam. As the overwhelming majority of the NO(A) had not undergone scattering, and the inelastic scattering which did occur was predominantly to low-N' rotational levels, which are strongly forward scattered, this background signal manifests as a beam-spot (an area of intensity localised around the velocity of the molecular beam). This non-resonant ionisation inherently occurred at the same point in time as the scattering signal, meaning that these ions could not be discriminated against by gating the detector, and therefore were removed purely through background subtraction. This was comfortably achieved for low rotational levels of product NO(A), where the scattering signal was intense, and the fluence of the ionisation beam could be kept to a minimum and hence the intensity of the beam-spot was kept low. However, for higher rotational levels, where the signal levels were much lower and the fluence of the ionisation laser was raised to compensate, the beam-spot was much more intense, and thus the background subtraction generated more noise. For the collisions of NO(A) with Ne at 523 cm^{-1}, described in Chapter 3, the lowest ionisation laser beam fluence was used in the detection of $N' = 3$, where the beam-spot was 23% ± 3% of the intensity of the scattering signal. For the same system, the highest ionisation laser beam fluence was used in the detection of $N' = 10$, where the beam-spot was 12,000% ± 4,000% of the intensity of the scattering signal (QS calculations predict that the integral cross sections for these two processes are 7.9 $Å^2$ and 0.84 A^2 respectively). Because the collider beam was removed from the experiment when recording the background image, there were no collisions and so the population of unscattered NO(A) was slightly higher in the background image, while the population of scattered NO(A) is only present in the signal image. This difference is small (estimated at 0.5%), but does result in a trend in the images with the largest background contribution of over-subtraction in the region of the beam-

spot, with small peaks corresponding to scattering signal visible on either side of the beam-spot region. The result of both the over-subtraction of the beam-spot and the non-resonant ionisation of rotationally excited NO(A) can be clearly seen in the background-subtracted image for $N' = 10$ in Figure 2.8. However, this imperfect background subtraction of the non-resonant background signal typically did not interfere with the analysis, as the effect is largest for the product states which have low signal levels. These states are typically highly rotationally excited, and so the beam-spot appeared in a position on the detector outside of the projected scattering sphere, is shown for $N' = 10$ from the NO(A) + Ne scattering in Figure 2.8.

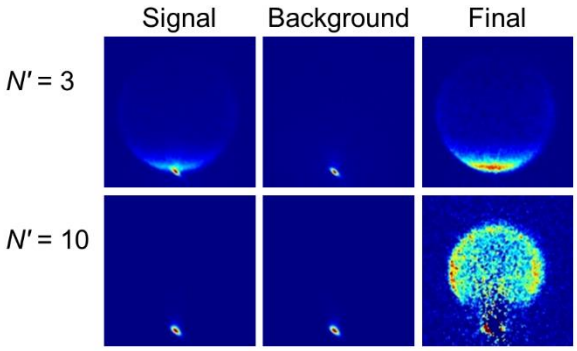

Figure 2.8: Velocity mapped images showing the effect of the non-resonant 532 + 532 nm ionisation in individual images where the fluence of the ionisation laser is low ($N' = 3$) and high ($N' = 10$) for collisions of NO(A) with Ne. The colour scale of the images is scaled to the most intense pixel of each image.

In situations where a trace amount of NO had contaminated the secondary beam, a background signal arising from 532 + 532 nm ionisation of NO was seen in some images appearing as a secondary beam-spot. As this source of background necessarily requires the secondary molecular beam to be active, it was not removed by the background subtraction, and thus remained in the background-subtracted images. In all the experiments described in this thesis, when the collider beam-spot has appeared, it has not intersected the scattered signal and could be safely ignored. In fact, these beam-spots proved beneficial to the analysis of several systems, as they provided a direct measurement of the secondary molecular beam velocity from the experimental images, which would otherwise need to be measured in a separate experiment.

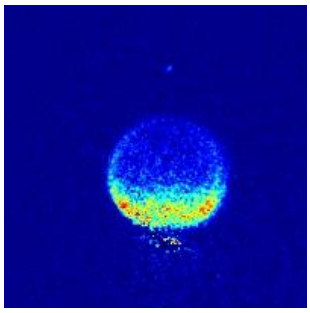

Figure 2.9: Background-subtracted velocity map image showing inelastic collisions of NO(A) with Ne, $N' = 9$. A faint NO beam-spot formed from 532 + 532 nm non-resonant ionisation is observed above the scattered signal, corresponding to the velocity of the secondary molecular beam.

The final source of background involved the resonant 600 + 532 nm ionisation of NO(A) which has been unintentionally prepared in the quantum state being probed. A spectrum is shown in Figure 2.10 of the NO(A ← X) (0,0) band in the region surrounding the $Q_1(0.5)$ transition, which is the strongest transition with which to generate NO(A) in the $N = 0$ rotational level. The spectrum was recorded with a preparation beam fluence of 0.65 mJ cm^{-2}, and so the saturation broadening of the transitions is representative of the final experiments (see Section 2.6.1). $Q_1(0.5)$ occurs in a moderately spectrally congested region, with most disruptive overlapping transitions being $Q_1(4.5)/P_{21}(4.5)$, which sit on the shoulder of $Q_1(0.5)$. This means that when the wavelength of the preparation laser was tuned to the peak of $Q_1(0.5)$, the low-frequency wing of the laser spectral profile overlapped $Q_1(4.5)/P_{21}(4.5)$, and NO(A) in $N = 4$ was unavoidably generated alongside $N = 0$. While the population of $N = 4$ was negligibly small compared to $N = 0$ (estimated at <0.05%, based on the population of NO(X) in the rotational level $j = 4.5$), it was comparable to the population of $N = 4$ generated through inelastic collisions. This meant that the generated background signal, which appeared as a beam-spot in the same position as the non-resonant ionisation beam-spot, was large enough to make recording experimental images for the product state $N = 4$ effectively impossible, even with background subtraction, as long as NO(A) was prepared using the $Q_1(0.5)$ transition.

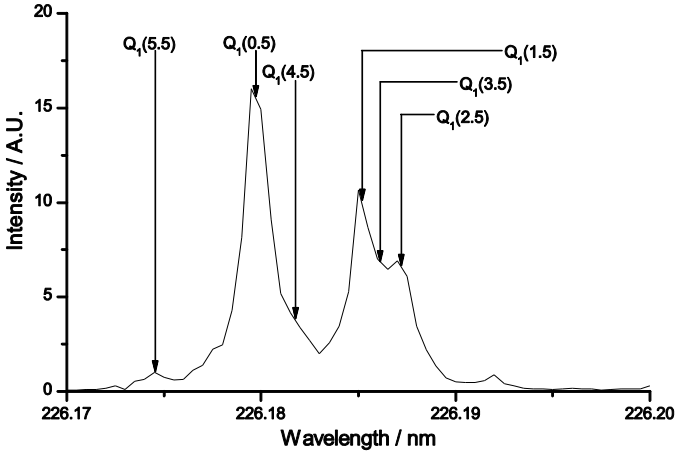

Figure 2.10: 1 + 1 REMPI spectrum of the NO(A ← X) (0,0) band, obtained from a molecular beam of NO seeded in He at 10% with a backing pressure of 3 bar. Q_1 transitions are labelled.

This 600 + 532 nm background signal was also observed for the NO(A) rotational levels N = 1 and 2, which were populated through the $Q_1(1.5)/P_{21}(1.5)$ and $Q_1(2.5)/P_{21}(2.5)$ transitions. While these transitions are much more removed from $Q_1(0.5)$ than $Q_1(4.5)/P_{21}(4.5)$, this is offset by the much larger populations of the relevant rotational levels of NO(X), and so the background signal arising from these transitions was also large enough to prevent satisfactory images from being recorded for these product states. In addition, these low-N' rotationally excited product states were typically very strongly forward scattered, and so the background beam-spot overlaps the area of the image which is of experimental interest, further reducing the viability of measurements of these product states. A possible alternative method to record experimental images of these product states, which was used in the proof-of-concept experiments,[47] is to prepare NO(A, N = 0) using the spectrally isolated $P_1(1.5)$ transition. However, this method proved ineffective, as the population of NO(X, j = 1.5) required for the $P_1(1.5)$ transition was sufficiently low that acceptable experimental images would require a prohibitively long acquisition time, and it was decided instead to avoid the product states N' = 1, 2 and 4. This effect was also seen for the transitions $Q_1(3.5)/P_{21}(3.5)$ and $Q_1(5.5)/P_{21}(5.5)$, which generated a beam-spot when probing the collisions to product states N = 3 and 5. For these transitions though, the population of NO(X) in the corresponding rotational levels was sufficiently small, and the transitions were sufficiently displaced in frequency from $Q_1(0.5)$, that these background signals were very small and were safely removed through background subtraction.

2.6 Optimisation of the Experiment

Once the experimental setup described above had been assembled and shown to work as intended, various parameters of the experiment were optimised to maximise the scattering signal levels, while simultaneously minimising the levels of the background processes.

2.6.1 Preparation Laser Fluence

The first parameter of the experiment to be optimised was the fluence of the three laser beams used for the preparation of NO(A) and in the detection scheme. The first of these was the 226 nm preparation laser, where the competition between two ionisation processes needed to be optimised. The first was the preparation of NO(A) by a one-photon excitation, which was to be maximised. The second was the ionisation of NO(A) by the absorption of a second 226 nm photon. As discussed in Section 2.5, while the signal was mostly blocked by gating the detector, ions were still observed, which were isotropically distributed across the detector, which reduced the signal-to-noise levels of the scattering images.

The effect of the preparation laser fluence on these two processes was measured by varying it, and measuring the signal levels of unscattered NO ionised in a 226 + 600 + 532 nm process, while keeping the fluences of the probe and ionisation beams constant. The fluence of the preparation laser was varied in the range 0.02-10.5 mJ cm^{-2}, and those of the probe and ionisation lasers were fixed at 23 μJ cm^{-2} and 51 mJ cm^{-2} respectively (only a single ionisation laser beam was used, in contrast to the final experiments). The high-voltage state of the detector was lengthened, so that ions produced by both the preparation and ionisation laser beams were detected. The photodiode was used to make measurements of the integral phosphor intensity, recording the signal intensity corresponding to the ionisation of NO, seeded in a molecular beam of Ar at 0.005%, with a backing pressure of 2 bar. The preparation laser was tuned to the peak of the $Q_1(0.5)$ transition of the A ← X (0,0) band, with the wavelength of the probe laser scanned over

the R(0) transition of the E ← A (0,0) band. Photodiode signals at each wavelength point were recorded from the average of 90 measurements, over three sweeps of the transition, in steps of 0.001 nm. At each fluence, a Gaussian function was fitted to the resulting lineshape, as shown in Figure 2.11(a). The intensity of the one-photon preparation process is described by the area of the peak, while the intensity of the two-photon background ionisation is described by the y-offset. The values obtained for these parameters across the fluence range of the preparation laser is shown in Figure 2.11(b).

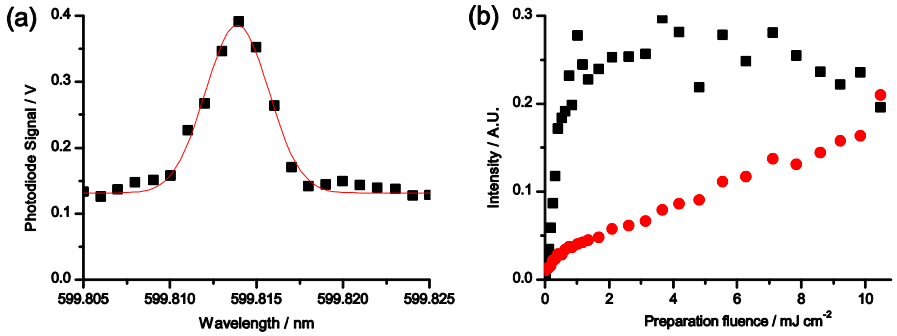

Figure 2.11: (a) Doppler profile of the R(0) transition of the of the NO(E ← A) (0,0) band, fitted with a Gaussian function. (b) Saturation curve for the preparation laser, showing the one-photon NO(A ← X) transition (black) and the 1 + 1 REMPI background signal (red).

These results show a clear trend, with the single-photon preparation signal rising approximately linearly with the fluence, up to 0.4 mJ cm^{-2}, after which the signal becomes partially saturated, but continues to rise until about 2 mJ cm^{-2}, after which it levels out. After about 5 mJ cm^{-2}, the one-photon preparation signal begins to drop, as the two-photon background ionisation process depletes the prepared NO(A) by an appreciable amount. At fluences above 0.5 mJ cm^{-2}, the two-photon background ionisation has an approximately linear relationship with the fluence, which is consistent with the NO(A ← X) transition becoming saturated, and the signal levels depending solely on the one-photon ionisation of NO(A).

As NO(A) is prepared in the j = 0.5 rotational level, it is not possible to generate an initial alignment with the linearly polarised preparation laser, and so this does not need to be considered when setting the fluence. The optimal fluence to run the experiment was chosen to be 0.65 mJ cm^{-2}, as this is the maximum before the preparation process begins to become strongly saturated, and so prepared the maximum population of NO(A), while minimising the two-photon background signal.

2.6.2 Probe Laser Fluence

The 600 nm probe laser is responsible for the rotational state selective excitation of NO(A) to NO(E). While there are no competing pathways bought about by the probe laser, the fluence of the beam must be carefully controlled to keep the transition within the perturbative regime, in order to ensure a known sensitivity to the alignment of the angular momentum vector is maintained. Outside of the perturbative regime, the detection scheme will still retain sensitivity to the rotational alignment, but it will not be possible to calculate the sensitivity, and so the experimental results cannot be quantified in a meaningful way. The effect of the probe laser beam fluence on the detection scheme was measured in a similar method to the preparation beam, with the fluence of the preparation and ionisation beams fixed at 23 μJ cm^{-2} and 51 mJ cm^{-2} respectively, and the fluence of the probe laser varied. Measurements of the integral phosphor signal were made using the photodiode, corresponding to the ionisation signal of a molecular beam of 0.005% NO seeded in Ar, with a backing pressure of 2 bar. The wavelength of the preparation laser tuned to the $Q_1(0.5)$ transition of the A ← X (0,0) band, and the probe laser scanning over the R(0) transition of the E ← A (0,0) band in steps of 0.001 nm. Results were recorded as the average of 90 data points, recorded over three sweeps of the transition, with a Gaussian function fitted to the resulting lineshape and the area of the fit recorded. The results of these measurements, plotted in Figure 2.12(a), show clear saturation effects.

More detailed information regarding the saturation of the probe laser was obtained by investigating the sensitivity of the detection scheme in the measurement of a prepared alignment of NO(A) as a function of probe laser beam fluence. The linearly polarised preparation laser was used to generate a sample of NO(A, $N = 4$, $j = 4.5$), for which j was aligned. In these measurements, a gas mix of 0.005% NO seeded in Ar, with a backing pressure of 2 bar was used. NO(A) was prepared by excitation using the preparation laser tuned to the peak of the $R_{21}(3.5)$ transition of the A ← X (0,0) band. The preparation laser was set to a fluence of 32 μJ cm^{-2}, and polarised vertically in the lab frame. The probe laser was tuned to the peak of the R(4) transition of the E ← A (0,0) band, with its polarisation alternated between being aligned parallel (vertical) and perpendicular (horizontal) to the preparation laser, using the PEM. The fluence of the ionisation laser was varied to compensate for difference in signal caused by changing the fluence of the

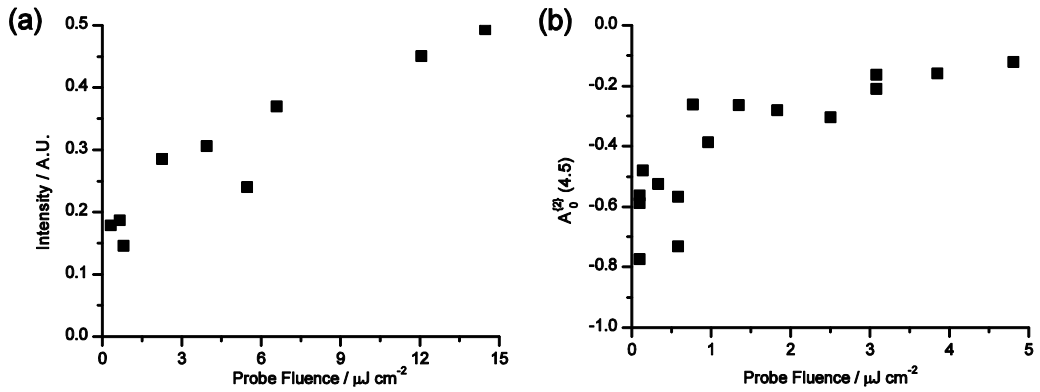

Figure 2.12: (a) Saturation curve for the probe laser, NO(E ← A) transition. (b) Measured prepared alignments for NO(A) relative to the electric vector of the preparation laser, calculated to be $A_0^{\{2\}}(4.5)$ = -0.533.

probe laser, and the polarisation of the ionisation laser was kept at a consistent angle to the preparation and probe lasers throughout the measurements. With both the preparation and probe lasers tuned to the peaks of their corresponding transitions, measurements of the integral phosphor intensity were made using the photodiode, for both polarisations of the probe laser, averaged over 500 laser shots for each.

As the fluence of the preparation laser was set to be well within the perturbative limit (see Section 2.6.1), angular momentum theory can be used to calculate the value of the prepared alignment, relative to the polarisation of the preparation laser, $A_0^{\{2\}}(j)$, using the equation:[58]

$$A_0^{\{2\}}(j) = \frac{\sum_{m=-j}^{m=+j} \begin{pmatrix} j & 1 & J \\ m & 0 & -m \end{pmatrix}^2 \frac{\left[3m^2 - j(j+1)\right]}{j(j+1)}}{\sum_{m=-j}^{m=+j} \begin{pmatrix} j & 1 & J \\ m & 0 & -m \end{pmatrix}^2} \qquad (2.1)$$

Where J and j are the rotational levels of the NO molecule before and after the transition respectively, and m is the projection of j onto the reference axis. For excitation on $j \leftarrow J = 4.5 \leftarrow 3.5$, this leads to a calculated value of $A_0^{\{2\}}(4.5)$ = -0.533. As long as the probe laser is also within the perturbative limit, the measured value of $A_0^{\{2\}}(j)$ will match the calculated value, whereas, if the probe beam is partially saturating the transition, then the measured value will be smaller as the sensitivity is reduced. The

experimental value of $A_0^{\{2\}}(j)$ can be obtained from the equation given by Fano and Macek for the intensity of a one-photon transition:[126]

$$I = CS\left[\frac{1+\frac{3}{2}h^{(1)}A_0^{\{1\}\mathrm{det}}\sin(2\beta)}{\sqrt{J(J+1)}} - \frac{1}{2}h^{(2)}A_0^{\{2\}\mathrm{det}} + \frac{\sqrt{3}}{2}h^{(2)}A_{2+}^{\{2\}\mathrm{det}}\cos(2\beta)\right] \quad (2.2)$$

Where C is a constant, S is a line strength factor, $h^{(1)}$ and $h^{(2)}$ are polarisation sensitivity factors for the polarisation moments,[127] $\beta = 0$ for linearly polarised light, and $A_{q+}^{\{k\}\mathrm{det}}$ are rotational angular momentum polarisation moments in the detection frame (relative to the electric vector of the probe laser, distinct from $A_0^{\{2\}}(j)$ which in this case is relative to the electric vector of the preparation laser). Rearranged to give $A_0^{\{2\}}(j)$ in the reference frame of the electric vector of the preparation laser this becomes:

$$A_0^{\{2\}} = 1 \Big/ \left(h^{(2)}\left[\frac{1.5I_{\parallel}}{I_{\parallel}-I_{\perp}} - 1\right]\right) \quad (2.3)$$

Here, $I_{\parallel}$ and $I_{\perp}$ are the measured intensities of the REMPI signal with the probe laser aligned parallel and perpendicular to the preparation laser respectively. The delay between the preparation and probe lasers was set to zero, and so no correction was required for the effect of nuclear hyperfine depolarisation, given that the timescale for the depolarisation is much longer than the pulse length of the lasers (see Section 2.10.2). The resulting experimental values of $A_0^{\{2\}}(4.5)$ are plotted as a function of probe beam fluence in Figure 2.12(b).

Figure 2.12(b) clearly shows that that at the lowest probe fluences, the measured value of the alignment are consistent the theoretical value of $A_0^{\{2\}}(4.5)$ = -0.533, and as the fluence is increased, this measured value gradually becomes closer to zero as the NO(E ← A) transition becomes saturated. A probe beam fluence of 0.65 μJ cm^{-2} was used in all experiments, as it is the highest fluence before saturation effects become visible in the measured values of $A_0^{\{2\}}(j)$.

2.6.3 Ionisation Laser Fluence

The 532 nm ionisation laser beam ionises the NO(E) molecules which have been state selectively generated by the probe laser, but it can also directly ionise NO(A) molecules directly through a non-resonant two-photon process. The intensity of both of these processes increases with the fluence of the ionisation beam, and experiments were performed to observe these effects and to determine an optimum ionisation beam fluence with which to perform experiments.

For the measurement of the saturation curve of the one-photon ionisation of NO(E), a gas mix of 0.1% NO seeded in Ar with a backing pressure of 2 bar was used. The preparation laser was set to a fluence of 260 μJ cm^{-2}, and was tuned to the peak of the $Q_1(0.5)$ transition of the of the A ← X (0,0) band, while the probe laser was set to a fluence of 13 μJ cm^{-2} and was scanned over the R(0) transition of the E ← A (0,0) band, and the integral phosphor signal was recorded using the photodiode. The wavelength of the probe laser was scanned in steps of 0.001 nm across the profile of the transition and the acquired signal was averaged over three sweeps of the laser, for a total of 90 shots per wavelength point. A Gaussian function was fitted to the lineshape of the peak, and the area was recorded as the signal intensity corresponding to the one-photon ionisation of NO(E), as shown in Figure 2.13.

The y-offset of the Gaussian fit depends solely on the preparation and ionisation laser beams, and so represents the non-resonant ionisation of NO(A). However, even at the

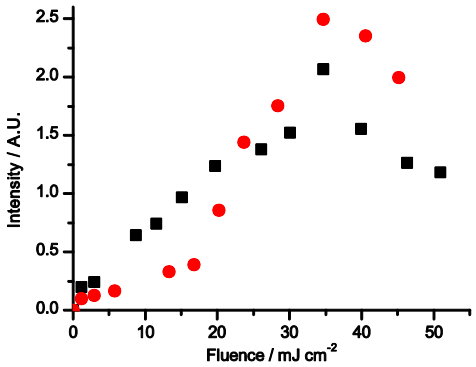

Figure 2.13: Saturation curve for the ionisation of NO resulting from the ionisation laser, showing the one-photon ionisation of NO(E) (black) and the non-resonant two-photon ionisation of NO(A) (red).

highest fluence, no observable offset was observed, and so a separate experiment was required to make this measurement. To measure the saturation curve for this non-resonant process, a gas mix of 5% NO seeded in Ar with a backing pressure of 2 bar was used. The preparation laser was set at 260 μJ cm^{-2} and was tuned to the peak of the $Q_1(0.5)$ transition of the A ← X (0,0) band and the probe laser was blocked. The photodiode signal was averaged over 100 shots, to measure the integral phosphor signal, which was recorded as a function of the ionisation beam fluence. The saturation curve for this ionisation process is also shown in Figure 2.13.

The signal intensities resulting from the two measurements act as would be expected for one and two-photon processes, respectively. The one-photon ionisation of NO(E) has a broadly linear dependence at low-fluences of the ionisation beam, while the two-photon ionisation of NO(A) clearly has a non-linear dependence. In both cases, the signal becomes saturated at roughly 35 mJ cm^{-2}. It is expected that the two-ionisation laser beam setup used in the experiments will supress the non-resonant ionisation pathway, relative to the one-photon ionisation. This is because the photon for the one-photon ionisation can originate from either laser beam, while both photons of the two-photon process must originate from the same beam. However, no saturation tests were performed with the two-ionisation beam arrangement.

In the final scattering experiments, the ionisation laser fluence was varied depending on the scattering cross section of the state being probed, with the minimum required to obtain a suitable signal level used. In a typical set of measurements, the fluence of each of the ionisation beams was varied in the range 4-40 mJ cm^{-2}, with higher fluences used for large ΔN transitions, where the scattering signal was small.

2.6.4 Preparation-Probe Laser Timing

In addition to the fluences of the laser beams used in the experiment, obtaining the highest possible signal levels also relied on having optimal timings between the three laser pulses. The first timing to be examined is the delay between the preparation and probe laser pulses, which determines the length of time over which collisions can occur.

There are two factors which need to be balanced when determining the optimal delay between these two pulses. The first is the number of collisions which occur in the time between the preparation and probe laser pulses, which will clearly be larger at longer delays. The second is that NO(A) molecules will fluoresce back to the ground state, and so the longer the delay, the fewer NO(A) molecules will remain. These two processes are at odds with each other: with too short a delay, there will be too few collisions to generate a sufficient scattering signal, but with too long a delay, the population of NO(A) will have been depleted by fluorescence. An additional factor is the presence of the background signal resulting from the preparation laser (see Section 2.5), which becomes more intense at shorter delays. Finally, the longer the delay between the preparation and probe lasers, the further the scattered NO(A) molecules can travel, and if the delay is too long, the faster moving molecules will leave the detection region, leading to a detection bias.

In order to determine the optimal preparation-probe delay, a scattering experiment involving the collisions of NO(A) with Ne was conducted, in which the scattering signal was measured as a function of preparation-probe delay. The preparation and probe lasers were tuned to the peaks of the $Q_1(0.5)$ transition of the A ← X (0,0) band and the R(7) transition of the E ← A (0,0) band respectively, and the number of centroided objects was recorded with both molecular beams active, and with only the NO beam active, for a total of 1,000 laser shots each. From these values, the number of centroided objects resulting from scattering and background processes were calculated. Figure 2.14(a) shows the number of scattered and background objects as a function of the preparation-probe laser delay time. While it is clear that the number of scattered objects is higher at shorter delays, this is offset by the increased number of background objects, which becomes unusably large at shorter delays. While there is no clear optimal value, it was decided that 360 ns gave the best compromise between number of scattered molecules and the background signal, and so was used in the experiments. As the number of inelastic collisions varies for different collision systems, because of the different molecular beam speeds and the different ICSs, the optimal delay may change as well. However, this is expected to be a small effect, and the measurement was not repeated for different collision systems.

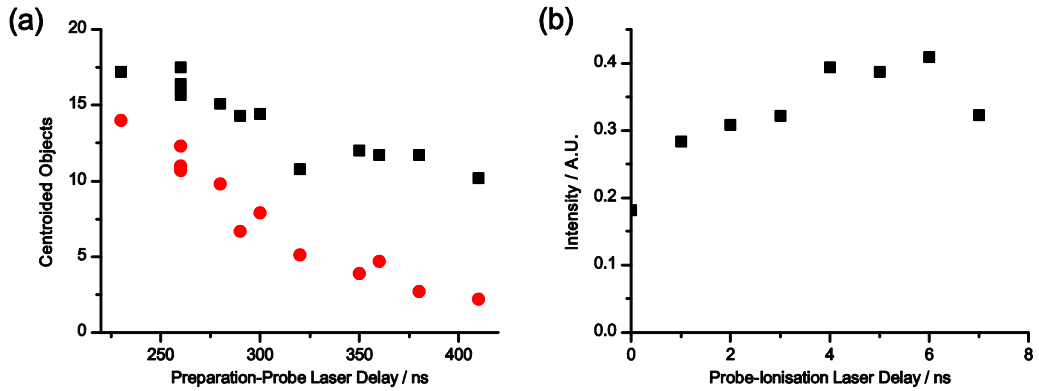

Figure 2.14: (a) Number of centroided objects as a function of preparation-probe laser delays, showing scattered objects (black) and background objects (red). (b) Signal intensity as a function of probe-ionisation delay.

2.6.5 Probe-Ionisation Laser Timing

The only significant process during the delay between the probe and ionisation lasers is the fluorescence of NO(E), and so, a shorter delay time will give more signal, up until the point where the temporal profiles of the two laser beams begin to overlap. The delay between the two lasers was varied by altering the length of the delay line of the ionisation laser (see Figure 2.4), with the arrival time of the two laser pulses at the vacuum chamber measured using a fast photodiode (200 ps risetime, Electro-Optics Technology 2000). A gas mix of 1% NO seeded in Ar with a backing pressure of 2 bar was used, with the preparation laser generating NO(A) through the $Q_1(4.5)$ transition of the A ← X (0,0) band, the probe laser probing on the R(4) transition of the E ← A (0,0) band, and the ionisation laser ionising NO(E) molecules. The probe laser was scanned over the transition in steps of 0.001 nm, with the average integral phosphor signal measured using the photodiode, with 10 scans of the transition made, for a total of 100 shots at each wavelength point. A Gaussian function was fitted to this lineshape, and the area recorded to give the signal size. The resulting signal sizes are plotted as a function of probe-ionisation delay time in Figure 2.14(b). There is a clear trend, with the signal size increasing with delay time for the first 4 ns, which is consistent with the ≈4 ns temporal profiles of the two laser pulses becoming separated. After 4 ns, there is very little change in the signal, and a probe-ionisation delay of 4 ns was chosen for use in experiments.

2.6.6 Photoelastic Modulator Timings

As described in Sections 2.2 and 2.3, the PEM was used to control the polarisation of the probe laser beam. The PEM changes the polarisation of the laser beam by passing the light through a vibrating quartz crystal, which exhibits a birefringence proportional to the strain applied to it. This means that the birefringence, and as such, the resulting polarisation of the light, was different at different points in the compression cycle. In order to generate horizontal and vertical linear polarisations of the light, the timing of the entire experiment was synchronised relative to the PEM cycle, as described in Section 2.3, such that the probe laser passed through the PEM at the correct points in the compression cycle. These timings were optimised by placing a linear polariser in the laser beam path, after the PEM, followed by an energy meter. To set the polarisation of the probe laser to be vertical in the laboratory frame, the polariser was set to allow the passage of horizontally polarised light, and vice versa. The timing of the experiment was then altered to produce a null energy for each polarisation arrangement and the two optimal delays were recorded, to be subsequently used in the scattering experiments. A typical polarisation purity of >99% was obtained through this method. These timings were checked and reoptimised if necessary at the start of data collection for every new system (typically every 1-2 months), although the optimal delays were not found to vary by a significant amount on this timescale.

2.6.7 Detector Voltages and Timings

The front face of the MCPs was grounded, with a single high-voltage applied to the rear MCP, which was switched between two levels, providing a high-voltage and a low-voltage state. Each of these voltages was generated by an independent power supply. A separate high-voltage was applied to the phosphor screen, which was generated by a third independent power supply. The voltages applied to the MCPs need to be set in such a way that ion strikes are only registered by the camera during the high-voltage state, preventing the detection of the large number of background ions produced by the preparation laser (see Section 2.5).

In principle, 0 V could be applied to the MCPs in the low-voltage state, however, this would lead to a large difference between the low- and high-voltage states, which would cause rapid degradation of the detector. The low-voltage state was set to the maximum voltage at which the beam-spot resulting from the preparation beam was not registered by the camera, which was found to be 950 V. The maximum voltage that the MCPs are rated to is 1,800 V. However, using this for the high-voltage stage would also lead to faster degradation, and a shorter working lifetime of the detector than using a lower voltage. Individual ion strikes were clearly resolved using the CCD camera when the MCPs were set to 1,550 V, and so this was used to supply the high-voltage state.

The voltage applied to the phosphor screen provides an acceleration field for the electrons emitted from the back face of the MCPs, and thus a higher voltage increases the kinetic energy of the electrons impacting the phosphor screen, resulting in a more intense emission from a given ion strike. The phosphor screen was rated to 5,000 V, and in these experiments, it was held at 4,800 V.

In addition to setting the voltages, it was also vitally important that the time at which the detector is switched between the low and high-voltage states was optimised, to match the arrival time of the NO^+ ions generated by the ionisation laser. It is important that the high-voltage state is not set for too short a time, because there will be scattered ions which are not detected, leading to an undefined detection bias (in addition to lowered overall signal levels). On the other hand, if the high-voltage state was set too long, the number of non-time-of-flight selected background ions resulting from the preparation laser would be higher than is necessary, reducing the signal-to-noise ratio. The duration of the high-voltage state was optimised to be 120 ns, where increasing the length did not give any significant increase in scattering signal.

2.6.8 Camera Threshold

As described in Section 2.5, dark counts in the camera resulted in non-zero pixel values, even when the camera lens cap was in place. Hence, when the raw camera shots were simply summed in an acquisition, the scattering signal in the resulting images was

dominated by the camera dark counts. This background was greatly reduced by applying a software threshold to each individual camera shot in the data acquisition code, in which pixels which fell below a pre-determined intensity were assigned a value of zero. The optimal threshold value was determined by recording a sequence of 4,000 shot images of the camera dark counts, applying a range of camera threshold values. The resulting summed images were integrated to give the results shown in Figure 2.15. A threshold value of 20 was applied for the experiments reported in this thesis, as this value of the threshold blocks essentially all of the camera dark noise, while still providing enough dynamic range to allow for the signals resulting from individual ion strikes to be clearly resolved.

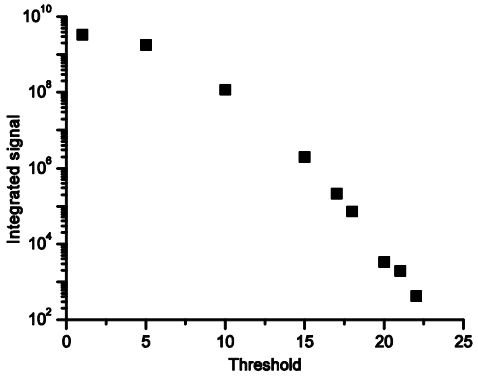

Figure 2.15: (a) Integrated camera signal, recorded over 4,000 camera shots with the experiment inactive, as a function of camera threshold.

2.6.9 Ion Optic Voltages

Optimal velocity map imaging requires very fine control of the voltages applied to the electrodes which make up the ion optics. Three power supplies were used to supply the seven powered electrodes, with the first three electrodes (V1, V2 and V3) each supplied independently. The remaining four electrodes (V4, V5, V6 and V7) were each supplied a voltage that was directly proportional to V3 (see Table 2.1), controlled using a custom-built voltage-divider network. An eighth electrode (V8) was grounded. An initial set of voltages for velocity mapping conditions was obtained by calculations using Simion, which were subsequently optimised by varying V2 and V3 across a grid of voltages (with V4-7 varying together with V3) and recording the resulting velocity map images. Ion

images were recorded with molecular beams of 10% NO seeded in Ar, from both pulsed valves simultaneously, with a backing pressure of 3 bar. NO was ionised through 1 + 1 REMPI using the preparation beam, which was tuned to the peak of the $Q_1(0.5)$ transition of the A ← X (0,0) band. As the imaged NO was in the molecular beams, a correctly focused velocity map image would contain well-defined beam-spots, which can be accurately described using a 2-D Gaussian function.

Table 2.1: Voltages applied to the electrodes V4-7 in the ion optics.

Electrode	Voltage / V
V4	V3 × 0.842
V5	V3 × 0.632
V6	V3 × 0.420
V7	V3 × 0.210

Initially, images were acquired across a coarse grid of voltages, as shown in Figure 2.16(a). It is clear from a visual inspection of the images that there is a distinct "valley of stability" running diagonally across the array, containing well-focussed beam-spots, while outside this, the focussing conditions are clearly sub-optimal. Images were acquired for a finer grid of voltages, in the centre of this coarse grid, shown in Figure 2.16(b). In order to gain more quantitative insight into these focussing conditions, the images were analysed by fitting 2-D Gaussian functions to both beam-spots in the image at each set of voltages. The quality of the fits was assessed by recording the integrated value of the absolute residuals of the fits, with the results displayed in Table 2.2. These results indicate that the best fits, and therefore optimal focusing conditions were obtained at V1 = 3,000 V, V2 = 2,656 V, V3 = 2,025 V, which were subsequently used in the acquisition of experimental data presented in this thesis.

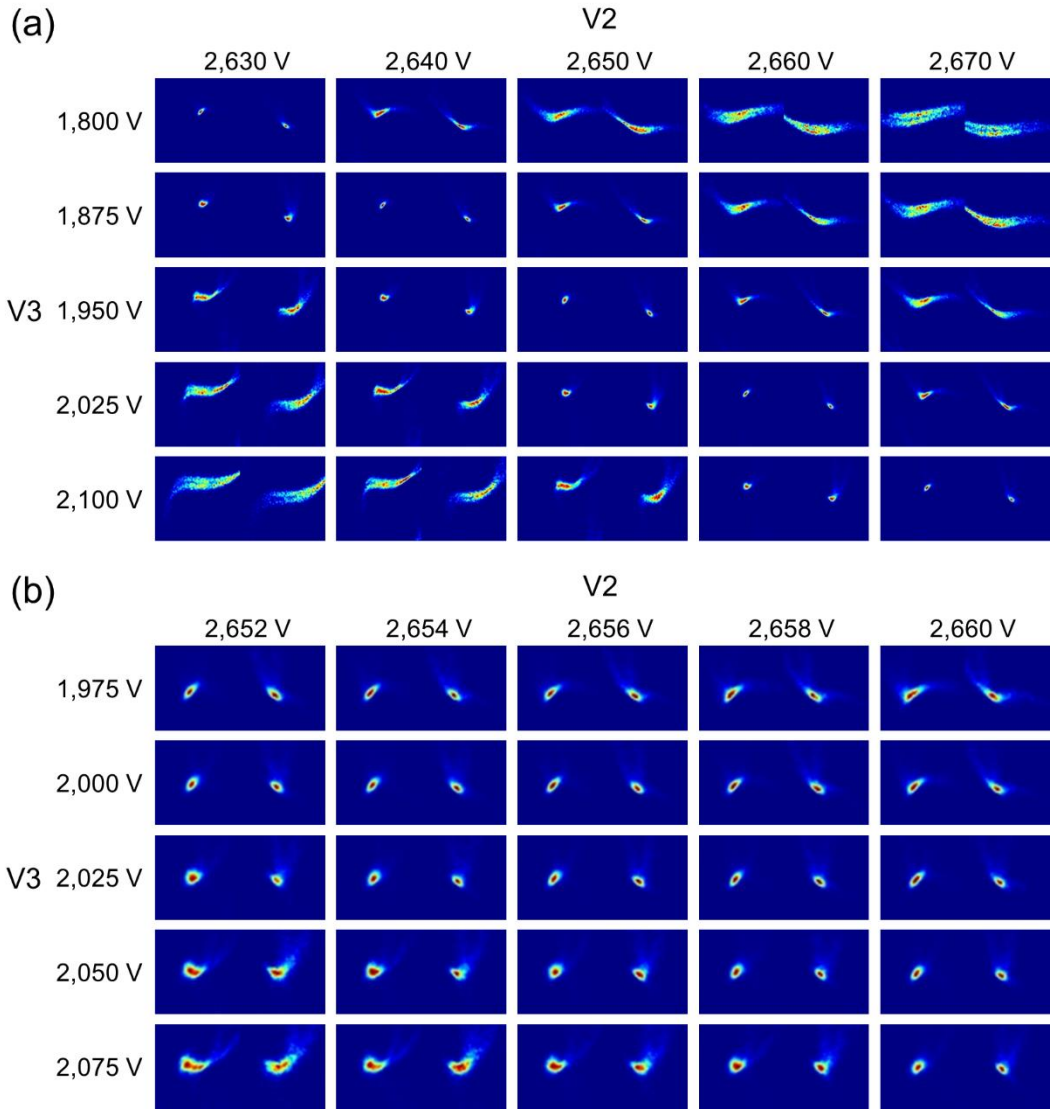

Figure 2.16: Velocity mapped beam-spots under different ion optic focussing conditions with V1 = 3,000 V. (a) Over a wide range of voltages, with colour maps showing 110×110 pixels, (b) over a narrow range of voltages, with colour maps showing 50×50 pixels.

Table 2.2: Integrated residuals for the fitting of 2-D Gaussian functions to the beam-spots displayed in Figure 2.16.

	V2 = 2,652 V	V2 = 2,654 V	V2 = 2,656 V	V2 = 2,658 V	V2 = 2,660 V
V3 = 1,975 V	0.909	1.061	1.119	1.241	1.484
V3 = 2,000 V	0.848	0.876	0.900	0.999	1.177
V3 = 2,025 V	0.895	0.861	0.845	0.909	0.895
V3 = 2,050 V	1.073	0.967	0.971	0.903	0.877
V3 = 2,075 V	1.227	1.102	1.012	0.955	0.897

2.7 Velocity to Pixel Ratio

In order to meaningfully analyse the images, it is necessary to know the velocity to pixel ratio of the apparatus at the optimised ion optic voltages. This value can be most easily determined through the imaging of a well-defined photodissociation process, for which the kinetic energy release and as such, fragment speed, is known to a high level of certainty. Two such systems were used in the measurements of the velocity to pixel ratio for the experiments described in this thesis: the 225 nm multiphoton dissociation and dissociative photoionisation of O_2,[70] and the 226 nm photodissociation of NO_2.[128]

O_2 is excited to the (v = 2, N = 2) level of the $3d\pi(^3\Sigma_{1g}^-)$ state by a two-photon absorption from the preparation laser, tuned to 224.999 nm. From this state, the O_2 molecule can dissociate to produce O atoms, which are subsequently ionised. Alternately, a third photon can ionise the O_2 molecule, which then dissociates to produce an O atom and an O^+ ion.[70] As both of these dissociations occur through a number of different channels, each with their own unique final O^+ speed, it is an ideal method for the calibration of the velocity to pixel ratios in VMI experiments. The details of the individual pathways are outlined in Reference [70]. A molecular beam consisting of 20% O_2 seeded in Ar, with a backing pressure of 3 bar was used in this measurement. The horizontally polarised preparation laser, with an energy of 6 mJ, was focussed using a 30 cm focal length lens onto the molecular beam in the centre of the focussing region of the ion optics, and was step scanned over the transition in steps of 0.001 nm. The timing of the high-voltage gate applied to the detector was set appropriately for the imaging of O^+ ions, and an image was recorded over 100,000 laser shots, with no background subtraction.

Table 2.3: Channels for O_2 photodissociation and dissociative photoionisation observed in the velocity mapped image in Figure 2.17.[70]

Transition	Total kinetic energy release / eV	O^+ speed / m s^{-1}
$O_2^+(X^2\Pi_g, v = 9) \rightarrow O(^3P) + O^+(^4S)$	0.79	2,183
$O_2^* \rightarrow O(^3P) + O^*(3p\ ^5P)$	0.68	2,025
$O_2^* \rightarrow O(^3P) + O^*(3p\ ^3P)$	0.43	1,610

The resulting velocity map image (Figure 2.17) was analysed using the basis set expansion (BASEX) method[129] to obtain a speed distribution for the O^+ photofragments, as is shown in Figure 2.18. As is apparent from a visual inspection of the image, there are three observed photofragments with clearly distinct speeds. A Gaussian function was fitted to each of the three peaks in the speed distribution to obtain the mean "speed" of the photofragment in pixels. By comparing these pixel values to the speeds calculated from the total kinetic energy release of the photofragmentation, the velocity to pixel ratio for the O^+ ions can be calculated to be 11.95 ± 0.03 m s^{-1} $pixel^{-1}$. As the velocity to pixel ratio is inversely proportional to the square root of the mass to charge ratio of the ion being mapped, this means that NO^+ ions will have a corresponding velocity to pixel ratio of 8.73 ± 0.02 m s^{-1} $pixel^{-1}$ under the same focussing conditions.

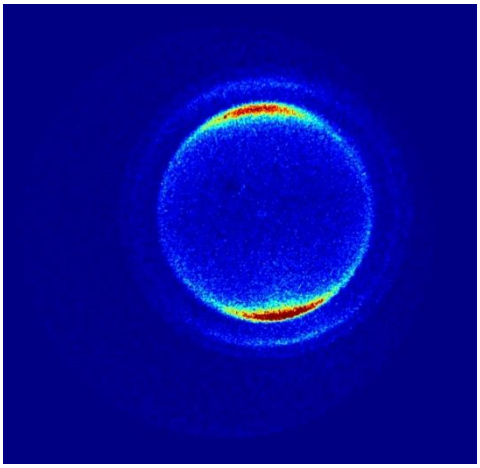

Figure 2.17: Velocity mapped image showing O^+ ions formed from the photodissociation and dissociative photoionisation of O_2 at 224.999 nm.

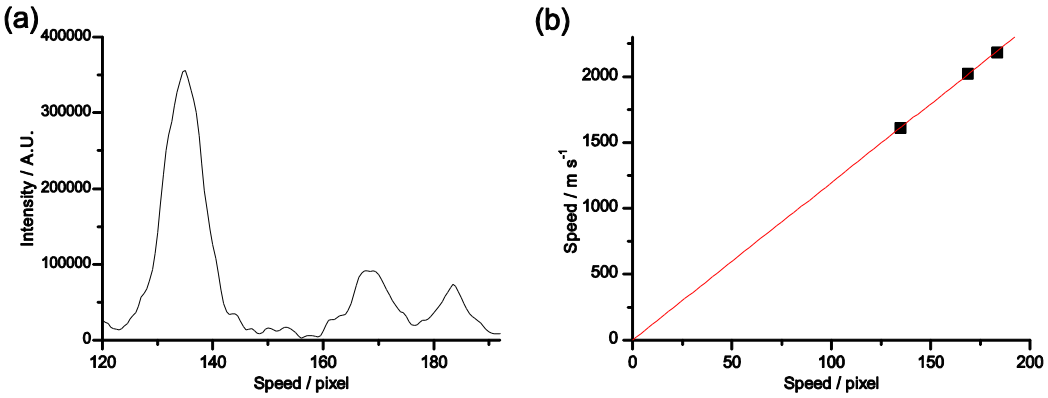

Figure 2.18: (a) O^+ photofragment velocity distribution for the photodissociation and dissociative photoionisation of O_2 at 224.999 nm. (b) The linear relationship between the calculated velocity for O^+ photofragments produced by the photodissociation of O_2 at 224.999 nm, and the image radius in pixels, with the y-intercept set to zero.

The photodissociation of NO_2 at 226 nm provides a second system with which to measure the velocity to pixel ratio, which can be used to support the results of the O_2 dissociation measurement. This process has the advantage of detecting NO^+ ions, the same as the scattering experiments presented in this thesis, and so the velocity to pixel does not to be scaled to account for differences in the mass to charge ratio. The photodissociation and ionisation is a three-photon process, with the first photon exciting NO_2 to the dissociative 2^2B_2 state, which generates NO(X) and O(^{1}D) photofragments. NO(X) is then ionised by 1 + 1 REMPI through a resonant transition in the A ← X (0,0) band, by photons from the same laser beam.

Table 2.4: Transitions in the NO(A ← X) REMPI spectrum probed in the photodissociation of NO_2.

Transition	Wavelength / nm	Total kinetic energy release / cm^{-1}	NO^+ velocity / m s^{-1}
$R_1(6.5)$	226.021	3,166	937
$R_1(13.5)$	225.715	2,980	909
$P_{21}(19.5)$	225.735	2,636	855
$P_{21}(26.5)$	225.288	2,178	777
$P_{21}(33.5)$	224.962	1,590	664

A molecular beam with 10% NO_2 seeded in Ar with a backing pressure of 3 bar was used in these measurements, and the high-voltage gate of the detector was set appropriately for the detection of NO^+ ions. The horizontally polarised laser beam was focussed onto the molecular beam using a 30 cm focal length lens. Velocity map images were recorded in this way for five different NO(X, v = 0, j, F_1) rotational levels, with 4,000-10,000 laser shots used in the acquisition of each, and are shown in Figure 2.19. The fluence of the laser was varied appropriately for each transition in order to obtain the optimal signal to noise levels. The five transitions were chosen to be spectroscopically isolated, to make analysis of the images as unambiguous as possible, and to cover as wide a range of photofragment speeds as possible. In addition to the clear signal arising from the expected photodissociation channel, there is also a separate signal localised around the velocity of the molecular beam. For the $R_1(6.5)$ and $R_1(13.5)$ transition images, this appears to be mostly the result of the ionisation of trace amounts of NO, which has

contaminated the molecular beam. This is clearly not the case for the signal in the $P_{21}(26.5)$ and $P_{21}(33.5)$ transition images, for which the population of the corresponding rotational levels of NO in the molecular beam would have been negligibly small. This signal did not interfere with the analysis of the images, and its origin was not investigated. A plausible explanation for this signal is that it results from NO molecules formed by the dissociation of N_2O_4, which had been produced by the dimerisation of NO_2 in the molecular beam.

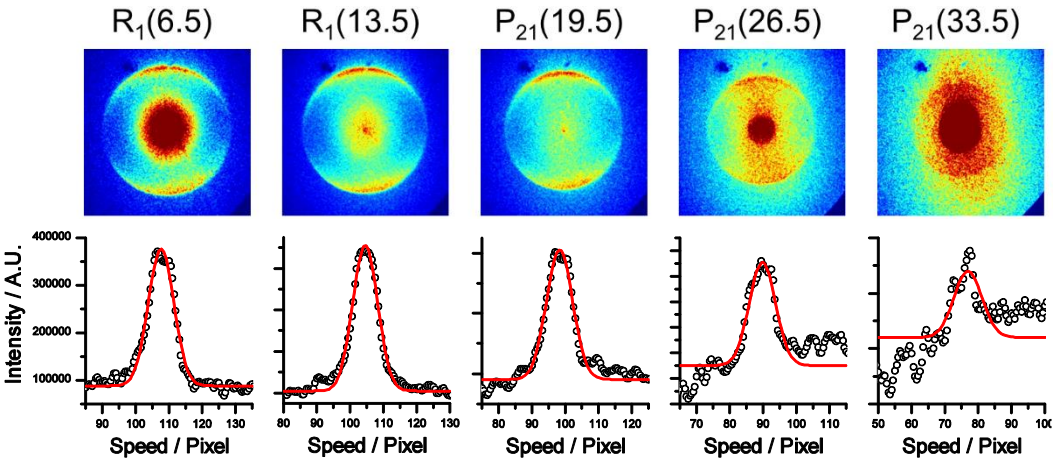

Figure 2.19: Top row: Velocity mapped images of NO^+ formed from the 226 nm photodissociation of NO_2. Bottom row: NO^+ photofragment speed distributions for the photodissociation of NO_2.

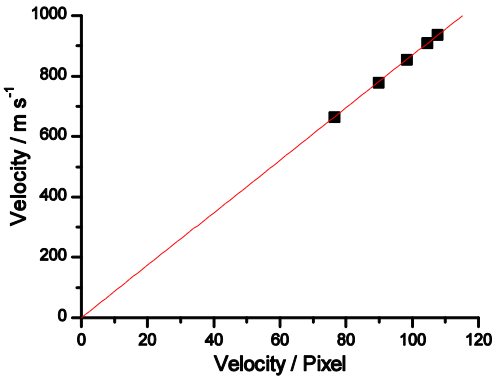

Figure 2.20: The linear relationship between the calculated velocity and the image radius in pixels for NO^+ photofragments produced by the photodissociation of NO_2, with the y-intercept fixed to zero.

As with the O_2 dissociation image, the NO_2 photodissociation images were each independently analysed using the BASEX method to obtain a speed distribution of the photofragments in pixels, which were compared to the calculated final speed of the NO^+ ions. Using this method, the velocity to pixel ratio for NO^+ was determined to be 8.68 ±

0.01 m s^{-1} $pixel^{-1}$, which compares favourably to the value of 8.73 ± 0.02 m s^{-1} $pixel^{-1}$ obtained from the photodissociation of O_2. A velocity to pixel ratio of 8.7 m s^{-1} $pixel^{-1}$ was used in the analysis of the scattering images presented in this thesis.

2.8 Centring Measurements

A velocity map image will have a set of coordinates which corresponds to zero velocity in the lab frame. Knowing this location is vitally important for a number of reasons. Most obviously, it is necessary for the analysis of the images, as it is required to accurately obtain the position of the scattering signal, as well as to correctly account for the effects of the spread of molecular beam speeds on the signal. To determine the zero-velocity coordinate, images were recorded in which NO, seeded in molecular beams produced by both valves simultaneously, was ionised in a 1 + 1 REMPI process, typically via the $Q_1(0.5)$ transition of the A ← X (0,0) band. Measurements were made sequentially with NO seeded in different carrier gases, typically He, Ne and Ar, from which the resulting molecular beams have substantially different velocities. The mean positions of the beam-spots on the image were determined by fitting 2-D Gaussian functions to each of the beam-spots individually. As is shown in Figure 2.21, lines of best fit were plotted through the mean beam-spot positions, which represent the propagation directions of the two molecular beams, and the point at which the two molecular beam propagation directions intersected corresponded to the zero-velocity coordinate. Multiple measurements on the same day indicated that the measured coordinates had an uncertainty of ±0.7 pixels in both the x and y coordinate.

When the first batch of experimental data was analysed, it became apparent that the position of the zero-velocity coordinate was unstable. Comparison of scattering images acquired on different days indicated that the position of the entire velocity map image on the detector varied by several pixels from day to day. As the scattering images were found to register well upon a simple translation, it was clear that this effect was not caused by unstable focussing conditions of the ion optics. These instabilities were found to be particularly pronounced immediately after maintenance had been conducted on the experimental apparatus. The most probable explanation for this effect was determined to

be mechanical instabilities in the apparatus, which were associated with the long time-of-flight tube and heavy detector chamber. The installation of an additional support frame, which securely clamped the heavy detector chamber to the framework supporting the rest of the experimental apparatus, reduced the instability. With the additional supports, the average drift per day was 1.5 pixels.

Since the measurement of the zero-velocity coordinate was a simple and rapid process (typically taking about 20 minutes), a measurement was taken prior to data acquisition every day. From these measurements, the position of the zero-velocity coordinate was tracked across multiple days. The instability in the zero-velocity coordinate was subsequently accounted for in the data analysis by translating the images by the appropriate number of pixels. As this effect was only discovered upon the analysis of the first batch of data, the centring measurements were not conducted for the earliest sets of experimental data (NO(A) + Ar and Ne). The alternate solution used to account for this variation in the zero-velocity pixel position is described in Sections 3.2.1 and 3.3.1.

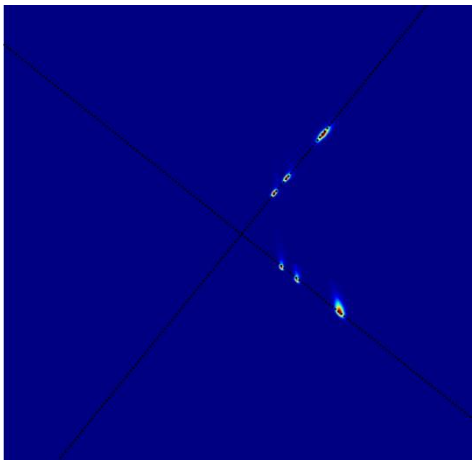

Figure 2.21: Sum of velocity map images of NO seeded in Ar, Ne and He used in centring measurements. Dotted black lines show the direction of travel of the two molecular beams, with the intersection of the lines showing the coordinates which correspond to zero lab frame velocity in the plane of the image.

2.9 Measurements of Molecular Beam Speed Distribution

While the mean molecular beam speeds can (with a few exceptions) be trivially obtained from the position of the beam-spot in the velocity map images, it is much more difficult to reliably measure the spread of the beam speed distribution, which is also required for analysis of the images. While a Gaussian function can be fitted to the velocity axis of a beam-spot, the width of this function will be a convolution of the spread of the molecular beam speed with an instrument function (which accounts for the resolution of the detection method, the multi-pixel dimension of each individual ion strike, and the recoil speed of the NO^+ resulting from its photoionisation).

To sidestep this issue, measurements of the molecular beam speed distributions were made in separate LIF measurements. The details of this experimental setup have been described elsewhere,[130] and so only a brief overview of the experiment, and the results relevant to the experiments presented in this thesis will be given here. The preparation laser was tuned to the $R_1(0.5)$ transition of the NO(A ← X) (0,0) band. The excited NO molecules fluoresced back to the ground state, into a range of vibrational levels, with v = 1 being the most populated.[131] The probe beam was tuned to the $R_1(0.5)$ transition of the NO(A ← X) (1,1) band, and intersected the molecular beam a further 192 mm downstream. A photomultiplier tube was positioned to detect LIF signal induced by the probe laser beam. As the NO in the molecular beam was initially exclusively in the v = 0 vibrational level, any LIF signal must originate from NO which has been "tagged" by the preparation laser. By recording LIF measurements at different delays between the two lasers, an appearance profile of the tagged NO was generated for a particular set of molecular beam conditions. This appearance profile was converted into a speed distribution of NO in the molecular beam, to which a Gaussian function was fitted to obtain the mean speed and the FWHM, which are shown in Table 2.5.

Table 2.5: Speed distributions of molecular beams consisting of NO seeded in a rare gas, with a backing pressure of 3 bar, obtained using LIF measurements.

Seed gas	10% NO mean / m s^{-1}	1% NO mean / m s^{-1}	10% NO FWHM / m s^{-1}	1% NO FWHM / m s^{-1}
He	1,396.8 ± 0.2	1,677 ± 2	91.2 ± 0.4	124 ± 5
Ne	803.1 ± 0.2	801.6 ± 0.6	57 ± 1	52 ± 1
Ar	575.1 ± 0.7	560.5 ± 1.0	53 ± 2	45 ± 3
N_2	-	763 ± 5	-	74 ± 12

2.10 Analysis and Fitting of Scattering Images

Once a set of V and H experimental images had been acquired, they needed to be analysed. The structure of the scattering images is sensitive to the differential cross section (DCS), and the angle-dependent rotational alignment moments, $A_0^{\{2\}}(\theta)$, $A_{1+}^{\{2\}}(\theta)$ and $A_{2+}^{\{2\}}(\theta)$.[58] These parameters were extracted using a forward simulation and back-fitting procedure developed by Dr T. R. Sharples and Prof. M. L. Costen. Images were simulated with DCS and $A_{q+}^{\{2\}}(\theta)$ moments described by a weighted expansion of Legendre polynomials, in scattering angle, θ. The simulated images were fitted to the experimental images by varying the weighting of the Legendre moments using a downhill-simplex minimisation routine to determine the values of the DCS and $A_{q+}^{\{2\}}(\theta)$ moments which best reproduce the experimental images.

2.10.1 Experimental Observables

The DCS quantifies the distribution of scattering angles induced by the collision, which describe the angle between the initial relative velocity vector (**k**) and the final

relative velocity vector (**k′**). The effect of the DCS can be clearly seen in the images, as the distribution of intensity around the edges of the scattering signal in both the V and H images. A large value of the DCS at a particular scattering angle will result in a large number of NO(A) molecules being scattered at that angle, and a large amplitude in the corresponding regions of the image. Similarly, a small value of the DCS leads to areas of low amplitude in the scattering signal at the corresponding angles.

The probability of detecting a scattered NO(A) molecule depends on how the final rotational angular momentum vector, **N′**, is aligned relative to the electric vector of the probe laser, the effect of which is quantified by the rotational alignment moments, $A_{q+}^{\{2\}}(\theta)$ (a quantitative description of this dependence is provided in Section 2.10.2). These rotational alignment moments fluctuate with scattering angle, and manifest in the scattering images as differences in sensitivity to the NO(A) molecules which have been scattered with different azimuthal angles, and differences in sensitivity between the two probe beam polarisations. These effects are shown for an idealised system in Figure 2.22.

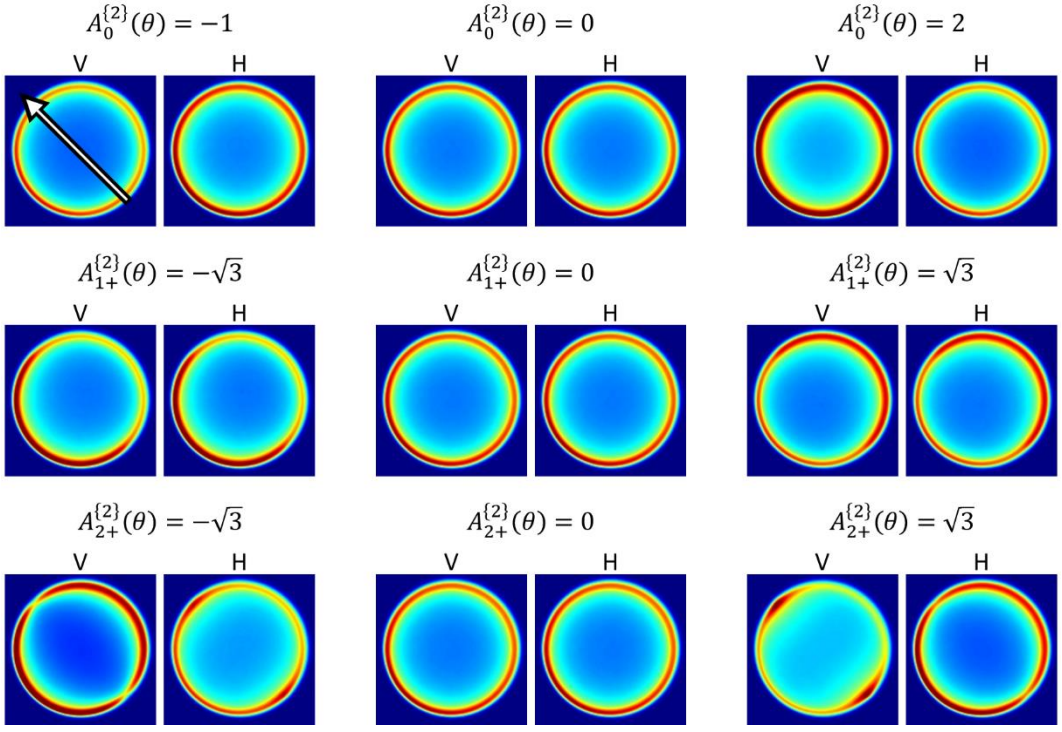

Figure 2.22: V and H simulated velocity map images showing the effects of the different rotational alignment moments. Images are simulated for an idealised system, with both molecular beam speed distributions having mean 435 m s^{-1} and FWHM 50 m s^{-1}, an isotropic DCS, and a $\mathbf{k}$-$\mathbf{k_p}$ angle of 45°. $A_{q+}^{\{2\}}(\theta)$ moments were set to zero, except where indicated otherwise. The arrow in the top-left panel shows the direction of **k**.

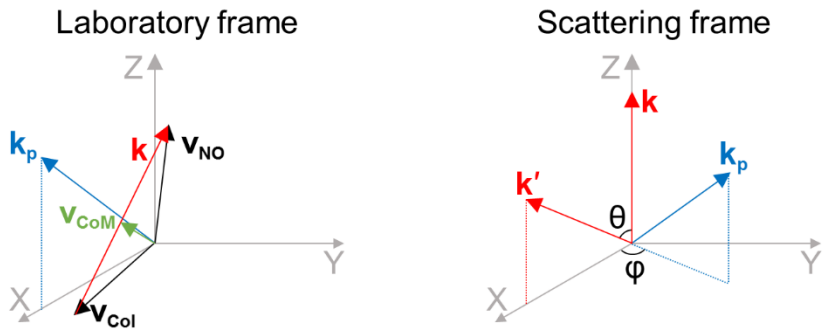

Figure 2.23: Left, the laboratory frame, defined such that the **Z** and **X** axis lie parallel to the average NO and molecular beam velocities respectively. The probe laser propagation direction, $\mathbf{k_p}$ lies in the **XZ** plane, while vectors $\mathbf{v_{NO}}$, $\mathbf{v_{Col}}$, $\mathbf{v_{CoM}}$ and **k** can lie out of the **XZ** plane. Right, the centre of mass scattering frame, defined such that the **Z** axis lies parallel to **k** and **k′** lies in the **XZ** plane.[132]

$A_0^{\{2\}}(\theta)$ describes the alignment of **N′** relative to the **Z** axis of the scattering frame (**k**), where for positive values of $A_0^{\{2\}}(\theta)$, **N′** is preferentially aligned parallel to **Z**, while negative values of $A_0^{\{2\}}(\theta)$ lead to **N′** preferentially aligned perpendicular to **Z**. This manifests in the scattering images as a difference in intensity between the V and H images. For a region of the image where $A_0^{\{2\}}(\theta)$ at the corresponding scattering angle is positive, the V image will have a larger amplitude than the H image. Correspondingly, if $A_0^{\{2\}}(\theta)$ is negative, the H image will have a larger amplitude than the V image.

The projection of **N′** onto the **XY** plane of the scattering frame (shown in Figure 2.23), defined by **k** and **k′**, is described by $A_{2+}^{\{2\}}(\theta)$. For positive values of $A_{2+}^{\{2\}}(\theta)$, **N′** is preferentially aligned parallel to the **X** axis (in the **k**-**k′** plane), whereas for negative values, **N′** is preferentially aligned parallel to the **Y** axis (out of the **k**-**k′** plane). This moment affects the detection probability of NO(A) molecules scattered in and out of the plane of the detector. For positive values of $A_{2+}^{\{2\}}(\theta)$ this leads to a higher detection probability of the molecules scattered in-plane (at the edges of the image) in the H image, and out-of-plane (in the centre of the image, along **k**) in the V image. For negative values of $A_{2+}^{\{2\}}(\theta)$, the effect is reversed, with higher detection probabilities for the in-plane scattered in the V image, and out-of-plane scattered molecules in the H image.

$A_{1+}^{\{2\}}(\theta)$ describes the way in which **N′** is tilted in the **XZ** plane of the scattering frame, with **N′** aligned preferentially parallel to the **X + Z** axis for positive values of $A_{1+}^{\{2\}}(\theta)$, and preferentially parallel to the **X – Z** axis for negative values. $A_{1+}^{\{2\}}(\theta)$ manifests as a reflection asymmetry of the intensity of both the V and H images about **k** in the images. $A_{1+}^{\{2\}}(\theta)$ is commonly not observed in experimental images, as the angle between **k** and the probe laser propagation is typically close to 90°, where there is no sensitivity to the moment (see Equation 2.7).

Both $A_{1+}^{\{2\}}(\theta)$ and $A_{2+}^{\{2\}}(\theta)$ necessarily have values of 0 at scattering angles of 0° and 180°. This is because they describe the alignment of **N′** relative to the **k**-**k′** scattering plane, which becomes undefined at these angles as **k** and **k′** are parallel or antiparallel, and so $A_{1+}^{\{2\}}(\theta)$ and $A_{2+}^{\{2\}}(\theta)$ become zero through symmetry. Additionally, $A_{0}^{\{2\}}(\theta)$ is necessarily constrained to its limiting negative value of -1 at 0° and 180° for diatom + atom collisions, as a result of conservation of angular momentum. This is because NO(A) has an initial rotational angular momentum, $N = 0$. This means that the total angular momentum of the system, ***J***, must be equal to the pre-collision orbital angular momentum, ***L***, which is necessarily perpendicular to **k**. When scattering at 0° (180°), **k′** is parallel (antiparallel) to **k**, and the final orbital angular momentum, ***L′***, will be perpendicular to both **k** and **k′**. In order to conserve ***J***, the collision induced angular momentum must also be perpendicular to **k**, leading to the negative limiting value of $A_{0}^{\{2\}}(\theta)$ at these angles. The magnitude of $A_{0}^{\{2\}}(\theta)$ observed for the experiments in this thesis will be reduced from the limiting value of -1 by nuclear hyperfine depolarisation by a known amount (see Section 2.10.2). Non-limiting values of $A_{0}^{\{2\}}(\theta)$ can also be observed in cases where there is an alternative depolarisation effect (such as the effect of the Earth's magnetic field, or multiple collisions), or if there is partial saturation of the probe laser in the detection scheme.[27,28,133]

2.10.2 Fitting Routine

The fitting routine to extract the DCS and $A_{q+}^{\{2\}}(\theta)$ alignment moments is a forward simulation process. The first half of this section will describe the method by which the scattering images are simulated, and the second half will describe the process by which these simulated images are used to provide a fit to the experimental images.

A pair of V and H scattering images can be simulated for any arbitrary DCS and set of $A_{q+}^{\{2\}}(\theta)$ alignment moments. First, a large number (typically 5×10^7) of collision trajectories were Monte Carlo selected, with initial collider speeds chosen from Gaussian distributions with means and standard deviations matching the experimental conditions. The initial directions of the two molecular beam trajectories were determined in a Monte Carlo simulation of the experimental geometry. A collision point was randomly selected from the experimentally defined preparation laser beam interaction volume, and origin points were randomly selected from the 0.5 mm diameters of the two valve orifices. If these points provide directions which both successfully passed through the 0.5 mm skimmers, the pair of directions was saved, otherwise they were discarded. For each of these initial pairs of trajectories, the centre-of-mass velocity and relative velocity vector, **k**, were calculated. The final speed of the recoiling NO(A) molecule was calculated, accounting for the collision energy partitioned into internal degrees of freedom (rotational energy), and into translation of the collider. Centre-of-mass scattering angles (θ, ϕ) were Monte Carlo selected from an isotropic distribution. The final centre-of-mass velocity of the NO(A) molecule was rotated into the lab frame, and added to the centre-of-mass velocity to generate the lab frame scattered velocity. A velocity of 8.5 m s^{-1}, selected from an isotropic angular distribution, was added to this to simulate the effect of the ion recoil. The trajectory was assigned a set of pixel coordinates, corresponding to its lab frame velocity in the plane of the detector. Finally, the rotational alignment detection sensitivity factors, $F_{q+}^{\{2\}}$ (see below) were evaluated. For each trajectory, the pixel coordinates, the polar scattering angles and the $F_{q+}^{\{2\}}$ factors were stored for further use. Pre-calculating and storing these parameters meant that they did not need to be calculated on the fly during the simulation, greatly reducing the computational cost of the simulation, at the expense of requiring a large, but manageable memory commitment (1-2 GB of RAM).

Simulated velocity map images for the V and H probe laser polarisations were constructed by summing over the previously sampled trajectories, where each trajectory corresponded to a single ion strike. The intensity of each simulated ion strike was varied to account for the effect of the DCS and $A_{q+}^{\{2\}}(\theta)$ moments:

$$I = \frac{d\sigma}{d\omega}(\theta) \times I_{\text{det}}\left(\phi, \mathbf{k}, A_{q+}^{\{2\}}(\theta), \chi\right) \tag{2.4}$$

Here I is the observed scattering intensity and represents the probability that a scattering event occurs at the scattering angles θ and φ, and is detected using the 1 + 1′ ionisation scheme of the experiment. $\frac{d\sigma}{d\omega}(\theta)$ is the DCS, which describes the probability of a collision leading to the scattering angle θ. $I_{\text{det}}\left(\phi, \mathbf{k}, A_{q+}^{\{2\}}(\theta), \chi\right)$ is the alignment dependent detection probability, described by:

$$I_{\text{det}}\left(\phi, \mathbf{k}, A_{q+}^{\{2\}}(\theta), \chi\right) = 1 + h^{\{2\}} g^{\{2\}} \left(1 + F_0^{\{2\}} A_0^{\{2\}}(\theta) + F_{1+}^{\{2\}} A_{1+}^{\{2\}}(\theta) + F_{2+}^{\{2\}} A_{2+}^{\{2\}}(\theta)\right) \tag{2.5}$$

In this expression, χ is the angle between the scattering plane and the electric vector of the probe laser, which was 90° and 0° for the V and H images, respectively. $h^{\{2\}}$ is the second rank polarisation sensitivity for a single photon transition, which for the R-branch transitions used in all experiments in this thesis is given by $h^{\{2\}} = -N/(2N+3)$, where N is the rotational level before the transition.[127] $F_{q+}^{\{2\}}$ are geometric terms which contain the information required to calculate the sensitivity to the corresponding $A_{q+}^{\{2\}}$ moment, and are defined as:

$$F_0^{\{2\}} = \frac{1}{4} h^{\{2\}} c_2(N)\left(3\sin^2\Theta\cos 2\chi - \left[3\cos^2\Theta - 1\right]\right) \tag{2.6}$$

$$F_{1+}^{\{2\}} = \frac{\sqrt{3}}{4} h^{\{2\}} c_2(N)\left(2\sin\Theta\cos\phi\sin 2\chi + 2\sin\Theta\cos\Theta\sin\phi\cos 2\chi - \sin 2\Theta\cos\phi\right) \tag{2.7}$$

$$F_{2+}^{\{2\}} = \frac{\sqrt{3}}{4} h^{\{2\}} c_2(N)\left(\left[1+\cos^2\Theta\right]\cos 2\phi\cos 2\chi - 2\cos\Theta\sin 2\phi\sin 2\chi - \sin^2\Theta\cos^2\phi\right) \tag{2.8}$$

Here Θ is the angle between **k** and the probe laser propagation direction, $\mathbf{k_p}$ and $c_2(N)$ is a scaling factor:

$$c_2(N) = \frac{(2N+3)(2N-1)}{N(N+1)} \tag{2.9}$$

The $g^{\{2\}}$ factor in Equation 2.5 accounts for nuclear hyperfine and spin depolarisation of the rotational alignment of the rotation of the bond axis, ***N***. The collisions lead to an alignment of ***N*** but leave the electron spin, **S**, and the nuclear spin of ^{14}N, ***I***, randomly oriented. As ***N*** and ***S*** recouple to ***N***, to give ***F***, the total angular momentum including nuclear spin, they will all precess around ***F***. As the collisions occur at a random time in the 360 ns between the preparation and probe laser pulses, which is much longer than the depolarisation timescale,[134] depolarisation leads to a time-averaged, bulk decrease in alignment, which for a Hund's case $b_{\beta J}$ molecule, such as NO(A), is equal to:[135–137]

$$g^{\{2\}} = \sum_{J,F} \frac{(2F+1)^2(2J+1)^2}{(2S+1)(2I+1)} \begin{Bmatrix} J & J & 2 \\ N & N & S \end{Bmatrix}^2 \begin{Bmatrix} F & F & 2 \\ J & J & 1 \end{Bmatrix}^2 \tag{2.10}$$

Finally, the simulated scattering image was convoluted with a 2-D Gaussian function, with a standard deviation of 2.06 pixels in both dimensions, to simulate the effect of blurring in the experimental images, caused by the finite resolution of the ion optics, and fact that the signal from a single ion strike is distributed over multiple pixels. This blurring function was determined from an analysis of individual ion strikes and analysis of the ion optics focussing characteristics using SIMION.[138]

Images simulated in this manner were used in the fitting routine to extract the DCS and $A_{q+}^{\{2\}}(\theta)$ alignment moments from the experimental images. In principle, the DCS and $A_{q+}^{\{2\}}(\theta)$ moments are inseparable, and have to be extracted simultaneously. However, in practice, the effects of the DCS and $A_{q+}^{\{2\}}(\theta)$ moments on the scattering images are very different, and it makes the fitting routine much simpler if the two sets of variables are treated separately in an iterative manner. The NO(A) + Ar results presented in Chapter 3 and NO(A) + N_2 results in Chapter 5 will provide clear evidence that this assumption that the DCS and $A_{q+}^{\{2\}}(\theta)$ moments are effectively separable is valid.

To begin the fitting process, the DCS was extracted, while assuming a set of known $A_{q+}^{\{2\}}(\theta)$ moments, typically those of the quantum scattering calculations. A series of *n* V and H basis images were simulated, as described above, with the $A_{q+}^{\{2\}}(\theta)$ moments fixed at their assumed value, and the DCSs corresponding to the first *n* Legendre polynomials, in either the x = cos(θ) or x = 1 – (θ/90°) basis set (see Figure 2.24). The weighting of these basis images was next optimised, so that the weighted sum of the images provided an optimal reproduction of the corresponding experimental images. This was defined by the χ^2 value, obtained from the integrated intensity in the squared residual images. There are two possible methods by which the weighting of the basis images can be optimised. The first method is a singular value decomposition (SVD).[139] The SVD method is computationally inexpensive, providing a minimum χ^2 value through a numeric method. However, constraints cannot be applied to the SVD function, which can lead to non-physically meaningful results being reached, such as negative values of the DCS. The second method uses a downhill-simplex (or amoeba) routine,[139] which is much more computationally expensive than the SVD, but does allow constraints to be applied to the fitted DCS. The routine begins with a starting "best guess", typically the DCS obtained from QS calculations, which is parameterised by the *n* Legendre moments to give the initial weighting of the coefficients. This "best guess" provides one vertex of an *n* + 1 dimensional simplex (a simplex is a hyperdimensional shape, with one more vertex than the number of dimensions, i.e. a triangle in 2-D or a tetrahedron in 3-D), where the remaining vertices are randomly distributed weightings of coefficients. The routine next evaluates the χ^2 value of the images simulated with the coefficient weightings at each vertex. The position on the hyperdimensional surface of the vertex with the lowest χ^2

value is maintained, while the other vertices are moved with respect to the static vertex and their χ^2 values are recalculated. This process is repeated until a predefined tolerance is reached, where the value of the highest and lowest χ^2 vertices are within a certain range of each other. The downhill-simplex algorithm has no way to distinguish a local minimum from the global minimum. To prevent optimisation into a local minimum, the routine is restarted, with the lowest χ^2 vertex used as the new best fit, and *n* new random vertices chosen and the simplex optimised to a new minimum. The routine undergoes restarts until a second tolerance threshold is met, where the χ^2 values from two successive restarts are within a predetermined range of each other.

Once the weightings of the basis images were optimised, and the DCS extracted, the fitting routine proceeded to use a similar process to extract the three $A_{q+}^{\{2\}}(\theta)$ moments simultaneously. New V and H basis images were simulated, this time using the DCS extracted in the previous step, and $A_{q+}^{\{2\}}(\theta)$ moments corresponding to the first *n* Legendre polynomials, either with the $x = \cos(\theta)$ or the $x = 1 - (\theta/90°)$ basis set. As with the DCS, the weightings of the basis images were optimised, either using the SVD or downhill-simplex routine, to minimise the χ^2 value and obtain the $A_{q+}^{\{2\}}(\theta)$ moments. The newly optimised set of $A_{q+}^{\{2\}}(\theta)$ moments were next used as an input, and the DCS refitted. The cycle of refitting the DCS and $A_{q+}^{\{2\}}(\theta)$ moments in an iterative fashion continued until the absolute values of the DCS and three $A_{q+}^{\{2\}}(\theta)$ moments at every angle were within 1% of the previous iteration, at which point the results had converged, and the fitting routine ended.

As noted above, the advantage of using the much more computationally expensive downhill-simplex algorithm to fit the experimental images is that it can apply constraints to the DCS and $A_{q+}^{\{2\}}(\theta)$ moments, preventing physically unreasonable results from being returned. The first of these constraints is that the returned DCS must not contain negative values, as this implies a negative number of scattered NO(A) molecules, which is nonsensical. Next are the $A_{q+}^{\{2\}}(\theta)$ moments, which necessarily must lie within their classical limits. Finally, in some cases, $A_0^{\{2\}}(\theta)$ was constrained to a value of -1 at 0° and

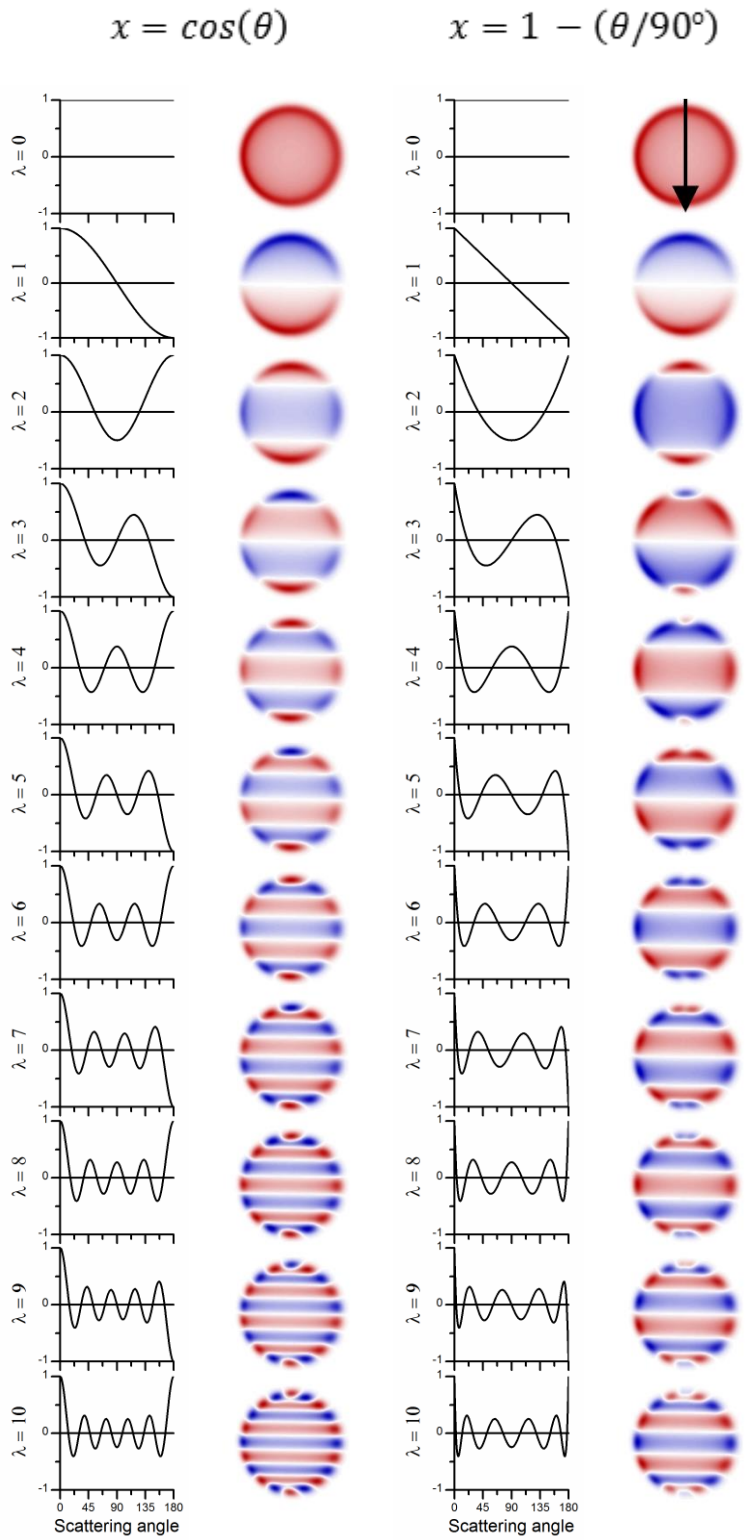

Figure 2.24: First and third columns: the first eleven Legendre polynomials in the $x = \cos(\theta)$ and $x = 1 - (\theta/90°)$ basis sets. Second and fourth columns: Simulated basis images for an idealised scattering image with molecular beam speed distributions of mean 435 m s^{-1} and FWHM 50 m s^{-1}, where red represents positive intensity and blue represents negative intensity. The black arrow shows the direction of **k**.

180°, and $A_{1+}^{\{2\}}(\theta)$ and $A_{2+}^{\{2\}}(\theta)$ to values of 0 at 0° and 180° (see Section 2.10.1 for the origin of these constraints).

The fitting routine reliably returned the distribution of scattering angles in the DCS, however, it contained no information regarding the absolute values, which the experiment is not sensitive to. To optimally compare the extracted DCS to the results of QS calculations, the fitted DCS was area normalised to the QS DCS where possible. The details of this normalisation will be provided in the relevant chapters.

2.10.3 Molecular Collider Fitting Routine

The above fitting routine describes how NO(A) + atom (or atom-like molecule) scattering images were analysed. These systems are comparatively simple, as the collision energy can only be partitioned into NO(A) internal energy (rotational) levels, and translational motion. On the other hand, NO(A) + molecule scattering can lead to rotational excitation of the NO(A) molecule, the collider molecule or both, with the remaining energy partitioned into translation. The detection scheme of the experiment is only sensitive to the final quantum state of NO(A), while the final speed of the NO(A) molecule depends on the final quantum states of both the NO(A) and collider molecules. This leads to multiple Newton spheres of NO^+ ions, corresponding to different unobserved collider states, and thus, the velocity map image will contain multiple scattering spheres for a given final NO(A) rotational level.

The NO(A) + molecule scattering images presented in Chapter 5 clearly show this effect, and so the fitting routine needed to be expanded to account for rotational excitation of the collision partner. The DCS and $A_{q+}^{\{2\}}(\theta)$ moments were extracted in the same iterative manner described in the previous section, however basis images were simulated not only for different Legendre moments, but also for different final NO(A) speeds, corresponding to different amounts of energy being partitioned into rotation of the collider molecule. The weighting of the basis images was optimised using either the SVD

or downhill-simplex algorithm, with the DCS and $A_{q+}^{\{2\}}(\theta)$ moments being extracted in an iterative process until convergence has been reached.

2.10.4 Comparison to Other Published Fitting Methodologies

CMB VMI experiments have been used by a number of groups to study the dynamics of different inelastic collisions, with the analysis employed by each varying depending on the exact needs of the experiment. Three of the most relevant recent analysis methods are described here.

The image analysis used by Brouard and co-workers is broadly similar to the process used in the experiments in this thesis, where a forward simulation fitting routine is used to iteratively extract the DCS and rotational alignment moments from a set of experimental images.[21,27] However, there are a number of substantial differences between this method and the fitting routine used in this thesis. Rather than optimising the weighting of the basis images by directly comparing the experimental and simulated images, both the experimental and basis images were parameterised into their radial dependence on a series of Fourier moments in angle relative to **k**, and fitted in this Fourier space. This has the advantage of greatly reducing the computational cost of calculating the χ^2 value, as there are far fewer points for comparison. A second difference is that rather than fitting to both the V and H images simultaneously, the fitting method used by Brouard and co-workers fitted to a single image. For extracting the DCS, this single image was the V + H image, which has a reduced dependence on the rotational alignment, and for the rotational alignment, the (V – H)/(V + H) image, which has a reduced dependence on the DCS was used.

The analysis method implemented by Suits and co-workers took a completely different approach, where rather than using a forward simulation process, the DCS and rotational alignment moments were directly extracted by integrating the experimental images.[77] The images were integrated to obtain the effective intensities for scattering in the plane of the detector (in an annulus around the edge of the image) and out of the plane of the image (in a strip along the centre of the image), for both V and H probe laser beam polarisations.

Linear combinations of these intensities were used to return the DCS and rotational alignment moments. While this method is much less computationally expensive than forward simulation fitting methods, it does require very high signal to noise level to be effective. This method also does not account for kinematic blurring, brought about by the spread of speeds in the molecular beams, and so is not generally applicable. This fitting technique is problematic at angles close to 0° and 180°, as blurring of the images makes distinguishing between molecules scattered in and out of the scattering plane difficult.

Thanks to their use of a Stark decelerator, which generated a molecular beam of NO with an extremely narrow velocity distribution, van de Meerakker and co-workers produced velocity map images with a much higher resolution than is typically observed in CMB experiments.[140] The measurement of the DCS from these images began with the extraction of the angular scattering distribution from a radial integration of the intensity in an annulus around the edge of the image. This angular distribution was corrected to account for shifts in features bought about by the projection of the Newton sphere into 2-D and from the velocity spread of the molecular beams (primarily the non-Stark controlled collider beam). Corrections were also made to account for the effects of Doppler selection and (an assumed) collision-induced rotational alignment. The resulting DCS was used to simulate a scattering image, which was compared to the experimental image. If the two images were within a certain tolerance of each other, the extracted DCS was necessarily correct, but in cases where there was significant deviation, the DCS was refined using a procedure described by Lorenz *et al.*[141] This refinement involved correcting the DCS based on systematic differences between the experimental and simulated scattering images. From this corrected DCS, a new image was simulated, and the refinement iterated until a defined tolerance was met. High-frequency features of the DCS, such as diffraction oscillations were not reliably returned by this refinement process, and so the DCS could not be obtained this way. In those cases, comparison between experiment and theory were obtained through comparisons of the angular scattering distribution for the experimental scattering image, and the image simulated from the results of QS calculations.

A final difference is that all three of the methods described above require a density-flux transformation step in the analysis, while the fitting method used in this thesis does not. In a typical CMB experiment, there is no fixed start time. Scattering typically occurs

for tens or hundreds of microseconds before detection, by which time a steady state will have formed, where rotationally excited molecules are formed at the same rate at which they leave the detection region. The molecules scattered into different angles, θ and ϕ, have different lab-frame speeds, and so will leave the detection region at different rates. The slower moving molecules therefore leave the detection region at a lower rate, and so have a higher density. This higher density leads to a detection bias, where a higher proportion of the slower moving molecules are detected. This detection bias is accounted for in the analysis methods of almost all CMB VMI experiments through the use of a computationally expensive density-flux transformation. In contrast, the use of optical pumping to prepare NO(A) allows the experiments in this thesis to set a "zero time", at which point collisions begin. There is a 360 ns delay between the preparation of the NO(A) molecules, and their detection, which does not give the scattered NO(A) molecules enough time to leave the detection region, so no detection bias is observed.

Chapter 3

Collisions of NO($A^2\Sigma^+$) with Atomic Partners: Ar and Ne

3.1 Introduction

As described in Section 1.10, there have been extensive studies of the collisions of NO with the different rare gases. Experiments investigating the collisions of molecules with atoms are far more common than similar studies probing the collisions of molecules with other molecules. This is for two reasons. First, atomic colliders have only electronic internal energy levels, which usually cannot be accessed by collisions, meaning that there are fewer possible transitions which can be induced by the collision, simplifying the results of the experiment (the effects bought about by rotational transitions of the unobserved collider are described in Chapters 4 and 5). Second, molecule + atom collisions are more amenable to theoretical work than molecule + molecule collisions, both for the calculation of *ab initio* PESs, and in the subsequent QS calculations.

Comparison between experimental and theoretical results often allow for a much more complete understanding of features in the experimental results. For example, Eyles *et al*. used a quantum, hard shell model to show that oscillations in the DCS for the inelastic collisions of NO(X) with Ar were caused by interferenc, from collisions at different ends of the NO molecule.[21,22] In a different experiment, Vogels *et al*. used QS calculations to show that dramatic changes in the DCS for NO($X^2\Pi$) + He inelastic collisions over small

ranges of collision energy were caused by the formation of short-lived, quasi-bound intermediate species.[121]

Comparisons of experimental and theoretical results can also be used to test the accuracy of the *ab initio* PES. If the experimental and theoretical results match, the PES is likely to be accurate in the regions probed by the collisions. More interestingly though, if the theoretical results diverge from the experiment, it indicates that there are inaccuracies in the PES. Kohguchi *et al*. found that QS calculations of the DCS for NO(X) + Ar inelastic collisions using a correlated electron pair approximation PES led to inaccuracies, showing that the PES contained errors. These inaccuracies were not present in the results of QS calculations performed on a CCSD(T) PES, showing that this more recent, and higher level of theory PES is accurate.[142]

This chapter will experimentally investigate the rotationally inelastic collisions of NO($A^2\Sigma^+$) with Ar and Ne. These measurements will be compared to the results of QS calculations performed on state-of-the-art literature *ab initio* PESs. These comparisons will be used to test the accuracy of the PESs, and will inform the interpretation of various features of the experimental results.

3.2 Collisions of NO($A^2\Sigma^+$) with Argon

3.2.1 Experimental Conditions

Velocity map images for the collisions of NO($A^2\Sigma^+$) with Ar were acquired using the methods outlined in Chapter 2. The primary molecular beam contained 10% NO (BOC, 99.998%) seeded in Ar (BOC, 99.998%) with a backing pressure of 3 bar, giving a Gaussian distribution of speeds, with a mean of 593 m s^{-1} and a FWHM of 52 m s^{-1}. The secondary molecular beam was a neat Ar beam, seeded at 5 bar backing pressure to give a mean speed of 617 m s^{-1} and FWHM of 52 m s^{-1}. Crossing at 90°, these give a Gaussian distribution of collision energies, with a mean of 525 cm^{-1} and FWHM of 64 cm^{-1}.

The mean beam speeds were determined by analysis of separate velocity mapped images of NO seeded in Ar at an appropriate concentration (either 10% or ~0.01%). NO^+ was generated using 226 + 226 nm ionisation, and a 2-D Gaussian function was used to fit each of the resulting beam-spots. The distance of the mean position of the beam-spots from the zero-velocity coordinate (determined using the method outlined in Section 2.8) was measured in pixels and converted into a speed. The FWHM of the two molecular beam speeds was measured using the downstream LIF method (see Section 2.9).

In accordance with the optimised values outlined in Section 2.6, the preparation laser was set to a fluence of 0.65 mJ cm^{-2} and diameter of 2 mm, the probe laser was set to a fluence of 0.65 μJ cm^{-2} and diameter of 3 mm, and the fluence of each beam of the ionisation laser was varied in the range 4-40 mJ cm^{-2} with diameters of 3 mm each.

Images were acquired for final NO(A) rotational levels $N' = 3$, 5-9, with a total of 8 individual images acquired for each quantum state, except for $N' = 9$, where 16 images were acquired to compensate for the low signal-to-noise levels. Each individual image was acquired from 64,000 individual camera shots, across both V and H, and total and background images, summed across five scans of the probe laser over the Doppler profile of the relevant transition in the R branch of the NO(E ← A) (0-0) band, with 200 laser shots acquired for each frame.

3.2.2 Data Analysis

The NO(A) + Ar data was analysed by Dr T. R. Sharples using the methods outlined in Section 2.9. This was the first scattering data to be analysed, and as a result, a simplified approach to the fitting was implemented. The differences between the final fitting routine outlined in Section 2.9 and the earlier method used to analyse this data will be described here.

The most significant difference between the fitting routine used here and the final version is that there was no attempt to measure the rotational alignment moments, and hence only the DCSs were extracted from the experimental images. However, the

scattering images were recorded with full sensitivity to the rotational alignment. The rotational alignment moments were therefore given an assumed form during the fitting routine, either as the results of QS or KA calculations (see Section 3.2.3 for more details regarding these calculations). Using different sets of assumed rotational alignment moments in the extraction of the DCS allowed for the effect of the choice of different rotational alignment moments of the measured DCS to be investigated. This proved to be an important stage in the development of the final fitting routine, and will be discussed in Section 3.2.5.

The second difference is that the analysis was conducted on a single data set, consisting of the averaged V and H images, obtained from the sum of all 8 (or 16) individual images. As a result, there was no error analysis conducted on the fitted DCSs.

At the time of recording the NO(A) + Ar experimental images, the instability in the observed position of the zero-velocity coordinate described in Section 2.8 had not been identified. As a result, the centring measurements were only made occasionally over the course of the measurements, and the translation and registering of the experimental images could not be made using the method described in Section 2.8. In order to register the images, the position of the first individual image acquired for each quantum state was taken as a reference, and the further images were translated to minimise the sum of the squared differences between them and the reference image.

The image simulation process used in the fitting routine was an earlier version of the one described in Section 2.10.2. The most prominent difference is that the incoming trajectories of the NO and Ar colliders were fixed exactly along the *z* and *x* axis of the lab frame, while later versions of the routine modelled a full 3-D distribution of the collider velocities. Additionally, the simulated images were not convoluted with a 2-D Gaussian function to model experimental blurring, instead, these effects were modelled by adding a velocity Monte-Carlo selected from a Gaussian distribution to the final velocity following scattering.

It would certainly be possible to refit the NO(A) + Ar images using the more refined process described in Section 2.10, which would allow for the rotational alignment moments to be measured, and for complete error analysis to be conducted, as has been

done for every other system presented in this thesis. However, as will be apparent from the agreement between experiment and theory shown below, doing so is unlikely to yield any new insights into the scattering system, and so no further analysis has been attempted.

The DCS was extracted using the $x = 1 - (\theta/90°)$ basis set, with 16 Legendre moments used to fit all six quantum states. The absolute magnitude of the DCS was not determined during the fitting routine, and so it was area normalised to the QS DCS to enable optimal comparisons between the two.

3.2.3 Calculations

QS calculations were performed by Dr T. R. Sharples, using the HIBRIDON suite of codes,[98] on the NO(A)-Ar PES calculated by Kłos *et al*.[14] From these calculations, the QS DCS and $A_{q+}^{\{2\}}(\theta)$ moments were determined. Calculations were performed at eleven collision energies, in evenly spaced steps spanning four standard deviations of the collision energy distribution. These results were averaged with appropriate weighting to model the distribution of the collision energy described in Section 3.2.1. The calculations were fully open shell, with reported DCSs for each N' rotational level obtained from the sum of the two $j' = N' \pm 0.5$ states and the $A_{q+}^{\{2\}}(\theta)$ moments obtained from a DCS-weighted average of the two $j' = N' \pm 0.5$ states. NO(A) was treated as a rigid rotor with rotational constants $B = 1.9869$ cm^{-1} and $\gamma = -0.0027$ cm^{-1}.[143] At each energy, calculations were performed up to values of total angular momentum, $J_{tot} = 450.5$, with a basis of rotational states up to $N = 20$ and numerical propagation from 4.2 to 200 Bohr.

The $A_{q+}^{\{2\}}(\theta)$ moments were also calculated by Dr T. R. Sharples, using the KA model[144] (see Section 1.8.3), at the mean collision energy.

3.2.4 Results

Figure 3.1(a) shows a typical velocity map image, obtained from the experiment. A Newton diagram is overlaid to display the correlation of the relevant velocity vectors in the experiment (see section 1.6.1 for a complete description of the Newton diagram). Example V and H images from individual acquisitions acquired during the experiment are presented in Figure 3.2, with the V and H images averaged across all acquisitions shown in Figure 3.3.

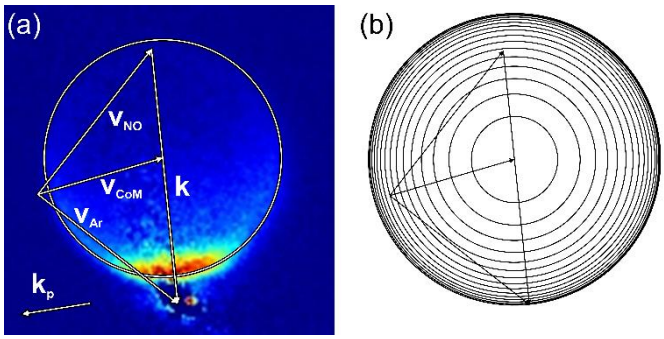

Figure 3.1: (a) Colour map for the V + H velocity map image corresponding to the N' = 9 product state for the NO(A) + Ar scattering system, at a mean collision energy of 525 cm^{-1}, with an overlaid Newton diagram corresponding to the mean collision energy, with arrows representing the relevant velocity vectors: $\mathbf{v_{NO}}$ and $\mathbf{v_{Ar}}$ show the velocities of the two colliders, $\mathbf{v_{CoM}}$ shows the velocity of the centre of mass, **k** shows the relative velocity vector. The circle shows the possible final velocities of NO(A) scattered in the plane of the image. The offset $\mathbf{k_p}$ vector shows the propagation direction of the probe laser. (b) Newton diagram for the NO(A) + Ar scattering system, with circles showing the centre of mass velocities of NO(A) scattered in the plane of the detector for all energetically accessible final NO(A) rotational levels, N' = 0-15.

Without any further analysis, a substantial amount of information can be obtained from a visual inspection of the V and H images. A qualitative sense of the distribution of scattering angles can easily be obtained by following the distribution of intensity around the edge of the scattering signal. Scattering at small angles leads to intensity at the forward region, corresponding here to the bottom of the images, while scattering at larger angles will lead to intensity in the sideward and backward directions, at the sides and the top of these images, respectively. The low-N' final rotational levels are dominated by scattering in the extreme forward direction, which appears as a bright spot at the bottom of the images, with a dimmer partial or full circle above shows scattering at larger angles. The proportion of the scattering signal observed at higher angles becomes progressively larger

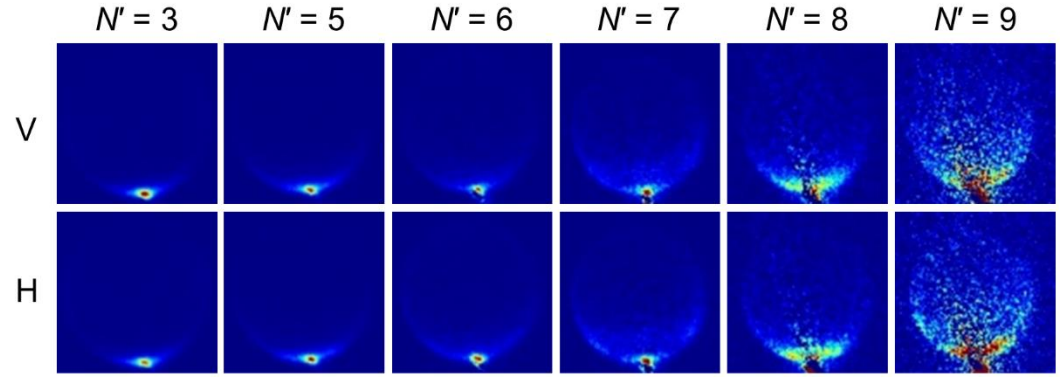

Figure 3.2: Example V and H velocity map images from a single acquisition for the collisions of NO(A) with Ar at a mean collision energy of 525 cm^{-1}, with final rotational levels N' = 3, 5-9.

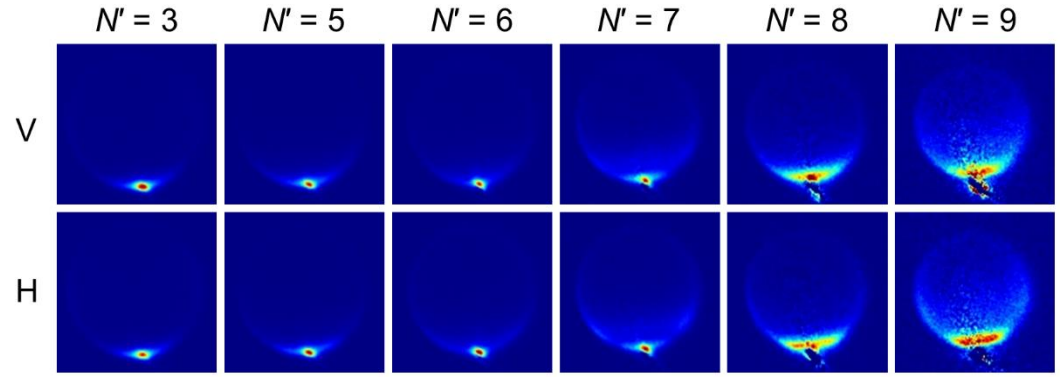

Figure 3.3: Experimental V and H velocity map images obtained for the collision of NO(A) with Ar at a mean collision energy of 525 cm^{-1}, with product states N' = 3, 5-9, averaged across all individual acquisitions.

for higher final rotational levels. Also as N' increases, the radius of the scattering image decreases. This effect is a result of the conservation of energy throughout the collision: for higher N' products, more energy is transferred into rotation of the N-O bond axis, and so there is less remaining energy to be partitioned into translational motion of the colliders, leading to a lower final speed, and a Newton sphere with a smaller radius. This effect is obscured by the extreme forward scattered distribution of most of the images, but the decreasing radii of the scattering images is shown clearly in the Newton diagram in Figure 3.1(b). There is an aberration visible at the bottom of the images, which is particularly noticeable in the high N' images. This occurs as a result of the imperfect subtraction of NO^+ ions produced by the non-resonant ionisation of unscattered NO(A), and is explained fully in Section 2.5. The effect of rotational angular momentum alignment induced by the collision can be observed prominently as the difference in intensities between the V and H images (see Section 2.10.1 for more details). These

effects can be most clearly seen as the differences in intensities of the forward scattered spot, and can also be seen as subtle differences in the intensity at higher angle signal in the N' = 7-9 images.

More detailed insight into the NO(A) + Ar system is provided by analysis of the images. As described in Section 3.2.2, only the DCS was determined in the analysis of these images, while the rotational alignment moments were assumed as either the results of the QS or KA calculations (see Section 3.2.3). Figure 3.4 compares the experimental V + H image with V + H images simulated with the DCS obtained from the fitting routine and the assumed rotational alignment moments (hereafter referred to as fitted images).

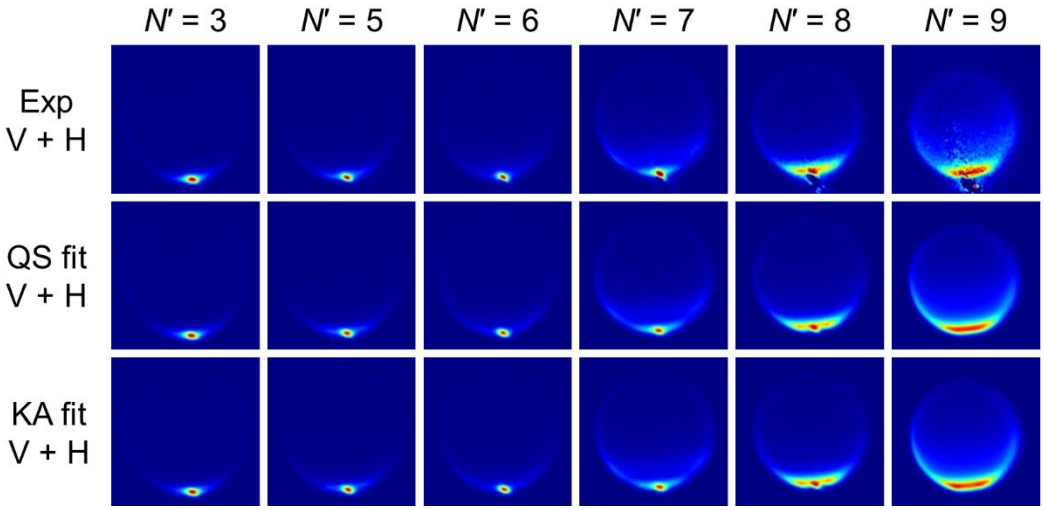

Figure 3.4: V + H velocity map images for the collisions of NO(A) with Ar with a mean collision energy of 525 cm^{-1}. Top row: experimental V + H images, middle row: V + H images simulated from the DCS acquired by fitting the experimental image using rotational alignment moments obtained from QS calculations, bottom row: V + H images simulated from the DCS acquired by fitting the experimental image using rotational alignment moments obtained from KA calculations

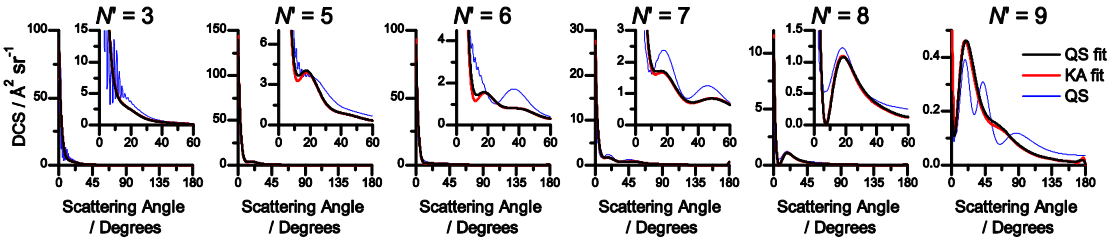

Figure 3.5: DCSs for the collisions of NO(A) with Ar at a mean collision energy of 525 cm^{-1}, obtained from fitting experimental images, assuming rotational alignment moments as the results of QS calculations (black), and KA calculations (red), and the theoretical DCS obtained from QS calculations (blue). Insets how the same plots across a smaller range of scattering angles and values of the DCS for visual clarity.

The V + H images are used for these comparisons, as they have a much reduced (though not completely eliminated) contribution from the rotational alignment moments, meaning that deviations in the rotational alignment moments have a lower impact on these images than the corresponding V and H images. The similarity between the experimental and fitted V + H images, as well as the two fitted images to each other shows that the extracted DCS is accurate. The extracted DCSs, obtained by fitting the images, assuming the two (very different, see Figure 3.11) sets of alignment moments are shown in Figure 3.5, alongside the theoretical DCS, obtained from the QS calculations using the PES of Kłos *et al.*[14] The fitted DCSs quantify the qualitative conclusions made from a visual inspection of the images. There is a large forward scattered peak at 0° across all N', which decreases in intensity as N' increases, thus increasing the prominence of additional maxima at angles between 15° and 60° for $N' \geq 5$.

3.2.5 Discussion

The use of two sets of assumed rotational alignment moments in the fitting process allowed the influence of the rotational alignment moments on the resulting DCS to be investigated. While there was no error analysis conducted for these results, the similarity of the two sets of DCSs is unmistakable. This shows that the choice of rotational alignment moments assumed in the fitting routine has only a small effect on the resulting DCS. Therefore, even if the QS rotational alignment moments are not in perfect agreement with reality, the resulting change in the extracted DCS will be small. This finding had an important consequence on the development of the fitting routine, as it showed that the DCS and the rotational alignment moments can be treated as separable in the fitting routine. This allowed the iterative procedure described in Section 2.10.2 to be implemented with confidence that treating the DCS and rotational alignment moments separately would not lead to incorrect results.

As has been explained in Section 3.1, comparison of experimental measurements of this sort to results of QS calculations provides a powerful test of the accuracy of the PES. The QS calculations run on the PES of Kłos *et al.*[14] produced DCSs which are broadly similar to their experimental counterparts, capturing both the forward scattered peak, and

the presence of further peaks at higher angles. This indicates that the PES is largely accurate in the regions which were accessible at the collision energy of the experiment. While the general structure of the DCSs are reproduced by the QS calculations, deviations are observed in the finer details of the higher angle peaks. These peaks are characteristic of rotational rainbows, and are attributable to scattering from the repulsive region of the PES. These rotational rainbow peaks can be explained purely classically, where collisions at multiple impact parameters lead to scattering into the same angle.[1] Collisions with the "N" end, the "O" end and the side of the NO molecule can lead to rotational rainbows at different scattering angles,[29,30] and further structure can result from interference between different trajectories that lead to the same scattering angle.[21,80] There are clear deviations in the structure of the rotational rainbow peaks in $N' = 6$ and 7, which occur at roughly the same angles in both the experimental and QS DCSs (it appears that the first rotational rainbow peak in the QS DCS of $N' = 6$ has been absorbed into the shoulder of the forward scattered peak), but the peaks are much sharper in the QS DCSs than in the experimental results. There is also a large deviation in the structure of the rotational rainbow peaks for $N' = 9$, in which the QS calculations predict three clearly resolved rainbow peaks, but only the first is actually observed in the experimental results. These deviations are evidence that the QS calculations are not correctly modelling the forces present in the collision, which can only be the result of inaccuracies in the repulsive region of the PES.

High frequency oscillations in the DCS are observed in the QS results for $N' = 3$, 5 and 6, which are absent from the experimental results. These are diffraction oscillations, which usually result from interference effects, between trajectories which pass through the attractive and repulsive regions of the PES and lead to the same scattering angle.[145] The absence of these oscillations from the experimental results is almost certainly the result of the angular resolution of the experiment not being high enough to resolve them. This lack of angular resolution occurs from a combination of the spread of collision energies, the finite spread of molecular beam crossing angles and the ion recoil speed. Other CMB VMI experiments are similarly limited in their angular resolution for the same reasons, and also fail to resolve these oscillations.[28,32,33,113,146,147] The CMB VMI experiment of van de Meerakker and co-workers uses a Stark decelerator to obtain scattering images with an extremely high angular resolution. This has allowed for the

successful observation of these diffraction oscillations for the inelastic collisions of NO(X) with different rare gasses,[20,52,53,119,140]

QS calculations using the NO(A)-Ne PES of Pajón-Suárez *et al.*[148] (see Section 3.3.3 for more details) indicate that the NO(A) + Ne DCS has similar rotational rainbow peaks to NO(A) + Ar, but lacks the sharp forward-scattered peak. Comparisons of the PESs for the two systems may therefore provide an important insight into the origin of this forward-scattered peak. However, the differences in the DCSs are not necessarily caused by the differences between the two PESs, as the masses of Ne and Ar are significantly different (20 u and 40 u respectively), and so the two systems have substantially different kinematics. Figure 3.6 shows single-energy QS DCSs using both PESs, with the kinematics for both systems. These results show that while the different kinematics do have a significant effect of the DCS, the forward-scattered peak is only observed with the NO(A)-Ar PES. This confirms that the origin of this feature lies in some feature of the NO(A)-Ar PES.

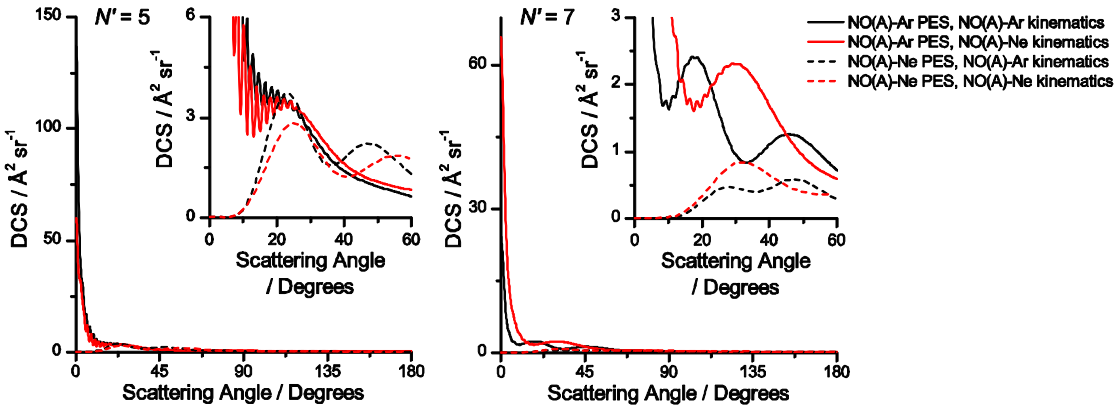

Figure 3.6: DCSs obtained by running QS calculations using the NO(A)-Ar PES (solid) and the NO(A)-Ne PES (dashed), and with the NO(A)-Ar kinematics (black) and the NO(A)-Ne kinematics (red), for final rotational levels $N' = 5$ and 7. Insets show the same plots across a smaller range of scattering angles and intensities of the DCS for visual clarity.

Contour plots showing the structure of the NO(A)-Ar and Ne PESs are shown in Figure 3.7. The structure of the repulsive regions of the two PESs is similar, and correspondingly, the rotational rainbow peaks are (broadly) similar in both scattering systems. On the other hand, the attractive regions are completely different. The attractive region of the NO(A)-Ne PES is very shallow, remaining smaller than -10 cm^{-1} at all angles, and is very

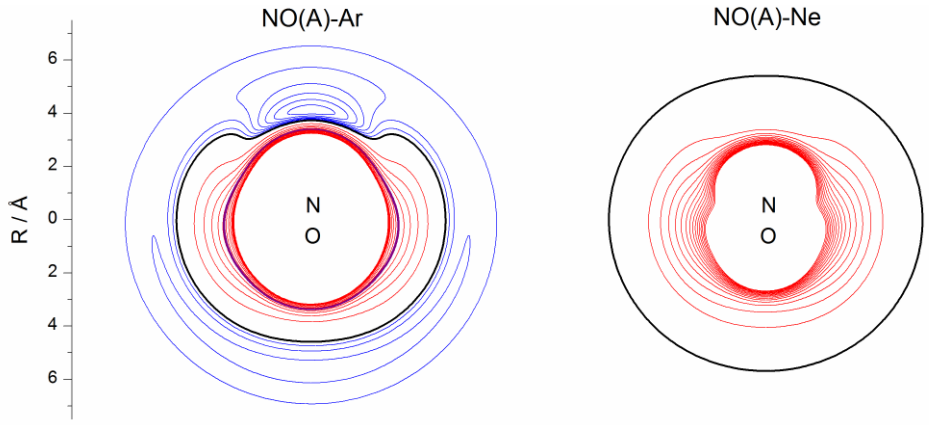

Figure 3.7: Contour plots of the potential energy surface for left: NO(A)-Ar, calculated by Kłos *et al.*,[14] right: NO(A)-Ne calculated by Pajón-Suárez *et al.*[148] Contours represent the potential energy of the coordinate, with red being positive (repulsive) energies in steps of 100 cm^{-1} and blue being negative (attractive) energies in steps of 10 cm^{-1}. The black contour represents 0 cm^{-1}, and the purple contour (NO(A)-Ar only) shows 525 cm^{-1}, corresponding to the mean collision energy.

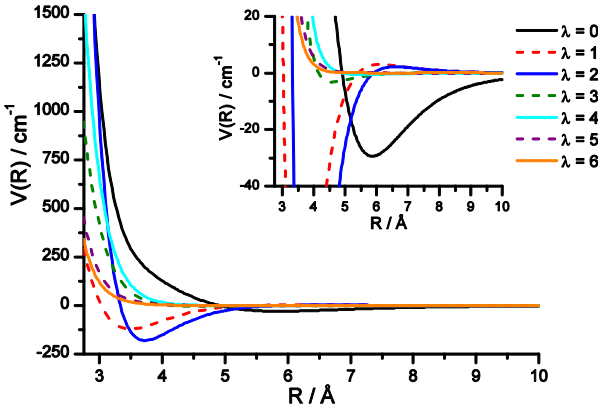

Figure 3.8: Radial dependences of the Legendre moments of the NO(A)-Ar PES. The inset displays the same plot with an expanded vertical scale for visual clarity.

isotropic (this attractive region is too shallow to be visible on the contour plot in Figure 3.7, but can be seen in the Legendre moments, plotted in Figure 3.14). In contrast, the NO(A)-Ar attractive region is much deeper, and is very anisotropic, with a -70 cm^{-1} attractive well, localised at the N end of the PES. It can therefore be postulated that the attractive region of the NO(A)-Ar PES is the origin of the forward-scattered peak. This was tested using QS calculations with different ranges of partial waves, corresponding to different ranges of the total angular momentum (J_{tot}). Because the initial rotational level of NO(A) is j = 0.5, J_{tot} is related to the magnitude of the orbital angular momentum, l, through the equation: $l = J_{tot} - 0.5$. l is also directly linked to the classical impact parameter, b, through the equation $l = \mu k b$, where μ is the reduced mass and k is the

magnitude of **k**. The NO(A) + Ne DCS is effectively converged at J_{tot} = 0.5-85.5, which corresponds to collisions up to a maximum impact parameter (b_{max}) of 4.5 Å, roughly equivalent with the edge of the repulsive region of the PES. On the other hand, at J_{tot} = 0.5-85.5 (b_{max} = 3.7 Å), the NO(A) + Ar DCS contains a higher-angle rotational rainbow peak, but there is no sign of the forward-scattered peak, which is clearly present at J_{tot} = 0.5-100.5 (b_{max} = 4.4 Å) and increases considerably in intensity at J_{tot} = 0.5-125.5 (b_{max} = 5.5 Å). After J_{tot} = 0.5-125.5, the DCS is effectively converged. This shows that the origin of the forward scattered peak is a feature of the PES, occurring at a radius of between 3.7 Å and 5.5 Å, which is consistent with the attractive well at the N end of the NO(A)-Ar PES. This peak at 0° is broadly consistent with the glory scattering observed for atom + atom elastic collisions, from collisions which probe the attractive region of the PES.[1]

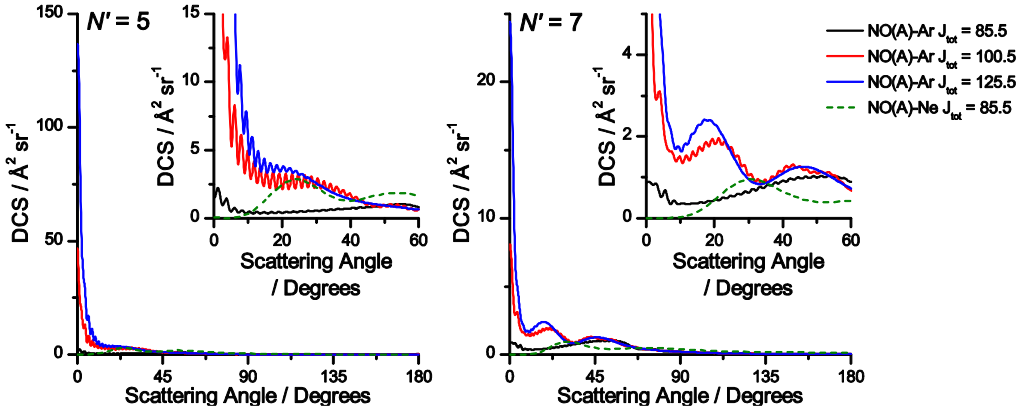

Figure 3.9: DCSs for the NO(A) + Ar inelastic scattering system, simulated with different partial waves, up to J_{tot} = 85.5 (black), 100.5 (red), 125.5 (blue) and for the NO(A) + Ne scattering system with partial waves up to J_{tot} = 85.5 (dashed green), for N' = 5 and 7. Insets show the same plots across a smaller range of scattering angles and intensities of the DCS for visual clarity.

While the rotational alignment moments were not extracted using the fitting routine in the measurements of this system, it is still possible to compare the experimental and theoretical moments through the use of simulated images. Figure 3.10 displays experimental V – H images, alongside images simulated from the results of the fitting process with the rotational alignment moments assumed to be the results of the QS or KA calculations. As was described in section 2.10.1, differences between the V and H images are strongly dependent on the rotational alignment moments (although the DCS still affects the magnitude of the V – H image). The feature which is most readily identifiable

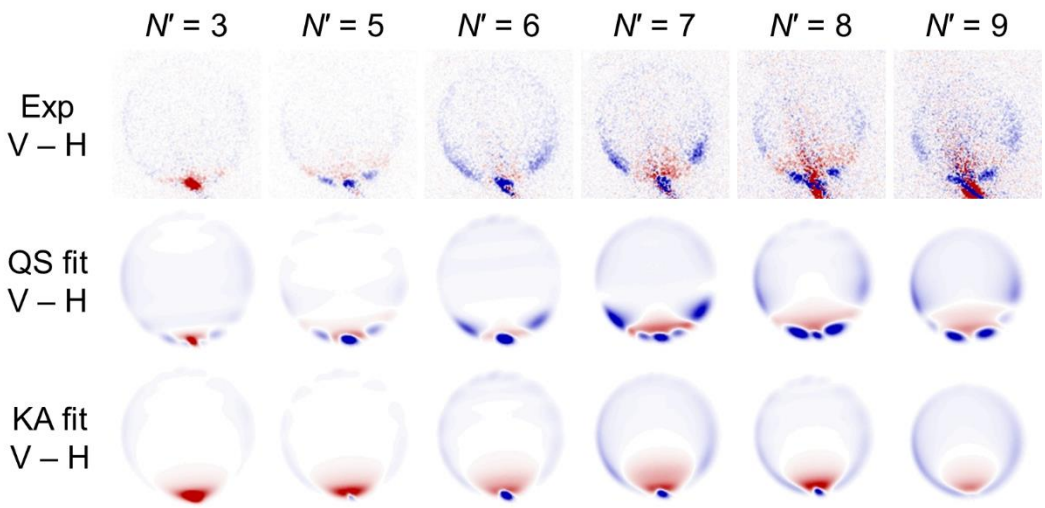

Figure 3.10: V – H velocity map images for the collisions of NO(A) with Ar with a mean collision energy of 525 cm^{-1}. Top row: experimental V – H images, middle row: V – H images simulated from the DCS acquired by fitting the experimental image using rotational alignment moments obtained from QS calculations, bottom row: V – H images simulated from the DCS acquired by fitting the experimental image using rotational alignment moments obtained from KA calculations

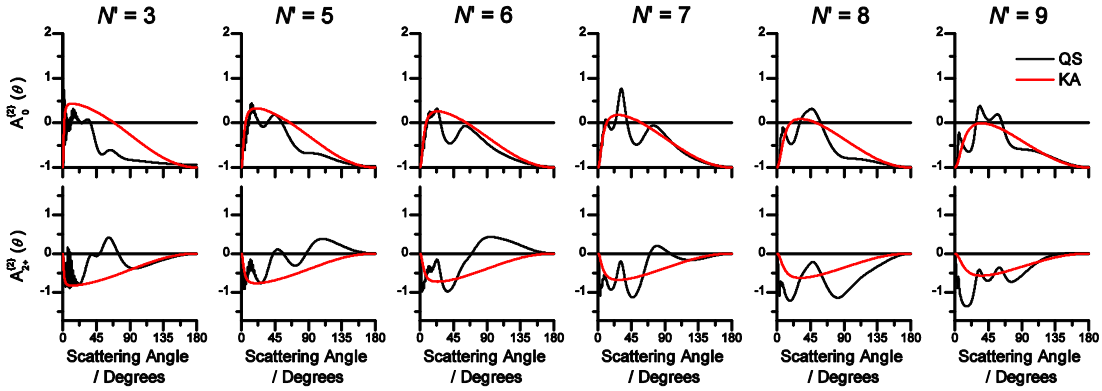

Figure 3.11: $A_{q+}^{\{2\}}(\theta)$ moments for the collisions of NO(A) with Ar, at an average collision energy of 525 cm^{-1}, generated from the results of QS calculations (black) and KA calculations (red).

from a visual inspection of the images is the sign of the signal at the edge of the scattering image at a given scattering angle. To the level which can be obtained from a simple visual inspection of these V – H images, there appears to be good general agreement between the experimental images and those simulated from the fitting results with the QS rotational alignment moments across all N'. However, there are subtle deviations in the finer details of the images, for example in the forward scattered region of the image for $N' = 7$. This confirms that the QS $A_{q+}^{\{2\}}(\theta)$ moments are in general qualitative agreement with the experimental values, however, there is not a quantitative agreement between the

two. On the other hand, the V – H images simulated from the fitting results with the KA rotational alignment moments are clearly completely different from the experimental V – H images across all N', showing that the KA $A_{q+}^{\{2\}}(\theta)$ moments do not provide a good description of the experimental values. The differences between the QS $A_0^{\{2\}}(\theta)$ and $A_{2+}^{\{2\}}(\theta)$ moments, and their KA counterparts for the NO(A) + Ar system are shown in Figure 3.11. There are clear angle-dependent fluctuations in the QS (and in the experimental) moments, while the KA moments vary smoothly with scattering angle. Similar features are seen in the NO(A) + Ne scattering system, which will be discussed more thoroughly in Section 3.3.

As described in Chapter 2, the experimental detection scheme was sensitive to NO(A) in quantum state N (where N describes the total angular momentum without electron spin), even though collisions populate well-defined j states (where j is the total angular momentum). It was asserted that this was not a limitation, as the electron spin, which couples to N to form j, is merely an observer to the collision, and any differences between the $j' = N' \pm 0.5$ levels are therefore not indicative of dynamical behaviour.[36,149] Differences between the $j' = N' \pm 0.5$ levels in the DCS reflect the probability of the electron spin coupling to the rotational motion to give the different spin-rotation states, while differences in the $A_{2+}^{\{2\}}(\theta)$ moments reflect the way that this recoupling of the

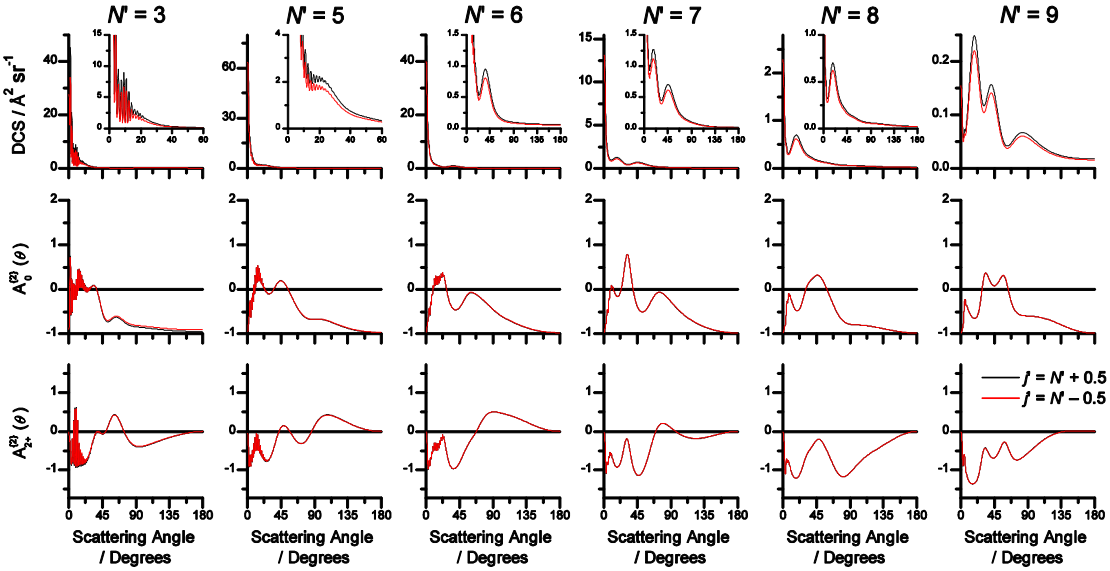

Figure 3.12: DCSs and rotational alignment moments obtained from single energy QS calculations for the collisions of NO(A) with Ar at 525 cm^{-1}, with spin-rotation resolution, $j' = N' + 0.5$ (black) and $j' = N' - 0.5$ (red).

electron spin affects the total rotational angular momentum. These differences are illustrated in Figure 3.12, which shows that the differences between the two spin rotation states are extremely small, and all maxima and minima in the DCSs and $A_{q+}^{\{2\}}(\theta)$ moments occur at the same scattering angles.

3.3 Collisions of NO($A^2\Sigma^+$) with Neon

3.3.1 Experimental Conditions

The experimental methods described in Chapter 2 were implemented to probe the collisions of NO(A) with Ne at two different collision energies. For the low-collision energy experiments, the first molecular beam consisted of 10% NO (BOC, 99.998%) seeded in Ar (BOC, 99.998%) with a backing pressure of 3 bar, to give a velocity of mean 623 m s^{-1} and FWHM 53 m s^{-1}. For the high-collision energy experiments, the first molecular beam contained 10% NO (BOC, 99.998%) seeded in He (BOC, 99.999%), with a backing pressure of 3 bar to give a velocity of mean 1,398 m s^{-1} and FWHM 91 m s^{-1}. In both cases, the second molecular beam consisted of neat Ne (BOC, 99.999%) with a backing pressure of 5 bar, to give a velocity of mean 809 m s^{-1} and FWHM of 54 m s^{-1}. The two molecular beams crossed at 90° to give a Gaussian collision energy distribution. The collision energy distribution for the low-energy collisions had a mean of 523 cm^{-1} and a FWHM of 57 cm^{-1}, while the high-energy collisions had a mean of 1,309 cm^{-1} and a FWHM of 137 cm^{-1}.

The molecular beam mean speeds were determined by a direct analysis of the experimental images, from the position of the non-resonant 532 + 532 nm beam-spots resulting from the two molecular beams. 2-D Gaussian functions were fitted to the non-resonant beam-spots, resulting from NO in the NO/Ar and NO/He molecular beams in the background image, and trace NO, which had unintentionally contaminated the neat Ne molecular beam (see Section 2.5) in the background subtracted image. The distances of the fitted beam-spots from the zero-velocity coordinate (see Section 2.8) were

measured and converted into speeds. The FWHM values of the speed distributions were taken from the downstream LIF measurements described in Section 2.9.

In accordance with the optimised values described in Section 2.6, the preparation laser was set to a fluence of 0.65 mJ cm^{-2} and diameter of 2 mm, the probe laser was set to a fluence of 0.65 μJ cm^{-2} and diameter of 3 mm, and the fluence of each beam of the ionisation laser was varied in the range 4-40 mJ cm^{-2} with diameters of 3 mm each.

In the low-collision energy measurements, images were recorded for NO(A) rotational levels $N' = 3$, 5-10, and in the high-collision energy measurements, $N' = 3$, 5-14 were recorded, with eight individual images recorded for each quantum state in both cases. Across all V, H, total and background frames, individual images were recorded over 38,400 laser shots for the low collision energy images, and 43,200 laser shots for the high collision energy images. Images were recorded with three scans of the probe laser over the Doppler profile of the relevant transition of the R branch of the NO(A ← X) (0,0) band and with 200 laser shots acquired per frame.

As was also the case for the NO(A) + Ar data, daily centring measurements were not conducted during the acquisition of this data. To compensate for the instability of the zero-velocity coordinate, images were translated based on the position of the non-resonant beam-spot in the corresponding background images. The result of these translations was found to be consistent with the few centring measurements which were conducted during the same time period.

3.3.2 Data Analysis

The experimental velocity map images were analysed using the methods outlined in Section 2.10. Rather than the analysis of a single set of data, individual V and H images were analysed for each quantum state, giving a total of eight values for the DCS and each of the rotational alignment moments. From these, the reported values and the error were obtained from the mean and standard error of the eight fits respectively.

For all final rotational levels of the low-collision energy system, and for $N' = 14$ of the high-collision energy system, the DCS was extracted using Legendre moments in the $x = \cos(\theta)$ basis set, and for $N' = 3$, 5-13 of the high-collision energy system, the $x = (1 - \theta/90°)$ basis set was used. The $A_{q+}^{\{2\}}(\theta)$ moments were extracted with the $x = (1 - \theta/90°)$ basis set for both the high and low-collision energy images. The number of Legendre polynomials used to fit the DCS was optimised by performing fits of the images using the SVD algorithm, with different numbers of polynomials. The optimal number was selected by examining the returned DCSs and simulated images. Too few polynomials, and the DCS would not have sufficient freedom to accurately reproduce the experimental image, and too many would lead to over-parameterisation, where the returned DCS contained sharp non-physical oscillations. The number of Legendre moments used to fit each of the rotational alignment moments was also optimised in the same way. The number of Legendre moments used to extract the DCS and rotational alignment moments are reported in Tables 3.1 and 3.2, respectively.

Experimental noise, caused by the imperfect background subtraction of the non-resonant beam-spot (see Section 2.5) was found to significantly affect the returned DCS, especially at high N', where the intensity of the beam-spot was highest. To eliminate this effect, a "mask" was applied to the region of the image affected by the beam-spot. Pixels within the masked region did not contribute to the χ^2 value during the fitting routine (see Section 2.10.2), excluding them from the fitting process.

In addition to constraining the DCS to remain positive, and the $A_{q+}^{\{2\}}(\theta)$ moments to remain within their classical limits, the values of $A_{0}^{\{2\}}(\theta)$ to a value of -1 at 0° and 180°, and $A_{1+}^{\{2\}}(\theta)$ and $A_{2+}^{\{2\}}(\theta)$ to values of 0 at 0° and 180°. These constraints are consistent with the features of the rotational alignment moments described in Section 2.10.1.

Because the fitting process does not give any indication of the absolute magnitude of the DCS, the extracted DCSs were area normalised to the DCSs obtained from the collision energy averaged quantum scattering calculations performed on the PES calculated by Cybulski and Fernández[150] (see Section 3.3.3). To obtain a more representative comparison between the experimental and theoretical DCS, regions where the experimental and theoretical DCSs clearly diverge (the region in the first 10° of both

collision energy measurements, where a peak is observed only in the experimental DCS, and the backwards direction for $N' \geq 11$ for the high-collision energy measurements, where a peak is observed only in the theoretical DCS, see below) were excluded from this area normalisation.

Table 3.1: Number of Legendre polynomials used to fit experimental scattering images for the low-collision energy NO(A) + Ne system.

N'	DCS	$A_0^{\{2\}}(\theta)$	$A_{1+}^{\{2\}}(\theta)$	$A_{2+}^{\{2\}}(\theta)$
3	27	13	4	8
5	20	11	4	11
6	23	12	4	8
7	19	10	4	10
8	18	8	4	8
9	9	9	4	10
10	8	8	4	9

Table 3.2: Number of Legendre polynomials used to fit experimental scattering images for the high-collision energy NO(A) + Ne system.

N'	DCS	$A_0^{\{2\}}(\theta)$	$A_{1+}^{\{2\}}(\theta)$	$A_{2+}^{\{2\}}(\theta)$
3	23	10	6	8
5	19	11	6	10
6	19	8	6	8
7	17	8	6	9
8	16	8	6	8
9	17	9	6	9
10	19	8	6	10
11	15	10	6	8
12	13	9	6	8
13	14	10	6	8
14	18	7	6	9

While all three $A_{q+}^{\{2\}}(\theta)$ moments were extracted in the fitting routine, $A_{1+}^{\{2\}}(\theta)$ is not reported in this section. This is because the sensitivity to this parameter is low in this experiment, as the angle between the relative velocity vector and the propagation direction of the probe laser is 97° and 75° for the low and high-collision energy experiments, respectively, while the sensitivity to $A_{1+}^{\{2\}}(\theta)$ is low at angles close to 90°.[27] Furthermore, the experimentally reported values of the $A_{q+}^{\{2\}}(\theta)$ moments are truncated to show areas in which the intensity in the DCS is above 10% of the maximum value outside of the first 10°. This is because the $A_{q+}^{\{2\}}(\theta)$ moments are fitted to differences in intensity in different regions of the images, which becomes unreliable in regions of low intensity.

3.3.3 Calculations

Using the HIBRIDON suite of codes,[98] QS calculations of the DCS and $A_{q+}^{\{2\}}(\theta)$ moments were performed by Dr T. R. Sharples on two different PESs, calculated by Pajón-Suárez *et al.*[148] (hereafter referred to as the PRRH PES) and Cybulski and Fernández[150] (hereafter referred to as the CF PES). For each PES, calculations were performed across two collision energy ranges, chosen to match the experimental conditions, with individual calculations conducted at evenly spaced collision energies, spanning a range of three standard deviations of the collision energy. The individual energy calculations were averaged with appropriate weightings to model the Gaussian distribution of collision energies observed in the experiment. DCSs for each N' quantum state were obtained from the sum of the two calculated $j' = N' \pm 0.5$ states and the rotational alignment moments were obtained from a DCS weighted average of the two $j' = N' \pm 0.5$ states. NO(A) was treated as a rigid rotor with rotational constants B = 1.9869 cm^{-1} and γ = -0.0027 cm^{-1}.[143] Calculations were performed up to values of total angular momentum, J_{tot} = 600.5, with a basis of rotational states up to N = 29 and numerical propagation from 3 to 300 Bohr.

The $A_{q+}^{\{2\}}(\theta)$ moments were also calculated by Dr T. R. Sharples using the kinematic apse method,[144] outlined in Section 1.8.3. Calculations were averaged over the same range of collision energies as the QS calculations to model the experimental conditions.

3.3.4 The NO(A)-Ne Potential Energy Surfaces

As was described in the introduction and demonstrated in Section 3.2, the comparison of experimental results to those obtained by QS calculations using an *ab initio* PES is a powerful tool, both to examine the origin of features in the experimental results, and to elucidate inaccuracies in the PES. The NO(A) + Ne scattering system provides a rare opportunity to perform these tests, as there are two recent *ab initio* PESs. The PRRH PES was calculated with a CCSD(T) level of theory, and the CF PES, at a RCCSD(T) level of theory. The results of QS calculations using these PESs can thus be compared directly against each other, and against a set of experimental results. The features of the PRRH and CF NO(A)-Ne PESs tested in this section are described here. The *ab initio* energies of the PESs were calculated on an angular grid, in intervals of 45° and 30° for the PRRH and CF PESs respectively. These energy points were parameterised to obtain a full representation of the PES at all angles and radii. As can be seen in the polar contour representations of the PESs in Figure 3.13, the structure of the two NO(A)-Ne PESs is very similar. The gradient of the repulsive region varies considerably as a function of radius, being very steep at short radii and much more shallow at long radii. The anisotropy also clearly varies as a function of the radius, with the PES being almost circular at the longest radii, and becomes much more ellipsoidal as the radius decreases. The anisotropy of the PESs is displayed much more clearly in Figure 3.14, which shows the Legendre moments of the PESs. The $\lambda = 0$ moment shows the isotropic radial distribution of the PES, while the $\lambda \geq 1$ moments each have an angular dependence, and thus provide a representation of the anisotropy of the PES. The λ = 1-4 moments all become much larger at shorter radii, as is commonly observed in diatom-atom PESs. The $\lambda = 1$ moment, which reflects the asymmetry between the N and O ends of the PES, and the $\lambda = 2$ moment, which reflects the differences between the ends and the side of the PES, have values with a larger magnitude in the CF PES. The λ = 3 and 4 moments are similarly larger in the CF

PES, reflecting its more anisotropic nature. The λ = 5 and 6 moments are unique to the CF PES due to the higher angular resolution of the calculated energy points, but these moments only become prominent at shorter radii, and so will only impact the PES in the region accessible in the high-energy collisions.

The attractive region is very shallow in both the PRRH and CF NO(A)-Ne PES, reaching a depth of 3.75 cm^{-1} and 5.12 cm^{-1} respectively, and in both cases, is very isotropic. The depth is too shallow to be visible in the contour plots, but can be seen in the Legendre plots, where the λ = 0 moment becomes negative at large radii, while the $\lambda \geq 1$ anisotropic moments are all close to zero.

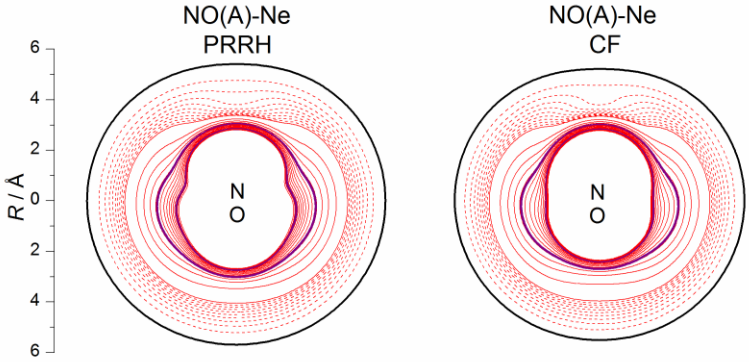

Figure 3.13: Contour plots of the NO(A)-Ne potential energy surface, calculated by left: Pajón-Suárez *et al.*,[148] right: NO(A)-Ne calculated by Cybulski and Fernández.[150] Contours represent the potential energy of the coordinate, with red being positive, with solid contours in steps of 100 cm^{-1} and dashed contours being in steps of 10 cm^{-1} in the range 10-90 cm^{-1}. Black represents 0 cm^{-1} and purple represents 523 cm^{-1} and 1,309 cm^{-1}, corresponding to the mean collision energies of the experiments.

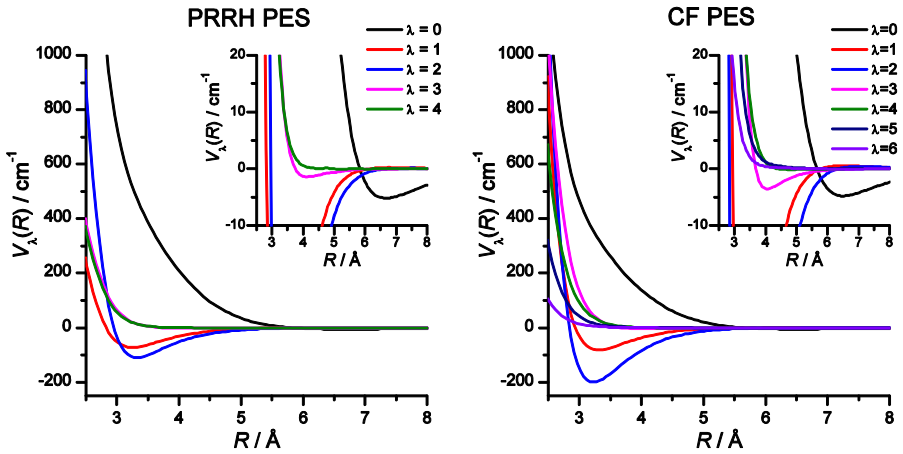

Figure 3.14: Radial dependences of the Legendre moments of the PRRH (left) and CF (right) PESs. The insets display the same plots with expanded vertical scales for visual clarity.

3.3.5 Results

Newton diagrams for the inelastic scattering of NO(A) with Ne at the two collision energies investigated are displayed in Figure 3.15, overlaid on the corresponding experimental images. Figure 3.16 shows the set of experimentally obtained V and H velocity map images for the low-collision energy system, summed across all eight individual images for each quantum state. There is a very clear trend, which was also present in the NO(A) + Ar system, that as N' increases, there is a general shift towards higher scattering angles. This effect is almost always observed in inelastic scattering systems. Rotational excitation to higher N' requires the collisions to occur through more anisotropic regions of the PES, as these regions apply a greater torque to the N-O bond axis. As was shown in Section 3.3.4, the repulsive core is much more anisotropic than the

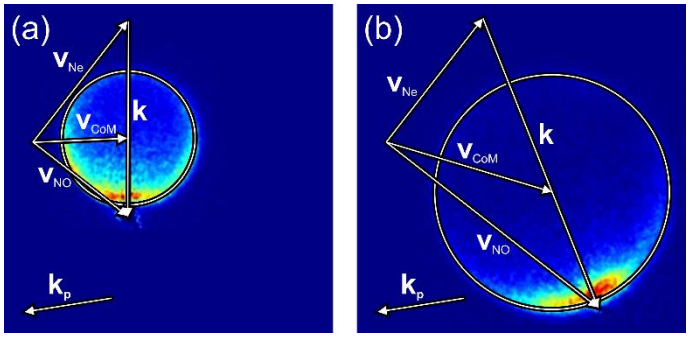

Figure 3.15: Newton diagrams corresponding to the mean collision energies for the inelastic collisions of NO(A) with Ne at (a) 523 cm^{-1}, (b) 1,309 cm^{-1}, overlaid on V + H colour intensity maps for final state $N' = 8$. Vectors represent, $\mathbf{v_{NO}}$ and $\mathbf{v_{Ne}}$: the lab frame velocity of the two colliders, $\mathbf{v_{CoM}}$: the velocity of the centre of mass, $\mathbf{k}$: the relative velocity vector, $\mathbf{k_p}$: the propagation direction of the probe laser. The circle represents possible final centre of mass velocities for NO(A) scattered in the plane of the detector.

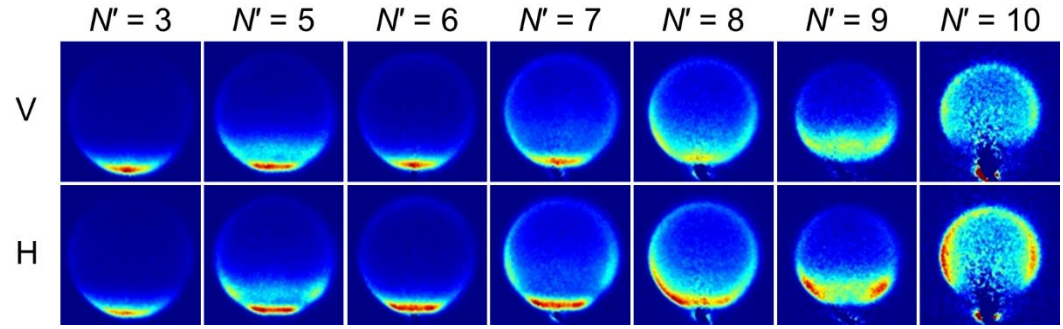

Figure 3.16: Experimental velocity map images for the collision of NO(A) with Ne at a mean collision energy of 523 cm^{-1}, obtained from the sum of all eight individual images for $N' = 3$, 5-10.

outer regions of the potential. This means high-N' final rotational levels will predominantly be formed through low-impact parameter collisions, which probe the repulsive core, and lead to scattering at high angles. On the other hand, low-N' final rotational levels can be prepared through scattering through the less-anisotropic outer regions of the PES, which lead to glancing collisions, and thus, lower scattering angles. This transition from low to high-scattering angles is not a smooth trend, with, for example, $N' = 6$ being considerably more forward scattered than $N' = 5$, and $N' = 9$ being more forward scattered than $N' = 8$. These deviations from the trend can largely be attributed to parity effects, where parity conserving (ΔN = even) collisions will probe different aspects of the PES than parity changing (ΔN = odd) collisions.[151] These effects will be discussed in more detail in Section 3.3.6.

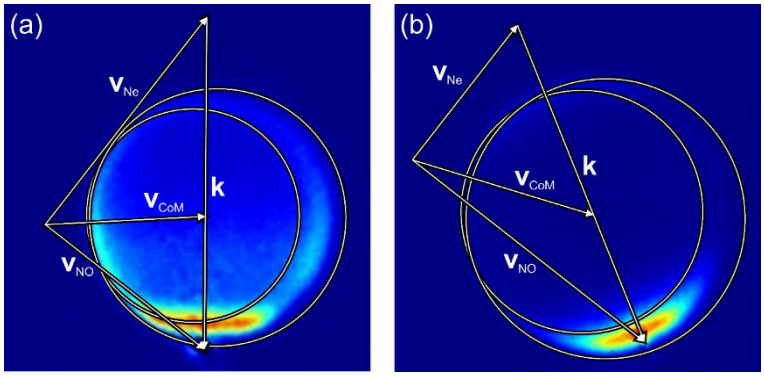

Figure 3.17: V + H Velocity map images for the product state $N' = 7$ for the collision of NO(A) with Ne at mean collision energies of (a) 523 cm^{-1} and (b) 1,309 cm^{-1}, overlaid with Newton diagrams. Vectors $\mathbf{v_{NO}}$, $\mathbf{v_{Ne}}$, $\mathbf{v_{CoM}}$ and $\mathbf{k}$ represent the correlations corresponding to the mean molecular beam speeds. The circles show the possible final velocities for NO(A) scattered in the plane of the image, corresponding to collisions with both molecular beam speeds one standard deviation above the mean (large circle) and one standard deviation below the mean (small circle).

A subtle asymmetry can be seen in both the V and H images, which is especially clear for $N' = 7$, 8 and 10, where there is prominent sideward-scattering. The maximum intensity on the left side of the image, which corresponds to slower lab-frame speeds, is higher than on the fast, right side. This effect is not caused by a difference in detection probability of the two sides of the image, rather it is a result of the kinematic blurring bought about by the distribution of speeds of the two molecular beams. As Figure 3.17 shows, as the collision energy increases with molecular beam speed, the Newton sphere changes in radius, reflecting the increased available energy to be partitioned into product translation. Additionally, the increased collision energy leads to a shift of $\mathbf{v_{CoM}}$, on which

the Newton sphere is centred, to faster lab-frame velocities. This means that the effect of the blurring resulting from the spread of speeds of the two molecular beams is different on the two sides of the image. As the blurring occurs over a smaller number of pixels on the slow side of the image, this leads to the sharper edge and higher maximum intensity observed.[152] This is a feature which affects all scattering systems where there is a significant spread of speeds in the molecular beams, but it is particularly visible in the data from this experiment, as a result of the high signal-to-noise ratio and the lack of a density-to-flux detection bias in the scattering images.

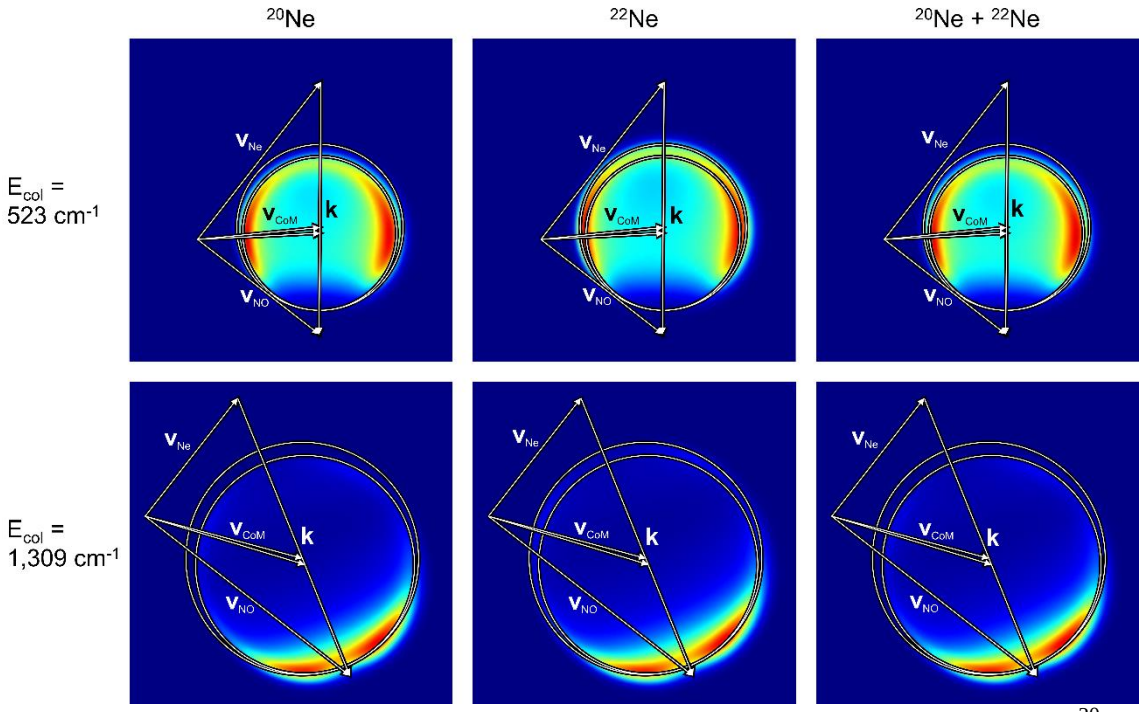

Figure 3.18: Simulated V + H velocity map images for the collision of NO(A) with ^{20}Ne (left column), ^{22}Ne (middle column) and ^{20}Ne and ^{22}Ne with their natural abundances (right column), at a mean collision energies of 523 cm^{-1} (top row) and 1,309 cm^{-1} (bottom row) for product state $N' = 10$. Overlaid Newton diagrams show the relevant velocity vectors and in-plane final velocity of NO(A) for the collisions with both ^{20}Ne and ^{22}Ne.

Another subtle blurring effect in the images occurs from the fact that neon used in the experiment was not monoisotopic, and collisions occur with both of the naturally occurring isotopes: ^{20}Ne and ^{22}Ne, which lead to collisions with different kinematics. As Figure 3.18 shows, collisions of NO(A) with the different isotopes of Ne lead to separate Newton spheres. This occurs because the different masses of Ne lead to collisions at subtly different energies, and different fractions of the collision energy are partitioned into translational motion of the NO(A). However, this effect is not readily observable in

either the experimental or simulated images, because the natural abundance of ^{22}Ne is only 9%, and the two projected Newton spheres occur in a very similar position, so the ^{22}Ne scattering signal can only be seen faintly above the main ^{20}Ne scattering signal. Because of the different kinematics, and the different collision energies, the DCS and rotational alignment moments are different for collisions with the two isotopes, although QS calculations indicate that this difference is only very subtle, and is not detectable under the current experimental conditions. Only a single set of DCSs and $A_{q+}^{\{2\}}(\theta)$ moments were extracted from the scattering images, fitting to the scattering signal of both isotopes simultaneously, and the results are considered representative of the collisions of NO(A) with ^{20}Ne, as this isotope dominates the scattering images.

The high-collision energy velocity map images are presented in Figure 3.19. As with the low-collision energy images, there is a clear trend towards higher scattering angles as N' increases. These images are considerably more forward scattered than the equivalent low-collision energy images. This is a commonly observed kinematic effect, which occurs due to higher energy collisions being able to impart the same torque to the N-O bond axis at larger impact parameters, meaning that rotational energy transfer can occur with less change in the direction of the colliders. Both the effects of kinematic blurring and of multiple isotopes of Ne are also visible in the high-energy collision images, as shown in Figures 3.17 and 3.18, although these effects are less readily visible than they were in the low-collision energy images, as there is much less scattering at higher angles. A subtle parity-dependent effect is observed in the high-collision energy images, where the scattering amplitude in the backwards region, while very low compared to the forward region, is consistently more intense in the even-N' images, than the odd-N' images. As with the NO(A) + Ar images, the differences in intensity between the V and H images are a clear indication that there is a strong collision-induced alignment of the rotational angular momentum in both the high- and low-collision energy systems.

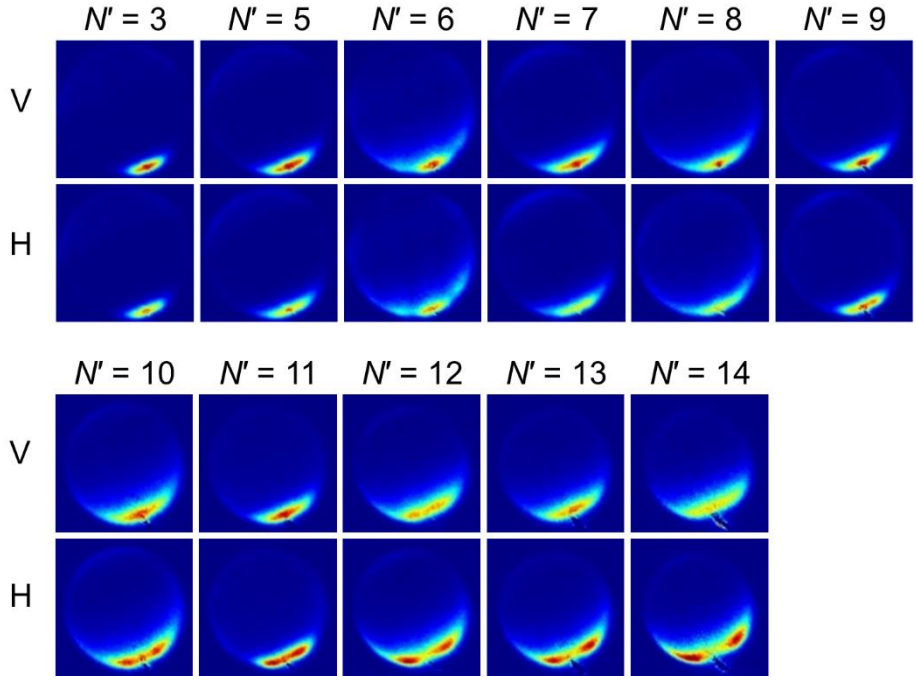

Figure 3.19: Experimental V and H velocity map images for the collision of NO(A) with Ne at a mean collision energy of 1,309 cm^{-1}, obtained from the sum of all eight individual images for N' = 3, 5-14.

An example set of individually acquired experimental images are compared to their corresponding fitted images for the low-energy collisions of NO(A) with Ne in Figure 3.20. Across all final rotational levels, there is excellent agreement between the experimental and fitted images, clearly showing that the fitting routine has converged on the correct DCS and rotational alignment moments to reproduce the experimental scattering image. The extracted DCSs and $A_{q+}^{\{2\}}(\theta)$ moments obtained from the low-collision energy experimental images are displayed in Figure 3.21. Comparisons are made to the results of QS calculations run on the PRRH and CF PESs, as well as to the results of KA calculations for the $A_{q+}^{\{2\}}(\theta)$ moments. The DCSs from the two sets of QS calculations are similar, and ignoring the first 10°, they do a good job of replicating the rotational rainbows observed in the experimental DCSs. Consistent with a visual inspection of the scattering images, two maxima are observed in both the experimental and QS DCSs for N' = 5 and 7, while all other rotational levels exhibit a single maximum.

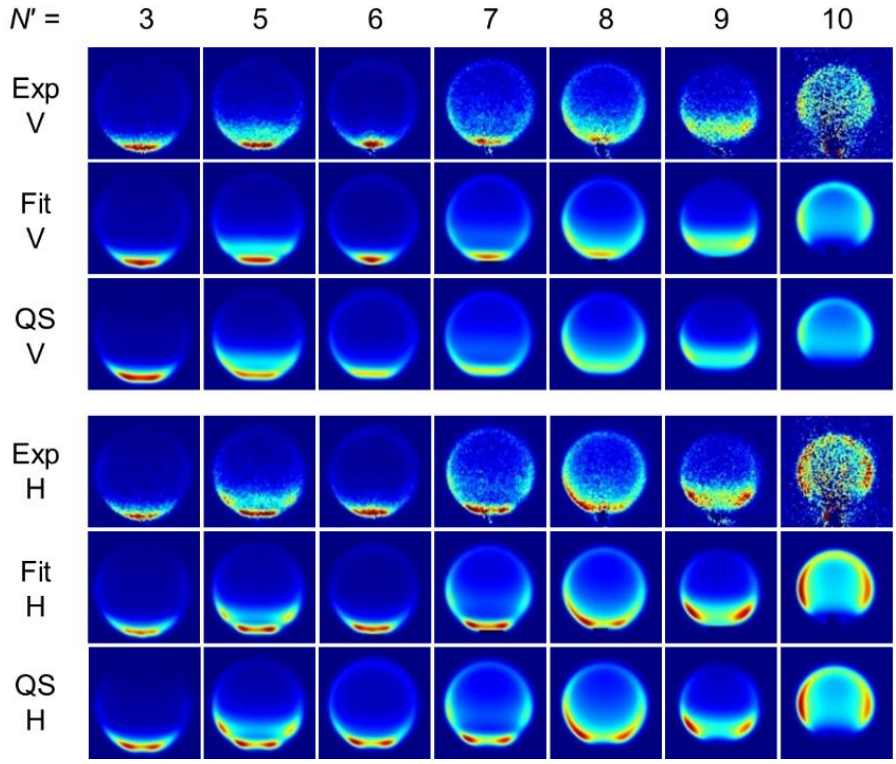

Figure 3.20: Comparison of individual experimental images (Exp V/H) to the images simulated from the corresponding results of the fitting routine (Fit V/H), and to images simulated from the results of QS calculations on the CF PES (QS V/H) for inelastic collisions of NO(A) with Ne at a mean collision energy of 523 cm^{-1}, for final rotational levels N' = 3, 5-10.

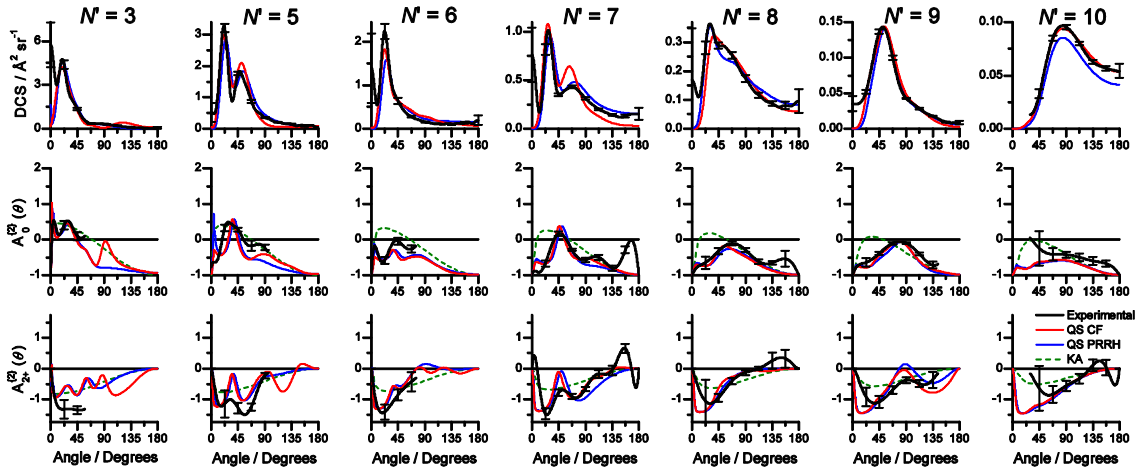

Figure 3.21: Plots showing the experimental (black) DCS and $A_{q+}^{\{2\}}(\theta)$ moments for the inelastic collisions of NO(A) with Ne at a mean collision energy of 523 cm^{-1}, compared to the results of QS calculations run using the CF PES (red) and the PRRH PES (blue), and for the $A_{q+}^{\{2\}}(\theta)$ moments, the results of KA calculations (dashed green). Error bars represent 95% confidence limits of the experimental results.

An equivalent set of individual experimental and fitted images for the high-energy collisions of NO(A) with Ne are presented in Figure 3.22, again showing high levels of agreement. Figure 3.23 shows the extracted DCS and $A_{q+}^{\{2\}}(\theta)$ moments, along with the results of QS calculations run on the two PESs, and KA calculations for the $A_{q+}^{\{2\}}(\theta)$ moments. Excluding the first 10°, the experimental DCS exhibits a single rotational rainbow maximum for all product states, except, $N' = 6$, which exhibits two maxima. This structure is well reproduced by the QS calculations for $N' \leq 10$, however, the QS DCSs for $N' \geq 11$ contains a further backward-scattered peak, for which there is no sign of in the experimental DCSs. This peak can be seen in the scattering images simulated from the QS calculations in Figure 3.22, but not in the experimental or fitted images, confirming that its absence in the experimental DCS is not an error.

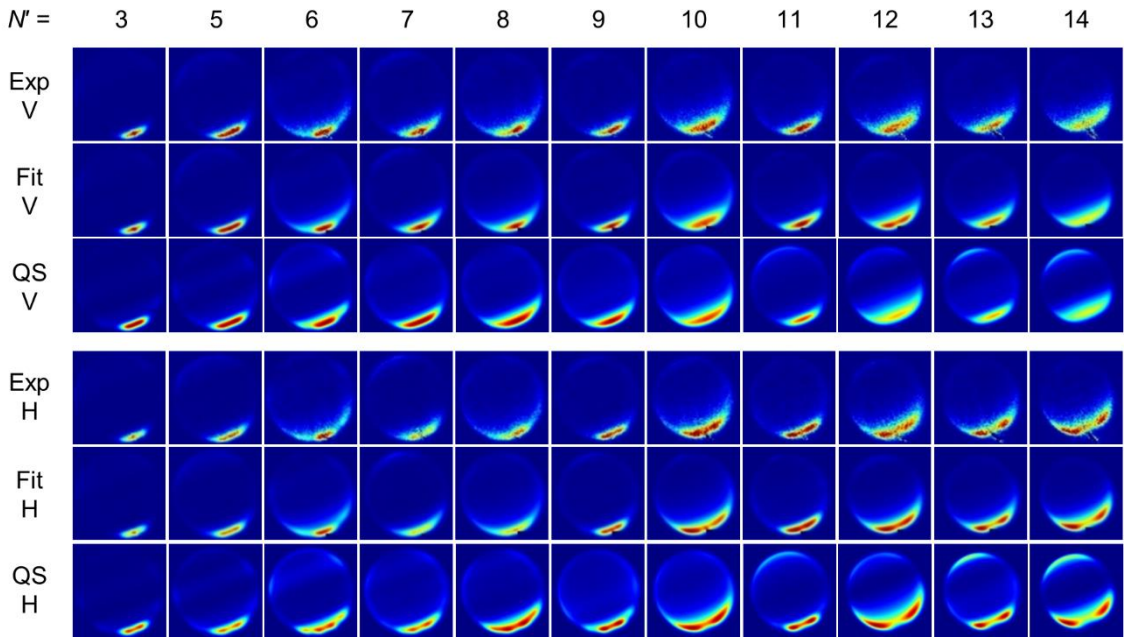

Figure 3.22: Comparison of individual experimental images (Exp V/H) to the images simulated from the corresponding results of the fitting routine (Fit V/H), and to images simulated from the results of QS calculations on the CF PES (QS V/H) for inelastic collisions of NO(A) with Ne at a mean collision energy of 1,309 cm^{-1}, for final rotational levels $N' = 3$, 5-14.

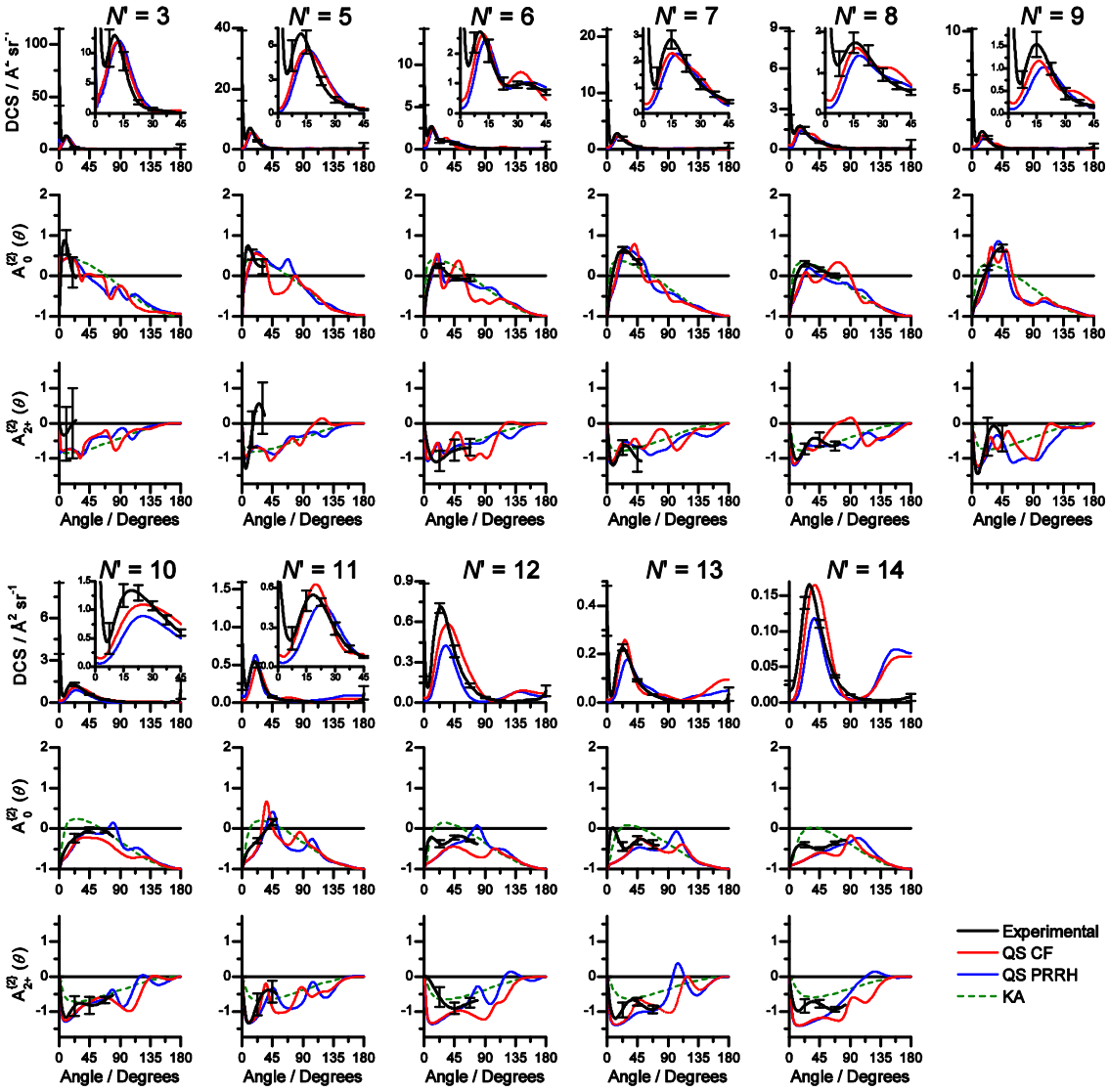

Figure 3.23: Plots showing the experimental (black) DCS and $A_{q+}^{\{2\}}(\theta)$ moments for the inelastic collisions of NO(A) with Ne at a mean collision energy of 1,309 cm^{-1}, compared to the results of QS calculations run using the CF PES (red) and the PRRH PES (blue), and for the $A_{q+}^{\{2\}}(\theta)$ moments, the results of KA calculations (dashed green). Error bars represent 95% confidence limits of the experimental results. Insets show the DCS on over a smaller range of scattering angles and intensities to better illustrate the rotational rainbow peaks.

In both the high and low-collision energy DCSs, the experimental results strongly deviate from the QS calculations in the smallest angles. While QS calculations at both collision energies, and with both PESs tend towards low amplitudes at 0°, there is a clear peak in the forward direction of the experimental results, reminiscent of the glory-like scattering peak observed in the NO(A) + Ar DCS. An obvious concern regarding this peak is that it is not a real feature, and is simply an artefact of the fitting routine. However, the peaks are certainly not artificial, as Figures 3.20 and 3.22 show, the images simulated

from the fitted results clearly reproduce the forward scattered region of the experimental images, whereas the images simulated from the QS calculation results contain a sizeable dip in intensity in the region centred around 0°. This clearly shows that the peak in the forward direction is required to correctly reproduce the structure of the experimental images, confirming that it is a real feature of the DCS. This feature of the DCS was also noted by Steill *et al.*[47] in the preliminary investigation of the NO(A) + Ne system. However, the improved signal to noise levels and more complete analysis provided by the current experiment provides a much more complete and unambiguous insight into this feature.

The fact that different basis sets were used to fit the DCSs to the low and high-collision energy images means that the intensities of the forward-scattered peak in the DCS cannot be directly compared between the two collision energies. The cos(θ) basis set used to fit the low-collision energy images forces the DCS to have a shallow gradient at 0° and 180°, meaning that the amplitude of the forward scattered peak is underestimated (attempts were made to use the (1 – θ/90°) basis set to fit the DCSs of low collision energy images, but the broad features of these DCSs could not effectively be reproduced in this way). This underestimation has only a tiny effect on the fitted image, because of the sin(θ) volume element of the DCS. While it cannot be demonstrated from this set of results, it is expected that the high-collision energy system contains a more intense forward-scattered peak, as the higher velocities mean that a greater amount of linear to angular momentum transfer can occur at a given impact parameter.

The $A_{q+}^{\{2\}}(\theta)$ moments extracted by the fitting routine are also compared to the QS results from the PRRH and CF PESs in figures 3.21 and 3.23. As was also observed in the NO(A) + Ar system, the QS $A_{q+}^{\{2\}}(\theta)$ moments at both collision energies exhibit strong scattering-angle-dependent fluctuations, which are not observed in the KA moments. Across both the high and low-collision energy measurements, there is generally a good agreement between the experimental and QS values of the rotational alignment moments, with oscillations in the QS $A_{q+}^{\{2\}}(\theta)$ moments occurring at similar angles to the experimental values.

3.3.6 Discussion

As was described in the previous section, the QS calculations conducted on each of the PESs did a good job of reproducing the structure of the DCS outside of the first 10°. However, there were features of the QS DCSs which clearly deviated from the experimental results, indicating shortcomings of the *ab initio* PESs. The first deviation to be discussed here is the peak in the backwards region of the DCS for $N' \geq 11$, which is observed in both the PRRH and CF DCSs, but for which there is no evidence in the experimental DCSs or scattering images. The highest N' states are necessarily the product of collisions which have probed the most anisotropic region of the PES, which corresponds to the highly-repulsive core of the PES. As the experimentally unobserved peak only occurs in the high N' final rotational levels, it therefore seems likely that the feature of the PESs which gives rise to these peaks is located within the repulsive core. Furthermore, collisions which probe the repulsive core typically result in high scattering angles, which is consistent with the angle of the anomalous peak. The highest-potential energy points directly calculated in the generation of the PRRH and CF PESs were 281.01 cm^{-1} and 572.51 cm^{-1} respectively,[148,150] with higher potential energy regions determined entirely by extrapolation of the lower-potential energy points. As the average collision energy of the high-energy measurements was 1,309 cm^{-1}, this extrapolated region is certainly probed in this measurement. The anomalous peak observed in the QS results is consistent with some feature which has been incorrectly modelled in the high-potential energy region, indicating that the extrapolation of the low-energy region is not suitable for this system, and higher-potential energy points need to be directly calculated to accurately model the NO(A)-Ne PES.

Next, the forward-scattered peak in the DCS, which is exclusively observed in the experimental results will be considered. This peak very strongly reminiscent of the feature in the NO(A) + Ar DCS, which did appear in the QS results, and was found to occur from collisions which probe the attractive region of the PES. While both the PRRH and CF PESs have attractive regions, they are very shallow, and in both cases, are extremely isotropic. It is therefore unsurprising that the attractive regions of these *ab initio* PESs do not give rise to significant inelastic scattering. A localised attractive well, similar to the one observed in the NO(A)-Ar PES, even if it only had a very shallow depth would likely

be sufficient to generate the anisotropy needed to lead to the forward scattered peaks seen in the experimental DCSs. It seems likely that such a localised well would be positioned at the N end of the NO(A)-Ne PES, as this is what is observed in the NO(A)-Ar, Kr and Xe PESs.[14] The attractive region has proven to be a recurring problem in the calculation of *ab initio* PESs, with adjustments frequently required to bring theoretical measurements in line with their experimental counterparts. For example, a spectroscopic study showed that the NO(A)-Ar PES had an insufficient attractive well depth, and a rescaling factor of 1.23 was required bring the theoretical spectrum into line with the experiment.[14] It is this rescaled PES which was used for the NO(A) + Ar QS calculations in Section 3.2.

Ayles *et al*. conducted a spectroscopic study on the A-X transition of NO-Rg complexes, where Rg = Ne, Ar, Kr and Xe.[153] While clear spectra were observed for the complexes with Ar, Kr and Xe, none could be obtained for the NO-Ne complex, despite strong evidence for the NO(X)-Ne complex being present. This result was attributed to the NO(A)-Ne complex being extremely weakly bound, consistent with the shallow, isotropic attractive region of the PRRH and CF PESs. An alternate explanation for the non-observation of the transition is that the Franck-Condon factor for the NO-Ne(A ← X) transition is very small. This is a plausible explanation, as the NO(X)-Ne complex has a "T" shaped geometry,[153] while, as described above, an attractive well in the NO(A)-Ne PES is likely to be localised at the N end, leading to a linear NO(A)-Ne complex geometry.

Another study of the NO-Rg complex was conducted by Holmes-Ross *et al*. where Rg = He, Ne and Ar.[154] The complex was excited on a A ← X transition, and a rotational state distribution was measured for the dissociated NO(A) molecules. For NO-He, a low rotational distribution of NO(A) was produced, which is consistent with the isotropic attractive region of the NO(A)-He PES. The opposite was observed for NO-Ar, where a large distribution of rotational levels was measured, indicating that a large torque was applied to the NO(A) molecule as the complex dissociated. This implies that the attractive region of the NO(A)-Ar PES is very anisotropic, which is consistent with the structure of the literature PES. The rotational state distribution for the dissociation of the NO-Ne complex was an intermediate of the NO-He and NO-Ar complexes. This indicates that there is some anisotropy in the NO(A)-Ne PES, but not as much as the NO(A)-Ar PES. This is inconsistent with the structure of both the PRRH and CF NO(A)-Ne PESs, in

which the attractive region has a similar level of anisotropy to the NO(A)-He PES (see Chapter 4), but is consistent with our observation of a forward scattered peak in the NO(A) + Ne DCSs.

Except for the two above mentioned discrepancies, both the CF and PRRH QS calculations do a generally good job of replicating the experimental DCSs at both collision energies. The quality of agreement between the experimental and theoretical DCSs can be partially quantified with a comparison of the angles at which the rotational rainbow maxima occur in the experimental and QS calculations. These rotational rainbow angles are presented for both the high and low-energy collisions in Figure 3.24. For the low-energy collisions, the first rotational rainbow angles are better described by the results of the QS calculations using the CF PES, in which the angles are, with the exception of $N' = 9$, within experimental uncertainty of the experimental rotational rainbow angles. The results of the calculations using the PRRH PES on the other hand, return angles which are consistently 3-5° higher than the experimental angles. These results provide a clear insight into the anisotropy of the repulsive region of the PES, as a more anisotropic repulsive region will lead to, with all other factors being equal, a smaller rotational rainbow angle. This is because inelastic collisions on a more anisotropic PES apply more torque to the N-O bond axis, allowing rotational excitation to populate a given rotational level with collisions at a higher impact parameter, leading to scattering at lower angles. From these results, it can be concluded that the more anisotropic (see Section 3.3.4) CF PES provides a better description of the repulsive region accessible to the low-energy collisions. It is evident from the rotational rainbow angles that QS calculations on both the PRRH and CF PESs have done a poor job of replicating the second rotational rainbow maxima in $N' = 5$ and 7. These multiple peaks result from the scattering from different ends of the NO molecule,[155] and so the discrepancy in the location of these peaks is evidence of an inaccuracy in the differences between the N and O ends of the PES, described by the odd-order Legendre moments.

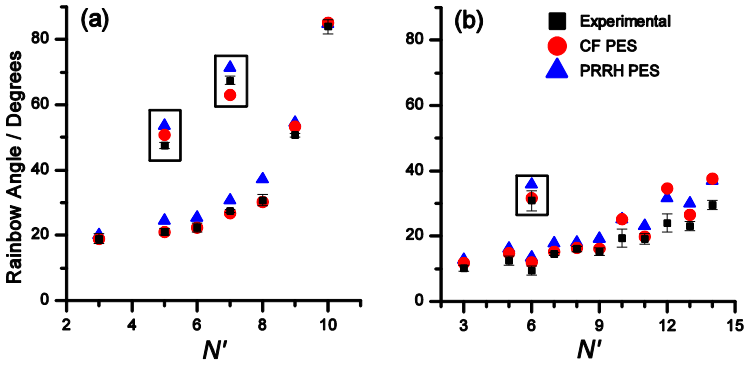

Figure 3.24: Plot showing the rotational rainbow angles for the collisions of NO(A) with Ne at a mean collision energy of (a) 523 cm^{-1} and (b) 1,309 cm^{-1}, comparing the experimental results (black) with the results of QS calculations run on the CF PES (red) and the PRRH PES (Blue). Results enclosed in boxes represent further rotational rainbow peaks in the DCS. The maxima in the eight individual fits were obtained, and the mean and standard error calculated. Error bars on the experimental results represent 95% confidence limits.

The agreement between the experimental rainbow angles, and those obtained from the QS results on the CF PES is noticeably worse for the high collision energy system, although they are still systematically better than the QS angles using the PRRH PES. The level of agreement between the experimental and QS rotational rainbow angles at high-collision energies becomes considerably worse for $N' \geq 10$. There is also a clear parity effect in the level of agreement for these $N' \geq 10$ product states, where the rotational rainbow angles predicted by QS calculations using the CF PES are closer to the experimental values for odd N' states than even N' states. This inaccuracy indicates that the odd Legendre moments of the PES are more accurate at the radii probed in these transitions. The same even/odd trend is observed in the rotational rainbow angles predicted by QS calculations using the PRRH PES, although it is subtler than in the results using the CF PES. The onset of this inaccuracy in the rotational rainbow angle in the QS calculations is broadly consistent with the point at which the unobserved backward scattering peak appears in the QS DCSs. This indicates that the inconsistency in rainbow angles for these final rotational levels is possibly linked in some way to the inaccurately modelled features in the high-potential energy region of the PES which led to the anomalously predicted backward scattered peak.

There is a clear parity effect observed in the low-collision energy DCSs in the range N' = 5-8, where after the first 10°, both the experimental and theoretical DCSs contain a single maximum in the even N' final rotational levels, and two maxima in the odd N'

levels. This occurs because parity conserving transitions, which in this case populate even N' states, and parity changing transitions, which populate odd N' states, probe different parts of the PES. Within the Born approximation, the even moments in the PES (see Figure 3.14) couple to parity conserving transitions, while the odd moments couple to parity changing transitions.[149] The Born approximation breaks down for large ΔN transitions; however, they can be considered as a series of smaller ΔN virtual transitions, where each virtual transition is either parity conserving or changing.[151,156] These high ΔN transitions still contain parity effects, as they sample the even and odd virtual ΔN transitions, and as such, the even and odd moments of the PES, differently. Odd ΔN overall transitions must sample an odd number of odd ΔN virtual transitions, and may also sample any number of even ΔN virtual transitions. On the other hand, even ΔN overall transitions may contain solely even ΔN virtual transitions, although they may also contain an even number of odd ΔN virtual transitions as well. This leads to an overall bias, where odd ΔN overall transitions will bias towards probing the odd moments of the PES, and even ΔN overall transitions will bias towards probing the even moments of the PES.[151]

As with the DCS, the $A_{q+}^{\{2\}}(\theta)$ moments are very similar in both sets of QS calculations, at both the high and low-collision energies. There are points where the QS $A_{q+}^{\{2\}}(\theta)$ moments on the two PESs do deviate substantially, such as at ~90° for the low-collision energy $N' = 3$ final rotational level. However, these large deviations only occur in regions where there is very little intensity in the DCS, and so large differences in the values of the rotational alignment moments do not reflect a significant change in the overall scattering dynamics.

As was also seen in the $A_{q+}^{\{2\}}(\theta)$ moments for the NO(A) + Ar system, the results from the QS calculations exhibit strong angle-dependent oscillatory behaviour, which are not observed in the results of KA calculations. This is in sharp contrast to comparisons between the QS and KA calculations in the NO(X) + Ne and Ar collision systems, in which both sets of rotational alignment moments were found to be extremely similar.[27,47,93,157] This difference between the NO(X) and NO(A) scattering systems is a consequence of the validity of applying the hard-shell KA model to the PESs. The NO(X)-Ne PES exhibits a shallow attractive region, followed by a steep repulsive core, which

leads to hard-shell models providing a good approximation at the energy ranges probed in the experiments, and thus the KA model is effective. On the other hand, both the NO(A)-Ne and NO(A)-Ar PESs have a much shallower gradient in the repulsive region, so a hard-shell approximation will have only limited accuracy. Similar features (although not nearly as extreme as the ones observed here) were observed in the NO(X) + Kr rotational alignment moments, which were also not observed in the KA moments.[28] These features were attributed to scattering through the deep attractive region of the NO(X)-Kr PES, which is not considered in the hard-shell KA model.

While the reason for the breakdown of the KA model is straightforward, the physical origin of these oscillations is not as clear. The fact that oscillatory features in $A_0^{\{2\}}(\theta)$ and $A_{2+}^{\{2\}}(\theta)$ track each other, as well as tracking features in the DCS implies that all of these oscillations are caused by the same feature of the collision dynamics. These correlations are most apparent in the low-energy collisions, as scattering typically occurs over a much wider range of angles. For example, in the low-energy $N' = 7$ state, the maxima observed at ~50° in $A_0^{\{2\}}(\theta)$ and $A_{2+}^{\{2\}}(\theta)$ occurs at the same angle as a minimum in the DCS, and the minima at ~25° in $A_0^{\{2\}}(\theta)$ and $A_{2+}^{\{2\}}(\theta)$ occurs at the same angle as a maximum in the DCS. Similar fluctuations are observed in other product states, and as a broad trend, the QS $A_{q+}^{\{2\}}(\theta)$ moments tend to match the KA moments in areas where there is low intensity in the DCS, and deviate where there is higher intensity in the DCS. A more complete understanding of this feature will require further investigation, using both QS calculations and other methods. For example, calculations using different partial waves may be used to identify the region of the PES which is responsible for these oscillations, and quasi-classical trajectory calculations can be used to show unambiguously whether the oscillations are classical or quantum in nature.

The sensitivity of the experimental images to the $A_{q+}^{\{2\}}(\theta)$ moments is lower than the DCS, as they involve the measurement of differences in intensity, rather than absolute intensities of the scattering signal. Therefore, the percentage error associated with the fitted $A_{q+}^{\{2\}}(\theta)$ moments are substantially higher than the DCS. Despite this, there is a good agreement between the results of the QS calculations and the experimental results,

with oscillations in the experimental $A_{q+}^{\{2\}}(\theta)$ moments generally matching those obtained from the QS calculations. The general agreement between experimental and theoretical $A_{q+}^{\{2\}}(\theta)$ moments provides further confidence that the broad features of both PESs have been modelled correctly, although it is not possible to say with any confidence whether either PES is more accurate purely from the $A_{q+}^{\{2\}}(\theta)$ moments.

3.4 Collisions of Rotationally Excited NO($A^2\Sigma^+$) with Neon

3.4.1 Experimental Conditions

Velocity map images with NO(A) prepared in the initial rotational levels N = 1 and N = 2 were acquired under the same conditions as the low-collision energy NO(A) + Ne system described in Section 3.3.1. The first molecular beam contained 10% NO (BOC, 99.998%) seeded in Ar (BOC, 99.998%) with a backing pressure of 3 bar to give a molecular beam with a velocity of mean 623 m s^{-1} and FWHM 53 m s^{-1}. This was crossed with a neat molecular beam of Ne (BOC, 99.999%) with a backing pressure of 5 bar, with a velocity of mean 809 m s^{-1} and FWHM 54 m s^{-1}, to give a collision energy distribution with mean of 523 cm^{-1} and FWHM of 57 cm^{-1}.

To generate the required initial rotational levels, NO(A) was prepared on a transition other than $Q_1(0.5)$. The N = 1 initial state was prepared through the $R_1(0.5)+Q_{21}(0.5)$ transition of the NO(A ← X) (0,0) band, generating NO(A) in rotational levels N = 1, j = 0.5 and 1.5. The N = 2 initial state was prepared through the $R_{21}(0.5)$ transition, generating NO(A) with the rotational level N = 2, j = 1.5. As was shown in Figure 3.12, the effect of spin-rotation splitting is negligibly small, so the different j states will not significantly affect the results. The fluence of the preparation laser was set to 0.6 mJ cm^{-2} and 1.1 mJ cm^{-2} for the preparation of N = 1 and 2 respectively, to account for the different absorption coefficients of the two transitions. The diameter of the preparation laser beam was set to 2 mm. Other than these, the conditions of the experiment were the same as described in Chapter 2, with the probe laser beam set to a fluence of 0.65 μJ cm^{-2} with a diameter of 3

mm, and the fluence of both ionisation laser beams varied in the range 4-40 mJ cm^{-2}, with diameters of 3 mm.

As neither of the preparation transitions used in this section suffered the same spectral congestion as $Q_1(0.5)$ (described in Section 2.5), all accessible final rotational levels with sufficient populations were investigated, including those populated by negative ΔN transitions. For the collisions of NO(A) with initial rotational level $N = 1$, images were recorded for product states $N' = 0$, 2-10 and for the collisions of $N = 2$, images were recorded for product states $N' = 0$, 1, 3-10. For both $N = 1$ and 2, final rotational levels $N' = 5$-9 were recorded over two images, one of which was recorded with the preparation laser vertically polarised and the second with it horizontally polarised in the lab frame. For the remaining product states, a single scattering image was recorded, with the preparation laser vertically polarised. Each scattering image was recorded over 64,000 laser shots across all total, background, V and H frames, and five scans of the Doppler profile of the corresponding transition of the R branch of the NO(E ← A) (0,0) band.

3.4.2 Data Analysis

Analysis was conducted in the same way as the other NO(A) + Ne systems, with fitting of the individual images to obtain the DCSs and $A_{q+}^{\{2\}}(\theta)$ moments. The DCS was fit with the $x = \cos(\theta)$ basis set for $N' \geq 5$ and the $x = 1 - (\theta/90°)$ basis set for $N' \leq 4$, and the $A_{q+}^{\{2\}}(\theta)$ moments with the $x = 1 - (\theta/90°)$ basis set, with the number of Legendre moments used in the fitting varied as shown in in Tables 3.3 and 3.4. $A_0^{\{2\}}(\theta)$ was constrained to a value of -1 at 0° and 180°, and $A_{1+}^{\{2\}}(\theta)$ and $A_{2+}^{\{2\}}(\theta)$ to values of 0 at 0° and 180°. For $N' \leq 2$, the sensitivity of the images to the rotational alignment was extremely low, as a result of hyperfine depolarisation, which has a larger effect at lower N', and the polarisation sensitivity factor, which is smaller at lower N'. For $N' = 0$, N cannot have an alignment. These factors resulted in the fitting routine not being able to converge on a solution for these final rotational levels on a reasonable timescale, and so no attempt to determine the $A_{q+}^{\{2\}}(\theta)$ moments was made for these rotational levels. In these cases, the

$A_{q+}^{\{2\}}(\theta)$ moments were assumed to be the results of the quantum scattering calculations and the DCS was determined. Because only one or two individual images were recorded for every final rotational level, no error analysis was conducted for the returned DCSs and $A_{q+}^{\{2\}}(\theta)$ moments.

Table 3.3: Number of Legendre polynomials used to fit experimental scattering images for the prepared NO(A) $N = 1$ with Ne.

N'	DCS	$A_0^{\{2\}}(\theta)$	$A_{1+}^{\{2\}}(\theta)$	$A_{2+}^{\{2\}}(\theta)$
0	19	-	-	-
2	12	-	-	-
3	20	9	4	8
4	17	9	4	8
5	22	7	4	9
6	19	8	4	10
7	16	9	4	9
8	13	10	4	10
9	10	10	4	9
10	7	9	4	8

Table 3.4: Number of Legendre polynomials used to fit experimental scattering images for the prepared NO(A) $N = 2$ with Ne.

N'	DCS	$A_0^{\{2\}}(\theta)$	$A_{1+}^{\{2\}}(\theta)$	$A_{2+}^{\{2\}}(\theta)$
0	15	-	-	-
1	13	-	-	-
3	14	9	4	9
4	15	8	4	8
5	21	8	4	8
6	17	9	4	7
7	17	9	4	9
8	13	7	4	9
9	11	7	4	8
10	8	9	4	7

3.4.3 Calculations

The HIBRIDON suite of codes[98] were used to perform QS calculations of the DCS and rotational alignment moments by Dr T. R. Sharples. The *ab initio* PES calculated by Cybulski and Fernández[150] was used to perform QS calculations with NO(A) in the initial rotational levels $N = 1$, $j = 1.5$ and $N = 2$, $j = 1.5$ at a single collision energy of 523 cm^{-1}. As the NO(A) prepared in $N = 1$ is actually a combination of $j = 0.5$ and 1.5, a more complete set of calculations would have involved the additional calculation for initial rotational level $N = 1$, $j = 0.5$ which would be averaged with the results for $N = 1$, $j = 1.5$. Additionally, the calculations were performed at a single energy, whereas a more complete set of calculations would involve the averaging of the results over the full collision energy range of the experiment. DCSs for each N' final rotational level were obtained from the sum of the two calculated $j' = N' \pm 0.5$ states and the rotational alignment moments were obtained from a DCS weighted average of the two $j' = N' \pm 0.5$ states. NO(A) was treated as a rigid rotor with rotational constants $B = 1.9869$ cm^{-1} and $\gamma = -0.0027$ cm^{-1}.[143] Calculations were performed up to values of total angular momentum, $J_{tot} = 600.5$, with a basis of rotational states up to $N = 29$ and numerical propagation from 3 to 300 Bohr.

3.4.4 Results and Discussion

A typical CMB experiment involves the use of collisional cooling of molecules in a molecular beam to generate a narrow range of rotational levels. Typically, this leads to the lowest energy level being the most populated, and measurements using higher-energy initial states are very rare. Both the hexapole state selector used by Brouard and co-workers and the Stark decelerator used by van de Meerakker and co-workers prepare NO(X) in the higher-energy Λ-doublet of $j = 0.5$, although this is only 0.01 cm^{-1} higher than the lower-energy Λ-doublet. Drabbles *et al*. used stimulated emission pumping to generate a sample of NO(X) in the vibrational level $v = 20$, from which the integral cross sections were measured for the rotationally inelastic collisions with Ne.[49] Dixit *et al*. used a photoinitiated reaction between $O(^1D)$ and N_2O to generate a vibrationally excited, $v = 5$ sample of NO(X), and measured the DCS for the rotationally inelastic collisions

with Ar, and compared the results to the collisions of NO(X, v = 0).[158] However, in all of these measurements, the molecules were still prepared primarily in the lowest rotational levels. Ziegler *et al*. provide a rare experiment with a rotationally excited precursor, in which $Na_2(X^1\Sigma_g^+)$, was prepared in the vibrational level v = 31 and rotational levels j = 5 and 7, for which DCSs were measured for the collisions with Ne, and the results used to test an *ab initio* PES for the Na_2(v = 31) + Ne system.[159] The preparation of NO(A) through the optical pumping method used in this experiment provides an extremely simple method to generate a well-defined rotationally excited precursor.

The kinematics of the collisions of rotationally excited NO(A) with Ne are identical to the collisions of non-rotating NO(A), and so the low-collision energy Newton diagram displayed in Figure 3.15 is also applicable to these velocity map images. The amount of energy transferred is subtly different for the production of a given final rotational level from the different initial rotational levels, meaning that the projected Newton spheres are slightly differently sizes. However, this is a very minor effect, as the difference in internal energy between the three initial rotational levels are so similar (E_{rot} = 0 cm^{-1}, 4 cm^{-1} and 12 cm^{-1} for N = 0, 1 and 2 respectively), compared to the collision energy of 523 cm^{-1}. Example experimental and fitted images are presented in Figures 3.25 and 3.27, and the results of the fitting procedure are compared to quantum scattering calculations in Figures 3.26 and 3.28, for initial states N = 1 and 2, respectively.

The structures of the DCS for the N = 1 and 2 initial states are broadly similar to those of N = 0, in that there is a glory-like forward scattered peak, attributable to scattering through the attractive region of the PES, and either one or multiple higher-angle rotational rainbow peaks, from scattering in the repulsive region. Forward scattered peaks can be seen in the QS DCSs for some of the lowest N' final states. These peaks are considerably sharper than the forward scattered peaks observed throughout this chapter, and appear to be part of an interference pattern. As the PES does not have a significant attractive region, the interference must come from purely repulsive trajectories, and are probably from Fraunhofer-type interferences.[20] Otherwise, the forward-scattered peak is absent from the QS DCSs, similarly to the collisions of non-rotating NO(A) with Ne. With the exception of the forward scattered peak, the experimental and QS DCSs show clear agreement, especially with the location of the rotational rainbow peaks, which appears at very similar

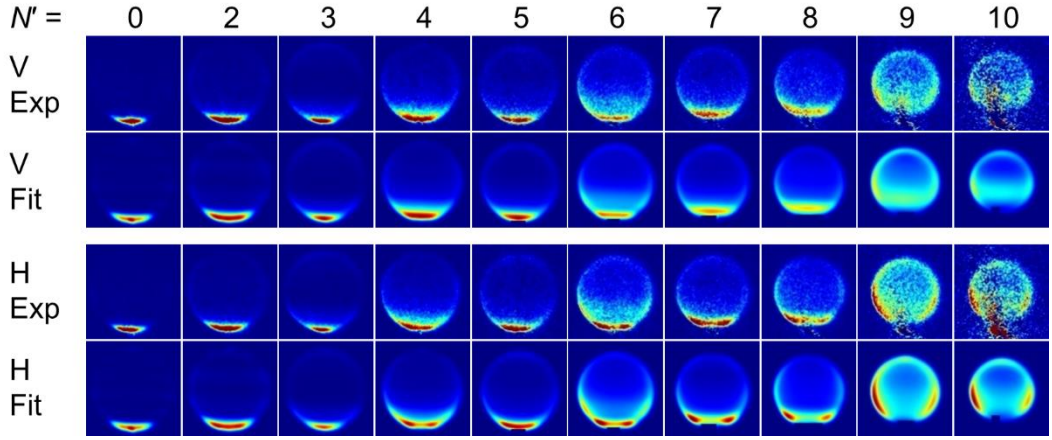

Figure 3.25: Experimental and fitted V and H images for inelastic collisions of NO(A) N = 1 with Ne, at a mean collision energy of 523 cm^{-1}, with final rotational levels N' = 0, 2-10 for a single acquisition.

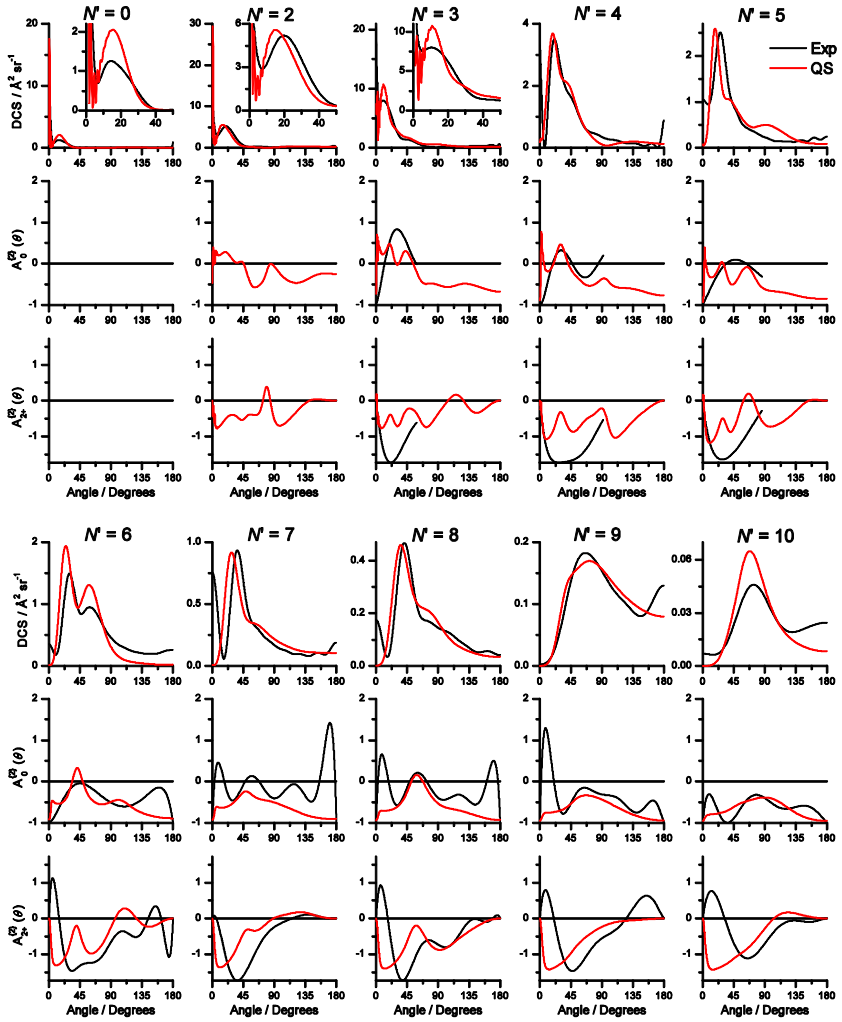

Figure 3.26: DCSs and $A_{q+}^{\{2\}}$ alignment moments for inelastic collisions of NO(A) N = 1, N' = 0, 2-10 with Ne at a mean collision energy of 523 cm^{-1}, fitted to the experimental data (black) and from QS calculations (red).

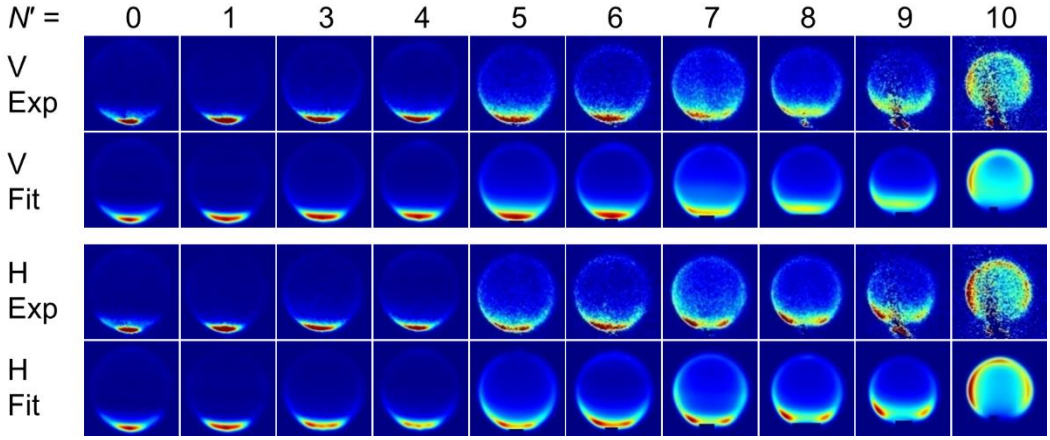

Figure 3.27: Experimental and fitted V and H images for inelastic collisions of NO(A) N = 2 with Ne, at a mean collision energy of 523 cm^{-1}, with final rotational levels N' = 0, 1, 3-10 for a single acquisition.

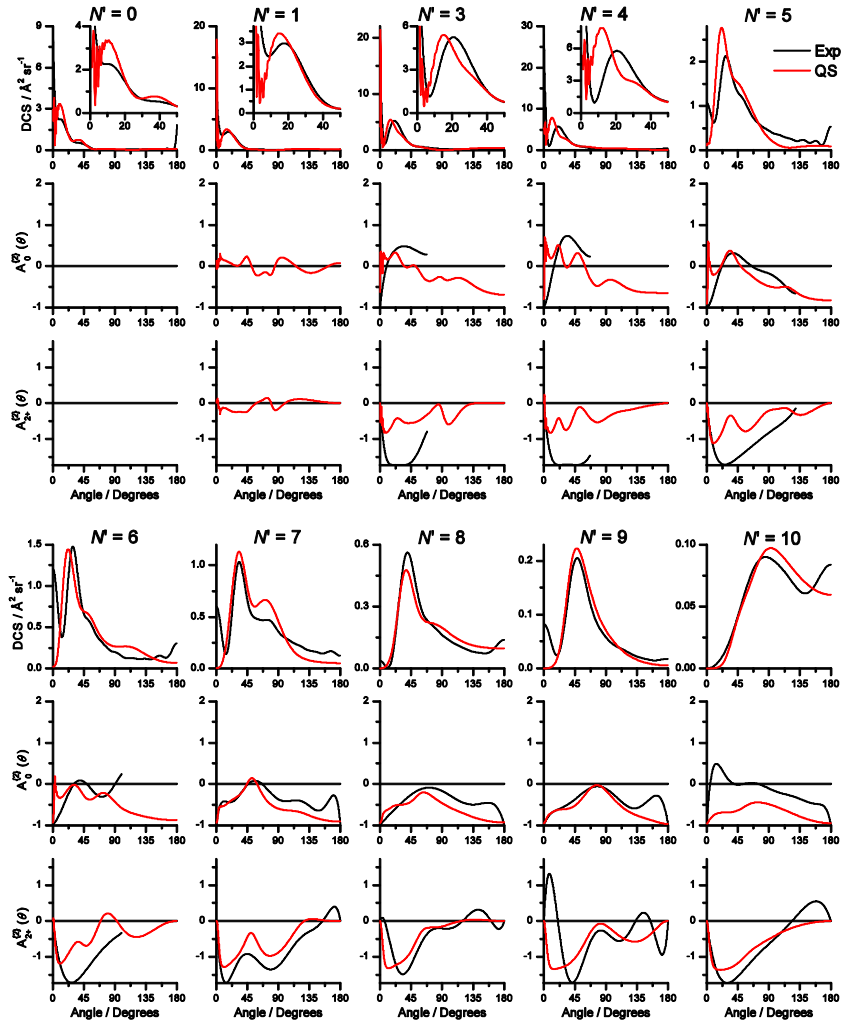

Figure 3.28: DCSs and $A_{q+}^{\{2\}}$ alignment moments for inelastic collisions of NO(A) N = 2, N' = 0, 1, 3-10 with Ne at a mean collision energy of 523 cm^{-1}, fitted to the experimental data (black) and from QS calculations (red).

angles both in the experimental and theoretical DCSs. The $A_{q+}^{\{2\}}(\theta)$ moments also show a good level of agreement between the experimental and theoretical values, and are clearly not consistent with the hard-shell KA model.

The experimental V + H images for the collisions of NO(A) N = 0-2 are compared to each other in Figure 3.29, and the area-normalised DCSs in Figure 3.30. The trends in the DCSs show clear parity effects, where parity conserving (ΔN = even) and parity changing (ΔN = odd) transitions lead to distinct features in the DCS as a result of the transitions probing different moments of the PES (see Section 3.3.6). This leads to the DCSs for a given final rotational level being similar for transitions from N = 0 and 2, while there are considerable differences in the DCS for transitions from N = 1. These parity effects are particularly evident for the final rotational levels N' = 4-7, where the first rotational rainbow peak occurs at a similar angle in the DCS across all three initial states, but a second rotational rainbow peak at a higher angle can be seen only in product states in which the parity of the NO(A) is changed. This is the inverse of the effects seen by Eyles *et al*., who observed multiple rotational rainbow peaks in the DCSs of parity conserving collisions of NO(X) with Ar, and single rotational rainbow peaks for parity changing collisions.[22] A second parity effect is observed in the highly rotationally excited product states, N' = 9 and 10. The DCSs for the preparation of these states exhibit a single rotational rainbow peak, which occurs at a smaller angle, and is considerably sharper in the parity changing transitions than parity conserving transitions. The parity-dependent trends are broken in N' = 8, where the DCSs are much similar for N = 1 and 2, and different for N = 0.

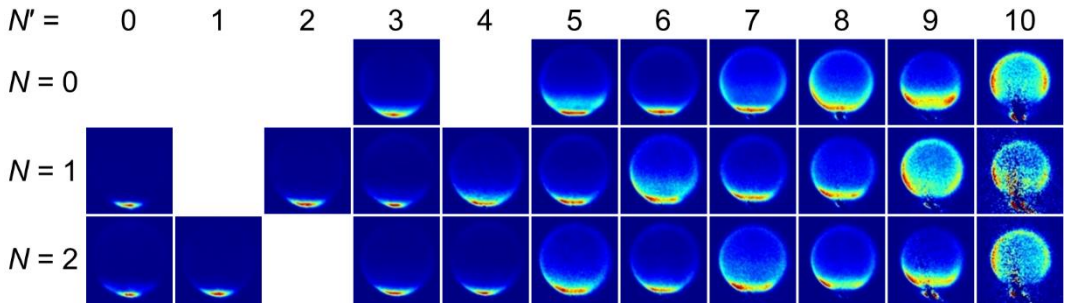

Figure 3.29: V + H experimental velocity map images for inelastic collisions of NO(A) N = 0-2, N' = 0-10 with Ne at a mean collision energy of 523 cm^{-1}, averaged across all individual acquisitions.

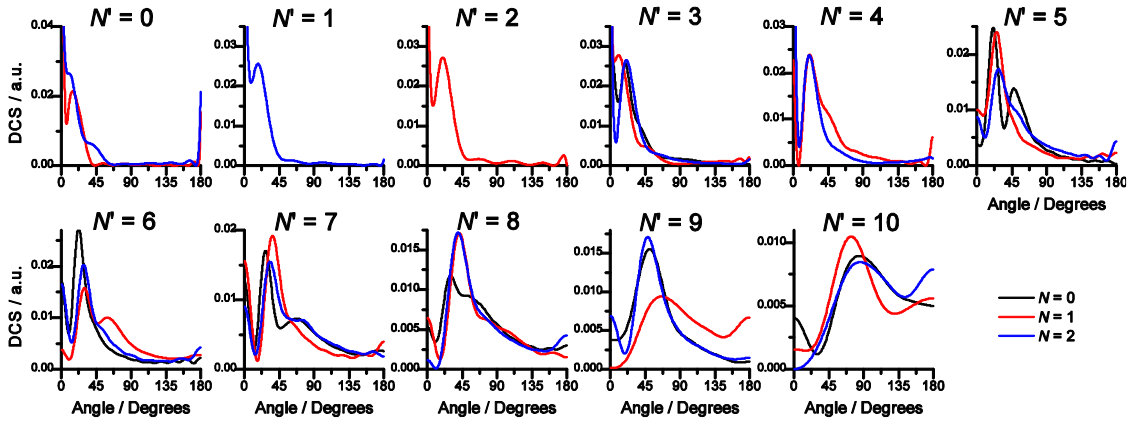

Figure 3.30: DCSs for the collisions of NO(A) Ne at a mean collision energy of 523 cm^{-1}, fitted to experimental images, with initial states N = 0 (black), 1 (red) and 2 (blue) and product states N' = 0-10. All DCSs have been normalised, such that the integral of the DCS (not the integral cross section) is equal to one to aid comparisons.

A possible concern with these measurements is that the linearly polarised preparation laser beam has generated an initial alignment of the NO(A), corresponding to rotation in a particular plane, relative to **k**. This would result in collisions occurring which preferentially sample either end-on or side-on collisions, which would result in a significant change in the collision dynamics, and with it, the measured values of the DCS and $A_{q+}^{\{2\}}(\theta)$ moments. While this would certainly be an interesting element to investigate (it is similar, but not identical, to the bond axis orientation measurements made by Brouard and co-workers[30,117]), it was not considered in the analysis, and so the effect would not be correctly accounted for in the results. This was not a concern with the preparation of NO(A, N = 0, j = 0.5) as there are only two possible m states, and so generating an alignment is not possible. However, it is possible to generate such an alignment in the preparation of NO(A, N = 1, j = 0.5, 1.5) and NO(A, N = 2, j = 1.5). The preparation of N = 1 involves the excitation through a mixed Q and R branch transition, which have orthogonal transition dipole moments,[58] which would reduce but not eliminate any generated alignment. Additionally, the high fluence of the preparation laser beam would cause the transitions to be strongly saturated, greatly reducing the magnitude of any prepared alignment. Any alignment which was generated would be substantially reduced by hyperfine depolarisation, which would lead to a precession of the rotational angular momentum. As the collisions occur at random times over the 400 ns between the preparation and probe laser pulses, which is slow compared to the precession timescale, a time-averaged depolarisation of the initial alignment would be observed, similar to the effect observed for the rotational alignment of the final N' (see Section 2.10.2). This

combination of factors all act to reduce the magnitude of the prepared alignment, and so it seems extremely unlikely that this would be a concern.

While it seems unlikely that the preparation step did generate an aligned sample of NO(A), it was tested for the final rotational levels where two sets of individual images were acquired. Of these, one individual image was acquired with the preparation laser pulse vertically polarised, and the other with it horizontally polarised. The two sets of images were analysed independently, with the resulting DCSs compared in Figures 3.31 and 3.32. Any differences in the two sets of DCSs would be evidence of a prepared alignment. However, there is generally a good agreement between the DCSs obtained using the V and H polarised preparation laser beam, which confirms that there is not any significant rotational alignment of the NO(A) prior to the collision.

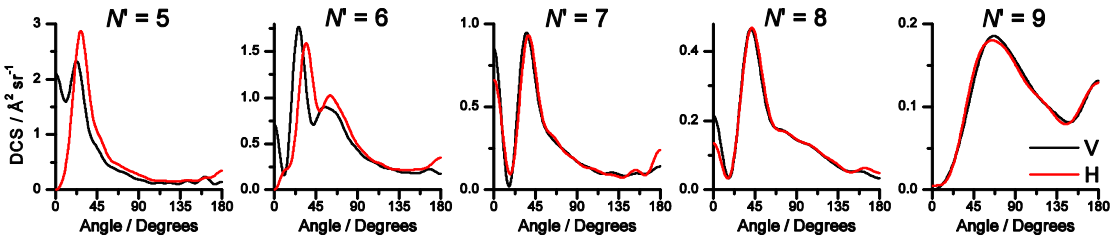

Figure 3.31: Experimental DCSs acquired for the collisions of NO(A) $N = 1$, $N' = 5$-9, with Ne at 523 cm^{-1} with the preparation laser polarised vertically (black) and horizontally (red).

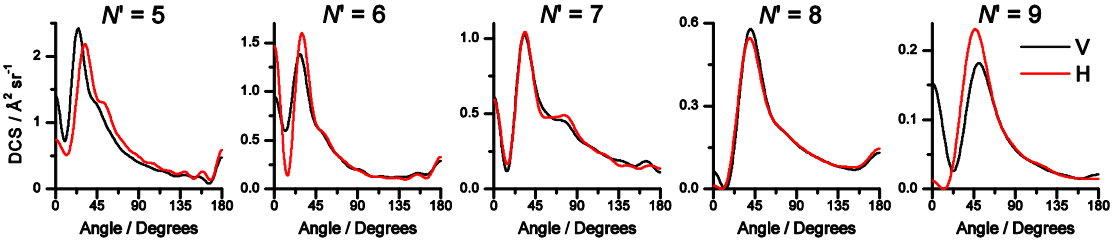

Figure 3.32: Experimental DCSs acquired for the collisions of NO(A) $N = 2$, $N' = 5$-9, with Ne at 523 cm^{-1}, with the preparation laser polarised vertically (black) and horizontally (red).

3.5 A Comparison of the Stereodynamics for Collisions of NO($A^2\Sigma^+$) with Ar and Ne

Comparisons of the experimental DCSs for the collisions of NO(A) with Ar and Ne are made in Figure 3.33. As has been described throughout this chapter, the structure of the DCSs is broadly similar in both collision systems, with a peak at 0°, resulting from scattering through the attractive region of the PES, and one or more rotational rainbow peaks at higher angles, resulting from scattering from the repulsive region of the PES. Because different basis sets were used to extract the DCSs for the two systems, the intensity of the forward scattered peak cannot be compared quantitatively. However, a visual inspection of the experimental images in Figures 3.3 and 3.16 show that the forward scattered peak dominates the NO(A) + Ar images, while it is much smaller in comparison to the higher-angle features in the NO(A) + Ne images. This difference is most likely a result of the deeper and more anisotropic attractive well present on the NO(A)-Ar PES, which has a depth of -70 cm^{-1}. The depth of the attractive region for the NO(A)-Ne PES is unknown, as there are clearly inaccuracies in this region of both *ab initio* PESs for the NO(A) + Ne system. The rotational rainbow peaks appear at consistently smaller angles in the NO(A) + Ar DCSs. This difference could either be caused by the different kinematics of the two scattering systems, or differences in the anisotropy of the repulsive regions of the two PESs. Figure 3.6 shows that both the kinematics and the PES used in the QS calculations contribute to the smaller rotational rainbow angles found in the NO(A) + Ar scattering system.

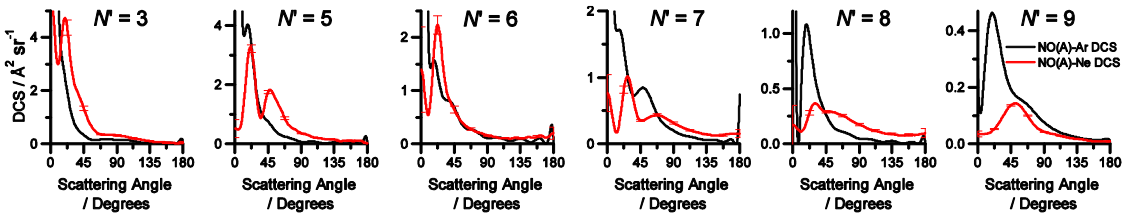

Figure 3.33: Comparison of experimental DCSs for the collisions of NO(A) with Ar at a mean collision energy of 525 cm^{-1} (black) and Ne at a mean collision energy of 523 cm^{-1} (red), for final rotational levels, N' = 3, 5-9. Error bars on the NO(A) + Ne DCS represent 95% confidence limits.

The ICSs for the different systems cannot be measured using the experimental setup in its current form. The ICSs obtained from the results of QS calculations are shown in

Figure 3.34 for the different final rotational levels probed by the experiment. These values show that the ICSs are similar for both systems, but are consistently slightly larger for the inelastic collisions of NO(A) with Ar. This is primarily the result of the attractive region of the NO(A)-Ar PES, which allows longer range inelastic scattering to occur. As the experimental results indicate that the scattering from the NO(A)-Ne attractive region has been underestimated in the QS calculations, it is expected that the actual value for the ICS in the NO(A) + Ne system will be slightly higher than the ones presented here. Interestingly, while the ICSs for the two scattering systems are similar, the signal levels obtained experimentally for the NO(A) + Ar collisions were found to be about half of those with Ne for a given quantum state, under the same conditions (although no quantitative measurements of this difference were made). The reason for this counterintuitive observation is unclear, but the most likely explanation is that the expansion conditions of the molecular beams leads to a lower density of the Ar molecular beam than the Ne beam in the crossing region of the experiment. A similar effect was observed for NO seeded in molecular beams of Ar and Ne, where a much more intense signal was observed for NO seeded in Ne than Ar under the exact same conditions.

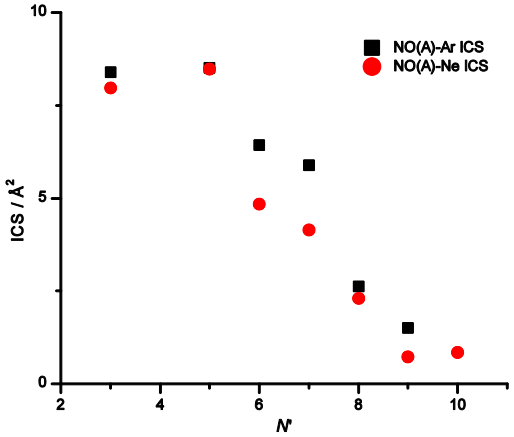

Figure 3.34: ICSs for the collisions of NO(A) with Ar, from QS calculations using the PES of Kłos *et al.*[14] at a mean collision energy of 525 cm^{-1} (black) and Ne, from QS calculations using the PES of Cybulski and Fernández[150] at a mean collision energy of 523 cm^{-1} (red).

The $A_{q+}^{\{2\}}(\theta)$ moments are shown for the collisions of NO(A) with Ar and Ne in Figures 3.11 and 3.21 respectively. Both of these scattering systems exhibit similarly sharp angle-dependent oscillations, which are not predicted by the hard-shell KA model. As was described in Section 3.3.6, the origin of these oscillations is not currently known, and will require further theoretical investigation to uncover.

3.6 Conclusions

In summary, vector correlations in the form of the DCS and rotational alignment moments have been measured for the inelastic collisions of NO(A) with Ar at a mean collision energy of 525 cm^{-1}, and Ne at mean collision energies of 523 cm^{-1} and 1,309 cm^{-1}. These experimental values were compared to the results of QS calculations performed on the PESs of Kłos *et al.*[14] for the NO(A) + Ar system, and the PESs of Pajón-Suárez *et al.*[148] and Cybulski and Fernández[150] for the NO(A) + Ne system. For both systems, sharp angle-dependent oscillations in the rotational alignment moments were observed, which closely tracked features in the DCS. The physical origin of this phenomenon is unclear, and further theoretical investigation will be required. The experimental and QS DCSs for the NO(A) + Ar collisions were generally in good agreement. There was a strong forward-scattered peak, and one or more higher angle maxima, which were shown to result from scattering from the attractive and repulsive regions of the PES respectively. A similar, but less intense forward scattered peak was observed in the NO(A) + Ne DCS, which was not reproduced by QS calculations using either literature PES, indicating that the attractive region of the NO(A)-Ne PES is modelled incorrectly in both cases. A second discrepancy in the NO(A) + Ne DCSs obtained from the results of QS calculations using both PESs is the presence of a peak in the backwards direction for the final rotational levels $N' \geq 11$ of the high-collision energy system, which do not appear in the experimental DCSs. The rotational rainbow peaks were well reproduced by QS calculations using both NO(A)-Ne PESs, but closer agreement was obtained from QS calculations using the PES of Cybulski and Fernández, indicating that the anisotropy of the repulsive region was modelled more accurately in this PES. The NO(A) + Ne DCS displayed a clear dependence on whether the parity of the NO(A) molecule was conserved or changed in the collisions. For final rotational levels within the range $N' = 5$-8, parity-changing collisions resulted in DCSs containing a second rotational rainbow peak, which was not observed in the parity-conserving DCSs. This presence of this second rotational rainbow peak was predicted by both the CF and PRRH PESs, but the position and relative intensity was poorly modelled, indicating inaccuracies in the odd order Legendre moments of both PESs.

By preparing the NO(A) through different transitions, initial rotational levels of $N = 1$ and 2 were produced, and the collisions of NO(A) in these rotational levels with Ne at a mean collision energy of 523 cm^{-1} were investigated. The parity effects observed for the collisions of NO(A) with an initial rotational level of $N = 0$ were found to also apply to these rotationally excited precursors, with multiple rotational rainbow peaks observed in the DCSs corresponding to parity changing collisions but not parity conserving collisions in the range $N' = 4$-7. For $N' = 9$ and 10, all transitions gave a single rotational rainbow peak, but this peak was sharper and appeared at a smaller scattering angle for parity changing transitions. These features lead to the structure of the DCSs for a given final state being very similar for the initial rotational levels $N = 0$ and 2, while the structure for $N = 1$ was considerably different.

Chapter 4

A Direct Comparison of Collisions of NO($A^2\Sigma^+$) with Atomic and Molecular Partners: He and D_2

4.1 Introduction

While molecule + atom inelastic collisions have been studied extensively, studies of molecule + molecule inelastic collisions are much more limited. For the molecule + molecule systems which have been examined, H_2 is a particularly appealing collision partner, as it is computationally simple to use, due to its relatively small number of electrons compared to other diatomic molecules. Furthermore, its isotopologue, D_2 has the same mass as He, allowing easy comparisons to be made between the two systems without needing to account for a change in the kinematics of the collision. CMB experiments have been conducted using H_2 or D_2 as the unobserved collider in rotational energy transfer of H_2O[160], CD_3[79] and notably ND_3,[161] for which the extracted DCS was compared to the results of QS calculations. Experiments have also been conducted by Westley *et al*. and Gijsbertsen *et al*., for the collisions of NO(X) with D_2, for which, at

the time, there was no available PES on which to run QS calculations[17,162] (although *ab initio* NO(X)-H_2 PESs have since been calculated[163,164]).

QS calculations are considerably more difficult for molecule + molecule collisions, compared to molecule-atom collisions, as a result of the higher dimensionality of these systems. Furthermore, this dimensionality also makes the PES more computationally expensive to calculate. For radical molecules such as NO, the unpaired electron needs to be accounted for in the calculation of the PES, which further increases the computational cost. NO($X^2\Pi$) has the unpaired electron in a doubly-degenerate π^* orbital, where each electron configuration has a separate PES, which must be calculated. In cases where no PES is available, all information about the system must come from experimental results.

This chapter will investigate the inelastic collisions of NO($A^2\Sigma^+$) with He and D_2. The DCS and rotational alignment moments for the He collider will be compared to the results of QS calculations using the literature PES of Kłos *et al.*[14] This comparison will test the accuracy of the PES, as was demonstrated for the NO(A)-Ar and Ne PESs in the previous chapter. These results will then be compared to those for the D_2 collision, to obtain as much information as is possible about the NO(A)-H_2 PES.

4.2 Experimental Conditions

The methods described in Chapter 2 were used for the acquisition of velocity map images, probing the inelastic collisions of NO(A) with He and D_2. The conditions of the molecular beams were carefully controlled to generate very similar collision energy distributions for the experiments with the two collision partners. For the collisions of NO(A) with He, the primary molecular beam contained 10% NO (BOC, 99.998%) seeded in Ne (BOC, 99.999%), with a backing pressure of 3 bar to give a mean speed of 807 m s^{-1} and FWHM of 57 m s^{-1}. The secondary molecular beam contained neat He (BOC, 99.999%), generated with a heated pulsed valve (343 K) and a backing pressure of 5 bar, to give a mean speed of 1,973 m s^{-1} and a FWHM of 101 m s^{-1}. For the collisions of NO(A) with D_2, the primary molecular beam contained 10% NO seeded in Ar (BOC, 99.998%), with a backing pressure of 3 bar to give a mean speed of 605 m s^{-1} and FWHM

of 52 m s^{-1}. The secondary molecular beam contained neat D_2 (BOC, 99.8%), with a backing pressure of 5 bar, to give a mean speed of 2,032 m s^{-1} and FWHM of 99 m s^{-1}. These conditions lead to Gaussian distributions of collision energies, with a mean of 670 cm^{-1} and FWHM of 64 cm^{-1} for the collisions of NO(A) with He, and a mean of 663 cm^{-1} and FWHM of 59 cm^{-1} for collisions with D_2.

The mean speeds of the NO molecular beams were determined from the location of the NO^+ beam-spots produced by non-resonant 532 + 532 nm ionisation in the background images, referenced to the zero-velocity coordinate, which was determined using the centring measurements previously described (see Section 2.5). The FWHM for the NO molecular beams was obtained from the LIF measurements described in Section 2.9. The mean beam speeds of the He and D_2 molecular beams were initially measured by seeding a trace amount (<0.01%) of NO in the He and D_2 molecular beams, and measuring the position of the resulting beam-spots, yielding mean speeds of 1,830 m s^{-1} and 1,918 m s^{-1}, respectively. However, upon analysis of the scattering images using these mean speeds, it was found that there were systematic residuals for the fitted images consistent with a significant underestimation of the He and D_2 molecular beam speeds. This discrepancy was most likely caused by "velocity slip", an effect which led to the relatively heavy NO molecules moving at a slightly slower speed than the relatively light He atoms and D_2 molecules in the molecular beams.[23] No LIF measurements of the FWHM of the He and D_2 beams were made. In order to determine the mean speeds and FWHM of the He and D_2 beams, iterative fits were performed on the experimental images, optimising the values independently for each quantum state of each system, with average values reported above.

For both scattering systems, the preparation laser was tuned to the peak of the $Q_1(0.5)$ transition of the (0,0) band of the NO (A ← X) spectrum, with a fluence of 0.65 mJ cm^{-2} and a laser beam diameter of 2 mm. The probe laser was scanned over the relevant transition of the R branch of the (0,0) band of the NO(E ← A) spectrum, with a fluence of 0.65 μJ cm^{-2} and a beam diameter of 3 mm. The fluence of the ionisation laser beams was varied in the range 4-40 mJ cm^{-2}, with beam diameters of 3 mm.

Velocity map images were acquired for final rotational levels $N' = 3$, 5-12 for both collisions of NO(A) with He and with D_2. For both systems, a total of four individual

images were acquired for each final rotational level, except $N' = 12$ of both systems, for which eight individual images were acquired, to compensate for low signal-to-noise levels. Each individual image consisted of 56,000 individual camera shots across all V, H, signal and background frames, recorded using five scans of the probe laser over the transition, and with 200 individual camera shots acquired in every frame.

The rotational state distribution of the D_2 molecular beam was investigated using (3 + 1) REMPI via the $B'^1\Sigma_u^+$ state.[165] With a molecular beam under the same conditions as the one used in the CMB experiment, D_2 was ionised by a Nd-YAG pumped dye laser. The laser was scanned over the range 267-268 nm, and the resulting D_2^+ ions were velocity mapped onto the detector, and the signal levels were measured using the avalanche photodiode. The spectrum, displayed in Figure 4.1 clearly shows lines relating to the different transitions, however, mainly as a result of the four-photon ionisation process, the signal-to-noise levels are poor. To obtain a more reliable distribution of intensities, the laser was tuned to the peak of each of the R-branch transitions in turn, and velocity map images were recorded over 5,000 laser shots, with interleaved signal and background frames. Using this method, the relative signal intensities for the R(0), R(1) and R(2) transitions were found to be 0.682, 0.257 and 0.061 respectively. Because there was no detailed analysis of the rotational linestrengths of this (3 + 1) REMPI process, it was not possible to convert this distribution of intensities into a relative population distribution of the rotational levels. However, it does provide good evidence that the D_2 in the molecular beam is efficiently cooled, and is almost entirely in the lowest three rotational levels.

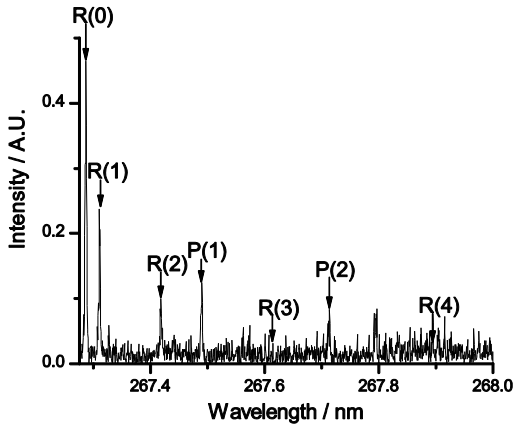

Figure 4.1: (3 + 1) REMPI spectrum of the (0,0) band of the $D_2(B' \leftarrow X)$ with transitions labelled.

Because ^{2}D is a $I = 1$ boson, the total wavefunction of D_2 must be symmetric with respect to rotation.[12] The rotational component of the wavefunction is symmetric for even-j rotational levels and is antisymmetric for odd-j rotational levels. The nuclear wavefunction is symmetric for ortho states, and is antisymmetric for para states. Therefore, the even-j rotational levels will pair with ortho nuclear spin states, and odd-j rotational levels will pair with para nuclear spin states to obtain the required symmetric total wavefunctions. For D_2, the ratio of ortho to para nuclear spin states is 2:1 at room temperature.[12] The observed intensities of the R(0) and R(1) transitions in the spectrum of D_2 in the molecular beam are broadly consistent with this ratio.

4.3 Data Analysis

The scattering images obtained for the inelastic collisions of NO(A) with He and D_2 were analysed using the fitting routine outlined in Section 2.10 to obtain the experimental DCSs and rotational alignment moments. D_2 was treated as if it were an atom, with basis images were only simulated for collisions which were elastic in D_2 rotation. For each final NO(A) rotational level, four separate sets of V and H images were independently analysed. These were the four individual images for all final rotational levels, except for $N' = 12$ for both He and D_2 colliders, for which each analysed V and H image was the sum of two individual images, to compensate for the lower signal levels for the high-N' states. The mean and standard error for the DCSs and rotational alignment moments were obtained from these four independent fits.

The DCSs and rotational alignment moments for both scattering systems were extracted using Legendre moments in the $x = \cos(\theta)$ basis set. The number of Legendre moments used to extract the DCS and rotational alignment moments was optimised independently for each final rotational level, as shown in Tables 4.1 and 4.2. The DCS was constrained to remain positive and the rotational alignment moments were constrained to lie within their classical limits at all angles, but additional constraints to fix the values of the rotational alignment moments at 0° and 180° were not applied.

Table 4.1: Number of Legendre polynomials used to fit the NO(A) + He images.

N'	DCS	$A_0^{\{2\}}(\theta)$	$A_{1+}^{\{2\}}(\theta)$	$A_{2+}^{\{2\}}(\theta)$
3	15	7	5	6
5	12	7	7	7
6	16	8	7	7
7	11	10	8	7
8	9	9	7	7
9	8	8	6	9
10	9	8	5	7
11	9	6	6	8
12	8	6	5	7

Table 4.2: Number of Legendre polynomials used to fit the NO(A) + D_2 images.

N'	DCS	$A_0^{\{2\}}(\theta)$	$A_{1+}^{\{2\}}(\theta)$	$A_{2+}^{\{2\}}(\theta)$
3	10	5	6	6
5	12	6	6	7
6	13	7	5	6
7	14	7	5	7
8	10	7	6	8
9	9	7	6	7
10	8	7	6	8
11	10	7	5	8
12	10	7	6	7

The extracted DCSs for the NO(A) + He collisions were area normalised to the corresponding DCSs obtained from QS calculations described Section 4.4. As no QS calculations were performed for the NO(A) + D_2 DCS, these results were instead area normalised to the corresponding NO(A) + He DCS to allow for comparison between the two.

4.4 Calculations

QS calculations were performed by Dr T. R. Sharples, using the HIBRIDON suite of codes,[98] with the PES of Kłos et al.,[14] to obtain DCSs and rotational alignment moments for the collisions of NO(A) with He. The Gaussian distribution of collision energies was represented by performing 18 single-energy calculations, evenly spaced and covering a range of three standard deviations of the collision energy distribution, which were averaged with appropriate weighting. The DCS for each N' final rotational level was obtained from the sum of the $j' = N' \pm 0.5$ rotational levels, and the rotational alignment moments were obtained from a DCS-weighted average of the two $j' = N' \pm 0.5$ rotational levels. NO(A) was treated as a rigid rotor with rotational constants B = 1.9869 cm^{-1} and γ = -0.0027 cm^{-1},[143] and calculations were performed up to values of total angular momentum, J_{tot} = 200.5, with a numerical propagation from 4.6 to 200 Bohr. No QS calculations were performed for the NO(A) + D_2 collisions.

KA calculations for the NO(A) + He and D_2 systems, described in Section 3.2.3 were performed over the same range of collision energies as the QS calculations. The results were averaged appropriately for the collision energy ranges of the NO(A) + He and D_2 collisions.

4.5 Results

Figure 4.2 shows the Newton diagrams for the NO(A) + He and D_2 collision systems. While the speeds of the molecular beams are different in the two systems, the length of the relative velocity vector, **k** is the same. Because the masses of He and D_2 are identical, the kinematics of the two systems are the same, and therefore, will not contribute to differences between the systems.

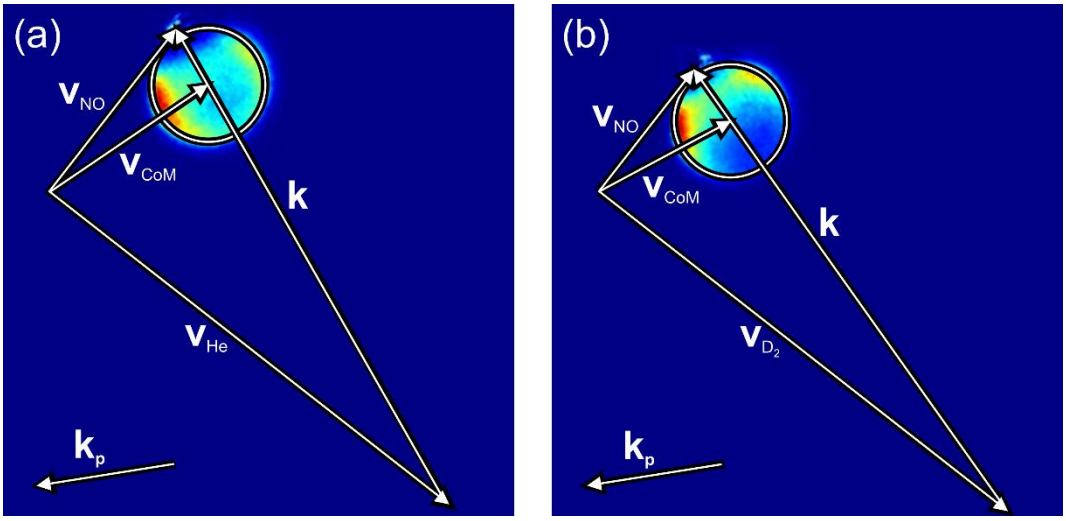

Figure 4.2: Newton diagrams for the collisions of NO(A) with (a) He and (b) D_2 for final rotational level $N' = 8$, overlaid on the experimental V + H experimental image, averaged across all data acquisitions. Arrows indicate the velocity vectors, with $\mathbf{v_{NO}}$, $\mathbf{v_{He}}$ and $\mathbf{v_{D2}}$ showing the velocity of the collider molecules, $\mathbf{v_{CoM}}$ showing the velocity of the centre of mass, and **k** showing the relative velocity vector. The circle represents the possible final velocities of NO scattered in the plane of the detector. The offset arrow $\mathbf{k_p}$ shows the propagation direction of the probe laser beam.

The V and H velocity map images combined from all acquisitions for the NO(A) + He system are shown in Figure 4.3. These images show a very smooth progression in the scattering angle distribution, from being primarily forward-scattered at low N' to being backwards scattered at high N'. The equivalent NO(A) + D_2 velocity map images are shown in Figure 4.4, and appear remarkably similar in structure to the NO(A) + He images. However, there are subtle differences, and the NO(A) + D_2 images are consistently slightly more forward-scattered than the NO(A) + He images for a given final rotational level. In both the NO(A) + He and D_2 images, there is a clear asymmetry, in which the lower-left hemisphere of the images is more intense than the upper-right hemisphere. This is not a result of kinematic blurring or a density-flux detection bias, rather it is an effect caused by the non-zero $A_{1+}^{\{2\}}(\theta)$ moment. Both the NO(A) + Ar and Ne systems in the previous chapter had $\mathbf{k}$-$\mathbf{k_p}$ angles close to 90°, which lead to an extremely low sensitivity to $A_{1+}^{\{2\}}(\theta)$ (see Equation 2.7). In contrast, the NO(A) + He and D_2 systems have $\mathbf{k}$-$\mathbf{k_p}$ angles of 61° and 67° respectively, meaning that there is significant sensitivity to $A_{1+}^{\{2\}}(\theta)$. As described in Section 2.10.1, $A_{1+}^{\{2\}}(\theta)$ manifests as a ϕ-dependent sensitivity in both the V and H images, which adds to one hemisphere of the image and subtracts from the other. The effect of the $A_0^{\{2\}}(\theta)$ and $A_{2+}^{\{2\}}(\theta)$ moments can be seen as

prominent differences in intensity between the V and H images, which is particularly large for the final rotational levels $N' \geq 8$.

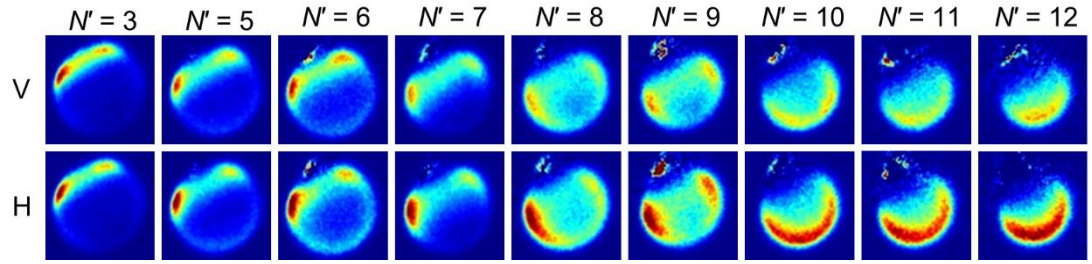

Figure 4.3: Experimental V and H velocity map images, averaged across all acquired data, for the collisions of NO(A) with He at a mean collision energy of 670 cm^{-1}, for final rotational levels N' = 3, 5-12.

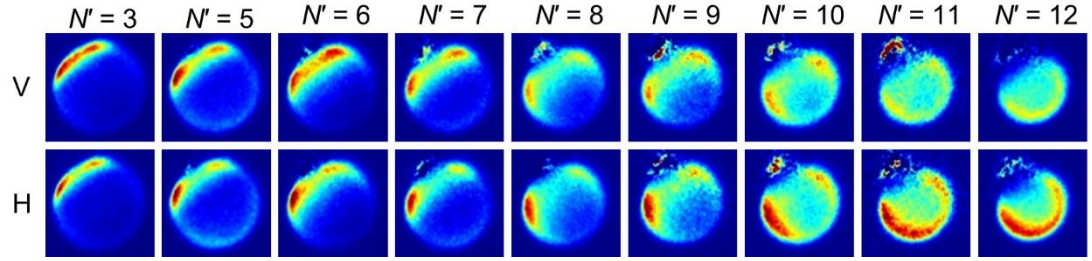

Figure 4.4: Experimental V and H velocity map images, averaged across all acquired data, for the collisions of NO(A) with D_2 at a mean collision energy of 663 cm^{-1}, for final rotational levels N' = 3, 5-12.

An example set of NO(A) + He experimental images used as inputs for the fitting routine, and the corresponding fitted images for the system, are shown in Figure 4.5. The excellent level of agreement between the experimental and fitted images indicates that the DCS and rotational alignment moments, shown in Figure 4.6, have been accurately returned by the fitting routine. The experimental DCSs show excellent, near-quantitative, agreement with the results of the QS calculations across all final rotational levels. For each final state, both the experimental and QS DCS exhibit a single rotational rainbow peak, which smoothly transitions to higher scattering angles as N' increases. The single discrepancy in the DCS is at angles greater than 135° for $N' \geq 8$, in which the QS DCS deviates from experiment, and is slightly more intense at 180°. The $A_{q+}^{\{2\}}(\theta)$ moments obtained from QS calculations closely match those obtained from hard-shell KA calculations for the lower-N' rotational levels, but the QS and KA calculations increasingly diverge as N' increases. Unlike the NO(A) + Ar and Ne systems, the $A_{q+}^{\{2\}}(\theta)$ moments obtained from QS calculations for the collisions of NO(A) with He vary

smoothly with angle, and do not exhibit any sharp scattering angle-dependent oscillations in regions where there is any intensity in the DCS. The experimental $A_0^{\{2\}}(\theta)$ and $A_{2+}^{\{2\}}(\theta)$ moments generally show a good level of agreement with those from QS calculations. For $A_{1+}^{\{2\}}(\theta)$, a similarly good level of agreement is observed in $N' = 9$ and 10, but for the other final rotational levels, the experimental $A_{1+}^{\{2\}}(\theta)$ moments are considerably larger than the results of the QS calculations.

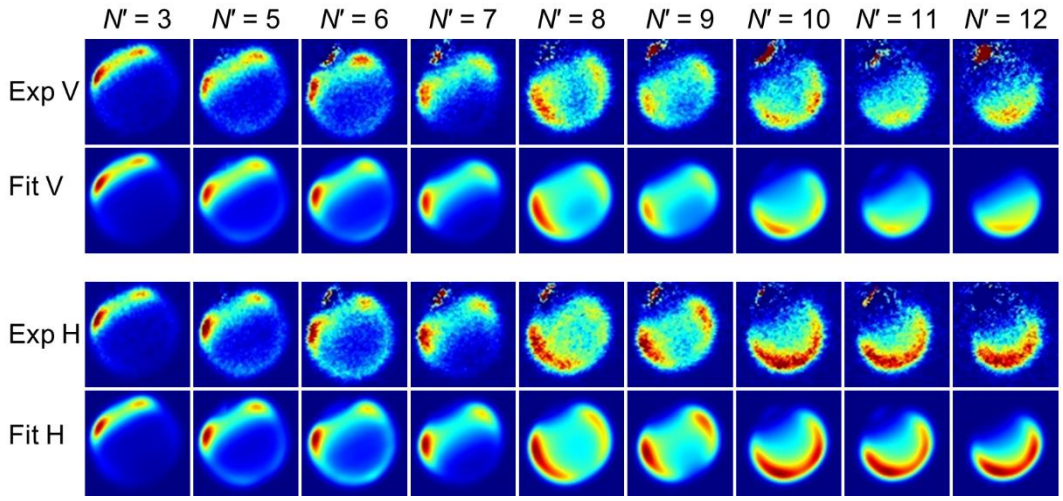

Figure 4.5: Comparison of individual V and H experimental images used as inputs for the fitting routine (Exp V/H) to corresponding images simulated from the fitting results (Fit V/H), for the inelastic collisions of NO(A) with He at a mean collision energy of 670 cm^{-1}, for final rotational levels $N' = 3$, 5-12.

Example experimental and fitted NO(A) + D_2 images are shown in Figure 4.7, with the two once again showing excellent agreement, and the DCS and rotational alignment moments obtained from the fitting routine are shown in Figure 4.8. Because no QS calculations were performed for the NO(A) + D_2 system, the experimental results are instead compared to the NO(A) + He experimental results, and for the rotational alignment moments, the results of KA calculations. As was concluded from a visual inspection of the images, the DCSs are similar for the two scattering systems, but are slightly more forward-scattered for the collisions with D_2 than He, with the rotational rainbow peaks occurring at a consistently smaller angle. The structure of the $A_{q+}^{\{2\}}(\theta)$ moments are also similar to those of the NO(A) + He system, with no sharp angle-dependent fluctuations. The $A_{1+}^{\{2\}}(\theta)$ and $A_{2+}^{\{2\}}(\theta)$ moments are generally within experimental uncertainty for the two systems across all final rotational levels. The

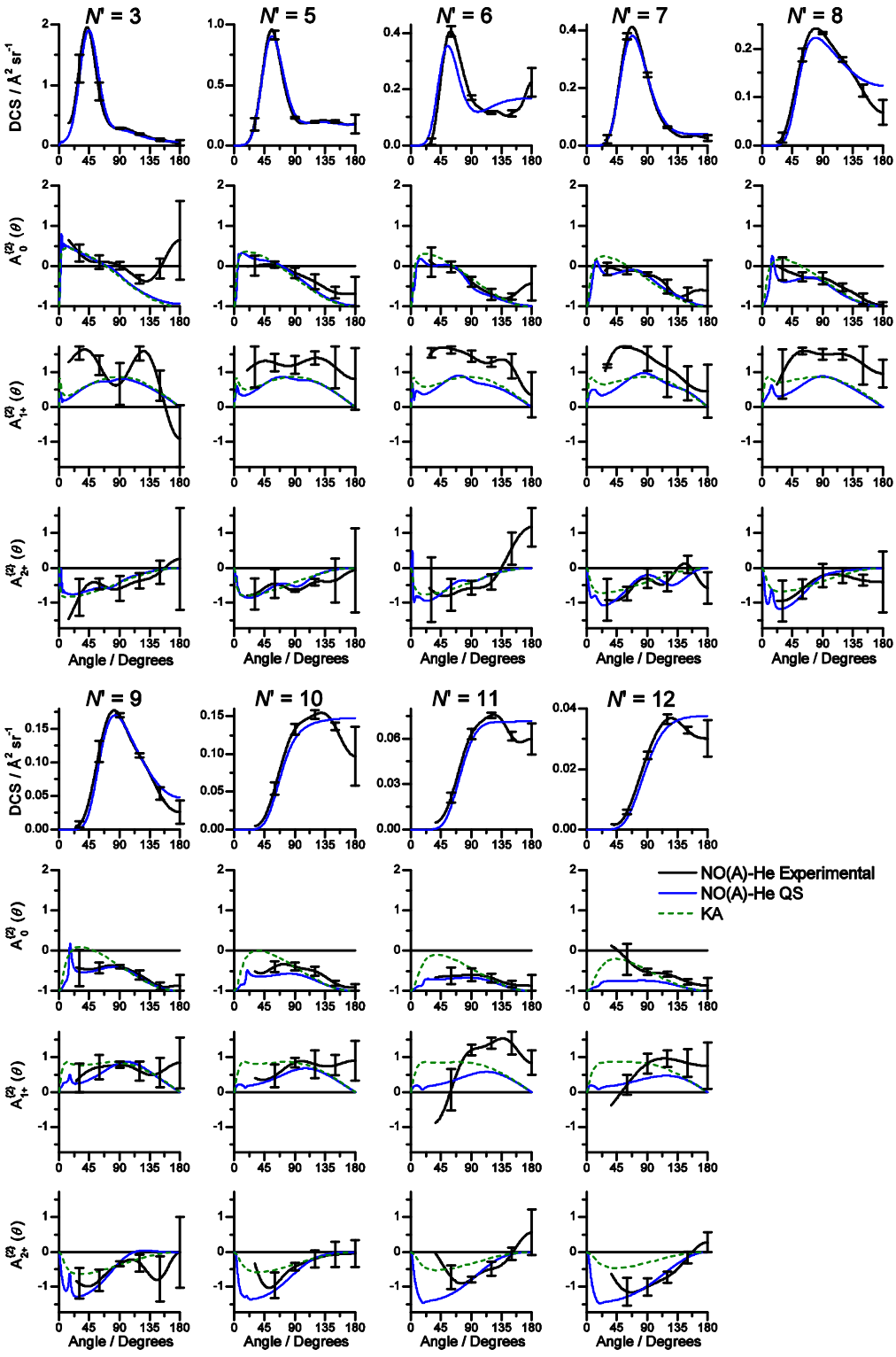

Figure 4.6: Plots showing the experimental (black) DCS and $A_{q+}^{\{2\}}(\theta)$ moments for the inelastic collisions of NO(A) with He at a mean collision energy of 670 cm^{-1}, for final rotational levels N' = 3, 5-12, compared to the results of QS calculations (blue) and, for the $A_{q+}^{\{2\}}(\theta)$ moments, the results of KA calculations (dashed green). Error bars represent 95% confidence limits for the experimental results.

$A_0^{\{2\}}(\theta)$ moments for the NO(A) + D_2 system are similar, but are consistently less negative than in the NO(A) + He system, matching more closely with the KA moments.

The plots of the experimental DCSs and rotational alignment moments have been truncated to exclude small scattering angles, which correspond to regions of the experimental images which were obscured by noise resulting from the non-resonant beam-spot (see Section 2.5). A visual inspection of both the NO(A) + He and D_2 experimental images shows that for the high-N' images, there is negligible scattering signal at these angles. This indicates that for both systems, the experimental DCS at small scattering angles tends towards zero, similar to the DCSs obtained from the QS calculations.

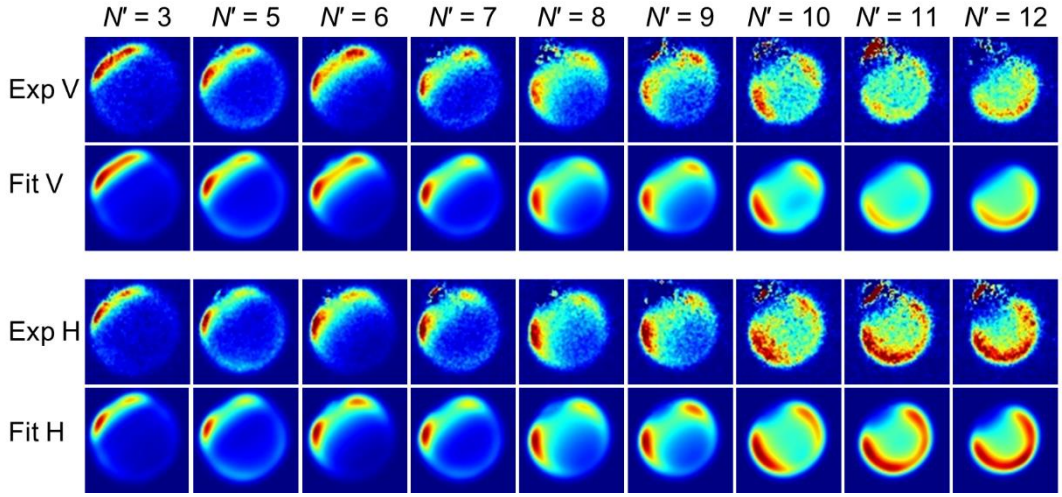

Figure 4.7: Comparison of individual V and H experimental images used as inputs for the fitting routine (Exp V/H) to corresponding images simulated from the fitting results (Fit V/H), for the inelastic collisions of NO(A) with D_2 at a mean collision energy of 663 cm^{-1}, for final rotational levels N' = 3, 5-12.

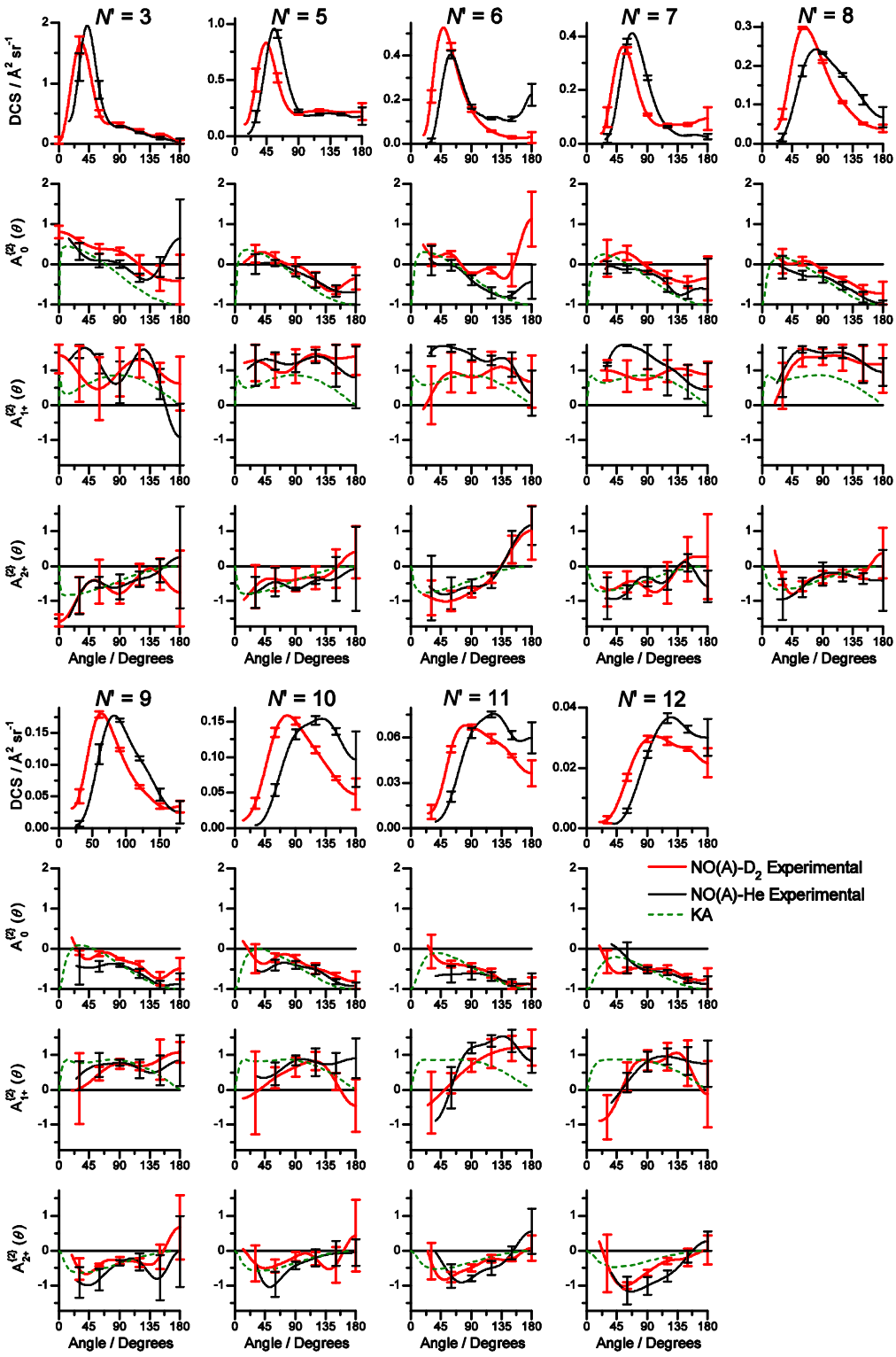

Figure 4.8: Plots showing the experimental DCS and $A_{q+}^{\{2\}}(\theta)$ moments for the inelastic collisions of NO(A) with D_2 at a mean collision energy of 663 cm^{-1} (red) for final rotational levels N' = 3, 5-12, compared to the experimental values for the collisions of NO(A) with He at 670 cm^{-1} (black) and, for the $A_{q+}^{\{2\}}(\theta)$ moments, the results of KA calculations (dashed green). Error bars represent 95% confidence limits for the NO(A) + He and D_2 experimental results.

4.6 Discussion

The NO(A) + He inelastic scattering system was previously investigated using a crossed molecular beam experiment by Kay *et al*.[45] This experiment had a much lower signal-to-noise ratio than the one presented in this chapter, and was not sensitive to the polarisation of the product rotational angular momentum. For the limited number of final rotational levels which were investigated, there was reasonable qualitative agreement with the results of QS calculations performed using the *ab initio* PES of Kłos *et al*.[14] For the NO(A) + He measurements presented in this chapter, the superior signal to noise levels of the scattering images, wider range of final rotational levels, and investigation of the product rotational alignment, make it a much more stringent test of the PES of Kłos *et al*. than the previous study.

The excellent agreement between the experimental and QS DCS for the collisions of NO(A) with He indicates that the *ab initio* PES calculated by Kłos *et al*., which was used in the QS calculations, is highly accurate. There is a small disagreement between the experimental and theoretical DCSs, which occurs at angles close to 180° for final rotational levels $N' \geq 8$. This suggests that there is a subtle inaccuracy in the region of the PES probed by low-impact parameter collisions, which lead to scattering at large angles. The absence of a forward-scattered peak in the DCS indicates that the PES lacks an attractive well that is significantly deep and anisotropic to cause significant inelastic scattering. This is consistent with the structure of the *ab initio* PES, for which the attractive region reaches a maximum depth of -0.8 cm^{-1}, and is only slightly anisotropic.[14] However, it is not clear whether an attractive well with a similar depth and anisotropy to the NO(A)-Ar PES would lead to significant scattering for the NO(A) + He system. He is much lighter than Ne and Ar, and so would require much more anisotropy in the PES to exert the same amount of torque on the NO(A) molecule. This could be tested by performing QS calculations on the NO(A)-Ar PES, with the NO(A) + He kinematics.

The experimental $A_0^{\{2\}}(\theta)$ and $A_{2+}^{\{2\}}(\theta)$ moments for the NO(A) + He system are in close agreement with the results of the QS calculations, with areas of disagreement typically limited to angles with low intensity in the DCS, and as such, a limited sensitivity to the rotational alignment moments. The similarity between the experimental and

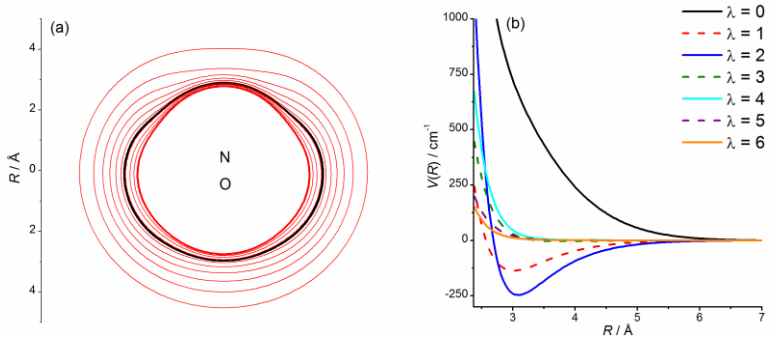

Figure 4.9: The NO(A)-He potential energy surface, calculated by Klos *et al.*[14] (a) Contour plot, with red representing positive (repulsive) energy in steps of 100 cm^{-1}, black represents the mean collision energy of 670 cm^{-1} for the NO(A) + He scattering system. (b) Legendre moments of the potential energy surface.

theoretical moments provides further support for the accuracy of the *ab initio* PES. For $N' \geq 9$, where the $A_0^{\{2\}}(\theta)$ and $A_{2+}^{\{2\}}(\theta)$ moments obtained from the results of QS and KA calculations diverge, the experimental results much more closely follow the values predicted by the QS calculations. As with the NO(A) + Ar and Ne systems, the breakdown of the KA model for the NO(A) + He system is most likely caused by the shallow repulsive region of the PES, which leads to effects which cannot be accounted for by a model with a purely hard-shell potential.

The agreement between experiment and theory is much poorer for $A_{1+}^{\{2\}}(\theta)$, where the QS moment is typically much smaller in magnitude than the experimental value. The exceptions to this are for $N' = 9$ and 10, where the experimental and theoretical values are within experimental uncertainty. Because of the excellent agreement between the experimental and theoretical values of the other $A_{q+}^{\{2\}}(\theta)$ moments, this discrepancy seems much more likely to be caused by an experimental artefact than a deficiency of the PES. Unlike the other systems described in this thesis, the NO(A) + He and D_2 images are sensitive to $A_{1+}^{\{2\}}(\theta)$, due to their respective **k-k$_P$** angles of 67° and 61°. The sensitivity factor for $A_{1+}^{\{2\}}(\theta)$ is similar to $A_{2+}^{\{2\}}(\theta)$, and so the absolute sensitivity of the experiment to the moment is not an issue. However, while both $A_0^{\{2\}}(\theta)$ and $A_{2+}^{\{2\}}(\theta)$ lead to differences in intensity between the V and H images, the sole effect of $A_{1+}^{\{2\}}(\theta)$ is an asymmetry in amplitude about **k**, which affects both the V and H images equally. $A_{1+}^{\{2\}}(\theta)$

will therefore be considerably more strongly influnced than the other two moments by subtle experimental artefacts, which have not been accounted for in the analysis. In these experiments, the probe laser was always scanned over the Doppler profile of the transition in the same direction, meaning that the scattering image will fill in from the left side to the right side (see Figure 2.7). Thus, a gradual decrease in the scattering signal over the course of an experiment, would lead to a systematic bias towards more intensity in the left side of the image, which is consistent with an overestimation of $A_{1+}^{\{2\}}(\theta)$. Such a drop in signal could be caused by the fluence of one of the laser beams dropping or the wavelength of the preparation laser changing. A simple test for this effect would involve reversing the direction in which the wavelength of the probe laser was scanned, thus filling in the right side of the image first. If a gradual decrease in signal was the cause of the problem, the value of $A_{1+}^{\{2\}}(\theta)$ would be systematically underestimated instead. At the time of writing, the only other reported measurement of $A_{1+}^{\{2\}}(\theta)$ in a CMB experiment is for collisions of CO($X^1\Sigma^+$) with He, by Song *et al*., who reported an experimental $A_{1+}^{\{2\}}(\theta)$ moment which was considerably lower than the theoretical moment, across a range of final rotational levels.[77] It seems plausible that the accurate measurement of $A_{1+}^{\{2\}}(\theta)$ requires much greater experimental stability than is needed for the other rotational alignment moments, although more experiments will be required to confirm this.

As described in Chapter 2, there are physical constraints on the values of the rotational alignment moments, at 0° and 180°, including that $A_0^{\{2\}}(\theta)$ must take its negative limiting value, which classically is -1. This has been a recurring problem in similar measurements of the rotational alignment for the NO(X) + Ar and Kr inelastic collisions, where the measured values of $A_0^{\{2\}}(\theta)$ at 180° were significantly less negative than the real value of -1.[27,28,133] This was postulated to be the result of depolarisation of the rotational angular momentum, either by multiple collisions, or stray magnetic fields. As can be seen for the final rotational levels $N' \geq 10$, for both He and D_2 colliders, where there is a large intensity in the DCS at 180°, the values of $A_0^{\{2\}}(\theta)$ consistently reach -1 at 180°, indicating that these measurements do not suffer from the same problem.

The results for the NO(A) + D_2 system provide insight into structure of the NO(A)-D_2 PES. The fact that the kinematics for the NO(A) + He and D_2 scattering systems are the same means that any differences between the two must arise solely from differences in the PESs. The general similarity of the results for the collisions of NO(A) with D_2 to those with He indicates that the PESs for the two systems are similar, and the NO(A)-He PES of Kłos *et al*., used in the QS calculations, can serve as a good starting point for the NO(A)-D_2 PES. The observation that the rotational rainbows in the NO(A) + D_2 DCSs appear at a slightly lower scattering angle than NO(A) + He indicates that the repulsive regions of the NO(A)-D_2 PES probed by these inelastic collisions are more anisotropic than equivalent regions in the NO(A)-He PES. As H_2 has a larger polarizability than He ($\alpha = 0.911 \times 10^{-40}$ and 0.22×10^{-40} J^{-1} C^2 m^2 for H_2 and He respectively),[13] it would be expected that the attractive region for the NO(A)-D_2 PES would be significantly deeper than in the NO(A)-He PES. However, no distinct forward-scattered peak, which could be attributed to scattering through the attractive region, was observed in the NO(A) + D_2 DCSs, which means that these measurements are not sensitive to features in the attractive region of the PES. Lower-N' final NO(A) rotational levels are more sensitive to the attractive region of the PES than the higher-N' states investigated here, and so measurements of the DCS for $N' = 1$ and 2 could potentially probe this feature. The less-negative values of $A_0^{\{2\}}(\theta)$ for the NO(A) + D_2 scattering system bring the values more into line with the hard-shell KA model. However, it seems unlikely that this is a result of the NO(A)-D_2 PES being more hard-shell-like, given that the polarizability of H_2 is larger than that of He.

The above inferences have provided information about the nature of the NO(A)-D_2 PES, however, they implicitly assume that the PES is isotropic with respect to the orientation of the D_2 molecule, as is the case for the He atom. In reality, the NO(A)-D_2 PES has additional degrees of freedom, notably including the variation of the PES based on the orientation of the D_2 molecule with respect to NO(A). Just as anisotropy in the PES with respect to NO(A) leads to rotational excitation of NO(A), anisotropy with respect to D_2 leads to rotational excitation of D_2. The REMPI detection scheme is purely sensitive to the final rotational level of NO(A), while rotational excitation of D_2 leads to NO(A) molecules in a given final rotational level moving at different speeds in the scattering frame. If rotational excitation of D_2 was occurring in the experiment, the

experimental images would contain NO(A) scattering signal for Newton spheres at multiple radii. Rotational excitation of D_2 would be most likely to be observed in the highest N' images. This is because the collisions which populate the highest-N' NO(A) rotational levels are typically at low impact parameters with respect to NO(A). These collisions are therefore necessarily also low-impact parameter with respect to D_2, and probe the most anisotropic region of the PES with respect to D_2. The V + H experimental image for $N' = 12$ of NO(A) + D_2 is shown in Figure 4.10(a), overlaid with a Newton diagram, indicating the possible in-plane velocities for NO(A) scattered in coincidence with different D_2 rotational transitions accessible at the mean collision energy (only even

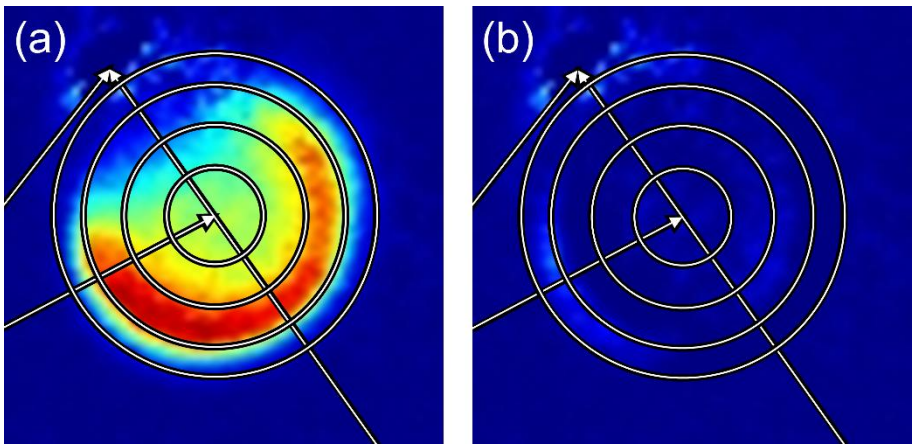

Figure 4.10: (a) Experimental V + H experimental image, averaged across all acquisition for the collisions of NO(A) with D_2 to final rotational level $N' = 12$. (b) Residual V + H image obtained from the subtraction of the corresponding fitted image from the experimental image shown in (a). Overlaid is the Newton diagram, showing velocity vectors associated with the collisions, and circles showing the possible in-plane NO velocities corresponding to different rotational energy transfer in D_2 ($j \rightarrow j'$). From largest to smallest circles: $2 \rightarrow 0$, $0 \rightarrow 0$, $0 \rightarrow 2$, and $1 \rightarrow 3$.

Table 4.3: All $j = 0\text{-}2 \rightarrow j'$ transition energies, in cm^{-1}, for D_2, which are energetically accessible at a collision energy of 663 cm^{-1}.

	$j = 0$	$j = 1$	$j = 2$
$j' = 0$	0		-183
$j' = 1$		0	
$j' = 2$	183		0
$j' = 3$		304	
$j' = 4$	609		426

Δj transitions of the D_2 molecule are accessible, as the collisions cannot change the nuclear spin state of the molecule). In this image, the only scattering signal visible corresponds to collisions which are elastic with respect to the D_2 molecule. Figure 4.10(b) shows the residual of the same experimental image and the corresponding fitted image, which assumes only elastic scattering of D_2. No systematic residuals which can be attributed to inelastic scattering of D_2 are observed, indicating that only an insignificant number of collisions occur which are inelastic for the D_2 molecule. The integrated intensity of this residual image, compared to the total experimental image provides an absolute upper limit of only 3% for the contribution of inelastic scattering of D_2. The images for the other final rotational levels of NO(A) similarly do not show any evidence for rotational excitation of D_2. The lack of any significant rotational excitation of D_2 implies that the NO(A)-D_2 PES has low levels of anisotropy with respect to the orientation of the D_2 molecule, and hence that sufficient torque cannot be applied to the D_2 molecule for rotational energy transfer to occur. A similar lack of H_2/D_2 inelastic scattering was observed for other experiments where H_2 or D_2 was the unobserved partner, in collisions with H_2O, CD_3, ND_3, and NO(X).[17,79,160–162]

As stated above, Westley *et al*. used a CMB experiment to measure the DCSs for the inelastic collisions of NO(X) with He and D_2.[162] The results of this experiment on the collisions of NO(X) were similar to those of NO(A) presented in this chapter. The DCSs exhibited a single rotational rainbow peak for collisions of NO(X) with both He and D_2, which shifted to higher scattering angles as the final rotational level of NO(X) increased. The rotational rainbow maxima were observed at consistently lower scattering angles in the NO(X) + D_2 DCS compared to NO(X) + He, indicating a more anisotropic NO(X)-D_2 PES. No significant rotational excitation of D_2 was observed, indicating that the NO(X)-D_2 PES is also isotropic with respect to the orientation of D_2. These measurements were repeated by Gijsbertsen *et al*., with full Λ-doublet selection of the initial NO(X) quantum state.[17] From these results, hard-shell ellipsoidal models of the NO(X)-He and NO(X)-D_2 PESs were constructed from the experimental results. The model NO(X)-He PES was found to compare favourably to the *ab initio* PES of Kłos *et al.*,[166] while the model NO(X)-D_2 PES was found to have a larger difference between the major and minor axis of the ellipse, consistent with it being more anisotropic than the NO(X)-He PES. Attempts to model the NO(A)-He and D_2 PESs in the same way using the experimental

results from this chapter did not lead to a meaningful result, most likely because the NO(A) PESs have much shallower gradient in their repulsive regions than the equivalent ground state PESs, and so a hard-shell model is not applicable. Because both of the NO(X) experiments were conducted at significantly lower collision energies than the experiments in this chapter, it is not possible to directly compare the results of NO(X) and NO(A) collisions with He and D_2.

Since the initial analysis of the data, a NO(A)-H_2 PES has been calculated by Pajón-Suárez *et al.*[163] Ideally, QS calculations would be performed using this PES to compare with the experimental results presented in this chapter. The attractive region of the NO(A)-H_2 PES is considerably deeper than in the NO(A)-He PES,[14] as was expected based on the polarizabilities of He and H_2.[13] The attractive region of the NO(A)-H_2 PES is also somewhat anisotropic, both with respect to NO(A) and to D_2. However, as discussed above, the measurements in this chapter are not sensitive to the attractive region of the PES. Only the longer-range potential energies were reported, to a minimum intermolecular distance of 5 Å, and a maximum potential energy of 40 cm^{-1} (although the potential energy was calculated down to an intermolecular distance of 2.5 Å), so there is no significant information about the anisotropy of the repulsive region of the PES as published.

4.7 Conclusions

In conclusion, DCSs and rotational alignment moments were recorded for the inelastic collisions of NO(A) with He and D_2, at mean collision energies of 670 cm^{-1} and 663 cm^{-1}, respectively. The experimental results for the NO(A) + He system were compared to the results of QS calculations performed on the *ab initio* PES of Kłos *et al.*[14] A discrepancy between the experimental and theoretical values of $A_{1+}^{\{2\}}(\theta)$ appears to be the result of an experimental artefact. Otherwise, excellent agreement was found between the experimental and theoretical rotational alignment moments, and the DCS, reflecting the high accuracy of the *ab initio* PES.

Comparison of the NO(A) + He and D_2 experimental results provided insight into the structure of the NO(A)-H_2 PES, where the general similarities between the two systems indicates that the NO(A)-H_2 PES is broadly similar to the NO(A)-He PES. The NO(A) + D_2 DCSs contained rotational rainbows at slightly smaller scattering angles than the corresponding NO(A) + He DCSs, indicating that the NO(A)-H_2 PES contains a higher degree of anisotropy in the repulsive region. Understanding of the NO(A) + D_2 scattering system would be greatly improved by performing QS calculations using the recently calculated PES of Pajón-Suárez *et al*.[163] Additionally, these calculations would provide an insight into the accuracy of the, currently untested, PES.

Chapter 5

Collisions of NO($A^2\Sigma^+$) with Molecular Partners: N_2, O_2 and CO

5.1 Introduction

The previous chapters have examined the collisions of NO(A) with atoms, and atom-like molecules. The collisions of a molecule with an atom are relatively simple, when compared to collisions with another molecule, as rotation and vibration of the collision partner do not need to be considered. The reduced dimensionality of the molecule + atom collisions allows extremely detailed calculations to be performed for these systems, which aid the interpretation of the experimental results. Additionally the experiments themselves are simpler for collisions of a molecule with an atom, as energy cannot be transferred to or from internal states of the unobserved collider. However, there are very few real-world systems in which molecule + atom collisions pay a key role.

This chapter will use the same experimental methods as the previous chapters to investigate the collisions of NO(A) with N_2, O_2 and CO, which are all important

molecules in important chemical systems which are likely to interact with NO. NO is an important molecule in a number of atmospheric systems, for example in controlling the distribution of ozone in the stratosphere.[167] The atmosphere is comprised of 78% N_2 and 21% O_2, meaning that collisions with these two molecules will be the most prevalent for NO in the atmosphere. CO and NO both plays important roles as intermediates in combustion systems, and collisions between the two are important in the formation of certain products.[168,169]

For the reasons described above, it is unsurprising that studies of vector correlations in rotational energy transfer using crossed molecular beams have primarily focussed on the collisions of molecules with atoms, and comparatively few experiments have investigated molecule + molecule collisions. The most prominent collision partner to have been studied in molecule + molecule experiments is H_2 which, as described in the previous chapter, tends to act like an atom. Wade *et al*. used a CMB VMI experiment to measure the DCS for rotationally inelastic collisions of HCl with N_2 and CH_4.[170] Tkáč *et al*. used the same methods to study the inelastic collisions of CH_3 with N_2.[171] In these two experiments, the effect of rotational excitation of the unobserved collider could be seen, from which qualitative conclusions were drawn, including that the DCS changes as a function of final rotational level of the unobserved collider. However, in both cases, this change of the DCS was not measured, as a single DCS was assigned to each experimental image, covering all rotational transitions of the unobserved collider.

N_2, O_2 and CO are particularly interesting for their collisions with NO(A), as they can induce an electronic transition, quenching the NO(A) to the ground state. The size of the quenching cross section, and thus the probability that a collision will lead to quenching of NO(A), varies considerably for these molecules, as is shown in Table 5.1. These quenching collisions proceed through conical intersections, which are geometries at which the two PESs are degenerate and are non-adiabatically coupled together. The experiments presented in this thesis involve the detection of NO(A) molecules which have been rotationally excited by collisions, and so there is no sensitivity to the quenched products. However, the quenching collisions will still affect these measurements, as the quenching collisions occur instead of purely rotationally inelastic collisions.

Table 5.1: Room temperature quenching cross sections for the collisions of NO(A) with the collision partners used in this thesis.

	σ / Å^2
N_2[172]	0.007
CO[172]	5.5
O_2[172]	28.5
Ar[173]	0.0020
Ne[173]	0.0023
He[173]	0.0016
H_2[172]	0.0019

The majority of the experiments investigating quenching collisions have been kinetic, and under thermalized conditions, rather than dynamic state-to-state measurements.[172–176] The large quenching cross sections and negative temperature dependence observed for certain collisions, including NO(A) + O_2 and CO in these experiments, was explained using a "harpoon" mechanism.[172] In this mechanism, as the NO(A) and the quenching molecule approach, an electron transfer occurs to form a NO^+M^- (where M is the collision partner) intermediate ion pair. As the ion pair continue to approach, a second electron transfer occurs, producing a neutral ground-state pair of molecules.

The experiments presented in this chapter investigate the rotationally inelastic collisions of NO(A) with molecular collision partners N_2, O_2 and CO. There were two aims of these experiments. The first was to test an extended version of the analysis routine (described in Section 2.10.3), which accounts for rotational energy transfer in the unobserved collision partner. The second was to use the extended analysis routine to investigate the dynamics of these collisions, including the effects of quenching collisions.

5.2 Collisions of NO($A^2\Sigma^+$) with N_2

5.2.1 Experimental Conditions

Velocity mapped scattering images were recorded for the collisions of NO($A^2\Sigma^+$) with N_2 using the methods described in Chapter 2. 10% NO (BOC, 99.998%) was seeded in Ne (BOC, 99.999%) with a backing pressure of 3 bar to produce a molecular beam with a speed distribution of mean of 815 m s^{-1} and full width at half maximum (FWHM) of 57 m s^{-1}. This NO molecular beam was crossed with a neat beam of N_2 (BOC, 99.999%), seeded at 5 bar, with a mean speed of 800 m s^{-1} and a FWHM of 74 m s^{-1}. These conditions resulted in a Gaussian distribution of the collision energy, with mean 790 cm^{-1} and FWHM 92 cm^{-1}.

The mean speeds of the molecular beams were determined from the positions of the non-resonant beam-spots, resulting from NO in the two molecular beams in the experimental images (see Section 2.5). The FWHM values for the molecular beams were measured in the separate downstream LIF experiments (see Section 2.9).

Velocity map images were recorded for final NO(A) rotational levels $N' = 3$, 5-11. For each final rotational level, six individual images were recorded, except $N' = 11$, where twelve images were recorded to compensate for low signal-to-noise levels. Each individual image was the sum of 64,000 camera shots across all V, H, signal and background frames, and five scans of the Doppler profile of the NO(E ← A) transition.

No REMPI spectrum was recorded for the N_2 molecular beam to determine the initial rotational state distribution of N_2, as there is no easily accessible REMPI scheme. Instead the rotational state distribution of N_2 was estimated based on the rotational state distribution of trace NO seeded in N_2, measured using the LIF apparatus described in Section 2.9. The obtained rotational temperature of 10 K would result in the majority of the N_2 molecules being in the $j = 0$ and 1 rotational levels, with a smaller, but still significant population in $j = 2$.

5.2.2 Data Analysis

The NO(A) + N_2 scattering images were analysed using the extended fitting routine described in section 2.10.3 to extract the DCS and rotational alignment moments as a function of rotational excitation of N_2 from the images. Briefly, basis images were simulated not only for different Legendre polynomial representations of the DCS and $A_{q+}^{\{2\}}(\theta)$ moments, but also corresponding to collisions in which different proportions of the collision energy was transferred into rotation of the N_2 molecule. Collisions which induced different rotational transitions of N_2, resulted in NO(A) molecules moving at different centre-of-mass speeds, as different amounts of energy were left to be partitioned into translation of the recoiling colliders. Basis images were chosen which corresponded to the inelastic collisions of N_2: $j = 0 \rightarrow j' = 0$, 6 and 8 (ΔE = 0, 84 and 144 cm^{-1} respectively) for all N' images. The basis images used to fit the images were chosen to extract the maximum amount of information from the scattering images. The method used to select which N_2 rotational transitions to use is provided in Section 5.6.

It was found that the sharp forward peak of the NO(A) + N_2 scattering images required a large number of Legendre moments to replicate in the fitted image, and thus a large number of basis images to be used in the fitting routine. The resulting large parameter space was not probed effectively using the downhill-simplex algorithm, and the images could not be fit in this way. To avoid this problem, the forward scattered peak was excluded from the fitting process by applying a "mask" to it in the same way the non-resonant beam-spot was masked when fitting the NO(A) + Ne images. This meant that the DCS could be represented with a much smaller number of Legendre moments, and the downhill-simplex routine could effectively fit the images.

The number of Legendre polynomials required to represent the DCSs in the different N_2 transition basis images were optimised independently, with the number used for each quantum state shown in Table 5.2. The number of Legendre polynomials used to fit the $A_0^{\{2\}}(\theta)$ and $A_{2+}^{\{2\}}(\theta)$ moments was fixed at five for all basis images, and $A_{1+}^{\{2\}}(\theta)$ (which the system had an extremely low sensitivity to) was fixed at one moment. For all parameters, the $x = \cos(\theta)$ basis set was used. The returned DCSs were truncated to exclude angles for which fewer than 20% of the simulated ion strikes (see Section 2.10.2)

fell in the unmasked region of the image. The truncated DCSs were renormalized, such that the largest value of the DCS across all N_2 rotational transitions was equal to one, while the relative intensity of the DCSs for the different N_2 transitions was retained. The $A_{q+}^{\{2\}}(\theta)$ moments were truncated to exclude angles where fewer than 20% of the simulated ion strikes were unmasked, or where the intensity of the DCS was less than 10% the maximum reported value of the DCS.

Table 5.2: Number of parameters used to extract the DCSs for the NO(A) + N_2 images.

	$j' = 0$	$j' = 6$	$j' = 8$
$N' = 3$	11	11	11
$N' = 5$	13	13	13
$N' = 6$	11	11	11
$N' = 7$	9	9	9
$N' = 8$	7	7	9
$N' = 9$	9	9	9
$N' = 10$	7	7	7
$N' = 11$	17	11	11

5.2.3 Results

A Newton diagram for the NO(A) + N_2 scattering system is shown in Figure 5.1. The circles represent the mean-collision energy, in-plane scattering of the rotationally excited NO(A) molecules which have been produced in coincidence with different N_2 final rotational levels. As was also the case for D_2 (see Section 4.2), only parity conserving (Δj = even) transitions of the N_2 molecule are permitted. For clarity, in this chapter the initial and final rotational levels of NO(A) will be labelled as N and N' respectively, and the initial and final rotational levels of N_2, CO and O_2 will be labelled as j and j' respectively.

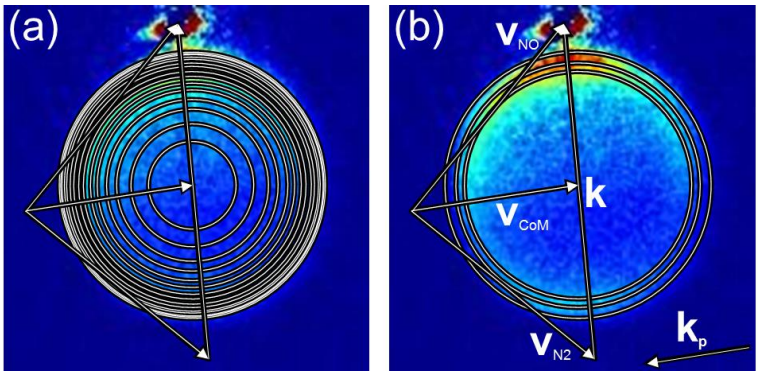

Figure 5.1: Newton diagrams for the NO(A) + N_2 collision system at a mean collision energy of 790 cm^{-1}, overlaid on V + H experimental images for product state $N' = 11$. Arrows show the velocity vectors of the systems, and the rings represent the velocity of NO scattered into the plane of the detector, showing: (a) all energetically accessible final rotational transitions of N_2 originating from $j = 0$ and 1 (see Table 5.3, (b): $j = 0 \rightarrow j' = 0$, 6 and 8.

Table 5.3: All $j = 0\text{-}2 \rightarrow j'$ transition energies, in cm^{-1}, for N_2, which are energetically accessible at a collision energy of 1,627 cm^{-1}.

	$j = 0$	**$j = 1$**	**$j = 2$**		**$j = 0$**	**$j = 1$**	**$j = 2$**
$j' = 0$	0		-12	**$j' = 15$**		476	
$j' = 1$		0		**$j' = 16$**	544		532
$j' = 2$	12		0	**$j' = 17$**		607	
$j' = 3$		20		**$j' = 18$**	683		671
$j' = 4$	40		28	**$j' = 19$**		755	
$j' = 5$		56		**$j' = 20$**	839		827
$j' = 6$	84		72	**$j' = 21$**		919	
$j' = 7$		108		**$j' = 22$**	1,011		999
$j' = 8$	144		132	**$j' = 23$**		1,099	
$j' = 9$		176		**$j' = 24$**	1,199		1,187
$j' = 10$	220		208	**$j' = 25$**		1,295	
$j' = 11$		260		**$j' = 26$**	1,403		1,391
$j' = 12$	312		300	**$j' = 27$**		1,507	
$j' = 13$		360		**$j' = 28$**	1,623		1,611
$j' = 14$	420		408				

The full range of experimental NO(A) + N_2 images are shown in Figure 5.2. At a glance, the structure of the images is similar to the NO(A) + Ar system presented in Chapter 3, with an intense forward-scattered peak, and some sideward and backward scattered signal. As N' increases, the ratio of the two shifts, with the sideward scattered signal becoming more intense relative to the forward-scattered peak. Evidence for rotational excitation of N_2 can be clearly seen, as the images are slightly non-circular, which occurs because the different rotational transitions of N_2 lead to different scattering distributions. This is most apparent in the scattering images for N' = 9-11, where the proportion of scattering outside of the extreme forward region is the highest. As with the other systems described in the previous chapters, the difference in intensity in the V and H images is clear evidence of collision-induced rotational alignment in the scattered NO(A) molecules.

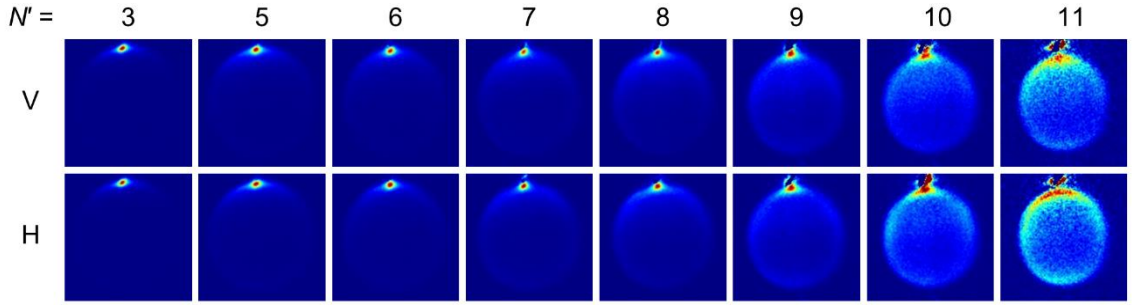

Figure 5.2: Experimental V and H images, averaged over all individual acquisitions for the collisions of NO(A) with N_2 at a mean collision energy of 790 cm^{-1}, for final NO(A) rotational levels N' = 3, 5-11.

Figure 5.3 shows an example set of individually acquired NO(A) + N_2 experimental images, together with simulated images from the results of fitting using the atomic-collider fitting routine successfully used throughout the previous two chapters. The simulated images clearly contain large systematic errors, where the rotational excitation of the N_2 molecule has not been accounted for. These results demonstrate the need for the extended molecular-collider fitting routine to deal with different N_2 rotational transitions. Another set of experimental and fitted images are shown in Figure 5.4, this time using the molecular-collider code, in which each fitted image contains basis images corresponding to N_2 rotational transitions $j = 0 \rightarrow j' = 0$, 6 and 8 (with excitation energies of 0, 84 and 144 cm^{-1} respectively, see Table 5.3). These fitted images using the molecular-collider code have a much better agreement with the experimental images than those with the atomic-collider code. The quality of the two fitting methods is more rigorously compared

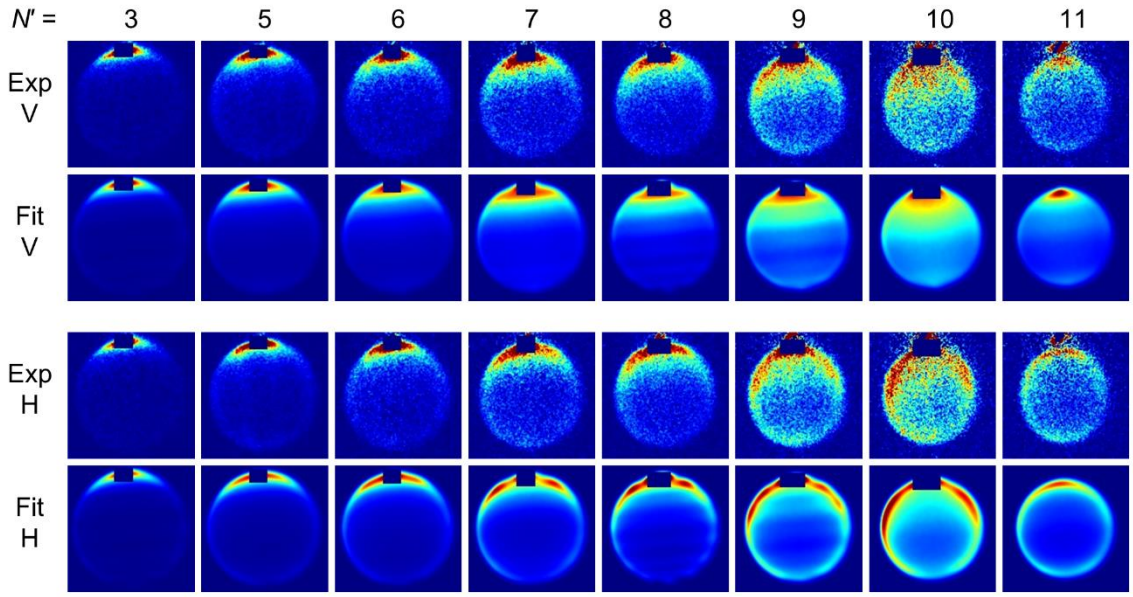

Figure 5.3: Example individual experimental V and H scattering images for the collisions of NO(A) with N_2 at a mean collision energy of 790 cm^{-1}, for final NO(A) rotational levels N' = 3, 5-11. Also shown are corresponding fitted images, assuming purely elastic collisions of the N_2 molecule.

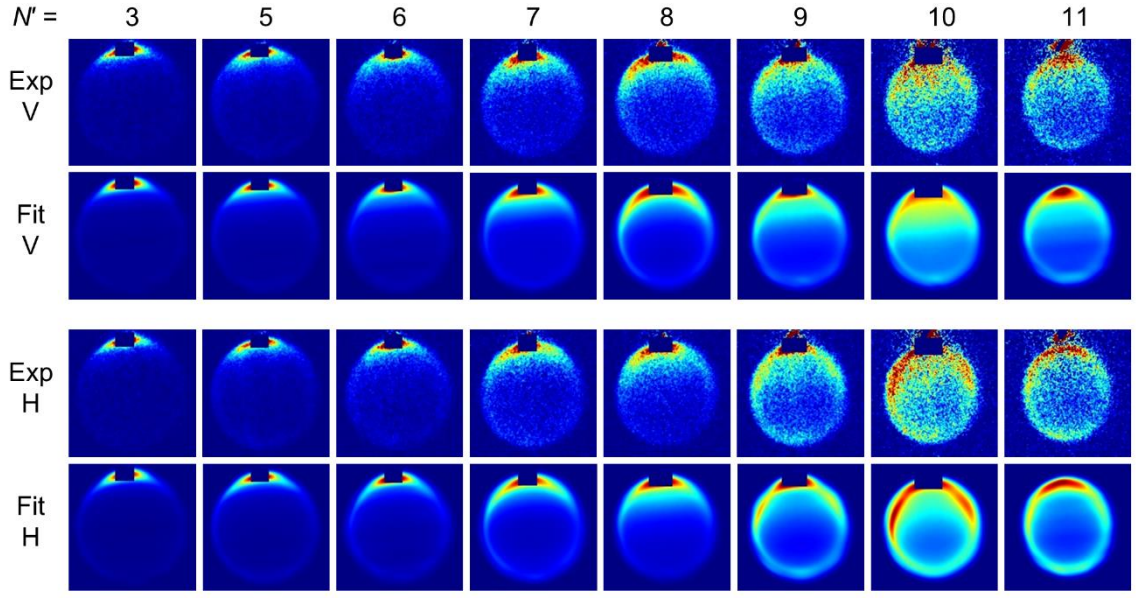

Figure 5.4: Example individual experimental V and H scattering images for the collisions of NO(A) with N_2 at a mean collision energy of 790 cm^{-1}, for final NO(A) rotational levels N' = 3, 5-11. Also shown are corresponding fitted images, simulating $j \rightarrow j'$ N_2 transitions of $j = 0 \rightarrow j' = 0$, 6 and 8.

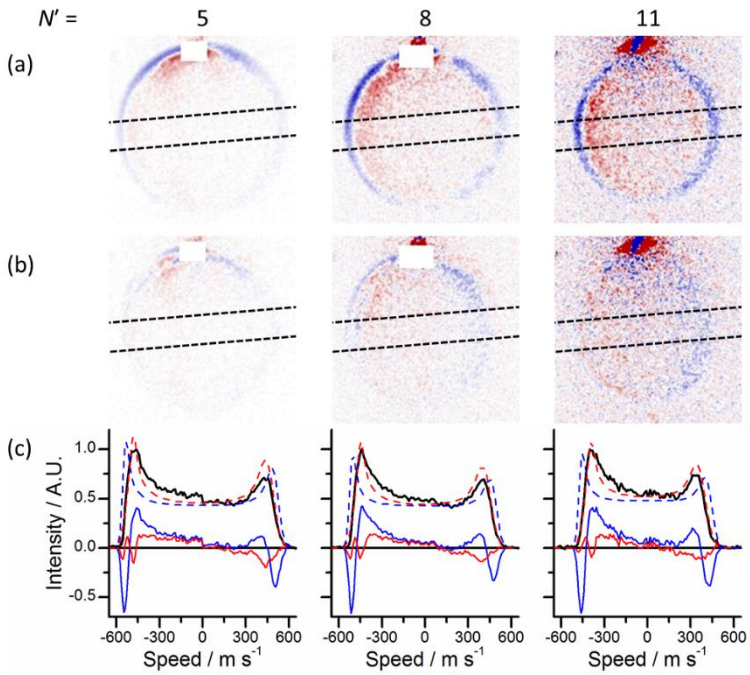

Figure 5.5: (a) V + H residual images, for the experimental and fitted image using the atomic fitting routine, (b) V + H residual for the experimental and fitted image using the molecular fitting routine, set to the same colour intensity scale as (a). (c): A projection of the intensity of the scattering images between the dashed lines shown in (a) and (b), with: black: the experimental image, dashed blue: the fitted image using the atomic fitting routine, dashed red: the fitted image using the molecular fitting routine, red: the residual of the experimental and atomic code fitted image in (a), blue: the residual of the experimental and molecular code fitted image in (b).

in Figure 5.5, which shows the systematic residuals for the fitted images from the atomic and molecular routines, compared to the corresponding experimental images. Because of the spread of collision energies, the basis images for the individual $j \rightarrow j'$ transitions each cover a range of N_2 rotational transitions. j' is used as a convenient label for the DCS and rotational alignment moments returned from fitting with the different basis images described above, but these are not truly j-j' state-to-state results. Instead, they represent broad trends in the results across multiple transitions in which different amounts of energy is partitioned into N_2 rotation.

The extracted DCSs and $A_{q+}^{\{2\}}(\theta)$ moments are shown in Figure 5.6. No corresponding QS calculations were performed for these results, as there is currently no suitable NO(A)-N_2 PES with which to perform the calculations. While the forward-scattered peak was excluded from the fitting process, and so is not reported in these results, its wings are still visible as a peak at the smallest reported scattering angles. For j' = 0 and 6, the wings of

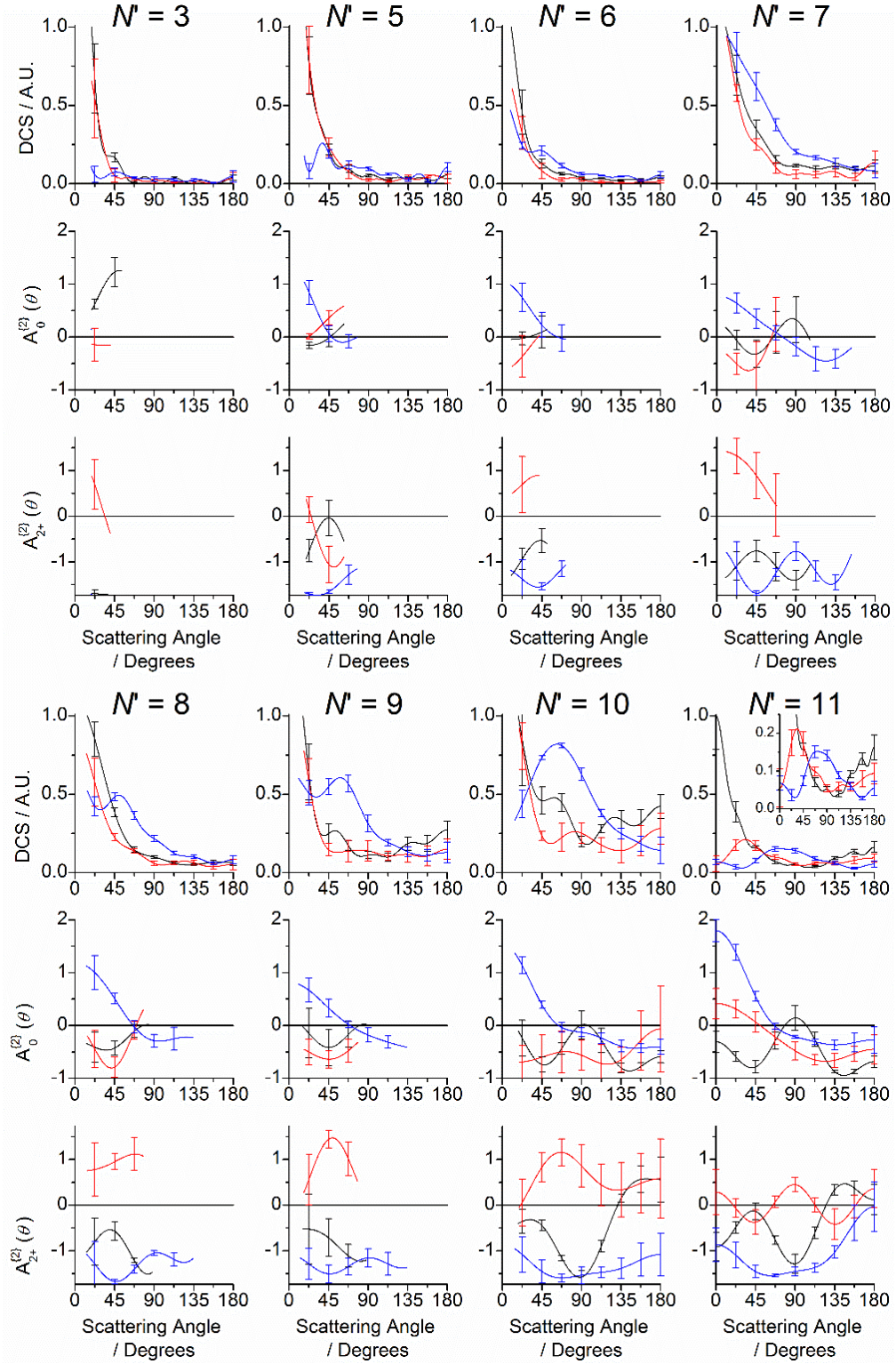

Figure 5.6: Differential cross sections and rotational alignment moments for the collisions of NO(A) with N_2 at a mean collision energy of 790 cm^{-1}, for final NO(A) rotational levels N' = 3, 5-11. Different plots on the same axis represent different degrees of rotational excitation of the N_2 molecule: black: j' = 0, red: j' = 6 and blue: j' = 8. Error bars represent 95% confidence limits.

the forward scattered peak dominate the DCS, with no significant secondary peaks visible for $N' \leq 8$. For $N' \geq 9$, comparatively small secondary peaks are present in the shoulder of the forward scattered peak, and a further peak is present in $j' = 0$ at 180°. This peak in the backwards direction is not an artefact, and can be clearly seen in the experimental images (most obviously in Figure 5.1(b), with the scattering signal between the circles representing $j' = 0$ and 6 scattering, which is clearly more intense at 180° than at 90°). Except for $N' = 7$, the DCS for $j' = 8$ contains a clear peak, which progressively shifts to higher angles as N' increases. This feature appears to be a rotational rainbow peak, which was also observed in the NO(A) + Ar, Ne, He and D_2 scattering systems presented in the previous chapters. The intensity of the rotational rainbow peak observed in $j' = 8$ relative to the DCS in $j' = 0$ and 6 steadily increases with N'. For all three j' states, $A_0^{\{2\}}(\theta)$ acts broadly as would be expected for impulsive scattering. At low angles, it is positive or close to zero, and at higher scattering angles becomes more negative. $A_{2+}^{\{2\}}(\theta)$ acts in a very unusual manner, with the extracted values being predominantly negative for $j' = 0$ and 8, but positive for $j' = 6$.

5.2.4 Discussion

The $A_0^{\{2\}}(\theta)$ moments for the NO(A) + N_2 system appear to broadly match the impulsive scattering exhibited by the atomic collision partners in the previous chapters. Because only five Legendre moments were used to fit $A_0^{\{2\}}(\theta)$, any high-frequency oscillations, such as those observed in the NO(A) + Ar and Ne systems in Chapter 3, would not be successfully returned. The experimental V – H images presented in Figure 5.7 have intensities which vary smoothly with scattering angle, showing that these rapid oscillations do not appear in the NO(A) + N_2 system. Unlike atomic collider systems presented in this thesis, the value of $A_0^{\{2\}}(\theta)$ does not tend towards -1 at 180°. For the collisions of NO(A) with an atom, this is a necessary constraint, required by conservation of angular momentum, as described in Section 2.10.1. In contrast, for NO(A) + molecule collisions, angular momentum can be transferred into rotation of both the NO(A) and collider molecules, removing this constraint.

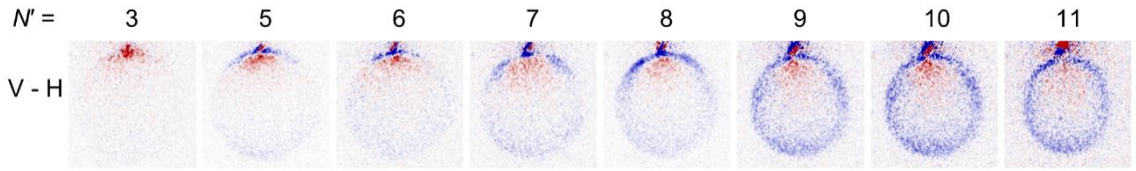

Figure 5.7: Experimental V – H images, averaged over all individual acquisitions for the collisions of NO(A) with N_2 at a mean collision energy of 790 cm^{-1}, for final NO(A) rotational levels N' = 3, 5-11.

$A_{2+}^{\{2\}}(\theta)$ does not appear to match the impulsive scattering observed in the other systems, with the moment being negative for j' = 0 and 8 positive for and j' = 6. It seems extremely unlikely that such a major dynamical change could occur over such a small range of N_2 transitions. The most likely explanation for this feature is that it is an artefact of the fitting routine, which does a poor job of distinguishing between the different j' states when dealing with $A_{2+}^{\{2\}}(\theta)$. As Figure 2.22 shows, $A_{2+}^{\{2\}}(\theta)$ affects the images by causing a detection bias for the NO(A) molecules scattered in and out of the plane of the detector. This means that for the different j', the effect of $A_{2+}^{\{2\}}(\theta)$ is similar, with differences in intensity occurring in the same locations of the image, and so it is extremely easy to attribute them to $A_{2+}^{\{2\}}(\theta)$ in the wrong j' state. This means that while the average $A_{2+}^{\{2\}}(\theta)$ across all three j' states is likely to be reasonably well determined, independently assigning the contribution for the different states is much more difficult.

These artefacts observed in the $A_{2+}^{\{2\}}(\theta)$ results are troubling, as they imply that incorrectly extracted parameters can compensate for each other in the molecular-collider code. To ensure that these anomalies in the rotational alignment moments did not interfere with the extracted DCSs, the fitting process was repeated, this time with an assumed, isotropic, rotational alignment. As Figure 5.8 shows, the resulting DCSs are almost identical to the values extracted while also fitting the $A_{q+}^{\{2\}}(\theta)$ moments, and the two are well within experimental uncertainty. These results confirm that the conclusion drawn in Chapter 3, namely that the alignment moments and the DCS can be treated separately, is still applicable in this expanded version of the fitting routine, and they confirm that the physically implausible $A_{2+}^{\{2\}}(\theta)$ moments have not led to an incorrect measurement of the DCSs.

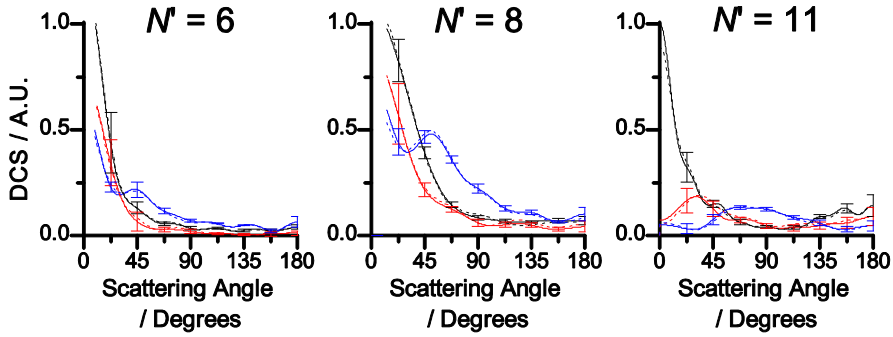

Figure 5.8: Differential cross sections for the collisions of NO(A) with N_2 at a mean collision energy of 790 cm^{-1}, for final NO(A) rotational levels N' = 6, 8 and 11. Different plots on the same axis represent different degrees of rotational excitation of the N_2 molecule: black: j' = 0, red: j' = 6 and blue: j' = 8. Solid lines show the DCS returned when the fitting routine uses an assumed, isotropic rotational alignment, and dashed shows the returned DCS when fit simultaneously with the rotational alignment moments. Error bars represent 95% confidence limits of the DCS returned with isotropic rotational alignment moments.

Returning to the DCSs, there is a general trend towards sideward and backwards scattering, both as N' and j' increases. This shows that there is more rotational energy transferred in low-impact parameter collisions, which probe the repulsive region. This is consistent with the repulsive region of the NO(A)-N_2 PES being anisotropic with respect to both colliders. The general similarities of the rotational rainbow peaks to those observed in the NO(A) + He, Ne and Ar scattering systems indicates that the amount of anisotropy in the repulsive region of the PES with respect to NO(A) is similar to the NO(A)-Rg PESs.

The forward-scattered peak in the DCS observed at both collision energies strongly resembles the peak in the NO(A) + Ar system, which was caused by scattering through the attractive region of the PES. This strongly implies that the NO(A)-N_2 PES has a substantial attractive region. The most probable location for this would be localised at the N end of the NO molecule, as this is what is seen in the NO(A)-Rg PESs.[14] The forward scattered peak is present both for N_2 molecules which have collided elastically and inelastically. The fact that the attractive region can lead to rotational excitation of both the NO(A) and N_2 molecules shows that it is anisotropic with respect to both colliders. This conclusion is supported by a 1 + 1 REMPI investigation of the NO-N_2 complex by Lozeille *et al*., the structure of the spectrum was attributed to a wide range of NO(X)-N_2 conformers transitioning to a single, linear conformer of NO(A)-N_2.[177] Supporting

electronic structure calculations in the same study indicated that O-N-N-N is the most stable linear geometry of the NO(A)-N_2 complex, although non-linear geometries were too computationally expensive to calculate.

5.3 Collisions of NO($A^2\Sigma^+$) with CO and O_2

5.3.1 Experimental Conditions

The experiments probing the NO(A) + CO and O_2 collisions were performed with a molecular beam of 10% NO (BOC, 99.998%) seeded in Ne (BOC, 99.999%), with a backing pressure of 3 bar, leading to a speed distribution with a mean of 815 m s^{-1} and a FWHM of 57 m s^{-1}. For the collisions with CO, the NO molecular beam was crossed with a neat molecular beam of CO (BOC, 99.999%), with a backing pressure of 5 bar, and a speed distribution with a mean of 767 m s^{-1} and a FWHM of 74 m s^{-1}. This resulted in a collision energy distribution with a mean of 759 cm^{-1} and a FWHM of 89 cm^{-1} for the NO(A) + CO collisions. For the collisions with O_2, the NO molecular beam was crossed with a beam of neat O_2 (BOC, 99.999%), with a backing pressure of 5 bar, to give a speed distribution with a mean of 759 m s^{-1} and a FWHM of 72 m s^{-1}. This led to a collision energy distribution of mean 803 cm^{-1} and FWHM of 93 cm^{-1} for the NO(A) + O_2 collisions.

The mean speeds of the NO and CO molecular beams were determined by fitting a 2-D Gaussian function to the 532 + 532 nm beam-spots resulting from NO present in these molecular beams (see Section 2.5). The FWHM of the NO molecular beam speed distribution was obtained from the downstream LIF measurements, described in Section 2.9. Trace NO in the O_2 molecular beam source reacts to form NO_2, and so these methods could not be used to measure the speed distribution of the O_2 molecular beam. To determine the mean and FWHM of the speed distribution of the O_2 beam, the O_2 molecules were directly ionised by 1 + 1 REMPI at 225 nm, and a 2-D Gaussian function was fitted to the resulting beam-spot. The mean position of the Gaussian fit and the FWHM were used to determine the mean and FWHM of the speed distribution

respectively (accounting for the differences in electron recoil speeds and velocity-to-pixel ratios for NO and O_2). The FWHM of the CO beam was not measured, and the value quoted above is the same as the value measured for the N_2 beam. Using this FWHM to fit the NO(A) + CO scattering images did not lead to any systematic residuals, showing that this speed distribution is accurate for the CO molecular beam.

For the CO collision partner, velocity map images were recorded for final NO(A) rotational levels $N' = 3$, 5-10, and for the O_2 collision partner, $N' = 3$, 5-8 were recorded. For each final rotational level of each system, six sets of individual images were recorded, each containing frames for the signal and background images, and with the V and H polarisations of the probe laser. Each individual image was the sum of 64,000 individual camera shots, across all V, H, signal and background frames, and five scans of the Doppler profile, over the NO(E ← A) transition.

As was done with D_2 in the previous chapter, it would be possible to investigate the rotational populations of the O_2 and CO molecular beams through an appropriate REMPI scheme. However, at the time of writing, these measurements have not been conducted. For the interpretation of the results, it is assumed that the majority of the molecules are in their lowest-energy rotational level.

5.3.2 Data Analysis

The NO(A) + CO and O_2 experimental images were analysed using the extended fitting routine, in the same way as the NO(A) + N_2 images, described in Section 5.2.2. The different final collider rotational levels for which basis images were simulated, as well as the number of Legendre polynomials used to fit the DCS for the CO and O_2 colliders, are shown in Tables 5.4 and 5.5 respectively. For every j' state of every image, five Legendre moments were used to extract the $A_0^{\{2\}}(\theta)$ and $A_{2+}^{\{2\}}(\theta)$ moments, and one moment for $A_{1+}^{\{2\}}(\theta)$. All parameters were extracted using the $x = \cos(\theta)$ basis set.

Table 5.4: Number of parameters used to extract the DCSs for the NO(A) + CO images.

	$j' = 0$	$j' = 7$	$j' = 9$
$N' = 3$	19	15	15
$N' = 5$	17	17	15
$N' = 6$	15	17	15
$N' = 7$	11	17	15
$N' = 8$	11	15	11
$N' = 9$	13	15	13
$N' = 10$	11	11	11

Table 5.5: Number of parameters used to extract the DCSs for the NO(A) + images.

	$j' = 1$	$j' = 7$	$j' = 11$
$N' = 3$	17	13	13
$N' = 5$	13	13	11
$N' = 6$	21	15	15
$N' = 7$	17	13	13
$N' = 8$	15	11	11

As with the NO(A) + N_2 system, the forward scattered peak was masked to reduce the number of Legendre moments needed to extract the DCS. The extracted DCSs were truncated to exclude angles for which fewer than 20% of the simulated ion strikes fell in the unmasked region of the image, and normalised so that the highest value of the DCS is equal to one. The DCS was truncated to exclude angles where fewer than 20% of the simulated ion strikes fell into the unmasked region, and the $A_{q+}^{\{2\}}(\theta)$ moments were truncated to exclude angles where less than 20% of the simulated ion strikes fell into the unmasked region, or where the DCS was less than 10% of its maximum reported value.

5.3.3 Results

Figures 5.9 and 5.10 show the Newton diagrams for the NO(A) + CO and O_2 scattering systems, overlaid on experimental images. The structure of these scattering images is very similar to the NO(A) + N_2 system, where rotational excitation of both the NO(A) molecule and the unobserved collider can occur, leading to scattered NO(A) molecules moving at different speeds superimposed on the same scattering image. The ground electronic state of O_2 is $^3\Sigma_g^-$, and so the lowest energy rotational level is $j = 1$. As with D_2 and N_2, the total wavefunction of O_2 must be symmetric with respect to rotation. Because the electronic wavefunction of O_2 is antisymmetric and the nuclear wavefunction is symmetric (for ^{16}O, $I = 0$), only antisymmetric, odd-j rotational levels can combine to produce the required symmetric total wavefunction. CO is a heteronuclear diatomic molecule, and so the selection rule which forbids parity changing transitions is not relevant, and both Δj = even and odd transitions are equally accessible.

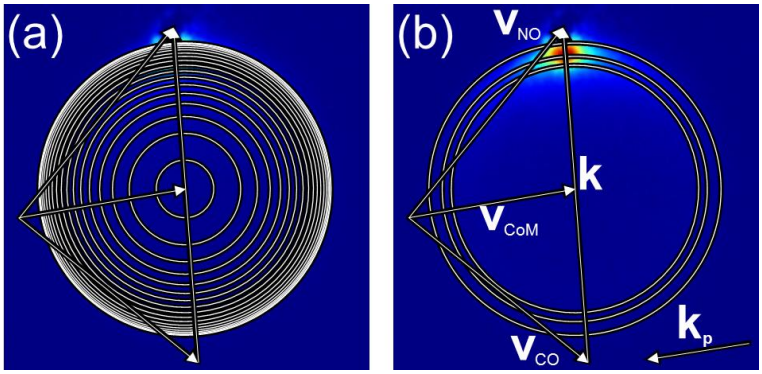

Figure 5.9: Newton diagrams for the NO(A) + CO collision system at mean collision energy of 759 cm^{-1}, overlaid on V + H experimental images for product state $N' = 8$. Arrows show the velocity vectors of the systems, and the rings represent the velocity of NO scattered into the plane of the detector, showing: (a) all energetically accessible final rotational transitions originating from CO $j = 0$ (see Table 5.6), (b) $j = 0 \rightarrow j' = 0, 7, 9$.

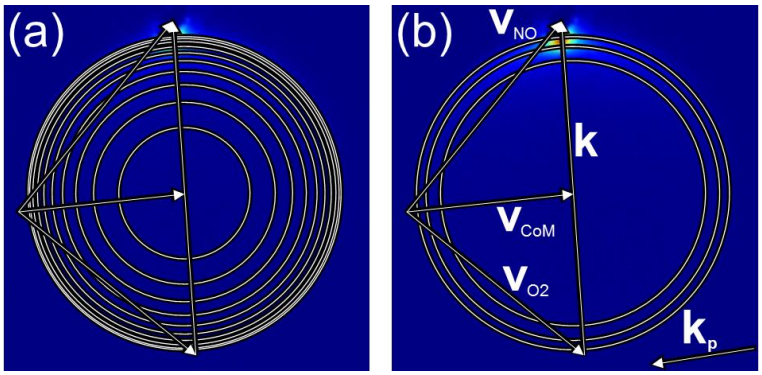

Figure 5.10: Newton diagrams for the NO(A) + O_2 collision system at mean collision energy of 803 cm^{-1}, overlaid on V + H experimental images for product state $N' = 8$. Arrows show the velocity vectors of the systems, and the rings represent the velocity of NO scattered into the plane of the detector, showing: (a) all energetically accessible final rotational transitions originating from O_2 $j = 1$ (see Table 5.7), (b) $j = 1 \rightarrow j' = 1, 7, 11$.

Table 5.6: All j = 0-2 → j' transition energies, in cm^{-1} for CO, which are energetically accessible at a collision energy of 1,595 cm^{-1}.

	***j* = 0**	***j* = 1**	***j* = 2**		***j* = 0**	***j* = 1**	***j* = 2**
***j′* = 0**	0	-4	-12	***j′* = 15**	464	460	452
***j′* = 1**	4	0	-8	***j′* = 16**	525	521	514
***j′* = 2**	12	8	0	***j′* = 17**	591	587	579
***j′* = 3**	23	19	12	***j′* = 18**	561	657	649
***j′* = 4**	39	35	27	***j′* = 19**	734	730	722
***j′* = 5**	58	54	46	***j′* = 20**	811	807	800
***j′* = 6**	81	77	70	***j′* = 21**	892	888	881
***j′* = 7**	108	104	97	***j′* = 22**	977	973	966
***j′* = 8**	139	135	127	***j′* = 23**	1,066	1,062	1,054
***j′* = 9**	174	170	162	***j′* = 24**	1,159	1,155	1,147
***j′* = 10**	212	209	201	***j′* = 25**	1,255	1,251	1,244
***j′* = 11**	255	251	243	***j′* = 26**	1,356	1,352	1,344
***j′* = 12**	301	297	290	***j′* = 27**	1,460	1,456	1,448
***j′* = 13**	351	348	340	***j′* = 28**	1,568	1,564	1,557
***j′* = 14**	406	402	394				

Table 5.7: All $j = 1, 3 \rightarrow j'$ transition energies, in cm^{-1} for O_2, which are energetically accessible at a collision energy of 1,697 cm^{-1}.

	$j = 1$	$j = 3$		$j = 1$	$j = 3$
$j' = 1$	0	-14	$j' = 19$	543	529
$j' = 3$	14	0	$j' = 21$	661	647
$j' = 5$	40	26	$j' = 23$	791	776
$j' = 7$	78	63	$j' = 25$	932	917
$j' = 9$	127	112	$j' = 27$	1,084	1,070
$j' = 11$	187	173	$j' = 29$	1,248	1,234
$j' = 13$	259	244	$j' = 31$	1,423	1,409
$j' = 15$	342	328	$j' = 33$	1,610	1,596
$j' = 17$	437	423			

Figure 5.11 shows the experimental V and H NO(A) + CO experimental images, averaged across all individual acquisitions. As with the NO(A) + N_2 system, the scattering images contain a forward-scattered peak, and intensity at larger angles which increases in intensity relative to the forward scattered peak as N' increases. The scattering images are non-circular, indicating that rotational excitation of the CO molecule is occurring, with the DCS varying for different $j \rightarrow j'$ transitions. The differences in intensity between the V and H images shows a clear rotational alignment of the scattered NO(A) molecules, which is clearly shown in the V – H images in Figure 5.12.

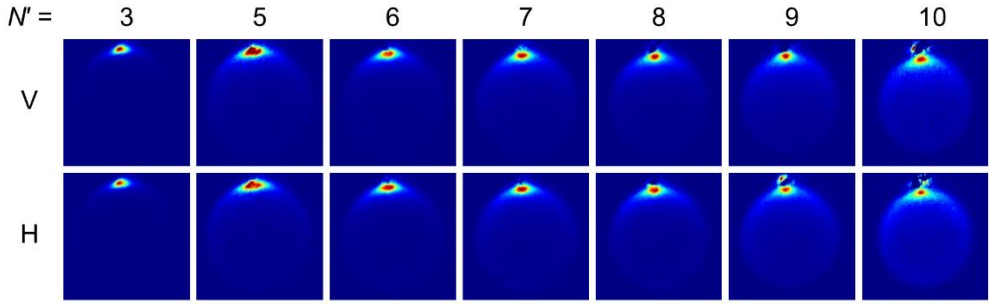

Figure 5.11: Experimental V and H images, averaged over all individual acquisitions for the collisions of NO(A) with CO at a mean collision energy of 759 cm^{-1}, for final NO(A) rotational levels $N' = 3, 5\text{-}10$

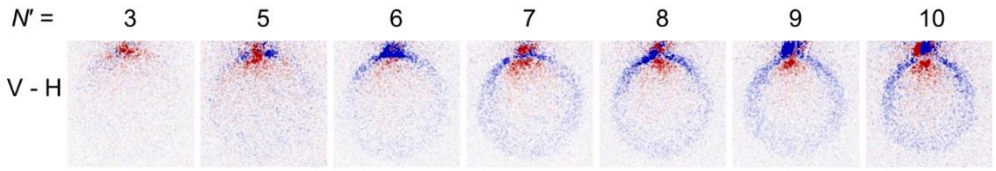

Figure 5.12: Experimental V – H images, averaged over all individual acquisitions for the collisions of NO(A) with CO at a mean collision energy of 759 cm^{-1}, for final NO(A) rotational levels N' = 3, 5-10.

Example individual NO(A) + CO experimental images are compared to the corresponding fitted images in Figure 5.13 and the returned DCSs and $A_{q+}^{\{2\}}(\theta)$ moments are presented in Figure 5.14. Basis images corresponding to j' = 0, 7 and 9 (with excitation energies of 0, 108 and 174 cm^{-1} respectively, see Table 5.6) were used in the fitting routine for these images, which are used as labels for the returned DCSs and $A_{q+}^{\{2\}}(\theta)$ moments. The returned DCSs and rotational alignment moments have a similar structure to those of the NO(A) + N_2 collisions. The DCSs for j' = 0 and 7 are dominated by the wings of the forward-scattered peak, while j' = 9 contains a rotational rainbow peak. $A_{2+}^{\{2\}}(\theta)$ is affected by the same problem that was observed for the NO(A) + N_2 moment, with j' = 0 and 9 being predominantly negative and j' = 7 predominantly positive. As with the NO(A) + N_2 system, this appears to be an artefact of the fitting procedure, rather than a real dynamical effect. $A_0^{\{2\}}(\theta)$ acts in a way which is consistent with impulsive scattering.

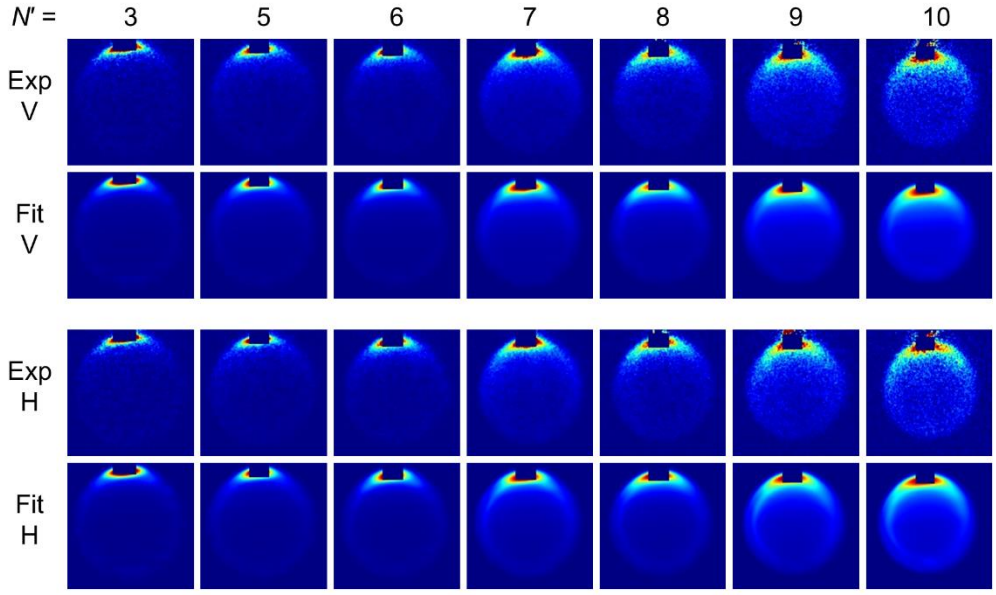

Figure 5.13: Example individual experimental and fitted V and H scattering images for the collisions of NO(A) with CO at a mean collision energy of 759 cm^{-1}, for final NO(A) rotational levels N' = 3, 5-10.

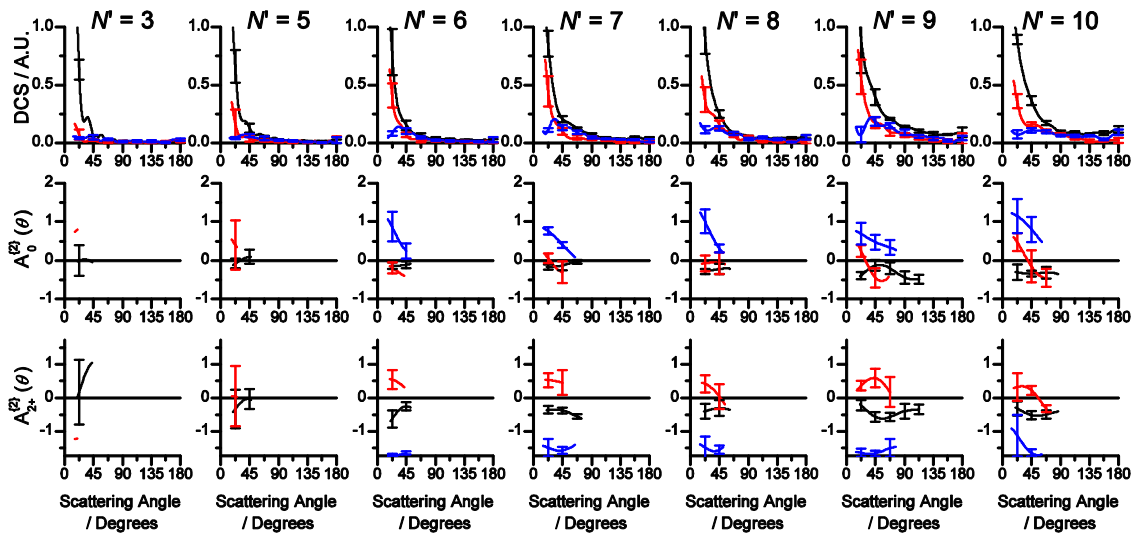

Figure 5.14: Differential cross sections and rotational alignment moments for the collisions of NO(A) with CO at a mean collision energy of 759 cm^{-1}, for final NO(A) rotational levels $N' = 3$, 5-10. Different plots on the same axis represent different degrees of rotational excitation of the CO molecule: black: $j' = 0$, red: $j' = 7$ and blue: $j' = 9$. Error bars represent 95% confidence limits.

The experimental NO(A) + O_2 scattering images shown in Figure 5.15 are very forward scattered, with only a small amount of scattering signal visible outside of the forward-scattered peak. Unlike the other systems in this chapter, the NO(A) + O_2 scattering images appear to be very close to circular, indicating that the amount of rotational energy transferred to the O_2 molecule is small compared to the collisions with N_2 and CO. Furthermore, the edges of the scattering circle appear to be much more well-resolved than in the NO(A) + N_2 or NO(A) + CO images, and are much more like the NO(A) + rare gas scattering images presented in the previous chapters. The V – H images in Figure 5.16 clearly show that there is strong rotational alignment in the scattered NO(A) molecules.

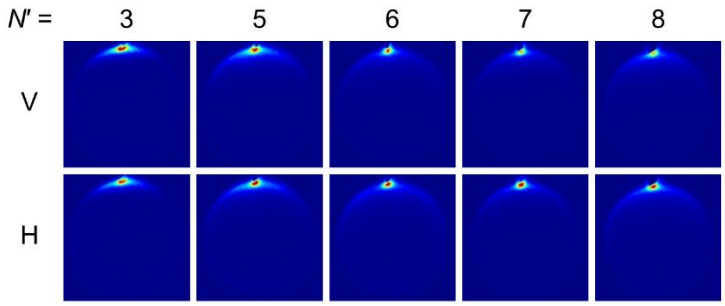

Figure 5.15: Experimental V and Himages, averaged over all individual acquisitions for the collisions of NO(A) with O_2 at a mean collision energy of 803 cm^{-1}, for final NO(A) rotational levels $N' = 3$, 5-8.

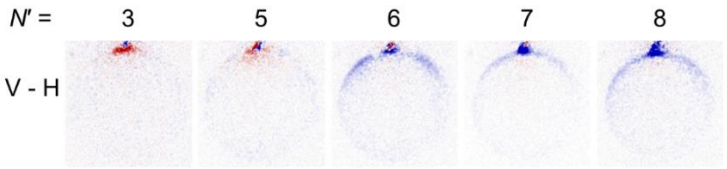

Figure 5.16: Experimental V – H images, averaged over all individual acquisitions for the collisions of NO(A) with O_2 at a mean collision energy of 803 cm^{-1}, for final NO(A) rotational levels N' = 3, 5-8.

Example individual experimental and fitted NO(A) + O_2 images are shown in Figure 5.17 and the extracted DCSs and $A_{q+}^{\{2\}}(\theta)$ moments are presented in Figure 5.18. Basis images with O_2 final rotational levels j' = 1, 7 and 11 (with excitation energies of 0, 78 and 187 cm^{-1} respectively, see Table 5.7) were used to fit the experimental images. These results show that there is some rotational excitation of the O_2 molecule, but it is considerably lower than the NO(A) + N_2 and CO systems. The most obvious feature of the NO(A) + O_2 DCSs is the wings of the forward scattered peak in j' = 1 and 7. There are no rotational rainbow peaks in any of the j' DCSs, or any other clear features. The rotational alignment moments are only reliably extracted over a small range of angles and so will not be considered in more detail here, but the V – H images show that there are no clear angle-dependent oscillations.

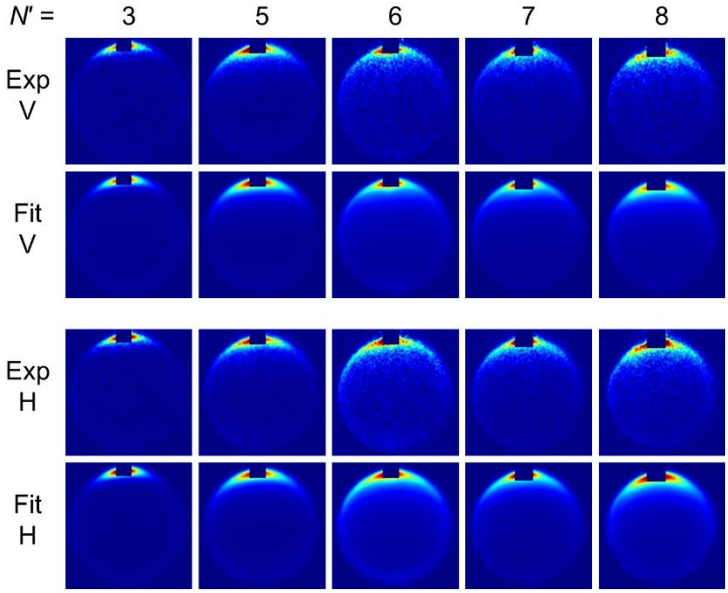

Figure 5.17: Example individual experimental and fitted V and H scattering images for the collisions of NO(A) with O_2 at a mean collision energy of 803 cm^{-1}, for final NO(A) rotational levels N' = 3, 5-8.

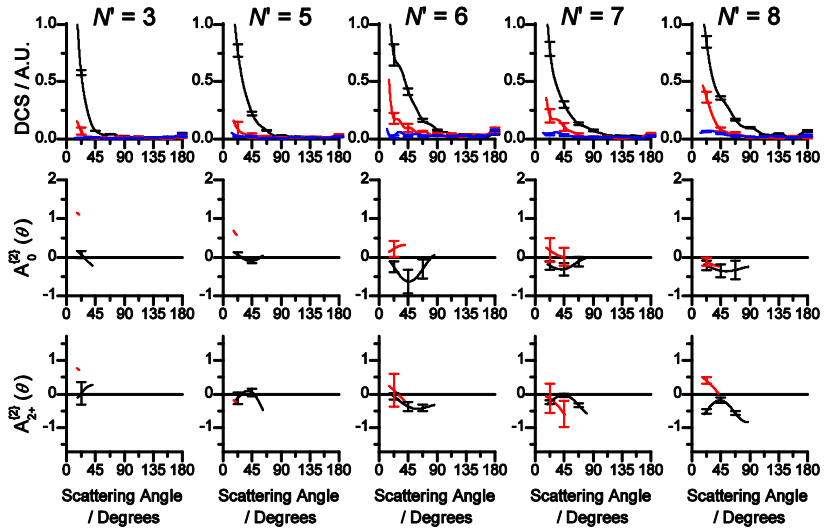

Figure 5.18: Differential cross sections and rotational alignment moments for the collisions of NO(A) with O_2 at a mean collision energy of 803 cm^{-1}, for final NO(A) rotational levels N' = 3, 5-8. Different plots on the same axis represent different degrees of rotational excitation of the O_2 molecule: black: j' = 1, red: j' = 7 and blue: j' = 11. Error bars represent 95% confidence limits.

5.3.4 Discussion

The main trends observed in the results obtained for the collisions of NO(A) with N_2, CO and O_2 will be discussed here. A visual inspection of the DCSs plotted in Figures 5.6, 5.14 and 5.18 suggests that the amount of rotational excitation of the unobserved collider is different for the different scattering systems, with N_2 undergoing the most rotational energy transfer and O_2 the least. This can be tested more rigorously by integrating the DCSs, to obtain the relative excitation probabilities to the different j', as shown in Figure 5.19. As was previously explained, the label j' does not represent a single $j \rightarrow j'$ transition, instead these results represent broad trends observed for collisions which have undergone different levels of rotational excitation. These results are further complicated, as the forward-scattered peak was masked during the fitting routine, and is thus not accounted for in these probabilities. This biases these results away from the low-j' states, where the forward-scattered peak is most intense. The forward-scattered peak in the image for the N' = 11 final NO(A) rotational level with the N_2 collider was not masked, meaning that the values are inconsistent with those from lower N', and therefore has been excluded from this plot. As was indicated above, the proportion of the unobserved collider in the

highest-energy j' is largest for collisions of NO(A) with N_2 and smallest with O_2. The simplest explanation for this trend is that, in the regions probed by the collisions, the NO(A)-N_2 PES is the most anisotropic with respect to the unobserved collider, and the NO(A)-O_2 PES is the least anisotropic.

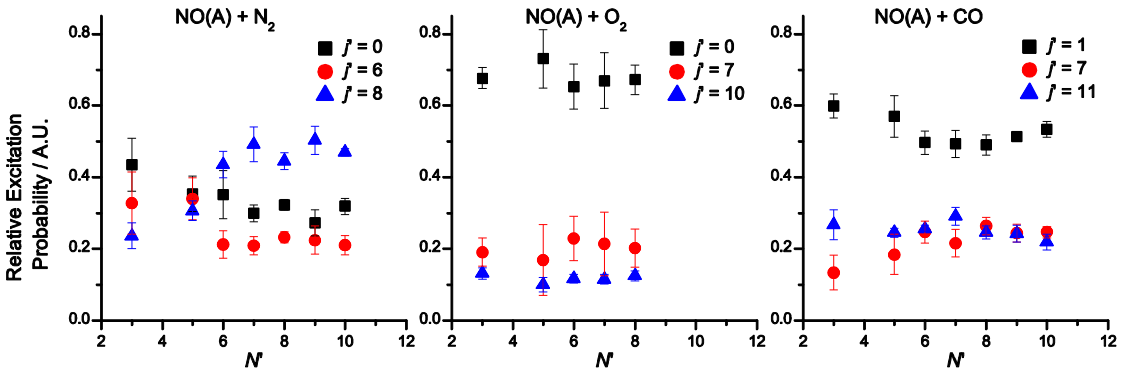

Figure 5.19: Relative excitation probabilities for the collision partners, for the collisions of NO(A) with left: N_2 at a mean collision energy of 790 cm^{-1}, centre: O_2 at a mean collision energy of 803 cm^{-1}, right: CO at a mean collision energy of 759 cm^{-1}. The low scattering angles, which were excluded from the fitting process are also excluded here. Error bars represent 95% confidence limits. The mean and standard errors of the values were obtained from the six individual fits performed for each data set.

A second trend is in the scattering angle distributions of the collisions with the different molecular collision partners. The scattering signal can be assigned to either the forward-scattered peak, which occurs from scattering through the attractive region of the PES, or sideward and backward scattering, which occurs from the repulsive region of the PES. The intensity of the sideward-scattered signal, relative to the forward-scattered peak cannot be quantitatively obtained from the DCSs, as the forward-scattered peak was excluded from the fitting process. The most convenient way to compare the different colliders is through the experimental V + H images, which are shown in Figure 5.20, in which the colour intensity scale is normalised to the intensity of the forward-scattered peak. These images clearly show that, for a given N', the sideward-scattered signal is most intense, relative to the forward-scattered peak, in the NO(A) + N_2 image and is least intense in the NO(A) + O_2 image. As rotational excitation of NO(A) is caused by anisotropy in the PES with respect to the NO(A) molecule, this trend can be explained based on the relative anisotropies of the attractive and repulsive regions of the PESs. If correct, this would indicate that the anisotropy of the attractive region, compared to the repulsive region is smallest for N_2 and largest for O_2.

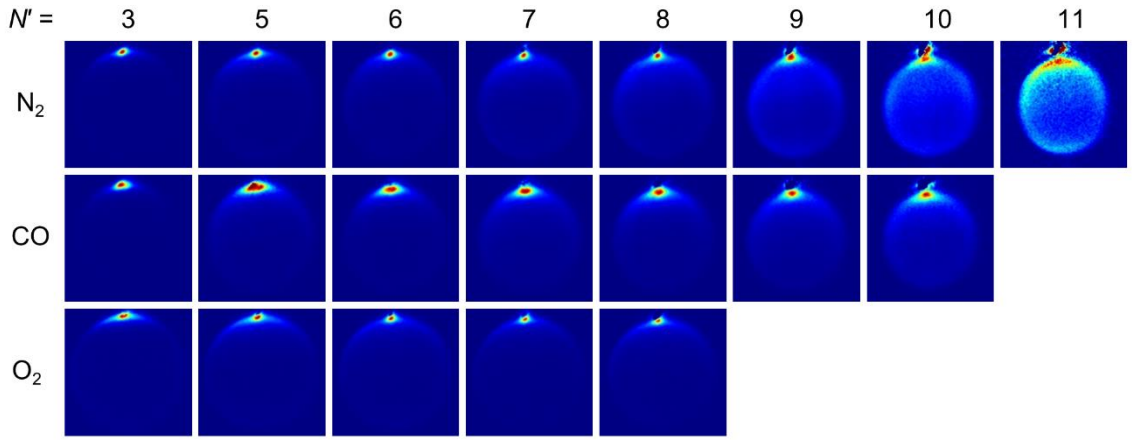

Figure 5.20: Experimental V + H images, averaged across all acquisitions for the collisions of NO(A) with N_2 at 790 cm^{-1}, CO at 759 cm^{-1} and O_2 at 803 cm^{-1}.

An alternate explanation for these two trends for the different collision partners is that this is an effect of quenching collisions. If collisions with certain parts of the PESs lead to quenching of the NO(A), then there will be a corresponding drop in the inelastically scattered signal. Of the molecular colliders examined here, the quenching cross section is largest for O_2 and smallest for N_2 (see Table 5.1). This interpretation suggests that quenching collisions occur on trajectories which would otherwise lead to the formation of highly-rotationally excited states of the collision partner, and scattering at higher angles. These two effects are consistent with quenching occurring for collisions which probe the repulsive region of the PES, as it is collisions which probe the repulsive region which lead to scattering at higher angles and high degrees of rotational excitation.

Clearly, the quenching collisions also affect the overall scattering signal. If the total collision cross sections and the molecular beam densities are similar for the three colliders (which seems like a reasonable assumption, given that they are three diatomic molecules with similar masses), larger quenching cross sections would correlate with lower signal levels for rotationally inelastic collisions. As conducted, the experiments in this thesis are not suitable for the measurement of the relative state-to-state signal levels, as the fluence of ionisation laser beam is varied to obtain similar signal levels for every measurement. Attempts were made to make quantitative measurements of the relative intensities for the different colliders, by fixing the fluence of the ionisation laser between measurements. However, instabilities in the signal levels, primarily caused by small fluctuations in the wavelengths and fluences of the laser beams, made these measurements extremely difficult. A qualitative sense of the relative signal levels can be obtained from the

maximum NO(A) rotational level, N' investigated for the different systems. The signal levels decrease with N', and experimental images were recorded to as high an N' as could be obtained with sufficient signal levels. Based on the highest maximum N' measured for the different systems, the largest signal was obtained for the N_2 collider, which has the smallest quenching cross section, and the lowest signal level was obtained for O_2, which has the largest quenching cross section. These results are consistent with the state-to-state rate coefficients for the NO(A) + N_2 and O_2 collisions measured by Lee *et al*.[178] In these measurements, for a given transition, the rate coefficient was typically a third to a half smaller for collisions of NO(A) with O_2 than with N_2, which was attributed to the effect of competing quenching collisions.

As was described above, the trends in the scattering angles and degrees of rotational excitation of the unobserved collider are consistent with the conical intersection located in the repulsive region of the PES. This conflicts with the proposed harpoon mechanism, which, as described in Section 5.1, proceeds through an ion-pair intermediate.[172] The harpoon mechanism is necessarily a long-range interaction, which would proceed through an initial conical intersection located in the attractive region of the PES. The harpoon mechanism would therefore be expected to lead to quenching collisions which deplete the population of NO(A) in the forward scattered peak, and measured in coincidence with low-j' collider products, as these are the products which are generated by scattering through the attractive region. This is the opposite of what is observed here, where it appears that quenching collisions depletes the population of NO(A) scattered at high angles, and in coincidence with high-j' collider products. The results presented here therefore imply that the NO(A) + CO and O_2 quenching collisions do not proceed via the harpoon mechanism.

A separate study of the quenching of NO(A) was conducted by Settersten *et al*., who measured the branching ratio of the NO(X) quenching product for collisions of NO(A) with O_2, CO and H_2O.[174] The branching ratios for these collisions were found to be consistent with a sudden quenching process, with a significant proportion of the quenched NO repopulating the lowest vibrational level of NO(X). In contrast, the harpoon mechanism would be expected to populate a much wider range of NO(X) vibrational levels. This is because the Franck-Condon factors lead to the preferential coupling of NO^+ with vibrationally excited levels of NO(X), over the ground vibrational level.[179]

Turning back to the relative excitation probabilities in Figure 5.19, for a given collision partner, the relative excitation probabilities for the different j' states remain surprisingly stable as a function of N'. There is some increase in the highest j' and corresponding decrease in the lowest j' as a function of N', but it is small. It would be expected that the collisions which probe the most anisotropic regions of the PES with respect to the NO(A) molecule would also probe the most anisotropic regions of the PES with respect to the collision partner. However, this is clearly not the case, indicating that the regions of the PESs which are anisotropic with respect to the NO(A) molecule are not necessarily anisotropic with respect to the unobserved collider. This means that the torque applied to the NO(A) molecule and the collision partner are not strongly correlated, and the rotational excitation of the two molecules is effectively independent.

5.4 High-Energy Collisions of NO($A^2\Sigma^+$) with N_2, CO and O_2

5.4.1 Experimental Conditions

Scattering images were recorded for the collisions of NO(A) with N_2, CO and O_2 at a second, higher, collision energy. In these measurements, 10% NO (BOC, 99.998%) was seeded in He (BOC, 99.999%) with a backing pressure of 3 bar to give a molecular beam with a speed distribution of mean 1,430 m s^{-1} and FWHM of 91 m s^{-1}. For the collisions of NO(A) with N_2, a molecular beam of neat N_2 (BOC, 99.999%), seeded at 5 bar to give a mean speed of 800 m s^{-1} and a FWHM of 74 m s^{-1} was used, giving a mean collision energy of 1,627 cm^{-1} and a FWHM of 173 cm^{-1}. For the collisions of NO(A) with CO, a molecular beam of neat CO (BOC, 99.999%), seeded at 5 bar to give a mean speed of 767 m s^{-1} and a FWHM of 74 m s^{-1} was used, giving a mean collision energy of 1,595 cm^{-1} and a FWHM of 178 cm^{-1}. For the collisions of NO(A) with O_2, a molecular beam of neat O_2 (99.999%, BOC), seeded at 5 bar to give a mean speed of 759 m s^{-1} and a FWHM of 72 m s^{-1} was used, giving a mean collision energy of 1,697 cm^{-1} and a FWHM of 138 cm^{-1}. The methods used to obtain these speed distributions is outlined in Sections 5.2.1 and 5.3.1.

For the high-collision energy collisions with N_2, experimental scattering images were recorded for final NO(A) rotational levels $N' = 3$, 5-11; for collisions with CO: $N' = 3$, 5-10; and for O_2: $N' = 3$, 5-8. Six individual images were recorded for each final rotational level, six individual images were recorded, with 72,000 camera shots, recorded across all V, H, signal and background frames, and with five scans of the probe laser wavelength over the NO(E ← A) Doppler profile.

5.4.2 Data Analysis

The analysis of the high-collision energy NO(A) + N_2, CO and O_2 scattering images was conducted in the same way as the low-collision energy, described in Sections 5.2.2 and 5.3.2. The choice of $j \rightarrow j'$ transitions, and the number of Legendre moments used to fit the images is provided in Tables 5.8-5.10. For every N' final rotational level, five Legendre moments were used to extract $A_0^{\{2\}}(\theta)$ and $A_{2+}^{\{2\}}(\theta)$, and one moment was used to extract $A_{1+}^{\{2\}}(\theta)$. The DCS and $A_{q+}^{\{2\}}(\theta)$ moments were all extracted using the $x = \cos(\theta)$ basis set. The forward-scattered peak was masked to reduce the number of Legendre moments required to extract the DCS. The DCS was truncated to exclude angles where fewer than 20% of the simulated ion strikes fell into the unmasked region, and the $A_{q+}^{\{2\}}(\theta)$ moments were truncated to exclude angles where fewer than 20% of the simulated ion strikes fell into the unmasked region, or where the DCS was less than 10% of its maximum reported value.

Table 5.8: Number of parameters used to extract the DCSs for the high-collision energy NO(A) + N_2 images.

	$j' = 0$	$j' = 10$	$j' = 14$
$N' = 3$	21	13	15
$N' = 5$	19	11	11
$N' = 6$	21	17	11
$N' = 7$	19	11	11
$N' = 8$	21	11	13
$N' = 9$	15	15	15
$N' = 10$	15	13	15
$N' = 11$	15	13	13

Table 5.9: Number of parameters used to extract the DCSs for the high-collision energy NO(A) + CO images.

	$j' = 0$	$j' = 10$	$j' = 14$
$N' = 3$	17	11	13
$N' = 5$	13	11	11
$N' = 6$	15	15	13
$N' = 7$	13	13	13
$N' = 8$	21	9	9
$N' = 9$	13	13	13
$N' = 10$	15	13	13

Table 5.10: Number of parameters used to extract the DCSs for the high-collision energy NO(A) + O_2 images.

	$j' = 1$	$j' = 11$	$j' = 17$
$N' = 3$	17	13	13
$N' = 5$	13	13	11
$N' = 6$	21	15	15
$N' = 7$	17	13	13
$N' = 8$	15	11	11

5.4.3 Results and Discussion

Newton diagrams for the NO(A) + N_2, CO and O_2 systems at the high-collision energy, overlaid with Newton diagrams are shown in Figure 5.21. Because of the greater spread of the collision energy distribution, a larger energy spacing of basis images is required to prevent significant cross-talk from occurring.

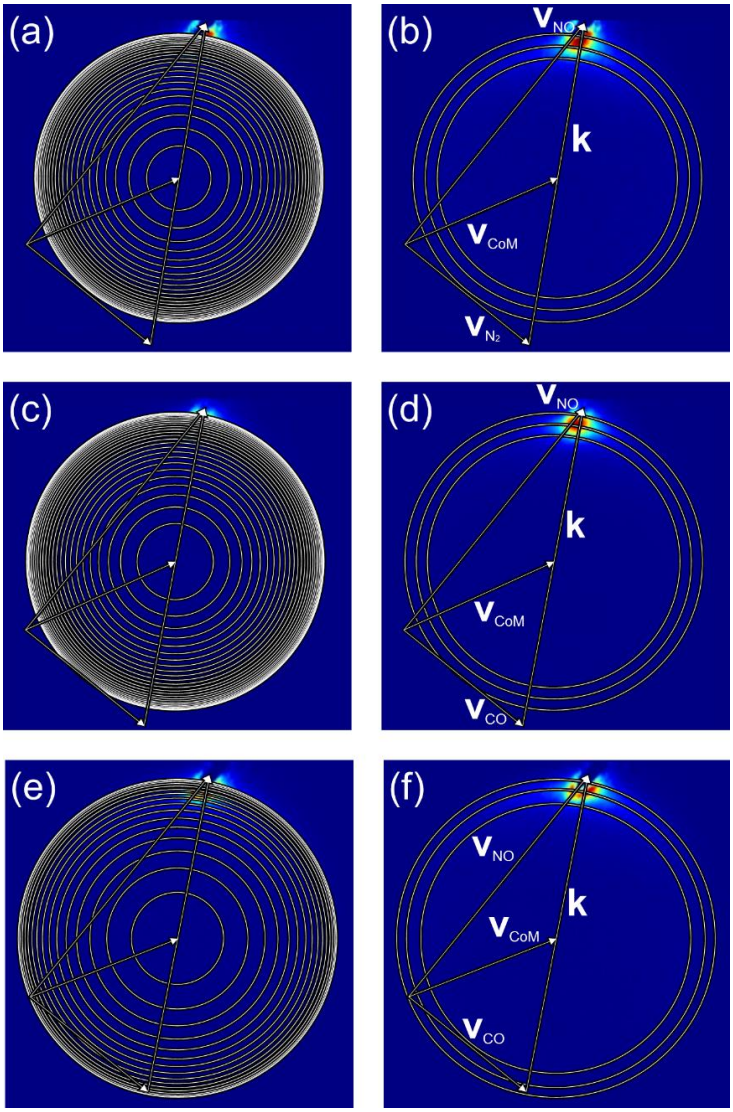

Figure 5.21: Experimental images for NO(A) final rotational levels $N' = 8$, with overlaid Newton diagrams for collisions with (a) and (b) N_2 at a mean collision energy of 1,627 cm^{-1}, (c) and (d) CO at a mean collision energy of 1,595 cm^{-1}, (e) and (f) O_2 at a mean collision energy of 1,697 cm^{-1}. Circles represent the velocity of NO scattered into the plane of the detector in coincidence with transitions of (a) all energetically accessible transitions from N_2 originating from $j = 0$ and 1 (see Table 5.7), (b) N_2 $j = 0 \rightarrow j' = 0$, 10 and 14, (c) all energetically accessible transitions from CO originating from $j = 0$ (see Table 5.6), (d) CO $j = 0 \rightarrow j'$ 0, 10 and 14, (e) all energetically accessible transitions from O_2 originating from $j = 1$ (see Table 5.7), (f) O_2 $j = 1 \rightarrow j' = 1$, 11 and 17.

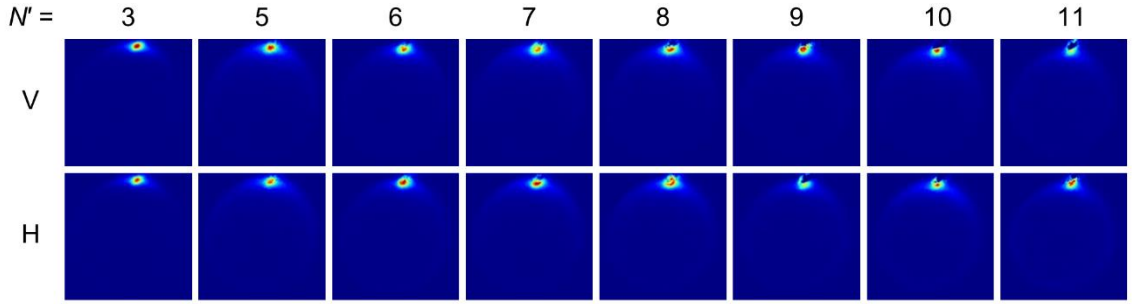

Figure 5.22: Experimental images, averaged over all individual acquisitions for the collisions of NO(A) with N_2 at a mean collision energy of 1,627 cm^{-1}, for both V and H probe laser polarisations, and final NO(A) rotational levels N' = 3, 5-11.

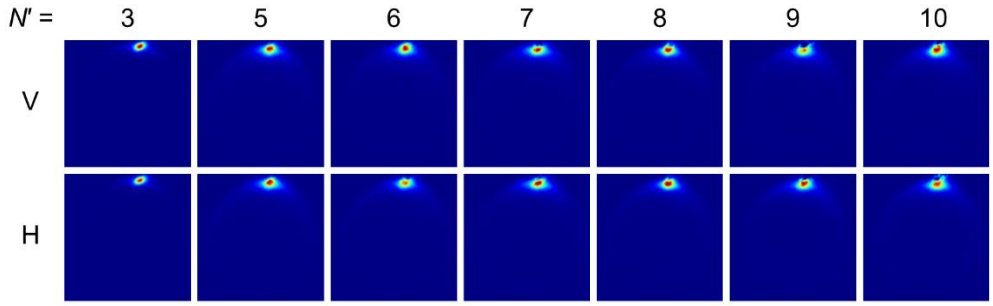

Figure 5.23: Experimental images, averaged over all individual acquisitions for the collisions of NO(A) with CO at a mean collision energy of 1,595 cm^{-1}, for both V and H probe laser polarisations, and final NO(A) rotational levels N' = 3, 5-10.

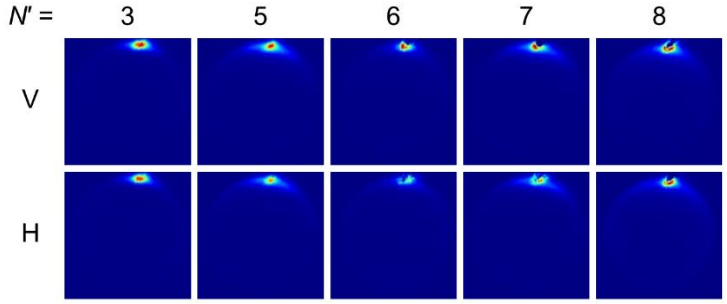

Figure 5.24: Experimental images, averaged over all individual acquisitions for the collisions of NO(A) with O_2 at a mean collision energy of 1,697 cm^{-1}, for both V and H probe laser polarisations, and final NO(A) rotational levels N′ = 3, 5-8.

The full range of experimental V and H images are shown for the high-energy NO(A) + N_2, CO and O_2 collisions in Figures 5.22, 5.23 and 5.24 respectively. All three systems are extremely forward scattered, with only a very small amount of signal observed outside of the forward scattered peak, even at the highest final NO(A) rotational levels. It is to be expected that these images are considerably more forward scattered than the low-collision energy images, due to the kinematic effect described in Chapter 3 for the NO(A) + Ne

scattering system. Differences between the V and H are still visible in these images, mainly in the differences in intensity of the forward scattered peak for the different polarisations, so there is clearly rotational alignment of the rotationally excited NO(A). These differences are made clearer in the V – H images shown in Figure 5.25 for the three systems.

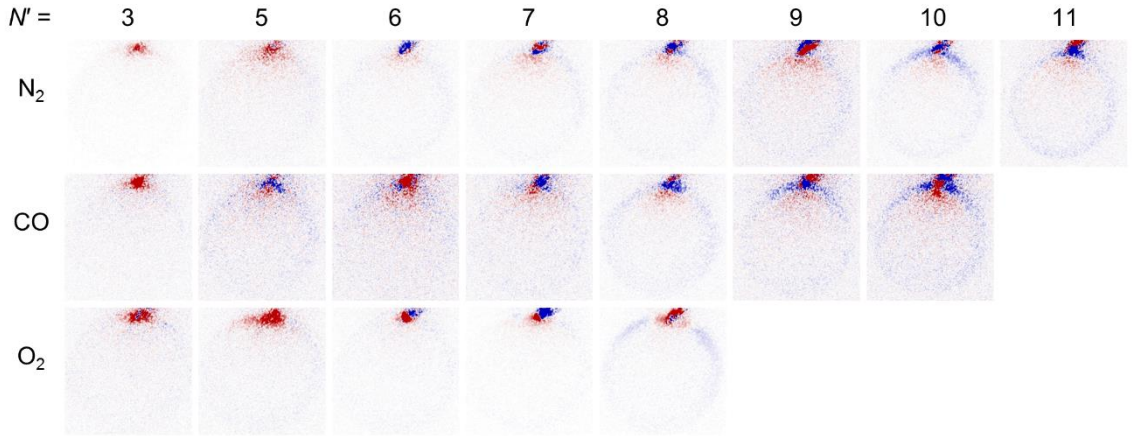

Figure 5.25: Experimental V – H images, averaged over all individual acquisitions for the collisions of NO(A) with top row: N_2 at a mean collision energy of 1,627 cm^{-1}, middle row: CO at a mean collision energy of 1,595 cm^{-1}, bottom row: O_2 at a mean collision energy of 1,697 cm^{-1},

For the high-energy NO(A) + N_2 collisions, example individual experimental and fitted images are compared in Figure 5.26, and the returned DCSs and $A_{q+}^{\{2\}}(\theta)$ moments are shown in Figure 5.27. Similar comparisons of individual experimental and fitted images, and returned DCSs and $A_{q+}^{\{2\}}(\theta)$ moments for the high-collision energy NO(A) + CO system are shown in Figures 5.28 and 5.29, and for the high-collision energy NO(A) + O_2 system in Figures 5.30 and 5.31. For all three high-collision energy systems, the DCSs are strongly peaked in the forward direction, and no higher-angle features are visible for any j' state. The $A_{q+}^{\{2\}}(\theta)$ moments are reliably returned over a narrow range of angles, and so it is not possible to draw any conclusions from them. However, the V – H images shown in Figure 5.25 indicate, as with the low-collision energy systems, there are no sharp angle-dependent oscillations in the moments.

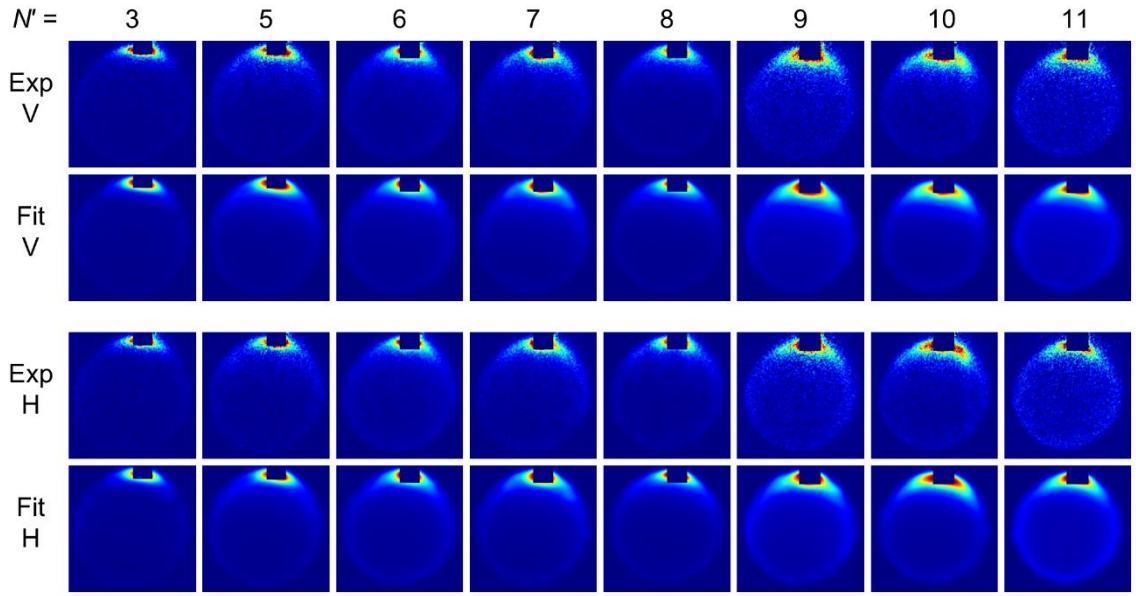

Figure 5.26: Example individual experimental V and H scattering images for the collisions of NO(A) with N_2 at a mean collision energy of 1,627 cm^{-1}, for final NO(A) rotational levels N' = 3, 5-11. Also shown are corresponding fitted images, simulating scattering circles for N_2 transitions $j = 0 \rightarrow j' = 0$, 10 and 14.

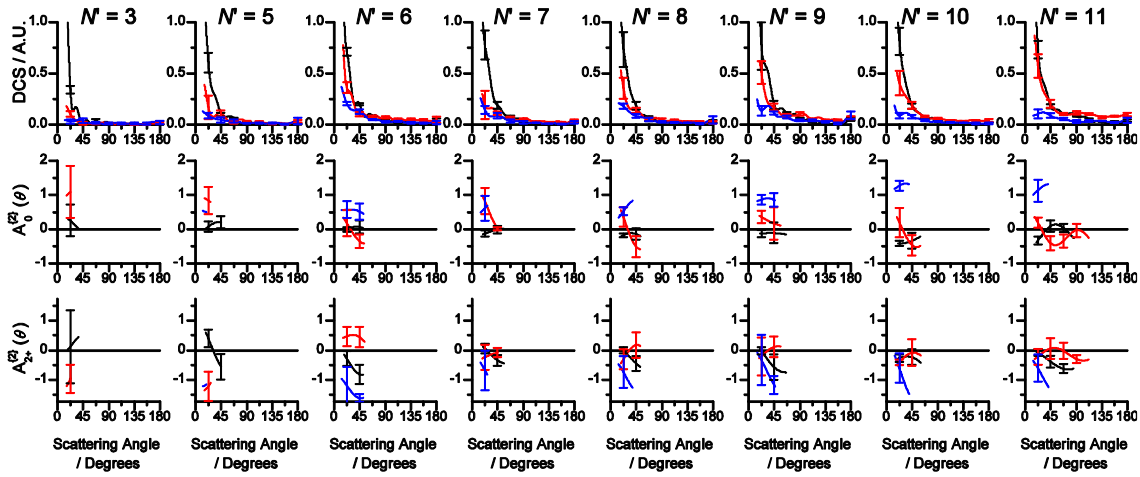

Figure 5.27: Differential cross sections and rotational alignment moments for the collisions of NO(A) with N_2 at a mean collision energy of 1,627 cm^{-1}, for final NO(A) rotational levels N' = 3, 5-11. Different plots on the same axis represent different degrees of rotational excitation of the N_2 molecule: black: j' = 0, red: j' = 10 and blue: j' = 14. Error bars represent 95% confidence limits.

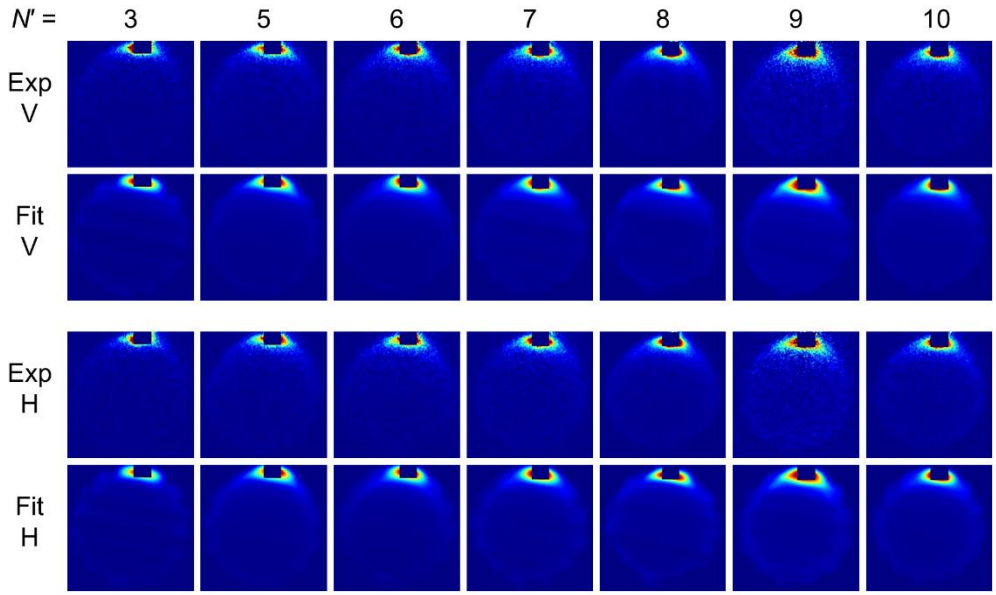

Figure 5.28: Example individual experimental and fitted V and H scattering images for the collisions of NO(A) with CO at a mean collision energy of 1,595 cm^{-1}, for final NO(A) rotational levels N' = 3, 5-10.

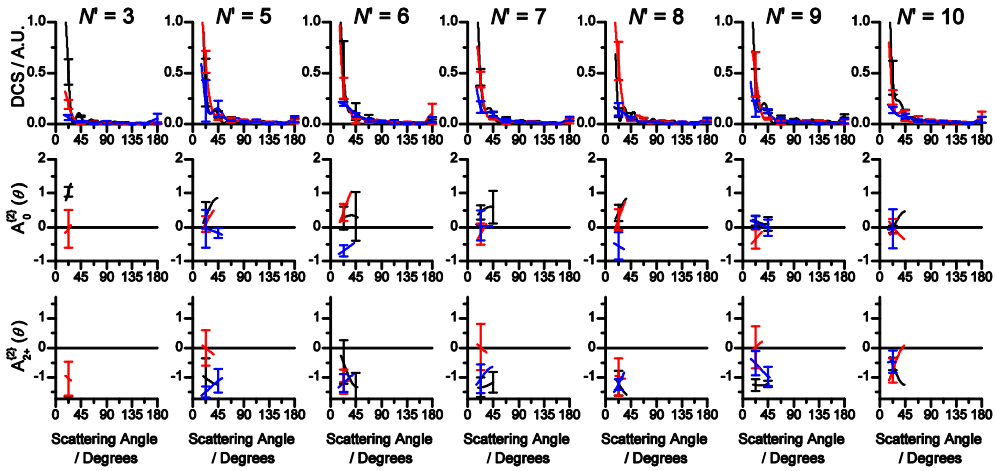

Figure 5.29: Differential cross sections and rotational alignment moments for the collisions of NO(A) with CO at a mean collision energy of 1,595 cm^{-1}, for final NO(A) rotational levels N' = 3, 5-10. Different plots on the same axis represent different degrees of rotational excitation of the CO molecule: black: j' = 0, red: j' = 10 and blue: j' = 14. Error bars represent 95% confidence limits.

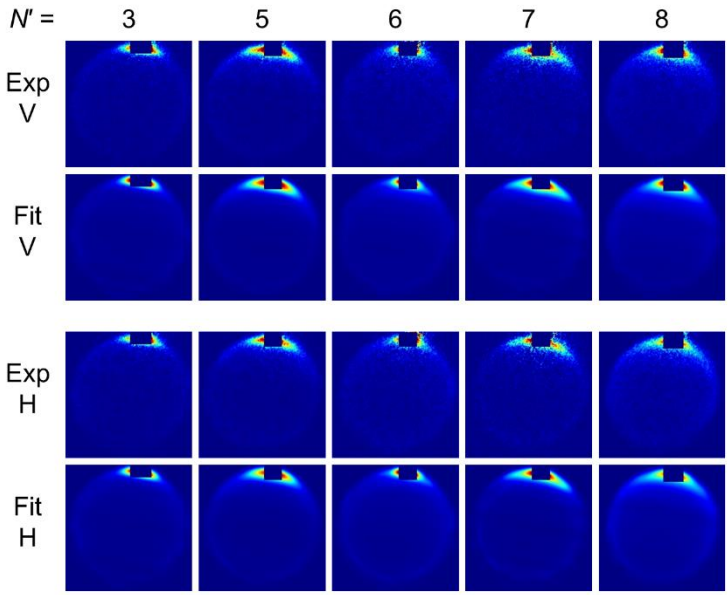

Figure 5.30: Example individual experimental and fitted V and H scattering images for the collisions of NO(A) with O_2 at a mean collision energy of 1,697 cm^{-1}, for final NO(A) rotational levels N' = 3, 5-8.

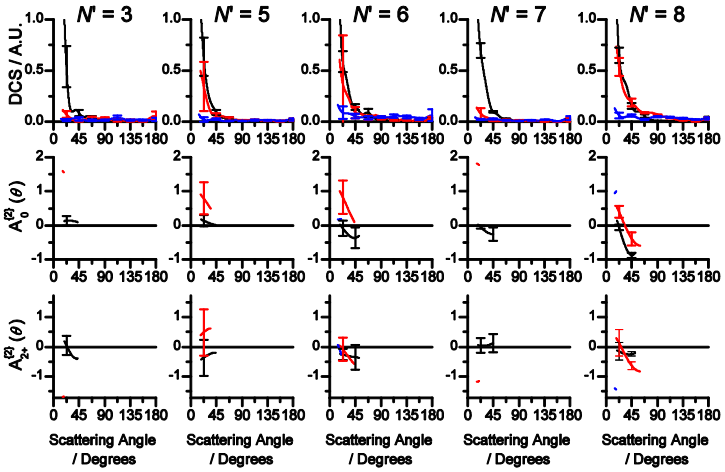

Figure 5.31: Differential cross sections and rotational alignment moments for the collisions of NO(A) with O_2 at a mean collision energy of 1,697 cm^{-1}, for final NO(A) rotational levels N' = 3, 5-8. Different plots on the same axis represent different degrees of rotational excitation of the O_2 molecule: black: j' = 1, red: j' = 11 and blue: j' = 17. Error bars represent 95% confidence limits.

An interesting feature of the quenching collisions is how the quenching cross section varies with collision energy. The quenching cross sections for NO(A) + N_2 and O_2 remain similar across different collision energies, while the NO(A) + CO quenching cross section dramatically increases, due to a small energetic barrier.[172,176] It would therefore be expected that the trends in the j' populations and scattering-angle distribution observed for the low energy collisions would change to reflect this difference. To compare the

scattering-angle distributions, the V + H scattering images are shown for the three high-collision energy systems in Figure 5.32. However, because the scattering images are so extremely forward-scattered, it is not possible to tell whether the distribution of the scattering signal has changed significantly in the NO(A) + CO image, relative to the NO(A) + N_2 and O_2 images. Similarly, the lack of signal outside of the forward-scattered peak leads to large errors in the relative excitation probabilities, which are therefore not shown. Unfortunately, with the current results, it is not possible to draw any conclusions about the trends in the distribution of the signal. It is possible that further analysis of these experimental images, especially fitting of the forward-scattered peak, could lead to more conclusive results for these systems.

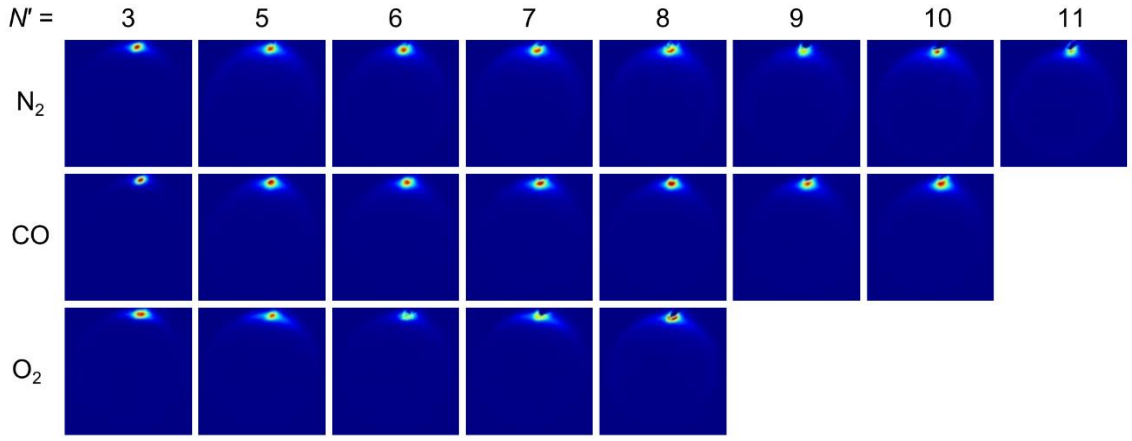

Figure 5.32: Experimental V + H images, averaged across all acquisitions for the collisions of NO(A) with N_2 at 1,627 cm^{-1}, CO at 1,595 cm^{-1} and O_2 at 1,697 cm^{-1}.

5.5 Conclusions

In conclusion, an extended version of the fitting routine has been used to analyse scattering images for the collisions of NO(A) with diatomic molecules. The differential cross sections and rotational alignment moments were recorded for the inelastic collisions of NO(A) with N_2, CO and O_2 as a function of energy transferred to the unobserved collision partner.

These results were compared to the results of NO(A) + rare gas experiments of Chapter 3 to determine as much information as possible about the currently unknown NO(A)-N_2,

CO and O_2 PESs. All three PESs appeared to contain an attractive well, which is anisotropic with respect to both NO(A) and the unobserved collider molecules. Rotational rainbows are seen in the NO(A) + N_2 DCS, with a similar structure to the NO(A) + rare gas results, indicating a broadly similar level of anisotropy in the repulsive region of the PES. Similar comparisons cannot be made for the NO(A) + CO and O_2 collisions, as differences in the dynamics are likely to be influenced by quenching collisions, which prevent certain collisions from leading to purely rotationally energy transfer. For all systems, the degree of rotational excitation of the NO(A) and unobserved collider was not strongly correlated, implying that the anisotropy of the PES is different with respect to the NO(A) and unobserved collision partner.

Qualitative differences in the overall signal levels were correlated with the size of the quenching cross sections for the different collision partners, with a larger quenching cross section corresponding to lower observed signal levels. Trends in the product rotational distribution of the unobserved collider, and the distribution of scattering angles could be attributed to differences in the anisotropy of the three PESs or to the conical intersection preventing certain collision from leading to purely rotationally energy transfer. If the cause of these trends is quenching collisions, it implies that the conical intersection is located on the repulsive region of the PES. This is inconsistent with the harpoon model for quenching, for which the quenching processes occur primarily through long-range interactions.

Scattering images were recorded and analysed for the NO(A) + N_2, CO and O_2 scattering systems at a second, higher collision energy. These results were very strongly forward scattered, which combined with the forward-scattered peak being masked in the fitting routine, made the results extremely difficult to interpret. Further analysis without masking the forward-scattered peak may provide more information about the systems.

5.6 Appendix: Selection of Optimal Basis Image Energies

Ideally, the molecular-collider fitting routine would fit a basis image corresponding to every accessible transition of the collision partner. For the molecular-collision partners

examined in this chapter however, the rotational constants are small relative to the collision energy, and so using the full range would lead to significant overlap of the intensity of the different basis images. This means that in the fitting process, intensity of a given pixel could be attributed to multiple basis images, which would lead to "cross-talk" between the DCSs returned by the different j' states. This would cause the fitting process to be unstable and lengthy, with no guarantee that the returned values are correct. Ideally the energy spacing of the basis images should be as small as possible, to extract the maximum amount of information from the scattering images, while simultaneously being large enough to avoid significant cross-talk.

Because the NO(A) + N_2 DCSs were not initially known, the corresponding images were not ideal to use for optimisation of the fitting routine, as there was no way of testing whether the returned results were correct. Instead, scattering images were simulated with a known DCS and fitted to see if the input DCSs could be recovered using the SVD algorithm (see Section 2.10.2).

To begin, a scattering image was simulated with two transitions in the unobserved collider, corresponding to energy transferred of 0 and 100 cm^{-1}. This image was simulated using the molecular beam speed distributions of the low-collision energy NO(A) + N_2 system, and with DCSs corresponding to the $N' = 5$ and 12 QS DCSs of the NO(A) + He scattering system from the PES of Kłos *et al.*[14] (see Chapter 4). The input DCSs and the simulated scattering image are shown in Figure 5.33. The simulated scattering image was analysed to extract the DCSs, with basis images corresponding to energies transferred to the unobserved collider of 0 and 100 cm^{-1} (the energies used in the initial simulation of the image). Additionally, DCSs were fit to regularly spaced energies between 0 and 100 cm^{-1}, for which there no scattering signal simulated. If there is no cross-talk occurring, the returned DCSs for 0 and 100 cm^{-1} will match the input DCSs, and the intermediate energies will return DCSs with zero amplitude. The returned DCSs are shown in Figure 5.34. The amount of cross-talk is comparatively low for energy spacing down to 33 cm^{-1}, but it is very clearly affecting the DCSs with a spacing of 25 cm^{-1} or lower.

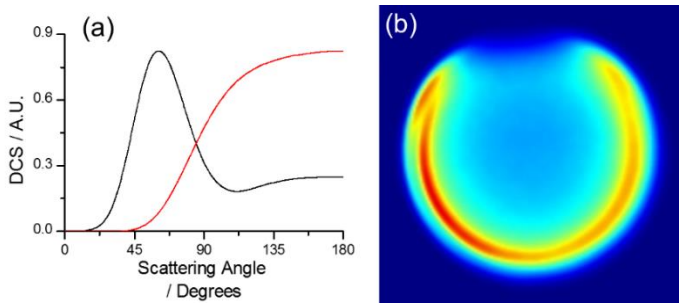

Figure 5.33: (a) DCSs used to simulate the basis images corresponding to energy transfer to the unobserved collider of 0 cm^{-1} (black) and 100 cm^{-1} (red). (b) Simulated scattering image used to test the fitting routine.

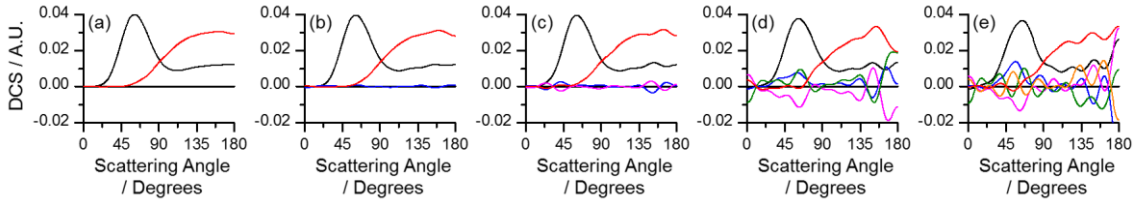

Figure 5.34: DCSs fitted to the simulated image in Figure 5.33(b), with basis images in steps of energy (a) 100 cm^{-1}, (b) 50 cm^{-1}, (c) 33 cm^{-1}, (d) 25 cm^{-1}, (e) 20 cm^{-1}. Black line: DCS fitted for the basis image at 0 cm^{-1}, red line: DCS fitted for the basis image at 100 cm^{-1}, blue, magenta, green and orange: DCSs fitted for basis images between 0 and 100 cm^{-1}.

Next, a scattering image was simulated with energy spacings more closely matching those of the NO(A) + N_2 system. The scattering image (shown in Figure 5.35) were simulated using DCSs corresponding to $j = 0 \rightarrow j' = 0$, 2, 4, 6, 8 and 10, and $j = 1$ to $j' =$ 1, 3, 5, 7 and 9 (see Table 5.3). The DCSs corresponded to the results of QS calculations for the NO(A) + He system, using the PES of Kłos *et al.*,[14] and were chosen as they smoothly progress from forward to backward scattering as j' increases, in a physically plausible manner. For the elastic, $j' = 0$ and 1 transitions, NO(A) + He DCSs for $N' = 3$ was used, and for the transitions to $j' = 2$-10, NO(A) + He DCSs for $N' = 4$-12 were used. This simulated image was analysed using basis images with different energy spacing. Figure 5.36 shows the DCSs used to simulate the scattering image at the different j', as well as DCSs extracted by fitting to $j' = 0$, 4, 6, 8 and 10. Fitting this selection of basis images, for which the smallest energy gap is 40 cm^{-1}, reproduces the inputted DCSs well, notably including the rotational rainbow angles, and there is only a small amount of cross-talk visible. Repeating these fits at a finer energy spacing of basis images led to a considerably larger degree of cross-talk occurring. The presented results both simulated and fitted the scattering images with an assumed isotropic distribution of rotational alignment moments, but very similar results were obtained when simulating the scattering

image with a non-isotropic rotational alignment, corresponding to the KA moments, and fitting the DCS along with the rotational alignment moments.

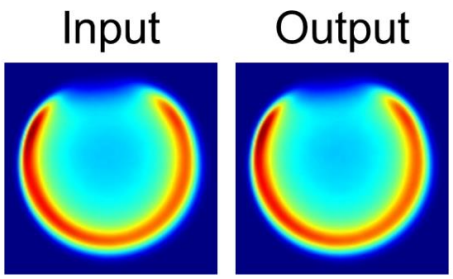

Figure 5.35: Scattering image simulated from the conditions of the NO(A) + N_2 experiment, and the DCSs for the NO(A) + He scattering system (see main text for details). Right: Fitted image returned by the fitting procedure of the simulated image.

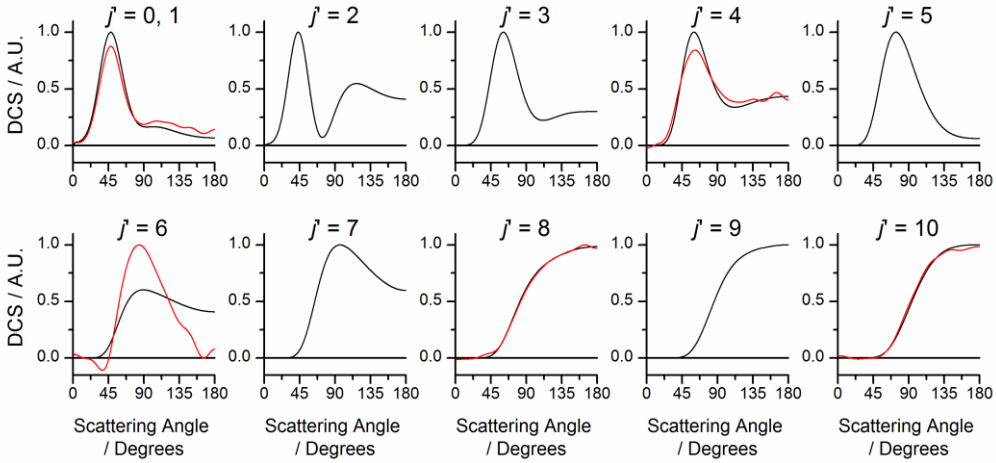

Figure 5.36: Black lines: DCSs used to simulate the scattering image shown in Figure 5.35. Red lines: DCSs returned by fitting the simulated image.

Fitting these simulated images established that, under ideal conditions, the smallest energy spacing possible for the basis images is approximately 40 cm^{-1} in the NO(A) + N_2 images (approximately half the FWHM of the collision energy spread). Using these conditions to fit real NO(A) + N_2 scattering images resulted in significant cross-talk, indicating that the experimental noise, and sharper features of the NO(A) + N_2 DCS, required a larger energy spacing of the basis images. As described in Section 5.4.3, the energy spacing for the basis image was required to be approximately the FWHM of the collision energy distribution. Independent SVD fits were made to optimise the energy spacing of the basis images for every quantum state of every system. A subset of these fits are shown in Figure 5.37 for the $N' = 11$ image of the NO(A) + N_2 system. The final fitting was conducted with basis images corresponding to final N_2 rotational levels $j' = 0$, 6 and 8 (ΔE_{N2} = 0, 84 and 144 cm^{-1} respectively), as shown in Figure 5.37(b). Here, the

DCSs show a minimal amount of cross-talk and the experimental and fitted images are very similar. The scattering images were also fitted using additional basis images, corresponding to more rotationally excited N_2, with $j' = 0$, 6, 8 and 10 (ΔE_{N2} = 0, 84, 144 and 220 cm^{-1} respectively), and $j' = 0$, 6, 8 and 12 (ΔE_{N2} = 0, 84, 144 and 312 cm^{-1} respectively), as shown in Figures 5.37(c) and (d). The fitted images contain clearly distinct scattering signal, corresponding to highly rotationally excited N_2, $j' = 10$ and 12 products, which are not visible in the experimental image. The corresponding DCSs for these additional N_2 rotational levels have an extremely low amplitude, and are nearly isotropic. It appears that there is little to no real contribution to the scattering signal for these j' rotational levels, and the small amplitude is consistent with fitting to the high-frequency noise of the experimental image. As a result, the fitting routine has been limited to fitting N_2 rotational levels up to $j' = 8$. Figure 5.37(e) shows the fitted image and returned DCSs, for fitting with basis images corresponding to final N_2 rotational levels, j' = 0, 4, 6 and 8 (ΔE_{N2} = 0, 40, 84 and 144 cm^{-1} respectively), showing the effect of using a more finely spaced range of energies for the basis images. While the fitted image resembles the experimental image, correlations in the sharp fluctuations in the DCSs show that there is a large amount of cross-talk occurring, and that a larger energy spacing of the basis images is required.

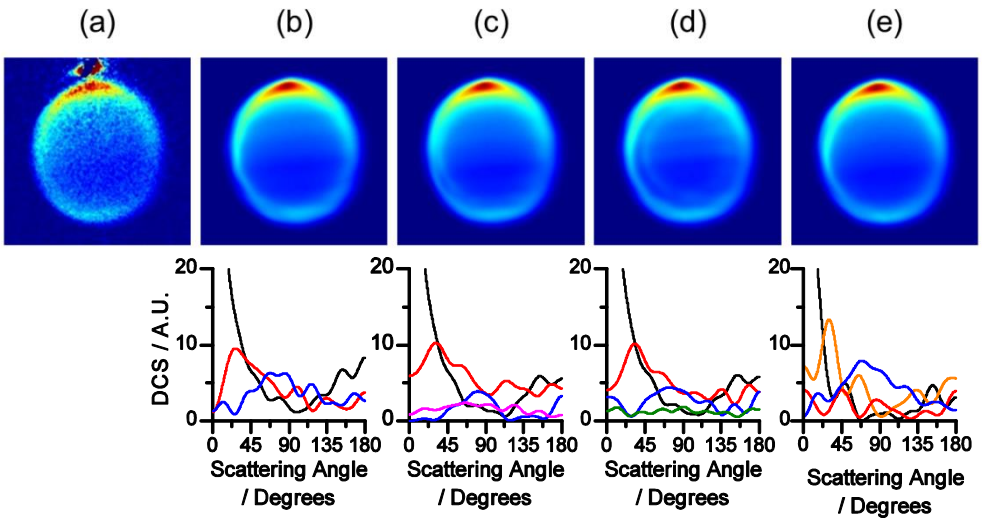

Figure 5.37: (a) Experimental NO(A) + N_2 V + H scattering image, averaged over all acquisitions. (b)-(e): Simulated V + H images and differential cross sections returned by the fitting routine, for different combinations of N_2 rotational transitions. (b): $j' = 0$, 6, 8; (c): $j' = 0$, 6, 8, 10; (d): $j' = 0$, 6, 8, 12; (e): $j' = 0$, 4, 6, 8. Top row: simulated images. Bottom row: Returned differential cross sections, Black: $j' = 0$, orange: $j' = 4$, red: $j' = 6$, blue: $j' = 8$, magenta: $j' = 10$, green: $j' = 12$.

Chapter 6

Conclusions and Outlook

6.1 Conclusions

This thesis presented experiments which studied vector correlations in the rotationally inelastic collisions of NO($A^2\Sigma^+$) with a wide range of atomic and molecular partners, in the form of the DCS and the rotational alignment moments. These experimental results were used in combination with QS calculations to understand the forces which govern the collisions. The experimental measurements were made using a newly-constructed CMB VMI apparatus, the methodology of which was described in Chapter 2.

Chapter 3 described experiments probing the inelastic collisions of NO(A) with the rare gas atoms Ar and Ne. The NO(A) + Ar DCS contained two distinct types of scattering signal: a sharp peak at 0°, and a broader peak, or set of peaks, at higher angles. QS calculations using the PES of Kłos *et al.*[14] showed that collisions which probe the attractive region of the PES led to the forward-scattered peak, while collisions which probed the repulsive region led to the higher angle, rotational rainbow peaks. There was good agreement between experiment and theory for the structure of the forward scattered peak, which showed that the attractive region of the PES was modelled accurately. While the general structure of the rotational rainbow peaks predicted in the QS DCS was in

agreement with the experiment, significant specific differences for high N' states showed that there are inaccuracies in the repulsive region of the PES.

A similar forward-scattered peak was observed in the DCS for the NO(A) + Ne system at two collision energies, which was not returned by the QS calculations using either the PESs of Pajón-Suárez *et al*.[148] or Cybulski and Fernández.[150] This indicated that the depth and anisotropy of the attractive region is significantly underestimated in both PESs. An anomalous peak, present at high-N' in both sets of high-collision energy QS DCSs, but not in the experimental results indicated that there is an error present in the repulsive region of the PESs, which was only accessible for the high-energy collisions. Other than these two shortcomings, there was generally very good agreement between the experimental and QS DCSs, indicating that, while there are specific inaccuracies, the general form of the PESs is accurate. Comparison of the rotational rainbow angles indicated that the anisotropy of the repulsive region in the PES calculated by Cybulski and Fernández is more accurate, with it being underestimated in the PES of Pajón-Suárez *et al*.

In contrast to the hard-shell KA model, sharp angle-dependent fluctuations were observed in the rotational alignment moments in both the NO(A) + Ar and Ne collisions. These oscillations were reproduced in the QS calculations, which used the shallow-gradient literature *ab initio* PESs for the systems. These oscillations tracked closely with features in the DCS, indicating that the same process is responsible for both features. Further theoretical work will be required to fully understand this phenomenon.

DCSs were recorded in experiments probing the collisions of rotationally excited, NO(A, N = 1 and 2) with Ne, demonstrating that experiments starting from initially rotationally excited states of NO(A) are possible. The DCSs contained clear parity-dependent features, where collisions which populated a given N' were typically similar from initial rotational levels N = 0 and 2, but different from N = 1.

Experiments studying the inelastic collisions of NO(A) with He and D_2 were described in Chapter 4. The experimental NO(A) + He DCSs and rotational alignment moments were compared to the results of QS calculations using the PES of Kłos *et al*.[14] The

experimental and QS DCSs had excellent, near-quantitative agreement across all final NO(A) rotational levels, showing that the PES is extremely accurate in the regions probed by the collisions. A single rotational rainbow peak was present for every final NO(A) rotational level, and the lack of a forward-scattered peak confirms that the NO(A)-He PES does not have a significant attractive region. Experimental and QS rotational alignment moments were also compared for the NO(A) + He collisions. There was good agreement for $A_0^{\{2\}}(\theta)$ and $A_{2+}^{\{2\}}(\theta)$, adding further confidence to the accuracy of the PES. However, $A_{1+}^{\{2\}}(\theta)$ was typically much more positive in the experimental moments than in the results of QS calculations, which appeared to be an experimental artefact, rather than a real dynamical effect. While no sharp, angle-dependent fluctuations were observed in the NO(A) + He rotational alignment moments, significant deviations from the KA predictions were observed, which were particularly large at high-N'.

Because the kinematics of the NO(A) + He and D_2 collisions are identical, differences in the results obtained for the two systems were used to provide insight into the NO(A)-H_2 PES. The similarity of the DCSs and rotational alignment moments for the two systems shows that the two PESs share the same general structure. The NO(A) + D_2 DCS was consistently more forward scattered at a given N', which showed that the repulsive region of the NO(A)-D_2 PES is more anisotropic than the NO(A)-He PES. There was no evidence for rotational excitation of the D_2 collider, indicating that the NO(A)-D_2 PES is not very anisotropic with respect to the orientation of the D_2 molecule. All of these results are qualitatively consistent with the features of the recent *ab initio* NO(A)-H_2 PES calculated by Pajón-Suárez *et al.*[163]

Chapter 5 investigated the collisions of NO(A) with important molecules in atmospheric and combustion systems: N_2, O_2 and CO. DCSs and rotational alignment moments were extracted as a function of rotational excitation of the unobserved collision partner using an extended version of the analysis routine. The DCS and $A_0^{\{2\}}(\theta)$ were successfully extracted from the experimental images, however the routine could not always distinguish $A_{2+}^{\{2\}}(\theta)$ for different transitions of the collision partner.

The structure of the DCSs for the NO(A) + N_2, O_2 and CO systems broadly matched the NO(A) + Ar and Ne systems, with a forward scattered peak attributed to scattering through the attractive region and rotational rainbow peaks caused by scattering from the repulsive region of the PES. There were clear trends in the DCSs for the rotationally inelastic collisions of NO(A) with N_2, O_2 and CO. Collisions with N_2 led to the highest degree of rotational excitation of the unobserved collision partner, and the most scattering at higher angles, while collisions with O_2 led to the lowest degree of rotational excitation and were the most forward scattered. These two trends are consistent with collisions with the repulsive region of the PES leading to quenching, rather than purely rotationally inelastic scattering. This is inconsistent with the proposed harpoon mechanism, which involves the quenching process being instigated by long-range forces.

6.2 Outlook

The experiments presented in this thesis represent an initial survey of the collisions of NO(A) with a range of atomic and diatomic partners. There are a number of potential follow-up experiments which could extend these results.

The first priority should be to complete the theoretical work alluded to in the previous chapters, which could be conducted in parallel with new experimental measurements. The fluctuations observed in the rotational alignment moments in the NO(A) + Ar and Ne collisions can be investigated using a range of theoretical methods to determine their origin. More in-depth analysis of the current QS calculations could provide a useful insight, such as whether a certain $m \rightarrow m'$ transition is responsible for these features. Quasi-classical trajectory calculations would show whether the effect is classical or quantum in nature, based on whether the fluctuations are reproduced in the results. Finally, calculations using model potentials could be used, with features of the literature PESs modified or removed, to determine which regions of the PES affect these fluctuations.

Further QS calculations could be conducted using the *ab initio* NO(A)-H_2 PES recently calculated by Pajón-Suárez *et al.*[163] This would test the accuracy of the PES, and may also illuminate some features in the NO(A)-D_2 experimental results which were not considered in Chapter 4. If a similar PES was prepared for the NO(A) + N_2, O_2 or CO systems, similar calculations could also be performed. However, the much greater number of electrons in these systems makes them much more computationally challenging, and so it is not likely that one will be calculated in the near future.

The most obvious follow-up experiments would involve the exact same techniques used in this thesis, applied to study the collisions of NO(A) with yet more species. These experiments would require very little preparation, and, as has been shown in this thesis, would yield a large amount of information about the systems. Some possible collision partners which could be investigated include Kr, Xe, CH_4 and CO_2. Additionally, the experiment could be modified to allow for the detection of collision-induced orientation, in the form of the $A_{1-}^{\{1\}}(\theta)$ moment, which the experiment is also able to measure.

As was shown in Chapter 3, different spectroscopic transitions can be used to prepare NO(A) in different quantum states. Experiments could prepare NO(A) in higher rotational levels that $N = 2$, however, doing so would lead to lower signal levels, as the NO(X) would have to be in rotational levels $j \geq 1.5$. These lower signal levels could be offset by saturating the probe laser in the 1 + 1′ REMPI scheme, which would improve the signal levels, at the expense of sensitivity to the rotational alignment of the scattered NO(A). Similarly, experiments could be conducted in which NO(A) is prepared in a vibrationally excited state, by excitation on a transition in the A-X(1,0) band.

As was discussed in Section 1.3.4, polarised lasers can be used to prepare a sample of molecules with an initial rotational angular momentum polarisation. Typically, CMB experiments, including the experiments in this thesis, investigate the collisions of molecules with an initially isotropic rotational distribution. A plausible experiment which could be conducted would have a circularly polarised preparation laser propagating parallel to **k**, which if tuned to the $R_{21}(0.5)$ transition used in Chapter 3, would enable NO(A, $v = 0$, $N = 2$, $j = 1.5$) to be generated with a non-zero $A_0^{\{1\}}$ moment. A circularly polarised probe laser could then be used to measure how much of this orientation is

transferred to the scattered NO(A) as a function of scattering angle, in the form of $A_0^{\{1\}}(\theta)$. This would be a ***k*-*j*-*k′*-*j′*** four-vector correlation.

Quenching collisions were discussed in Chapter 5, with their effect on the results obtained for the rotationally inelastic collisions of NO(A) with CO and O_2. An obvious continuation of this experiment would be to investigate the quenched products, thereby probing the quenching collisions directly. For the quenching of NO(A), the product NO(X) would be moving at a much higher speed than the experiments in this thesis, as a large proportion of the electronic energy would most likely be converted into translation of the recoiling colliders. Therefore, such an experiment would require a significant redesign of the experimental apparatus, especially the ion optics, in order to detect the quenched NO(X). An alternate approach would be to detect the collision partner, for example D in the NO(A) + D quenching collision. The speed distribution of the collision partner would correlate with the quantum state distribution of the quenched NO.

All of the above potential experiments involve studying the collisions of NO(A), but the apparatus could also be modified to allow for collisions of other diatomic molecules to be investigated. CH would be an interesting choice, while its collisions have been studied using scalar methods,[180–182] there have been no studies of vector correlations using CMB experiments. These possible experiments could either study the collisions of the ground $X^2\Pi$ state, or an excited state. Collisions with the $A^2\Delta$ state would be especially interesting, as they can induce electronic energy transfer in CH to form the $B^2\Sigma^-$ state.[182]

References

1 R. D. Levine and R. B. Bernstein, *Molecular Reaction Dynamics and Chemical Reactivity*, Oxford University Press, 1987.

2 A. Schiffman and D. W. Chandler, *Experimental measurements of state resolved, rotationally inelastic energy transfer*, 1995, vol. 14.

3 A. J. McCaffery, M. J. Proctor and B. J. Whitaker, *Annu. Rev. Phys. Chem.*, 1986, **37**, 223.

4 M. Gryziński, *Phys. Rev.*, 1965, **138**, 336.

5 G. W. Flynn, C. S. Parmenter and A. M. Wodtke, *J. Phys. Chem.*, 1996, **100**, 12817.

6 F. Wilkinson, *Q. Rev. Chem. Soc.*, 1966, **20**, 403.

7 P. Casavecchia, N. Balucani and G. G. Volpi, *Annu. Rev. Phys. Chem.*, 1999, **50**, 347.

8 A. Teslja and J. J. Valentini, *J. Chem. Phys.*, 2006, **125**, 132304.

9 L. J. Butler and D. M. Neumark, *J. Chem. Phys.*, 1996, **100**, 12801.

10 W. M. Gelbart, *Ann, Rev, Phys, Chon,* 1977, **28**, 323.

11 S. C. Althorpe and D. C. Clary, *Annu. Rev. Phys. Chem.*, 2003, **54**, 493.

12 P. Atkins and R. Friedman, *Molecular Quantum Mechanics, fourth edition*, Oxford University Press, 2005.

13 P. Atkins and J. de Paula, *Atkins' Physical Chemistry*, Oxford University Press, 2007.

14 J. Kłos, M. H. Alexander, R. Hernández-Lamoneda and T. G. Wright, *J. Chem. Phys.*, 2008, **129**, 244303.

15 M. S. Child, *Molecular Collision Theory,* Academic Press, 1974.

16 M. Yang and R. O. Watts, *J. Chem. Phys.*, 1994, **100**, 3582.

17 A. Gijsbertsen, H. Linnartz and S. Stolte, *J. Chem. Phys.*, 2006, **125**, 133112.

18 S. Bosanac, *Phys. Rev. A - At. Mol. Opt. Phys.*, 1980, **22**, 2617.

19 J. Onvlee, S. N. Vogels, A. Van Der Avoird, G. C. Groenenboom and S. Y. T. Van De Meerakker, *New J. Phys.*, 2015, **17**, 055019.

20 J. Onvlee, S. D. S. Gordon, S. N. Vogels, T. Auth, T. Karman, B. Nichols, A. van der Avoird, G. C. Groenenboom, M. Brouard and S. Y. T. van de Meerakker, *Nat. Chem.*, 2017, **9**, 226.

21 C. J. Eyles, M. Brouard, C.-H. Yang, J. Kłos, F. J. Aoiz, A. Gijsbertsen, A. E. Wiskerke and S. Stolte, *Nat. Chem.*, 2011, **3**, 597.

22 C. J. Eyles, M. Brouard, H. Chadwick, B. Hornung, B. Nichols, C.-H. Yang, J. Kłos, F. J. Aoiz, A. Gijsbertsen, a. E. Wiskerke and S. Stolte, *Phys. Chem. Chem. Phys.*, 2012, **14**, 5403.

23 G. Scoles, *Atomic and Molecular Beam Methods Volume 1*, Oxford University Press, 1988.

24 I. Estermann, *Rev. Mod. Phys.*, 1946, **18**, 300.

25 J. J. van Leuken, F. H. W. van Amerom, J. Bulthuis, J. G. Snijders and S. Stolte, *J. Phys. Chem.*, 1995, **99**, 15573.

26 A. Gijsbertsen, H. Linnartz, C. A. Taatjes and S. Stolte, *J. Am. Chem. Soc.*, 2006, **128**, 8777.

27 M. Brouard, H. Chadwick, C. J. Eyles, B. Hornung, B. Nichols, F. J. Aoiz, P. G. Jambrina and S. Stolte, *J. Chem. Phys.*, 2013, **138**, 104310.

28 M. Brouard, H. Chadwick, S. D. S. Gordon, B. Hornung, B. Nichols, J. Kłos, F. J. Aoiz and S. Stolte, *J. Chem. Phys.*, 2014, **141**, 164306.

29 B. Nichols, H. Chadwick, S. D. S. Gordon, C. J. Eyles, B. Hornung, M. Brouard, M. H. Alexander, F. J. Aoiz, A. Gijsbertsen and S. Stolte, *Chem. Sci.*, 2015, **6**, 2202.

30 M. Brouard, H. Chadwick, S. D. S. Gordon, B. Hornung, B. Nichols, F. J. Aoiz and S. Stolte, *J. Chem. Phys.*, 2016, **144**, 224301.

31 M. Kirste, X. Wang, H. C. Schewe, G. Meijer, K. Liu, A. van der Avoird, L. M. C. Janssen, K. B. Gubbels, G. C. Groenenboom and S. Y. T. van de Meerakker, *Science*, 2012, **338**, 1060.

32 O. Tkáč, A. K. Saha, J. Onvlee, C.-H. Yang, G. Sarma, C. K. Bishwakarma, S. Y. T. van de Meerakker, A. van der Avoird, D. H. Parker and A. J. Orr-Ewing, *Phys. Chem. Chem. Phys.*, 2014, **16**, 477.

33 G. Sarma, S. Marinakis, J. J. ter Meulen, D. H. Parker and K. G. McKendrick, *Nat. Chem.*, 2012, **4**, 985.

34 S. Y. van de Meerakker, H. L. Bethlem, N. Vanhaecke and G. Meijer, *Chem. Rev.*, 2012, **112**, 4828.

35 H. Bethlem, G. Berden and G. Meijer, *Phys. Rev. Lett.*, 1999, **83**, 1558.

36 H. Chadwick, M. Brouard, T. Perkins and F. J. Aoiz, *Int. Rev. Phys. Chem.*, 2014, **33**, 79.

37 M. Brouard, A. Bryant, I. Burak, S. Marinakis, F. Quadrini, I. A. Garcia and C. Vallance, *Mol. Phys.*, 2005, **103**, 1693.

38 M. Brouard, A. Bryant, Y. P. Chang, R. Cireasa, C. J. Eyles, A. M. Green, S. Marinakis, F. J. Aoiz and J. Kłos, *J. Chem. Phys.*, 2009, **130**, 044306.

39 M. Brouard, H. Chadwick, Y. P. Chang, R. Cireasa, C. J. Eyles, A. O. La Via, N. Screen, F. J. Aoiz and J. Kos, *J. Chem. Phys.*, 2009, **131**, 194307.

40 M. Brouard, H. Chadwick, Y. P. Chang, C. J. Eyles, F. J. Aoiz and J. Kłos, *J. Chem. Phys.*, 2011, **135**, 084306.

41 S. J. Mcgurk, J. B. Halpern, K. G. Mckendrick and M. L. Costen, *J. Phys. Chem. A*, 2014, **118**, 2007.

42 S. J. McGurk, K. G. McKendrick, M. L. Costen, M. H. Alexander and P. J. Dagdigian, *J. Chem. Phys.*, 2013, **139**, 124304.

43 I. Ballingall, M. F. Rutherford, K. G. McKendrick and M. L. Costen, *Mol. Phys.*, 2010, **108**, 847.

44 A. Alagappan, I. Ballingall, M. L. Costen, K. G. McKendrick and G. Paterson, *Phys. Chem. Chem. Phys.*, 2007, **9**, 747.

45 J. J. Kay, J. D. Steill, J. Kłos, G. Paterson, M. L. Costen, K. E. Strecker, K. G. McKendrick, M. H. Alexander and D. W. Chandler, *Mol. Phys.*, 2012, **110**, 1693.

46 J. J. Kay, G. Paterson, M. L. Costen, K. E. Strecker, K. G. McKendrick and D. W. Chandler, *J. Chem. Phys.*, 2011, **134**, 13.

47 J. D. Steill, J. J. Kay, G. Paterson, T. R. Sharples, J. Kłos, M. L. Costen, K. E. Strecker, K. G. McKendrick, M. H. Alexander and D. W. Chandler, *J. Phys. Chem. A*, 2013, **117**, 8163.

48 C. C. Wang, Y. P. Chen, T. L. Chin, H. Y. Huang and K. C. Lin, *J. Chem. Phys.*, 2000, **112**, 10204.

49 M. Drabbles, A. M. Wodtke, M. Yang and M. H. Alexander, *J. Phys. Chem. A*, 1997, **101**, 6463.

50 J. B. Halpern, R. Dopheide and H. Zacharias, *J. Phys. Chem.*, 1995, **99**, 13611.

51 C. B. Lucas, *Atomic and Molecular Beams: Production and Collimation*, CRC Press, 2014.

52 S. N. Vogels, J. Onvlee, A. Von Zastrow, G. C. Groenenboom, A. Van Der Avoird and S. Y. T. Van De Meerakker, *Phys. Rev. Lett.*, 2014, **113**, 263202.

53 A. von Zastrow, J. Onvlee, S. N. Vogels, G. C. Groenenboom, A. van der Avoird and S. Y. T. van de Meerakker, *Nat. Chem.*, 2014, **6**, 216.

54 M. a. Joffe, W. Ketterle, A. Martin and D. E. Pritchard, *J. Opt. Soc. Am. B*, 1993, **10**, 2257.

55 T. Cremers, S. Chefdeville, N. Janssen, E. Sweers, S. Koot, P. Claus and S. Y. T. van de Meerakker, *Phys. Rev. A*, 2017, **95**, 043415.

56 M. J. L. De Lange and M. Drabbels, *Chem. Phys. Lett.*, 1999, 491.

57 M. C. van Beek, J. J. ter Meulen and M. H. Alexander, *J. Chem. Phys.*, 2000, **113**, 637.

58 A. J. Orr-Ewing and R. N. Zare, *Annu. Rev. Phys. Chem.*, 1994, **45**, 315.

59 J. M. Hollas, *High Resolution Spectroscopy*, Butterworths, 1982.

60 W. Demtröder, *Laser Spectroscopy: Basic Concepts and Instrumentation*, Springer, 1998.

61 R. N. Zare and P. J. Dagdigian, *Science*, 1974, **185**, 4153.

62 J. L. Kinset, *Annu. Rev. Phys. Chem.*, 1977, **28**, 349.

63 J. Zhou, J. J. Lin, W. Shiu, S. C. Pu and K. Liu, *J. Chem. Phys.*, 2003, **119**, 2538.

64 C. R. Bieler, A. Sanov and H. Reisler, *Chem. Phys. Lett.*, 1995, **235**, 175.

65 Y. T. Lee, *Science*, 1987, **236**, 793.

66 L. Beneventi, P. Casavecchia and G. G. Volpi, *J. Chem. Phys.*, 1986, **85**, 7011.

67 P. Casavecchia, A. Lagana and G. G. Volpi, *Chem. Phys. Lett.*, 1984, **112**, 445.

68 M. A. Tesa-Serrate, B. C. Marshall, E. J. Smoll, S. M. Purcell, M. L. Costen, J. M. Slattery, T. K. Minton and K. G. McKendrick, *J. Phys. Chem. C*, 2015, **119**, 5491.

69 D. W. Chandler and P. L. Houston, *J. Chem. Phys.*, 1987, **87**, 1445.

70 D. H. Parker and A. T. J. B. Eppink, *J. Chem. Phys.*, 1997, **107**, 2357.

71 B. Whitaker, *Imaging in Molecular Dynamics: Technology and Applications*, Cambridge University Press, 2003.

72 D. Townsend, M. P. Minitti and A. G. Suits, *Rev. Sci. Instrum.*, 2003, **74**, 2530.

73 C. R. Gebhardt, T. P. Rakitzis, P. C. Samartzis, V. Ladopoulos and T. N. Kitsopoulos, *Rev. Sci. Instrum.*, 2001, **72**, 3848.

74 K. Amini, S. Blake, M. Brouard, M. B. Burt, E. Halford, A. Lauer, C. S. Slater, J. W. L. Lee and C. Vallance, *Rev. Sci. Instrum.*, 2015, **86**, 103113.

75 J. J. John, M. Brouard, A. Clark, J. Crooks, E. Halford, L. Hill, J. W. L. Lee, A. Nomerotski, R. Pisarczyk, I. Sedgwick, C. S. Slater, R. Turchetta, C. Vallance, E. Wilman, B. Winter and W. H. Yuen, *J. Instrum.*, 2012, **7**, C08001.

76 D. Rolles, Z. D. Pesic, M. Perri, R. C. Bilodeau, G. D. Ackerman, B. S. Rude, A. L. D. Kilcoyne, J. D. Bozek and N. Berrah, *Nucl. Instruments Methods Phys. Res. Sect. B Beam Interact. with Mater. Atoms*, 2007, **261**, 170.

77 A. G. Suits, C. K. Bishwakarma, L. Song, G. C. Groenenboom, A. van der Avoird and D. H. Parker, *J. Phys. Chem. A*, 2015, **119**, 5925.

78 C. K. Bishwakarma, G. van Oevelen, R. Scheidsbach, D. H. Parker, Y. Kalugina and F. Lique, *J. Phys. Chem. A*, 2016, **120**, 868.

79 O. Tkáč, Q. Ma, C. A. Rusher, S. J. Greaves, A. J. Orr-Ewing and P. J. Dagdigian, *J. Chem. Phys.*, 2014, **140**, 204318.

80 C. J. Eyles, M. Brouard, H. Chadwick, F. J. Aoiz, J. Kłos, A. Gijsbertsen, X. Zhang and S. Stolte, *Phys. Chem. Chem. Phys.*, 2012, **14**, 5420.

81 Z. Farooq, D. a Chestakov, B. Yan, G. C. Groenenboom, W. J. van der Zande and D. H. Parker, *Phys. Chem. Chem. Phys.*, 2014, **16**, 3305.

82 D. J. Hadden, G. M. Roberts, T. N. V Karsili, M. N. R. Ashfold and V. G. Stavros, *Phys. Chem. Chem. Phys.*, 2012, **14**, 13415.

83 Z. Lu, Y. C. Chang, Q. Yin, C. Y. Ng and W. M. Jackson, *Science*, 2014, **346**, 61.

84 J. H. D. Eland, R. Singh, J. D. Pickering, C. S. Slater, A. Hult Roos, J. Andersson, S. Zagorodskikh, R. J. Squibb, M. Brouard and R. Feifel, *J. Chem. Phys.*, 2016, **145**, 074303.

85 R. N. Zare and D. R. Herschbach, *Proc. IEEE*, 1963, **51**, 173.

86 Z. Xu, B. Koplitz and C. Wittig, *J. Phys. Chem.*, 1989, **90**, 2692.

87 A. Alagappan, I. Ballingall, M. L. Costen and K. G. McKendrick, *J. Chem. Phys.*, 2007, **126**, 041103.

88 M. L. Costen, S. Marinakis and K. G. McKendrick, *Chem. Soc. Rev.*, 2008, **37**, 732.

89 I. V. Hertel and W. Stoll, *Adv. At. Mol. Opt. Phys.*, 1978, **13**, 113.

90 T. P. Rakitzis and R. N. Zare, *J. Chem. Phys.*, 1999, **110**, 3341.

91 M. L. Costen, G. Hancock and G. A. D. Ritchie, *J. Phys. Chem. A*, 1999, **103**, 10651.

92 F. J. Aoiz, M. Brouard, P. A. Enriquez and R. Sayoss, *J. Chem. Soc. Faraday Trans*, 1993, **89**, 1427.

93 M. Brouard, H. Chadwick, C. J. Eyles, B. Hornung, B. Nichols, F. J. Aoiz, P. G. Jambrina, S. Stolte and M. P. De Miranda, *J. Chem. Phys.*, 2013, **138**, 104309.

94 M. P. De Miranda, F. J. Aoiz, L. Banares and V. S. Rabanos, *J. Chem. Phys.*, 1999, **111**, 5368.

95 R. N. Zare, *Angular Momentum: Understanding Spacial Aspects in Chemistry and Physics*, Wiley, 1988.

96 A. M. Arthurs and A. Dalgarno, *Proc. R. Soc. A Math. Phys. Eng. Sci.*, 1960, **256**, 540.

97 W. A. Lester, *At. Mol. Scatt.*, 1971, **10**, 211.

98 HIBRIDON is a package of programs for the time-independent quantum treatment of inelastic collisions and photodissociation written by M. H. Alexander, D. E. Manolopoulos, H.-J. Werner, B. Follmeg, and P. J. Dagdigian, with contributions by D. Lemoine, P. Vohralik, G. Corey, B. Johnson, T. Orlikowski, A. Berning, A. Degli-Esposti, C. Rist, B. Pouilly, J. Kłos, Q. Ma, G. van der Sanden, M. Yang, F. de Weerd, S. Gregurick, and F. Lique. More information and/or a copy of the code can be obtained from the website http://www2.chem.umd.edu/groups/alexander/hibridon/hib43.

99 F. J. Aoiz, M. Brouard, C. J. Eyles, J. F. Castillo and V. Sáez Rábanos, *J. Chem. Phys.*, 2006, **125**, 144105.

100 F. J. Aoiz, V. J. Herrero and I. Introduction, 1992, **97**, 7423.

101 M. A. Osborne and A. J. McCaffery, *J. Chem. Phys.*, 1994, **101**, 5604.

102 T. R. Sharples, T. F. M. Luxford, D. Townsend, K. G. McKendrick and M. L. Costen, *J. Chem. Phys.*, 2015, **143**, 204301.

103 R. T. Hall and J. M. Dowling, *J. Chem. Phys.*, 1966, **45**, 1899.

104 G. Herzberg, *Spectra of Diatomic Molecules*, Van Nostrand, 1950.

105 S. D. Jons, J. E. Shirley, M. T. Vonk, C. F. Giese and W. R. Gentry, *J. Chem. Phys.*, 1996, **105**, 5397.

106 M. T. Vonk, J. A. Bacon, C. F. Giese and W. R. Gentry, *J. Chem. Phys.*, 1997, **106**, 1353.

107 A. G. Suits, L. S. Bontuyan, P. L. Houston and B. J. Whitaker, *J. Chem. Phys.*, 1992, **96**, 8618.

108 L. S. Bontuyan, A. G. Suits, P. L. Houston and B. J. Whitaker, *J. Phys. Chem.*, 1993, **97**, 6342.

109 N. Yonekura, C. Gebauer, H. Kohguchi and T. Suzuki, *Rev. Sci. Instrum.*, 1999, **70**, 3265.

110 H. Kohguchi, T. Suzuki and M. H. Alexander, *Science*, 2001, **294**, 832.

111 J. I. Cline, K. T. Lorenz, E. A. Wade, J. W. Barr and D. W. Chandler, *J. Chem. Phys.*, 2001, **115**, 6277.

112 M. S. Elioff and D. W. Chandler, *J. Chem. Phys.*, 2002, **117**, 6455.

113 M. Brouard, H. Chadwick, C. J. Eyles, B. Hornung, B. Nichols, J. M. Scott, F. J. Aoiz, J. Kłos, S. Stolte and X. Zhang, *Mol. Phys.*, 2013, **111**, 1759.

114 M. Brouard, H. Chadwick, S. D. S. Gordon, B. Hornung, B. Nichols, F. J. Aoiz and S. Stolte, *J. Phys. Chem. A*, 2015, **119**, 12404.

115 H. Chadwick, B. Nichols, S. D. S. Gordon, B. Hornung, E. Squires, M. Brouard, J. Kłos, M. H. Alexander, F. J. Aoiz and S. Stolte, *J. Phys. Chem. Lett.*, 2014, **5**, 3296.

116 J. J. van Leuken, J. Bulthuis, S. Stolte and J. G. Snijders, *Chem. Phys. Lett.*, 1996, **260**, 595.

117 M. Brouard, S. D. S. Gordon, A. Hackett Boyle, C. G. Heid, B. Nichols, V. Walpole, F. J. Aoiz and S. Stolte, *J. Chem. Phys.*, 2017, **146**, 014302.

118 F. J. Aoiz, M. Brouard, S. D. S. Gordon, B. Nichols, S. Stolte and V. Walpole, *Phys. Chem. Chem. Phys.*, 2015, **17**, 30210.

119 J. Onvlee, S. N. Vogels, A. Von Zastrow, D. H. Parker and S. Y. T. van de Meerakker, *Phys. Chem. Chem. Phys.*, 2014, **17**, 12365.

120 M. Lemeshko and B. Friedrich, *J. Chem. Phys.*, 2008, **129**, 024301.

121 S. N. Vogels, J. Onvlee, S. Chefdeville, A. van der Avoird, G. C. Groenenboom and S. Y. T. van de Meerakker, *Science*, 2015, **350**, 787.

122 J. Onvlee, A. Van Der Avoird, G. Groenenboom and S. Y. T. Van De Meerakker, *J. Phys. Chem. A*, 2016, **120**, 4770.

123 P. Jansen, D. W. Chandler and K. E. Strecker, *Rev. Sci. Instrum.*, 2009, **80**, 083105.

124 T. F. M. Luxford, T. R. Sharples, K. G. McKendrick and M. L. Costen, *J. Chem. Phys.*, 2016, **145**, 174304.

125 Sirah Laser- und Plasmatechnik GmbH, *Pulsed Dye Laser Service Manual*, 1998.

126 U. Fano and J. H. Macek, *Rev. Mod. Phys.*, 1973, **45**, 553.

127 G. E. Hall and M. Wu, *J. Phys. Chem.*, 1993, **97**, 10911.

128 H. S. Im and E. R. Bernstein, *J. Phys. Chem. A*, 2002, **106**, 7565.

129 V. Dribinski, A. Ossadtchi, V. A. Mandelshtam and H. Reisler, *Rev. Sci. Instrum.*, 2002, **73**, 2634.

130 M. Reynolds, B.Sc. Dissertation, Heriot-Watt, 2013.

131 H. Scheingraber and C. R. Vidal, *J. Opt. Soc. Am. B*, 1985, **2**, 343.

132 T. F. M. Luxford, T. R. Sharples, D. Townsend, K. G. McKendrick and M. L. Costen, *J. Chem. Phys.*, 2016, **145**, 084312.

133 E. A. Wade, K. Thomas Lorenz, D. W. Chandler, J. W. Barr, G. L. Barnes and J. I. Cline, *Chem. Phys.*, 2004, **301**, 261.

134 M. Brouard, H. Chadwick, Y. Chang, B. J. Howard, S. Marinakis, N. Screen, S. A. Seamons and A. La Via, *J. Mol. Spectrosc.*, 2012, **282**, 42.

135 J. A. Guest, M. A. O'Halloran and R. N. Zare, 1984, **103**, 261.

136 K. L. Reid, *Chem. Phys. Lett.*, 1993, **215**, 25–30.

137 R. Altkorn, R. N. Zare and C. H. Greene, *Mol. Phys.*, 1985, **55**, 1.

138 D. Manura and D. Dahl, *SIMION (R) 8.0 User Manual*, Scientific Instrument Services, Inc., 2008.

139 W. H. Press, S. A. Teukolsky, W. T. Vetterling and B. P. Flannery, *Numerical Recipes in Fortran 90: The Art of Parallel Scientific Computing, Second Edition*, Cambridge University Press, 1997.

140 A. Von Zastrow, J. Onvlee, D. H. Parker and S. Y. T. Van De Meerakker, *EPJ Tech. Instrum.*, 2015, **2**, 11.

141 K. T. Lorenz, M. S. Westley and D. W. Chandler, 2000, **2**, 481.

142 H. Kohguchi, T. Suzuki and M. H. Alexander, *Science*, 2001, **294**, 832.

143 R. C. Woods and T. A. Dixon, *J. Chem. Phys.*, 1976, **64**, 5319.

144 V. Khare, D. J. Kouri and D. K. Hoffman, *J. Chem. Phys.*, 1981, **74**, 2275.

145 M. Faubel, *J. Chem. Phys.*, 1984, **81**, 5559.

146 O. Tkáč, A. G. Sage, S. J. Greaves, A. J. Orr-Ewing, P. J. Dagdigian, Q. Ma and M. H. Alexander, *Chem. Sci.*, 2013, **4**, 4199.

147 C. H. Yang, G. Sarma, J. J. Ter Meulen, D. H. Parker, U. Buck and L. Wiesenfeld, *J. Phys. Chem. A*, 2010, **114**, 9886.

148 P. Pajón-Suárez, G. Rojas-Lorenzo, J. Rubayo-Soneira and R. Hernández-Lamoneda, *Chem. Phys. Lett.*, 2006, **421**, 389.

149 G. C. Corey, M. H. Alexander and J. Schaefer, *J. Chem. Phys.*, 1986, **85**, 2726.

150 H. Cybulski and B. Fernández, *J. Phys. Chem. A*, 2012, **116**, 7319–28.

151 M. Yang and M. H. Alexander, *J. Chem. Phys.*, 1995, **103**, 6973.

152 M. Brouard and C. Vallance, *Tutorials in Molecular Reaction Dynamics*, RSC Publishing, 2012.

153 V. L. Ayles, R. J. Plowright, M. J. Watkins, T. G. Wright, J. Kłos, M. H. Alexander, P. Pajón-Suárez, J. Rubayo-Soneira and R. Hernández-Lamoneda, *Chem. Phys. Lett.*, 2007, **441**, 181.

154 H. L. Holmes-Ross, R. J. Valenti, H. G. Yu, G. E. Hall and W. D. Lawrance, *J. Chem. Phys.*, 2016, **144**, 044309.

155 S. Bosanac and U. Buck, *Chem. Phys. Lett.*, 1981, **81**, 315.

156 M. H. Alexander, *J. Chem. Phys.*, 1976, **64**, 4498.

157 Y. Kim, H. Meyer and M. H. Alexander, *J. Chem. Phys.*, 2004, **121**, 1339.

158 A. a. Dixit, P. J. Pisano and P. L. Houston, *J. Phys. Chem. A*, 2001, **105**, 11165.

159 G. Ziegler, S. V. K. Kumar, H.-G. Rubahn, A. Kuhn, B. Sun and K. Bergmann, *J. Chem. Phys.*, 1991, **94**, 4252.

160 C. H. Yang, G. Sarma, D. H. Parker, J. J. Ter Meulen and L. Wiesenfeld, *J. Chem. Phys.*, 2011, **134**, 204308.

161 O. Tkáč, A. K. Saha, J. Loreau, Q. Ma, P. J. Dagdigian, D. H. Parker, A. Van Der Avoird and A. J. Orr-Ewing, *Mol. Phys.*, 2015, **113**, 3925.

162 M. S. Westley, K. T. Lorenz, D. W. Chandler and P. L. Houston, *J. Chem. Phys.*, 2001, **114**, 2669.

163 P. Pajón-Suárez, M. Valentín-Rodríguez and R. Hernández-Lamoneda, *Chem. Phys. Lett.*, 2016, **658**, 176.

164 J. Kłos, M. H. Alexander and P. J. Dagdigian, *J. Chem. Phys.*, 2017, **146**, 114301.

165 S. T. Pratt, P. M. Dehmer and J. L. Dehmer, *J. Chem. Phys.*, 1987, **86**, 1727.

166 J. Kłos, G. Chałasiński, M. T. Berry, R. Bukowski and S. M. Cybulski, *J. Chem. Phys.*, 2000, **112**, 2195.

167 P. J. Crutzen, *Ann. Rev. Earth Planet. Sci.*, 1979, **7**, 443.

168 R. L. Klein, S. Schwartz and L. D. Schmidt, *J. Phys. Chem.*, 1985, **89**, 4908.

169 G. A. Lavoie, J. B. Heywood and J. C. Keck, *Combust. Sci. Technol.*, 1970, **1**, 313.

170 E. A. Wade, K. T. Lorenz, J. L. Springfield and D. W. Chandler, *J. Phys. Chem. A*, 2003, **107**, 4976.

171 O. Tkáč, Q. Ma, M. Stei, A. J. Orr-ewing, A. J. Orr-ewing, and P. J. Dagdigian, *J. Chem. Phys.*, 2015, **142**, 014306.

172 M. C. Drake and J. W. Ratcliffe, *J. Chem. Phys.*, 1993, **98**, 3850.

173 J. Few and G. Hancock, *Phys. Chem. Chem. Phys.*, 2014, **16**, 11047.

174 T. B. Settersten, B. D. Patterson, H. Kronemayer, V. Sick, C. Schulz and J. W. Daily, *Phys. Chem. Chem. Phys.*, 2006, **8**, 5328.

175 T. B. Settersten, B. D. Patterson, C. D. Carter, A. Force, A. Rza and W. A. Force, *J. Chem. Phys.*, 2009, **130**, 204302.

176 J. W. Thoman, Jr., J. A. Gray, J. L. Durant, Jr. and P. H. Paul, *J. Chem. Phys.*, 1992, **97**, 8156.

177 J. Lozeille, S. E. Daire, S. D. Gamblin, T. G. Wright and E. P. F. Lee, *J. Chem. Phys.*, 2000, **113**, 10952.

178 S. Lee, J. Luque, J. Reppel, A. Brown and D. R. Crosley, *J. Chem. Phys.*, 2004, **121**, 1373.

179 P. H. Paul, J. A. Gray, J. L. Durant and J. W. Thoman, *Appl. Phys. B Photophysics Laser Chem.*, 1993, **57**, 249.

180 C. Cerezo and M. Martin, *J. Photochem. Photobiol. A Chem.*, 2000, **134**, 127.

181 J. L. Cooper and J. C. Whitehead, *J. Chem. Soc. Faraday Trans.*, 1993, **89**, 1287.

182 G. Richmond, M. L. Costen and K. G. McKendrick, *J. Phys. Chem. A*, 2005, **109**, 542.